

2-1
mix



NATIONAL AERONAUTICS AND SPACE ADMINISTRATION

COLOR ILLUSTRATIONS REPRODUCED
IN BLACK AND WHITE

SECOND ANNUAL
EARTH RESOURCES AIRCRAFT PROGRAM
STATUS REVIEW

VOLUME III
HYDROLOGY AND OCEANOGRAPHY

Presented at the

NASA Manned Spacecraft Center
Houston, Texas

September 16 to 18, 1969

FACILITY FORM 602

N71-11151

(ACCESSION NUMBER)

372

(PAGES)

TMX-66481

(NASA CR OR TMX OR AD NUMBER)

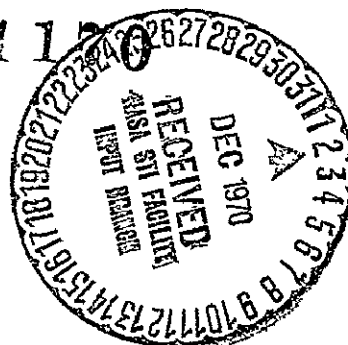
(THRU)

62

(CODE)

13

(CATEGORY)



MANNED SPACECRAFT CENTER
HOUSTON, TEXAS

Reproduced by
NATIONAL TECHNICAL
INFORMATION SERVICE
Springfield, Va. 22151

FOREWORD

On September 16, 17, and 18, a review of various aspects of the Earth Resources Program was held at the Manned Spacecraft Center, Houston, Texas. Particular emphasis was placed on the results of analysis of data obtained with the Manned Spacecraft Center and other aircraft which have contributed data to the program.

The review was arranged in conjunction with the Department of Interior, Department of Agriculture and the Department of the Navy. Attendees and participants at the meeting included program investigators, their immediate associates, and program representatives from the above named agencies and ESSA and NASA.

The review was divided into the disciplinary areas of Geology, Geography, Hydrology, Agriculture and Forestry, and Oceanography. An additional session was held on instrumentation. Program investigators presented the results of their work in each of these areas. The material presented is being published in three volumes:

Vol I - GEOLOGY AND GEOGRAPHY

Vol II - AGRICULTURE, FORESTRY, AND SENSOR STUDIES

Vol III - HYDROLOGY AND OCEANOGRAPHY

The review provided a current assessment of the program for both management and technical personnel. It is important to note that the material presented represented the current status on ongoing programs and consequently complete technical analyses will be available at a later date.

COLOR ILLUSTRATIONS REPRODUCED
IN BLACK AND WHITE

CONTENTS OF VOLUME I

Section		Page
	FOREWORD	iii
1	GEOLOGIC APPLICATIONS PROGRAM — SUMMARY OF RECENT PROGRESS AND PLANS	1-1
	By William R. Hemphill	
2	APPLICATION OF COMPUTER PROCESSED MULTISPECTRAL DATA TO THE DISCRIMINATION OF LAND COLLAPSE (SINKHOLE) PRONE AREAS IN FLORIDA	2-1
	By A. E. Coker, R. Marshall, and N. S. Thomson	
3	DIGITAL COMPUTER TERRAIN MAPPING FROM MULTI- SPECTRAL DATA, AND EVALUATION OF PROPOSED EARTH RESOURCES TECHNOLOGY SATELLITE (ERTS) DATA CHANNELS, YELLOWSTONE NATIONAL PARK: PRELIMINARY REPORT	3-1
	By Harry W. Smedes, Kenneth L. Pierce, Marc G. Tanguay, and Roger M. Hoffer	
4	GEOLOGIC ANALYSIS OF THE X-BAND RADAR MOSAICS OF MASSACHUSETTS	4-1
	By Lincoln R. Page	
5	THERMAL INFRARED INVESTIGATIONS, MILL CREEK AREA, OKLAHOMA	5-1
	By L. C. Rowan, T. W. Offield, Kenneth Watson, R. D. Watson, and P. J. Cannon	
6	REMOTE SENSING TECHNIQUES AS APPLIED TO COASTAL SEDIMENTATION, SOUTH TEXAS	6-1
	By Henry L. Berryhill, Jr.	
7	REMOTE DETECTION OF GEOCHEMICAL SOIL ANOMALIES	7-1
	By F. C. Canney	
8	GEOLOGIC UTILITY OF SMALL-SCALE AIRPHOTOS	8-1
	By Malcolm M. Clark	

Section		Page
9	EFFECTIVE RADAR LOOK-DIRECTION FOR GEOLOGIC INTERPRETATION	9-1
	By H. C. McDonald	
10	CARTOGRAPHY	10-1
	By Alden P. Calvocoresses	
11	SUMMARY OF OBJECTIVES AND PROGRESS IN THE GEOGRAPHIC APPLICATIONS PROGRAM	11-1
	By Arch C. Gerlach	
12	REMOTE SENSING ANALYSIS OF GRASSLAND FIRE PHENOMENA: THE FLORIDA TEST SITES, 1968-69	12-1
	By Merle C. Prunty	
13	THEMATIC LAND USE MAPPING: SOME POTENTIALS AND PROBLEMS	13-1
	By David S. Simonett	
14	IMPERIAL VALLEY LAND USE STUDIES: A CONTINUUM FROM MISSION 73 TO APOLLO IX	14-1
	By Claude W. Johnson	
15	HOUSING QUALITY IN URBAN AREAS: DATA ACQUISITION AND CLASSIFICATION THROUGH THE ANALYSIS OF REMOTE SENSOR IMAGERY	15-1
	By Frank E. Horton and Duane F. Marble	
16	SURFACE ENERGY EXCHANGE PHENOMENA INTERPRETED FROM IR EXPERIMENTS	16-1
	By Robert W. Pease	
17	GEOGRAPHY PROGRAM REVIEW AND INTEGRATION	17-1
	By Robert H. Alexander	

CONTENTS OF VOLUME II

Section		Page
18	VEGETATION RESOURCE — USER REQUIREMENTS VERSUS REMOTE-SENSING CAPABILITIES	18-1
	By Robert Colwell and William Draeger	
19	MULTISTAGE SAMPLING OF FOREST RESOURCES BY USING SPACE PHOTOGRAPHY	19-1
	By Philip G. Langley, Robert C. Aldrich and Robert C. Heller	
20	RANGE RESOURCE INVENTORY FROM SPACE AND SUPPORTING AIRCRAFT PHOTOGRAPHY	20-1
	By Charles E. Poulton	
21	MULTIPLE RESOURCE INVENTORY ON SPACE AND HIGH-ALTITUDE PHOTOGRAPHY	21-1
	By Lawrence R. Pettinger	
22	INTERACTION OF ELECTROMAGNETIC ENERGY WITH AGRICULTURAL CROPS	22-1
	By Craig L. Wiegand, Harold W. Gausman, William A. Allen, and Ross W. Leamer	
23	APPLICATION OF AUTOMATIC RECOGNITION TECHNIQUES TO EARTH RESOURCES	23-1
	By R. B. MacDonald	
24	AUTOMATIC PROCESSING OF EARTH RESOURCE DATA	24-1
	By D. A. Landgrebe	
25	MULTISPECTRAL DATA COLLECTION AND INSTRUMENTATION STUDIES	25-1
	By D. S. Lowe	

Section		Page
26	AIRBORNE INFRARED SPECTRAL STUDY OF IGNEOUS ROCKS IN SONORA PASS TEST SITE	26-1
	By I. A. Kilinc and R. J. P. Lyon	
27	DATA PROCESSING AND PATTERN RECOGNITION STUDIES OF MULTISPECTRAL SIGNALS	27-1
	By M. Holter	
28	USE OF PASSBAND INTERFERENCE FILTERS IN MULTISPECTRAL PHOTOGRAPHY	28-1
	By Philip N. Slater and Dean B. McKenney	
29	MULTISPECTRAL VIEWERS	29-1
	By Edward Yost	
30	MICROWAVE STUDIES AND INSTRUMENTATION FOR THE EARTH RESOURCES PROGRAM	30-1
	By John C. Blinn III	
31	GROUND TRUTH/SENSOR CORRELATION	31-1
	By Peter Chapman, Jack Quade, and Peter Brennan	
32	RADAR AND DATA PROCESSING	32-1
	By Richard K. Moore	
33	RECENT PROGRESS IN TANK, SHIPBOARD, AND HELICOPTER TESTS OF THE FRAUNHOFER LINE DISCRIMINATOR	33-1
	By George E. Stoertz and William R. Hemphill	
34	EXPERIMENTAL RESULTS IN THE REMOTE SENSING OF GASES FROM HIGH ALTITUDES	34-1
	By A. R. Barringer and J. H. Davies	

CONTENTS OF VOLUME III

Section		Page
35	APPLICATION OF INFRARED IMAGERY IN STUDYING THERMAL CHARACTERISTICS OF A COOLING RESERVOIR	35-1 ✓
	By J. F. Turner	
36	COLOR INFRARED AND THERMAL INFRARED SENSING OF HYDROLOGIC FEATURES IN NORTHERN COOK INLET, ALASKA	36-1 ✓
	By W. W. Barnwell	
37	RELATION OF REMOTE SENSING TO TRANSPIRATION OF FLOOD PLAIN VEGETATION	37-1 ✓
	By Richard C. Culler and Raymond M. Turner	
38	SYNOPTIC REMOTE SENSING SURVEY OF LAKES IN WEST-CENTRAL FLORIDA	38-1 ✓
	By J. W. Stewart	
39	REMOTE SENSING OF OFFSHORE SPRINGS AND SPRING DISCHARGE ALONG THE GULF COAST OF CENTRAL FLORIDA	39-1 ✓
	By J. D. Hun and R. N. Cherry	
40	THE USE OF COLOR INFRARED PHOTOGRAPHY AND THERMAL IMAGERY IN MARSHLAND AND ESTUARINE STUDIES	40-1 ✓
	By Richard R. Anderson	
41	A THERMAL SURVEY OF THE CONNECTICUT RIVER ESTUARY	41-1 ✓
	By F. H. Ruggles, Jr.	
42	MULTISPECTRAL DATA COLLECTION AND PROCESSING TECHNIQUES APPLIED TO HYDROBIOLOGICAL INVESTIGATION, EVERGLADES NATIONAL PARK, FLORIDA	42-1 ✓
	By M. C. Kolipinski	

Section		Page
43	SNOW AND ICE SENSING WITH PASSIVE MICROWAVE AND GROUND TRUTH INSTRUMENTATION: RECENT RESULTS, SOUTH CASCADE GLACIER	43-1 ✓
	By A. T. Edgerton and M. Meier	
44	USE OF INFRARED RADIOMETRY IN MEASURING GROUND-WATER INFLOW TO STREAMS, DELMARVA PENINSULA, MARYLAND AND DELAWARE	44-1 ✓
	By E. F. Hollyday	
45	PRELIMINARY REPORT ON REMOTE SENSING IN WATER-RESOURCES STUDIES IN YELLOWSTONE NATIONAL PARK, WYOMING	45-1 ✓
	By Edward R. Cox	
46	SNOWFIELD MAPPING WITH K-BAND RADAR	46-1 ✓
	By William P. Waite and Harold C. McDonald	
47	PASSIVE MICROWAVE STUDIES	47-1 ✓
	By James P. Hollinger	
48	RADAR AND OCEANOGRAPHY	48-1 ✓
	By Richard K. Moore	
49	SEA-SURFACE TEMPERATURE AND HEAT FLOW - BOMEX	49-1 ✓
	By E. D. McAlister	
50	EXPERIMENTAL RESULTS OF THE REMOTE MEASURE- MENT OF OCEAN FLOOR	50-1 ✓
	By Peter G. White	
51	EXPERIMENTS IN OCEANOGRAPHIC AEROSPACE PHOTOGRAPHY BEN FRANKLIN SPECTRAL FILTER TESTS	51-1 ✓
	By D. S. Ross and R. C. Jensen	

Section		Page	
52	DEPTH DETERMINATION BY MEASURING WAVE SURFACE EFFECTS	52-1	✓
	By F. C. Polcyn		
53	THE STUDY OF COASTAL ECOLOGY USING REMOTE PHOTOGRAPHY	53-1	✓
	By Mahlon G. Kelly		

TABLES

Table		Page
36-1	FLIGHT AND INSTRUMENTATION DATA, NASA AIRCRAFT 927 REMOTE-SENSING FLIGHTS OVER UPPER COOK INLET, ALASKA	36-10
41-1	ENVIRONMENTAL DATA FOR CONNECTICUT RIVER ESTUARY, SEPTEMBER 9, 1969	41-6
43-1	SNOW MOISTURE DATA	43-7
51-1	SUMMARY OF NORMALIZED DENSITIES	51-13
51-2	CALIBRATION DATA FOR WIDE SLITS	51-14

FIGURES

Figure		Page
	N71-11151	
35-1	Schematic diagram of the thermal loading and heat disposal processes	35-7
35-2	Map of Roxboro Lake showing location of temperature monitors and general circulation of heated water	35-8
35-3	Thermal map of Roxboro Lake during remote sensing flight	35-9
35-4	Map of Roxboro Lake showing thermal characteristics within the heated area	35-10
36-1	Upper Cook Inlet, area of remote-sensing study (including index map of Alaska and flight lines of 11 and 13 May, 1967)	36-11
36-2	Trace of infrared imagery showing indicated temperature variations in Cook Inlet water near Fire Island	36-12
36-3	Trace of infrared imagery showing relatively cold glacial-melt water flowing into warmer Turnagain Arm water	36-13
36-4	Color infrared photograph showing difference in color between silt-laden water (light, blue grey) and clear lake water (dark blue). Photograph of Palmer, Alaska, area 50 miles northeast of Anchorage	36-14
36-5	Color infrared photograph of part of Anchorage lowland showing tonal differentiation of well-drained areas (light tones) from swampy, low-lying areas (darker tones)	36-14
36-6	Anchorage Alaska Lowland	
a.	Trace of the pattern of infrared imagery of a part of the Anchorage lowland showing differentiation of swampy areas from well-drained areas	36-15

Figure		Page
	b. Map of the surficial geology of an area covered in Figure 6a showing correlation of "swamp deposit" with dark (= cold) areas on the infrared imagery	36-16
37-1	Mean optical density values from Ektachrome IR images of a 1300-acre saltcedar forest, Gila River, Arizona	37-6
37-2	Adjusted mean optical density valued from Ektachrome IR images of 364 forest plots within a 1300-acre saltcedar forest, Gila River, Arizona	37-7
37-3	Seasonal variance of adjusted red filter densities obtained from Ektachrome IR images of a saltcedar forest, Gila River, Arizona	37-8
38-1	Map of west-central Florida showing study area - 1968	38-16
38-2	Thermal IR imagery and color IR photography of a swamp - marsh area about 20 miles north-northwest of Tampa	
	a. Thermal IR imagery, October 10, 1968	38-17
	b. Color IR photography, November 8, 1968	38-17
38-3	A black and white print of color IR photograph and thermal IR image of Lake Iola	38-18
38-4	Thermal IR imagery and color IR photography of an artesian spring discharging into a stream, Tampa	
	a. Infrared imagery, October 10, 1968; predawn	38-19
	b. Infrared imagery, November 8, 1968; predawn	38-19
	c. Color infrared photography February 28, 1968	38-19

Figure		Page
38-5	Sunshine and Dosson Lakes	38-20
38-6	Lakes Horse and Bonnie	38-21
38-7	Artificial lake near a mine quarry about 5 miles north of Brooksville	38-22
38-8	Destruction of a small coastal lake, May 1964 and February 1968	38-23
38-9	Color IR photography and thermal IR imagery of an area north of Tampa illustrating the effects of changes in land use and land form on the hydrology of an area	38-24
38-10	Encroachment of subdivision in a swamp- marsh-lake area, Pasco County	38-25
38-11	Differences in color of water surface in lakes dredged at different periods for subdivision developments	38-26
38-12	Borrow pit lake showing differences in color of water surface and infestation of parts of lake by water hyacinth	38-27
38-13	The development of shore-line features and offshore islands in a lake showing large declines in water level in the ridge area	38-28
38-14	Color IR photography of a pond and a lake in the ridge area showing concentric banding of vegetation. Photography obtained by NASA November 8, 1968 at an altitude of 2,000 feet using Wratten 15G filter	38-29
38-15	Color and color IR photography of a lake in the ridge area draining a limestone quarry	
a.	Color photography of Lake Bystre	38-30
b.	Color IR photography of Lake Bystre using Wratten 15G filter	38-30

Figure		Page
38-16	White Turkey Pond	38-31
38-17	Lake discharging into a drainsink in ridge area	38-32
39-1	Map of Middle Gulf area	39-4
39-2	Imagery showing a temperature contrast caused by warmer ground water dis- charging into the Gulf of Mexico at Crystal Beach Spring	39-5
39-3	Spring discharge, when warmer than the Gulf of Mexico, is shown by a light area on the thermal imagery	39-6
39-4	Spring discharge shows as a dark area on 8-14 micron thermal imagery for May 15, 1969	
	a. Island	39-7
	b. Tidal flat	39-7
40-1	Imaging characteristics of marsh species with color IR film and selected filters	
	a. Wratten 15-G filter	40-19
	b. Wratten 57 filter	40-19
	c. Wratten 15-G filter	40-19
	d. Wratten 25-A filter	40-19
40-2	Shows ability of color IR film to delineate plant species important in wildlife ecology	40-21
40-3	Enhancement of image quality of submerged vegetation with overexposure of color IR film	
	a. Overexposed	40-22
	b. Normal exposure	40-22

Figure		Page
40-4	Shows seasonal change in image characteristics of marsh vegetation using color IR film .	
	a. Spring	40-23
	b. Fall	40-23
40-5	Distribution of mud flats along the estuary and light tonal quality of heavily sedimented water	
	a. Wratten 25 and Wratten 15-G filters	40-24
	b. Wratten 25 and Wratten 15-G filters	40-24
40-6	Day thermal image showing water temperature variation and tonal characteristics of Phragmites (Reed)	40-25
40-7	Day and night time imagery compared	40-26
40-8	Compares tonal variation of cool water entering the estuary from a creek	
	a. Day	40-27
	b. Night	40-27
40-9	Shows tonal variation and temperatures of marsh below area where ground water seepage occurs	40-28
40-10	Shows tonal variation and temperatures of marsh in area of ground water seepage	40-29
41-1	Location map of the Connecticut River estuary	41-7
41-2	Discharge and stage of the Connecticut River estuary at Haddam Neck, Connecticut on September 9, 1968	41-8
41-3	Infrared imagery data for periods of up-stream and downstream flow at the Connecticut Yankee Atomic Plant, September 9, 1968	41-9

Figure		Page
41-4	Infrared imagery data near the mouth of the Connecticut River estuary on September 9, 1968	41-10
41-5	Infrared imagery data for the Connecticut River estuary at Hartford, Connecticut on September 9, 1968	41-11
41-6	Recorded radiometer data for the Connecticut River estuary September 9, 1968	41-12
42-1	Map of Everglades National Park indicating the location of Shark River Slough, Taylor Slough, and the approximate position of the inter- face between fresh water and brackish water along the coast	42-20
42-2	Annotated diagram of the major plant communities in the Shark River Slough	42-21
42-3	The 50 percent sensitivity points of various film-filter combinations and of the 12-channel spectrometer	42-22
42-4	Multispectral data collection operations	42-23
42-5	Conceptual sectioned view of existing spectrometer detector system	42-24
42-6	Block diagram of multispectral data processing operations	42-25
42-7	Color-composite recognition map of hydrobiological features in a portion of the Shark Valley Slough in the Everglades National Park	42-26
43-1	Microwave field laboratory	43-8
43-2	Brightness temperature variations as a function of thermometric temperature and snow moisture	43-9

Figure		Page
43-3	Penetration experiment	43-10
43-4	Plate experiment to determine microwave penetration	43-11
43-5	Snow attenuation experiment	43-12
43-6	New microwave field laboratory	43-13
43-7	19.35 GHz microwave imagery of Mt. Rainier (white 281°K, 1-2°K per color step)	43-14
43-8	Shaded relief sketch of Mt. Rainier	43-14
43-9	Geometry of data obtained by a microwave imager flow over rugged terrain	43-15
44-1	Heat budget for determining ground-water inflow	44-10
44-2	Ground-Control survey of temperature and discharge of Little Burnt Branch	44-11
44-3	Example of heat-budget calculation of ground-water inflow using ground-control data	44-12
44-4	Correlation of radiometric temperature and true water-body temperature for field calibration of airborne radiometer	44-13
44-5	Results of remote and ground survey of ground- water inflow to Beaverdam Creek	44-14
45-1	Map of Yellowstone National Park, Wyoming, showing locations of site-reference points and approximate coverage of infrared imagery from the September 1967 mission	45-9
46-1	SLAR imaging system	
	a. Ground coverage	46-13
	b. Hypothetical swath width and respec- tive incidence angles	46-13
	c. Effect of terrain slopes on incidence angles	46-13

Figure		Page
46-2	Radar imagery and photography, Sonora Pass area, California	46-14
46-3	Radar imagery and photography comparison, Yellowstone Park area, Wyoming	46-15
46-4	Radar-photo comparison, Yellowstone River area, Wyoming	46-16
46-5	Effective snow penetration by radar	
	a. Radar look-direction, west	46-17
	b. Radar look-direction, east	46-17
	c. Simultaneous photograph	46-17
46-6	Mapped glaciers, Three Sisters area, Oregon	46-18
46-7	Radar imagery at Three Sisters area, Oregon, and Glacier Peak area, Washington	46-19
46-8	Relative dielectric constant of snow versus density	46-20
46-9	Loss tangent of ice versus frequency and temperature	46-21
46-10	Dielectric constant of wet snow versus volume percentage of liquid water	46-22
47-1	Temperature data versus angle of incidence, run no. 5, 1.6 cm	47-7
47-2	Temperature data versus angle of incidence, run no. 5, 3.6 cm	47-8
47-3	Brightness temperature data versus angle of incidence for horizontal and vertical components, 1.6 cm	47-9
47-4	Brightness temperature data versus angle of incidence for horizontal and vertical components, 3.6 cm	47-10

Figure		Page:
47-5	Percentage polarization data versus angle of incidence, 1.6 cm and 3.6 cm	47-11
47-6	Fifty degree incidence angle, 1.6 cm	47-12
48-1	Summary of sea-state scatterometry data	48-14
48-2	Differential scattering coefficient of ocean at 2.25 cm wavelength	48-15
48-3	Wind speed in knots	48-16
48-4	Comparison of crosswind and upwind data	48-17
48-5	Differential scattering coefficient of ocean	48-18
48-6	Doppler scatterometer measurement geometry	48-19
48-7	Block diagram of 13.3 GHz radar scatter- ometer	48-20
48-8	13.3 GHz scatterometer digital processing - present system	48-21
48-9	13.3 scatterometer power spectral density - for sea measurements	48-22
48-10	Typical scatterometer power spectrum - for agricultural terrain	48-23
48-11	Selective spectral editing to reduce interface	48-24
48-12	Procedure used in digital data processing for improving data validity by removal of the scatter- ometer system noise from the data spectrum	48-25
48-13	The effect of saturation on the scatter- ometer data frequency spectrum	48-26
48-14	Scheme for S/N enhancement - like noise signals	48-27

Figure		Page
48-15	Comparison of attenuation calculated from sky-brightness with attenuation measured by a sun-tracking radio-telescope	48-28
48-16	Satellite mounted scatterometer for sea-state measurements	48-29
48-17	Range of error as a function of the number of pulses averaged	48-30
49-1	Record 15, 27 May 1969, 2220Z	49-7
49-2	Summary of averages for each record and blackbody temperatures	49-8
49-3	Tabulation of radiation differences	49-9
49-4	Tabulation of final data reduction	49-10
49-5	Data reduction	49-11
49-6	Reflectivity ratio - rough sea to smooth sea . . .	49-12
49-7	Total heat flow calculation	49-13
49-8	Water temperature at depths indicated near FLIP	49-14
49-9	The need for sky corrections in radiometric sea surface readings	49-15
49-10	Preliminary BOMEX results	49-16
50-1	Remote measurement of the spectral reflectance of very clear waters	50-4
50-2	Remote measurement of the spectral reflectance of water with high plankton (chlorophyceae) content	50-5
50-3	Remote measurement of the spectral reflectance of water with high plankton (Gonyaulax) content	50-6
50-4	Remote measurement of water containing various chlorophyll concentrations	50-7

Figure		Page
50-5	Effect of atmospheric haze on reflectance versus wavelength measurements	50-8
50-6	Spectral reflectance curves recorded in a 3 mile flight path	50-9
51-1	Top deck of Grumman submersible, Ben Franklin	51-17
51-2	R4-B four-lens multispectral camera	51-18
51-3	Transmittance of filters in R4-B multispectral camera for Ben Franklin experiment	51-19
51-4	Ben Franklin	
	a. On the surface	51-20
	b. At 10 meters	51-21
	c. At 15 meters	51-22
	d. At 25 meters	51-23
51-5	Log decrease of Ben Franklin image density with depth by spectral band	51-24
51-6	Bimini Island area	
	a. Blue filter	51-25
	b. Green filter	51-26
51-7	Instrument response curve	51-27
51-8	Cross-sectional view looking forward	51-28
51-9	Ben Franklin on surface showing Black Port and S/R instrument mounted in Ben Franklin	51-29
51-10	Spectral response	51-30
51-11	Composite of fully correct irradiance measurements as a function of vehicle depth	51-31
51-12	Downward spectral irradiance in two bands as a function of water depth	51-32

Figure		Page
52-1	Lake Michigan shoreline at Grand Haven	52-18
52-2	Lake survey chart — Grand Haven, Michigan	52-19
52-3	Optical data processing of Grand Haven shoreline	52-20
52-4	Waves in open water	
	a. Aerial photograph	52-21
	b. Fourier transforms	52-21
52-5	Diffraction of water waves	
	a. Aerial photograph (west of Cayo Arenas)	52-22
	b. Fourier transform	52-22
52-6	Clouds and cloud shadows	
	a. Aerial photograph	52-23
	b. Fourier transform	52-23
52-7	Optical data processing of Apollo 7 frame AS 7-4-1607	52-24
53-1	Gemini photograph of the Florida Straits showing the test sites investigated	53-10
53-2	Sambo Reef, Keys test site	53-11
53-3	Well-sorted sand bottom between reef-line and Hawk Channel, Florida Keys site	53-11
53-4	Ceasar's Creek, south of Eliot Key, Biscayne Bay	53-12
53-5	Area of hard and soft bottom, edge of Bahama Banks and south of Bimini	53-12
53-6	Thermal effluent area from a power plant	53-13
53-7	Dredged channel, Biscayne Bay	53-13
53-8	Area behind Marathon airport, Florida Keys	53-14

Figure		Page
53-9	Area around Arsnicker Key, Biscayne Bay (drawing)	53-15
53-10	Area around Arsnicker Key, Biscayne Bay (photograph)	53-15
53-11	Grass patches and gorgonian - algal hard bottom cover	53-16
53-12	Current-scoured channel between Missouri and Ohio Keys, Florida Keys	53-16
53-13	Bottom cover map prepared from Gemini photograph of the west edge of the Bahama Banks	53-17

SECTION 35

APPLICATION OF INFRARED IMAGERY IN STUDYING
THERMAL CHARACTERISTICS OF A COOLING RESERVOIR

by

J. F. Turner, Jr. 1/

INTRODUCTION

N71-11152

Roxboro Lake is a cooling reservoir for a large steam-electric generating plant in north-central North Carolina. The generation of electric power with steam produces large quantities of thermal energy which must be dissipated into the environment.

Heat disposal at the Roxboro Lake installation involves circulating large quantities of cooling water from the lake through the condensing coils of the generators and then back to the lake. This thermal loading process and the important heat disposal processes are shown schematically in figure 1.

As the heated water enters the lake it spreads rapidly as a thin surface layer. Several things then happen: part of the heat is dissipated through evaporative cooling, long-wave radiation, and conduction. The remainder is retained in storage in the lake until physically transferred out of the lake by water outflow or until it is dissipated by other insignificant dissipation processes.

Evaporative cooling which is one of the most important processes for heat disposal, is important because large amounts of water are lost to the atmosphere in this process. Methods that are used in evaluating water losses associated with evaporative cooling require information concerning the thermal characteristics of the lake surface. For example, warmer areas of the lake have higher heat dissipation rates because evaporative cooling and the other heat disposal processes are more active in these areas.

Because detailed information on surface temperature was needed in studying the thermal characteristics of Roxboro Lake, infrared imagery was obtained during the predawn hours of April 22, 1967. The remaining sections of this paper will describe the subsequent processing, analysis and interpretation of these data in developing a thermal map of the reservoir. Several significant constraints that must be imposed when obtaining infrared imagery of a cooling reservoir will also be discussed briefly. Future project objectives, including data needs, will also be discussed.

1/ U. S. Geological Survey, Raleigh, N. C.

PROCEDURE

Although light rain and drizzle prevailed during the predawn hours of April 22, the study was made as originally scheduled (0330 to 0415).

The data that were collected include infrared imagery observed at altitudes of 2000 ft and 10,000 ft, continuous records of surface temperatures observed at selected points in the reservoir, and an extensive thermal survey of surface temperatures made by boat immediately after the flight. Locations of the temperature-monitors are shown in figure 2. This survey consisted of making spot temperature observations (every 100 yds or so) over the entire reservoir surface. These temperature data were needed to provide a basis on which the imagery could be quantitatively evaluated.

Other pertinent data that were collected include air temperature, relative humidity, wind speed, precipitation, streamflow, reservoir elevation, and power plant operating records.

The imagery was obtained by means of a conventional line scanning device, a Reconofax IV (scanner-imager) mounted in a U. S. Geological Survey aircraft. The output from the Reconofax IV was a film strip showing radiation intensity (as an image) that was emitted from the reservoir surface in the 8-14 μ electromagnetic band. Although imagery from the Reconofax IV does not provide actual radiant temperatures of the emitting body, tonal differences of the image are highly correlated with the radiant temperatures of the emitting body, therefore allowing us to get a relative view of the surface temperatures of the lake.

PRECISION OF DATA

Unfortunately, all of the imagery obtained in the study were of poor quality. The imagery that was observed at 2000 ft exhibited fair thermal resolution or tonal differences for areas of the lake where surface temperatures ranged from 70°F to 80°F, and extremely poor thermal resolution for the remaining portions. The imagery that was observed at 10,000 ft exhibited no distinguishable tonal variations for the entire lake surface and were therefore of no value to this study.

The poor quality of the imagery is believed to be primarily the result of adverse weather conditions that prevailed during the flight. Flight parameters including aircraft speed and drift appear not to have adversely affected the data. However, poor attitude of the aircraft while over several areas of the lake resulted in additional distortion of the imagery.

RESULTS

Method of computation

No attempt was made to quantify photo density of the imagery obtained so that it could be processed by computer because the equipment was not available and because of the poor thermal resolution. Therefore the imagery was analyzed on the basis of a composite (map) that was made from enlarged photographic prints of the film strip. Observed temperature (control) data were plotted on an overlay of the composite and a simple thermal map was developed by interpolating between control points on the basis of tonal variations in usable portions of the composite. Although the thermal map, which is shown in figure 3, is rather primitive, a more sophisticated analysis would not have significantly improved its quality.

INTERPRETATION OF RESULTS

The thermal map that was developed allowed the delineation of the portions of the reservoir that are heated as a result of the thermal load from the power generators, and subsequently aided in the determination of the amount of water that was lost to the atmosphere through the evaporative cooling process.

The imagery data were further significant in addition to development of the thermal map because hot and cold cells and a thermal interface were detected in the heated area of the reservoir as shown in figure 4.

This information is valuable because it indicates irregularities in circulation patterns in the reservoir and allows us to determine some of the factors that cause these irregularities in the heat dissipation processes. The probability of detecting these characteristics, especially the interface, by conventional methods is extremely remote.

The infrared imagery obtained in this and other studies also indicate several significant items relative to the technology of remote sensing of cooling reservoirs. Although only one set of imagery data have been collected and analyzed in the study, it is apparent that low-altitude predawn flights (preferably at altitudes of 2000 ft to 3000 ft) during clear weather are most desirable in obtaining infrared imagery of cooling reservoirs. Because the environmental system noise is minimal in the 8-14 μ band, this portion of the electromagnetic spectrum appears to be the most appropriate wavelength in which to monitor infrared emissions from the water surface of a cooling reservoir.

Although some positive results were obtained from portions of the imagery obtained on April 22, the study clearly indicates that computer processing will be required to obtain unbiased quantitative

thermal maps of large cooling reservoirs. Because of recent developments in remote sensing equipment, infrared sensing instruments now have the capability of recording infrared emissions on magnetic tape. Data recorded in this manner can be quickly processed by computer to obtain quantitative isothermal maps.

Although the imagery data recorded on film strips can also be digitized and subsequently processed by computer, the process is quite time-consuming and, in my opinion, much inferior to the use of the digital recording process initially. Imagery (film strip) data, however, are useful in showing thermal features of cooling reservoirs such as thermal interfaces and as such may require little or no quantitative evaluation.

FUTURE OBJECTIVES

Because of the results of the April 22 study and because several more generating units have been added to the Roxboro Lake power facility since April 1967, thermal loads have increased by about 270 percent. Additional imagery would therefore be helpful in assessing the effects of this increased load and in developing a functional-thermal model of the lake surface.

Another remote sensing flight is tentatively scheduled for February 1970. The data that are to be collected include thermal infrared imagery and color infrared photography.

The imagery data are to be obtained in 2 overflights at about 45-minute intervals, when the reservoir is under a large but constant generating load, and when other factors that affect the heated area are at or near normal levels. These data will be used to develop another thermal map of the reservoir that will reflect the increase in thermal load since the first flight.

Blue algae growth which is also becoming significant in many sections of Roxboro Lake, will be studied by the color infrared photography. This study will include determining the extent of algae growth and in its subsequent effect on the ability of the lake to assimilate, distribute, and dissipate the growing thermal loads.

CONCLUDING REMARKS

Although only one set of infrared imagery was obtained during the study, it is concluded that low-altitude, predawn remote sensing flights (2000 ft to 3000 ft) made during clear weather, will provide information needed in mapping surface temperatures of cooling reservoirs.

Even though the imagery was obtained during adverse weather conditions, portions of the imagery accurately described temperature variations in the reservoir and allowed the development of a thermal map.

For this reason, it is further concluded that the 8-14 μ band is an appropriate "window" in the electromagnetic spectrum to monitor infrared emission from a cooling reservoir.

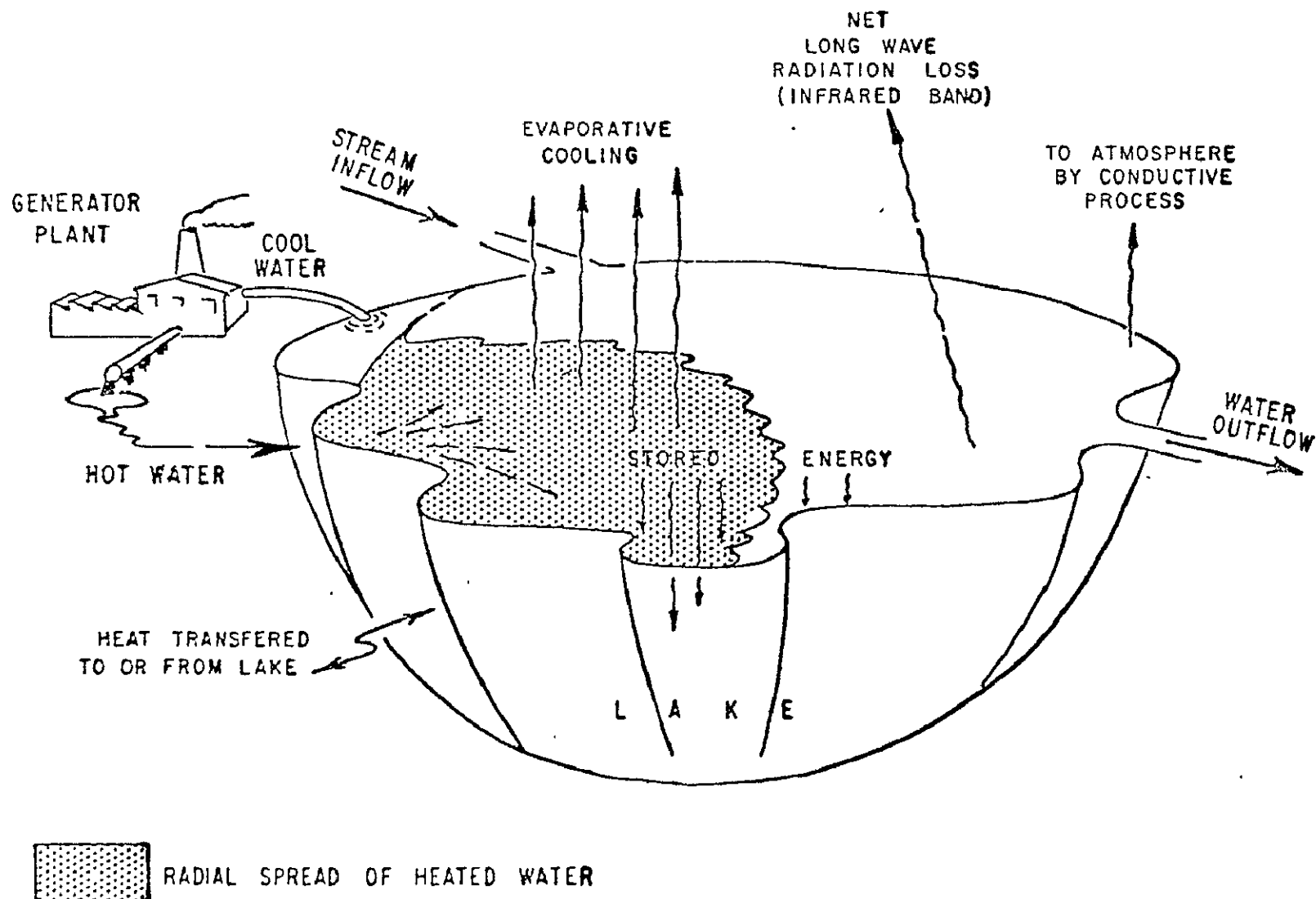


Figure 35-1.- Schematic diagram of the thermal loading and heat disposal processes.

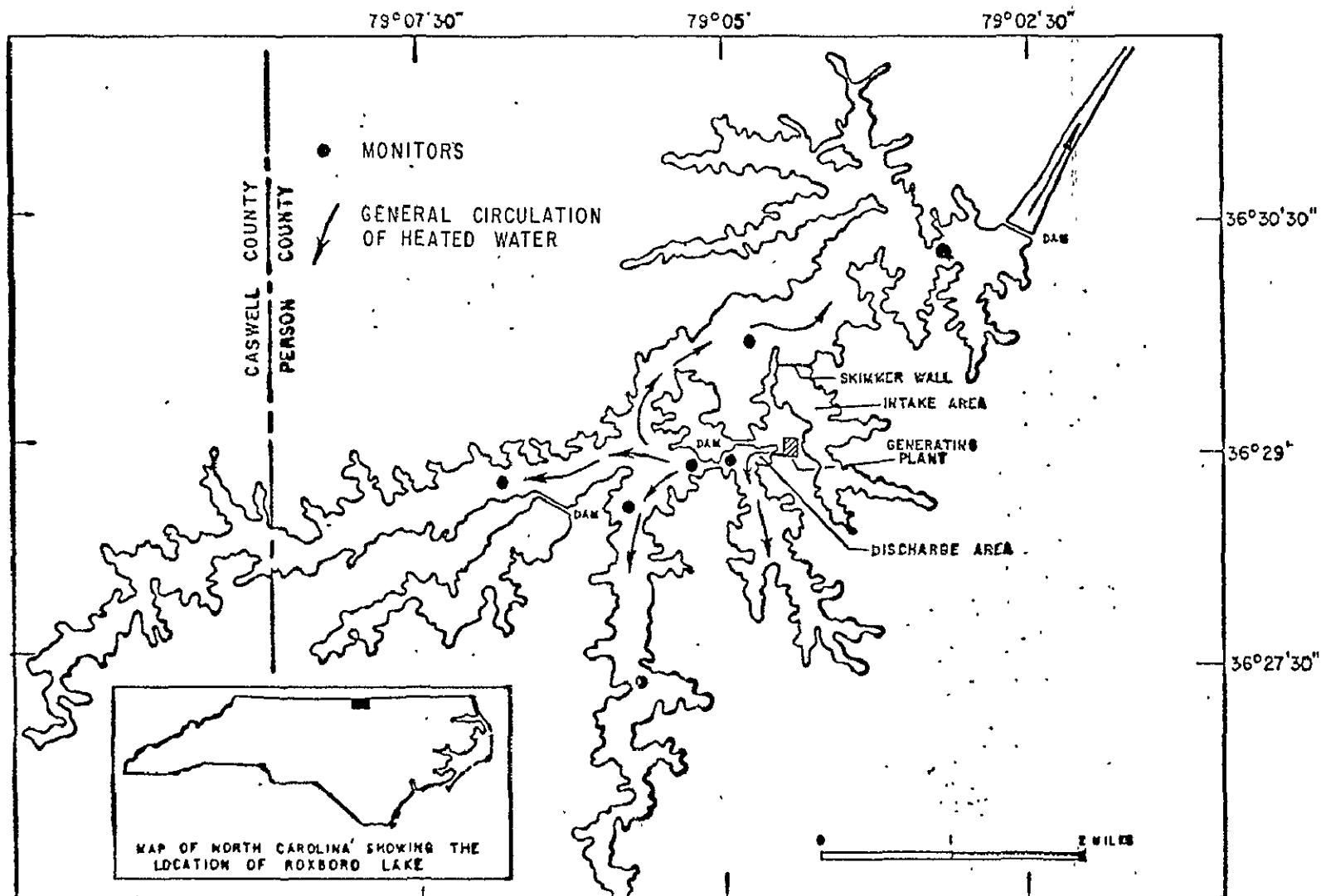


Figure 35-2.- Map of Roxboro Lake showing location of temperature monitors and general circulation of heated water.

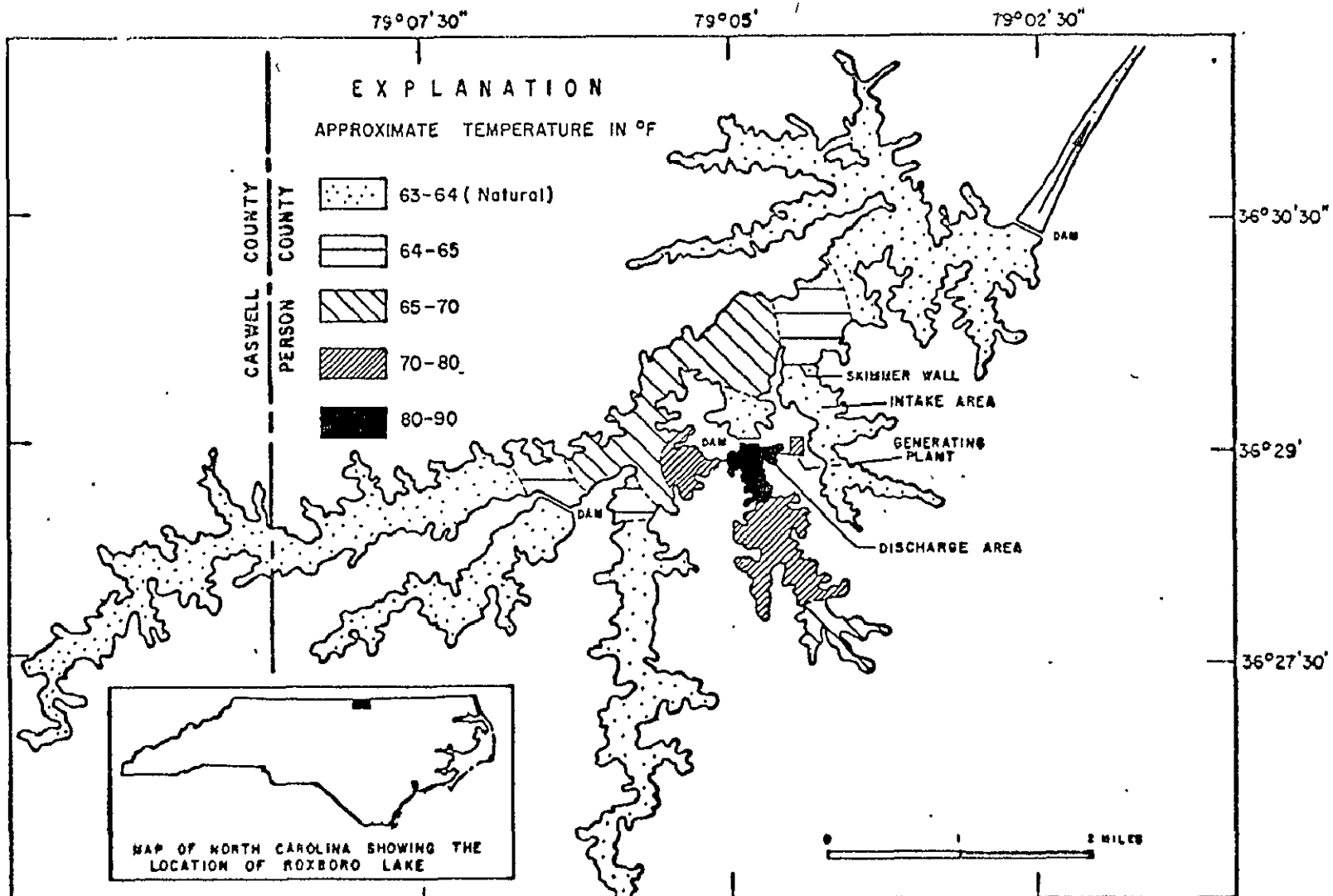
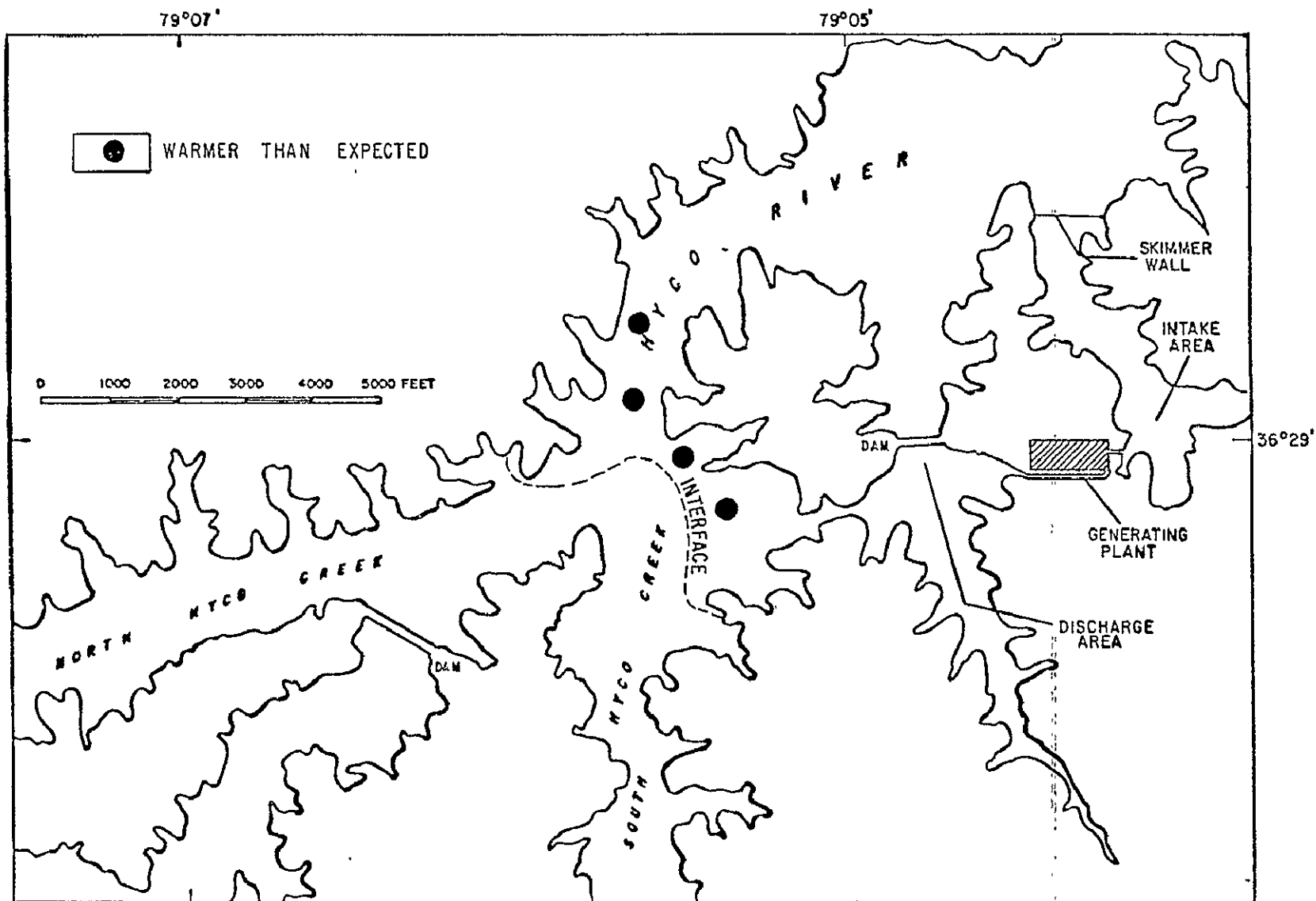


Figure 35-3.- Thermal map of Roxboro Lake during remote sensing flight.



35-10

Figure 35-4.- Map of Roxboro Lake showing thermal characteristics within the heated area.

Hydrology

UNITED STATES
DEPARTMENT OF THE INTERIOR
GEOLOGICAL SURVEY
WATER RESOURCES DIVISION

SECTION 36
HYDROLOGIC STUDIES IN NORTHERN COOK INLET, ALASKA
USING COLOR PHOTOGRAPHY AND THERMAL IMAGERY

By

W. W. Barnwell and Chester Zenone

Prepared by the
UNITED STATES GEOLOGICAL SURVEY
in cooperation with
NATIONAL AERONAUTICS AND SPACE ADMINISTRATION

N71-11153

36-3

HYDROLOGIC STUDIES IN NORTHERN COOK INLET, ALASKA

USING COLOR PHOTOGRAPHY AND THERMAL IMAGERY

By W. W. Barnwell and Chester Zenone¹

ABSTRACT

Photography and thermal infrared imagery of the Northern Cook Inlet area in south-central Alaska were obtained from NASA flights of May 1967. The color photographs provided sharp detail in landscape features, and thermal infrared imagery enabled delineation of swampy areas from well-drained areas. Color differences on the color infrared photographs correlated with warm and cold ground detected by the thermal infrared imagery. Both color and thermal patterns indicate current directions in Cook Inlet, where cool silt-laden fresh water mixes with the salt water.

INTRODUCTION

A series of three remote-sensing flights were made over the Upper Cook Inlet-Anchorage area in south-central Alaska. Cook Inlet is a large tidal inlet that opens to the Gulf of Alaska.

The flights were conducted by National Aeronautics and Space Administration (NASA) as a joint venture with the U.S. Geological Survey (USGS) and the Federal Water Pollution Control Administration (FWPCA). These flights on May 11 and 13, 1967, were designated by NASA as Mission 47, Site 143, Flights 1, 2, and 4 (fig. 1).

This report presents a preliminary evaluation of the photography and imagery obtained on those flights and suggests continuing studies.

¹U.S. Geological Survey, Water Resources Division,
Anchorage, Alaska

DESCRIPTION OF STUDY

1. Purpose of study

The main objective of the mission was to locate areas of possible ground-water discharge into Cook Inlet. Secondary objectives were to determine the feasibility of mapping tidal-current patterns, to attempt definition of areas of varying hydrogeologic character and evapotranspiration rates, and to test the feasibility of monitoring oil spills in the inlet.

2. Remote-sensor data

Color and color-infrared photography and thermal infrared imagery were obtained. Flight and sensor data are given in Table I. The overall quality of the data is good. However, the standard color (Ektachrome) prints have a reddish cast that obscures detail and some strips of thermal infrared imagery contain defects which may be caused by improper adjustment of gain control. For example, in the imagery of the western part of the Anchorage lowland, the International Airport runway and many lakes are so bright that they are almost washed out.

3. Ground control data

When the flights were made in May, ice had just melted on the lowland lakes, but was still present on lakes above 800 feet altitude. Grass and deciduous trees on south-facing slopes were beginning seasonal growth. In muskeg areas, the ground was frozen at or very near the surface. In well-drained areas underlain by gravel, the top of the frost layer was deeper.

Records of daily maximum and minimum temperatures were received from the U.S. Weather Bureau in downtown Anchorage. Similar data, as well as that of temperature and wind velocity at 3-hour intervals were obtained from Anchorage International Airport. Sky conditions for all flights were clear, with minimum haze.

Other ground data, including measurements of temperature, salinity and sediment content of water at various points in Cook Inlet were obtained in May 1966 by the University of Alaska, and supporting geologic and hydrologic data collected since June 1947 were obtained by the USGS.

A USGS comprehensive 5-year study of the engineering geology and hydrology of the Anchorage area has been in progress since July 1966. This study has provided a broad base of ground truth data. In turn,

data from the remote sensing flights are being incorporated into interpretative maps prepared in the engineering study.

DATA ANALYSIS

1. Ground-water discharge

This first study objective was to delineate areas of ground water outflow to Cook Inlet, believed to be present. However, no thermal anomalies along the coastline that could be correlated with such outflow were detected in the infrared imagery, and no color contrasts or gradations were visible on the photography. The lack of evidence of ground water discharge may be caused by: (1) an inadequate discharge to permit detection, (2) insufficient temperature contrast between ground and surface water, or (3) improper scanner characteristics and settings.

In May, inlet water is within 3°C of the ground water temperature. In August, a contrast of more than 10°C may be detectable. It is also possible that the discharge occurs well below the elevation of low tide and has no surface expression.

2. Tidal-current patterns

The 24 to 30-foot tidal range and 8-knot currents in Upper Cook Inlet move large sediment loads, causing major changes in bottom morphology with time. Thus, the proposed construction of highway crossings at the head of the inlet and the safe operation of large ships through the inlet require a good knowledge of tidal-current patterns.

The tidal-current pattern is exhibited by radiometric temperature variations in the imagery of Cook Inlet (fig. 2). The temperature distribution results from tidal mixing of sea water with colder water of the tributary glacier-fed stream. A cold-water inflow is clearly shown on the imagery of the Girdwood area near the head of Turnagain Arm (fig. 3).

Variations of silt concentration in water may be indicated by changes in reflectivities. Glacial, silt-laden waters appear on the color infrared photographs as light blue-grey, whereas clear-water lakes appear dark blue (fig. 4). Tonal gradations in photographs of Cook Inlet may indicate gross current directions where the heavily silt-laden waters of Knik and Turnagain Arms mix with Cook Inlet tidewater.

3. Plant vigor and distribution

Plant reflectance is believed to be an indicator of ecological, physiographical, and hydrological conditions. In the study area, deciduous cottonwood, aspen, and birch, growing on well-drained soil, registered as a reddish tone on the color infrared photographs (fig. 5). This tone was caused by the presence of green, newly formed leaves. On the lower, poorly-drained areas, vegetation consisting mainly of black spruce, but including other marsh plants, was still dormant and appeared as blue-green.

Swamps and other low, moist areas along stream channels were identified on thermal infrared imagery. In these areas the water table is at, or very near, the ground surface and moist areas were easily delineated because they were still frozen and registered in darker (or colder) tones than the better-drained areas (fig. 6a).

Data from these sensors, which aid in identifying plant distribution, stage of plant growth, and drainage characteristics of the soil, may be helpful in estimating evapotranspiration rates.

Colwell and Olson (1965) discussed the use of color infrared photography and thermal infrared imagery in vegetation analysis. They concluded that the time of the day, type of terrain, and weather conditions should be given careful consideration in both flight planning and data interpretation. It should be realized that the remote sensor data upon which this report is based were acquired in May. The delineation of the poorly drained areas by both infrared photography and thermal imagery may be dependent upon the day and season in which it is acquired. Later in the summer the muskegs probably will thaw and vegetation there may become vigorous. The delineation may still be possible on color infrared photography because of the different reflectance characteristics of muskeg species. Pre-dawn thermal imagery acquired late in the year may also change, depending on the extent of outgoing radiation at the time the imagery is taken. Late in the summer the dry areas may lose much of their heat and may even appear colder than the muskeg areas. If this occurs, it may still be possible to make the hydrogeologic delineation of moist areas.

4. Oil spill detection

Oil spills from tankers and from drilling and production facilities are a potential source of pollution in Cook Inlet.

To test a technique for monitoring oil spills, 55 gallons of diesel oil were dumped from an aircraft into the water near on oil-drilling platform (fig. 1). An observer on the inlet reported by radio to the aircraft that the oil was on the water during flight and was visible at the water surface as an irregular circle approximately 300 feet in

diameter. Inspection of the color and color-infrared photography indicated that the oily film was not recorded on the photographs. A recent study of the Santa Barbara, California, oil slick indicates that oil films are recorded in the ultra-violet wavelengths, and are rarely detected in the visible or thermal (IR) range. There may also be a difference in reflectivity of crude and refined oils.

5. Hydrogeologic mapping

Both color infrared photography and infrared imagery aid in hydrogeologic mapping. Infrared wavelengths penetrate atmospheric haze better than shorter wavelengths in the visible range, hence presenting greater detail and yielding better definition of stream channels, lake features, type and health of vegetation, extent of gravel deposits, and state of land drainage. The value of infrared imagery in mapping surficial geologic units is shown by a comparison of Figures 6a and 6b. There is a good correlation between dark-toned (cold) areas on the infrared imagery and areas mapped as "swamp deposits" on the surficial geology map of the Anchorage area (Miller and Dobrovolsky, 1959).

Research projects in Alaska coupling remote-sensor data and ground-measurement programs can provide new techniques in arctic and subarctic hydrology (Barnwell, in press). The heat-sensing capabilities of infrared systems may be applied to studies of temporal and spatial temperature variations intimately associated with the availability of water in permafrost regions.

FURTHER STUDY

Additional remote-sensor data can materially increase knowledge of Anchorage area hydrogeology and of Cook Inlet estuarine hydrology.

Overflights should be made in August, when the ground is thawed, when vegetation is fully developed, stream discharge and sediment concentration are near maximum, and maximum temperature contrasts exist between ground water and surface water. This data would then be compared to that taken in May 1967.

Potential pollution problems in Cook Inlet are caused by offshore oil production facilities, cannery-waste disposal, and sewage disposal from developing coastal cities. In addition, the east end of Turnagain

Arm of Cook Inlet subsided 6 to 8 feet during the March 1964 earthquake and rapid sedimentation is now occurring in this area.

Preliminary studies show that remote sensors can be used to investigate tidal current patterns, water temperature variations, and pollutants (Paulson, 1968).

- - SUMMARY

Although it is believed that ground-water discharges into Cook Inlet, it was not detected in the photography and infrared imagery of May 1967. Lack of detection may be due to: (1) insufficient temperature contrast between ground and surface water, (2) ground-water discharge points may be below low tide level, (3) the discharge may be too small, or (4) the scanner may not have the needed thermal sensitivity.

Tidal-current patterns in Cook Inlet can be detected by tonal variations of suspended sediment on the color-infrared photography and thermal patterns on the infrared imagery.

Both thermal infrared imagery and color-infrared photography are useful in hydrogeologic mapping. Low, poorly drained areas appeared cooler on the infrared imagery and seemed to have less vegetative vigor on the infrared color photography than the better-drained areas. This enabled a hydrogeologic delineation to be made.

Plant species, vigor, and stage of growth are indicated by differences in infrared reflectance. Infrared photography may be effective for studies of plant transpiration because rates of transpiration depend upon the species and vigor of different plants.

The Cook Inlet estuary is subject to considerable pollution by oils and wastes that may be detected by ultra-violet sensors.

REFERENCES

- Barnwell, W. W., 1969, Hydrological applications of remote sensing in Alaska in Remote Sensing Symposium and Exhibition Proc.: Anchorage, Alaska, Dec. (in press).
- Colwell, R. N., and Olson, D. L., 1965, Thermal infrared imagery and its use in vegetation analysis by remote aerial reconnaissance in Remote Sensing of the Environment, 3rd Symposium, 2nd ed., Proc.: Michigan Univ., Ann Arbor, p. 607-621.
- Miller, R. D., and Dobrovolsky, Ernest, 1959, Surficial geology of Anchorage and vicinity, Alaska: U.S. Geol. Survey Bull. 1093, 128 p.
- Paulson, R. W., 1968, Preliminary remote sensing of the Delaware estuary: U.S. Geol. Survey for Natl. Aeronautics and Space Adm., Tech. Letter NASA-128, 22 p.

TABLE 1 - Flight and Instrumentation Data, NASA Aircraft 927

Remote-Sensing Flights over Upper Cook Inlet, Alaska

	Flight 1	Flight 2	Flight 4	Remarks
Date	5-11-67	5-11-67	5-13-67	
Time (Alaska Standard)	4:01-5:06 PM	7:18-9:04 PM	2:58-4:21 PM	
Altitude (feet)	20,000	5,000	20,000	
Air temp. at altitude	-17°C	-12°C	-12 to -15°C	
Tidal stage at Anchorage	Lo at 2:12 PM	Hi at 7:54 PM	Lo at 3:24 PM	
Flight Lines flown	1,2,3,4,5,10	1,5,6,7,8 9,10	1,2,3,4,6,8	
System used on flight				
RS-7 infrared imager	x	x	x	8-14 micron band
RC-8 camera #1	x		x	Ektachrome film, 1/250 sec at f-8
RC-8 camera #2	x		x	Ektachrome IR film, 1/200 sec, at f-5.6, G-15 filter
Data obtained	Photographs Ektachrome Ektachrome IR IR imagery strips	IR imagery strips	Photographs Ektachrome Ektachrome IR IR imagery strips	

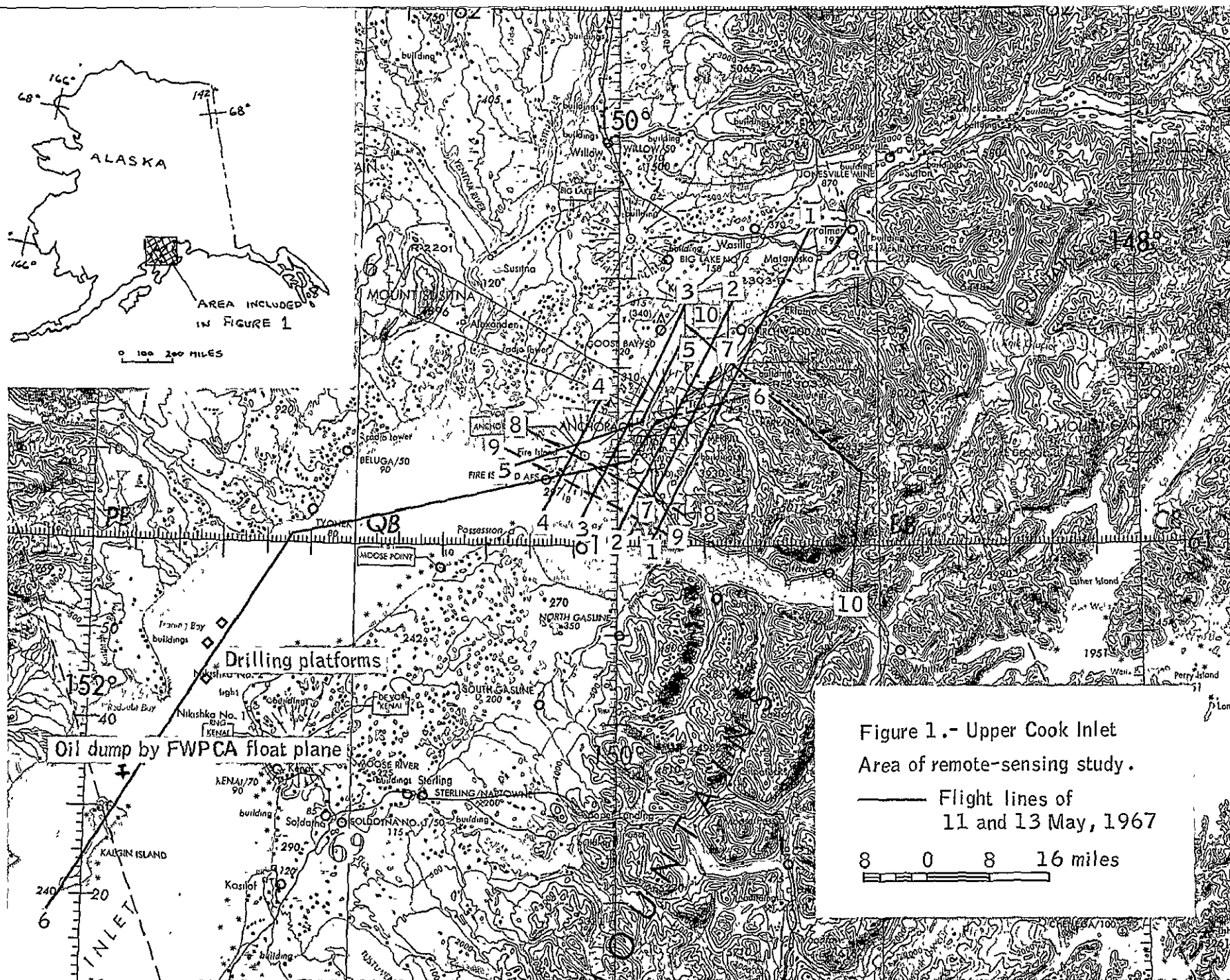


Figure 1.- Upper Cook Inlet
Area of remote-sensing study.

— Flight lines of
11 and 13 May, 1967

8 0 8 16 miles

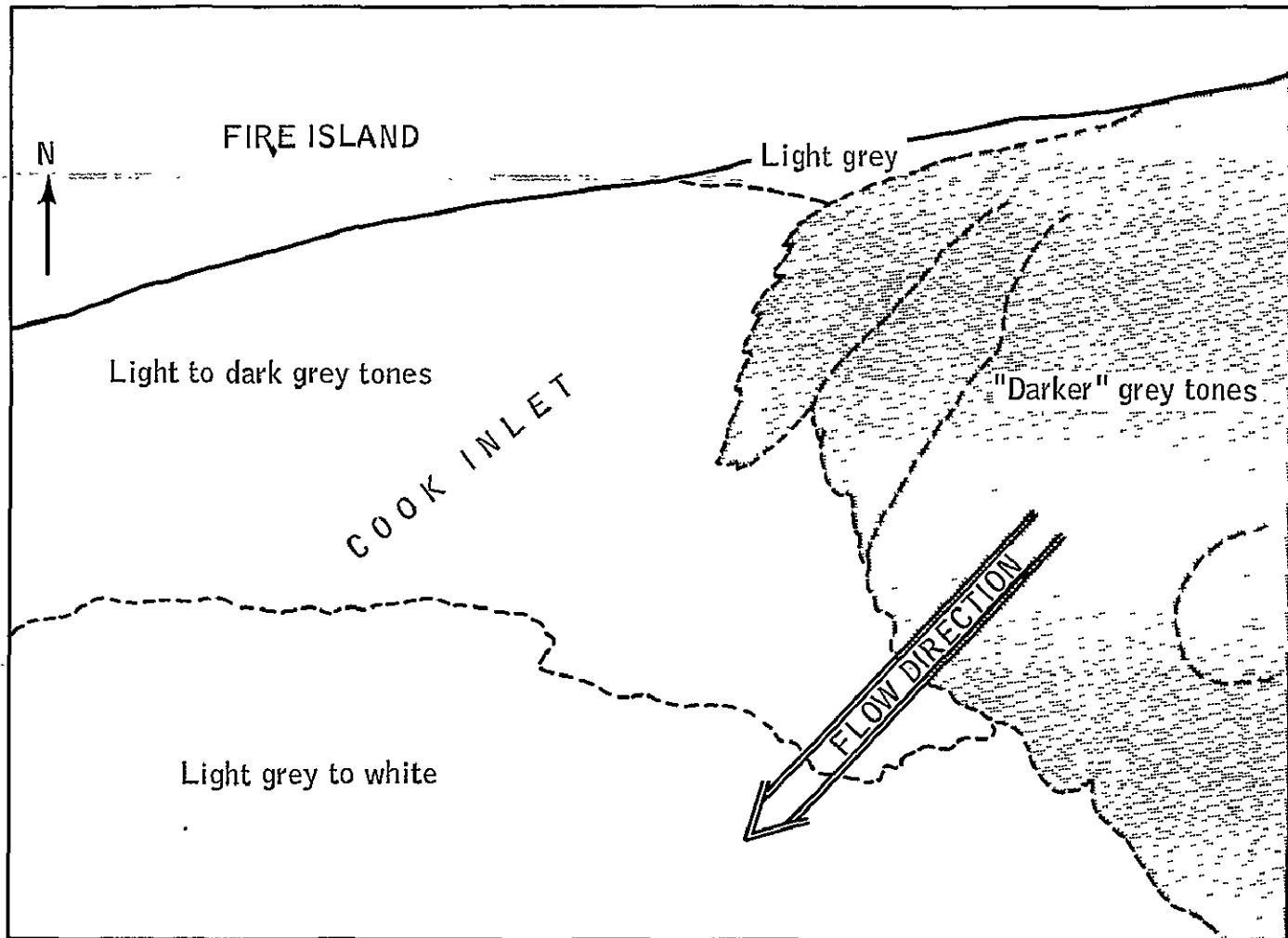


Figure 2.- Trace of infrared imagery showing indicated temperature variations in Cook Inlet water near Fire Island. This trace is from a negative print of the imagery, thus the darker tones indicate relatively warmer water temperatures.

0 1/2 1 Mile

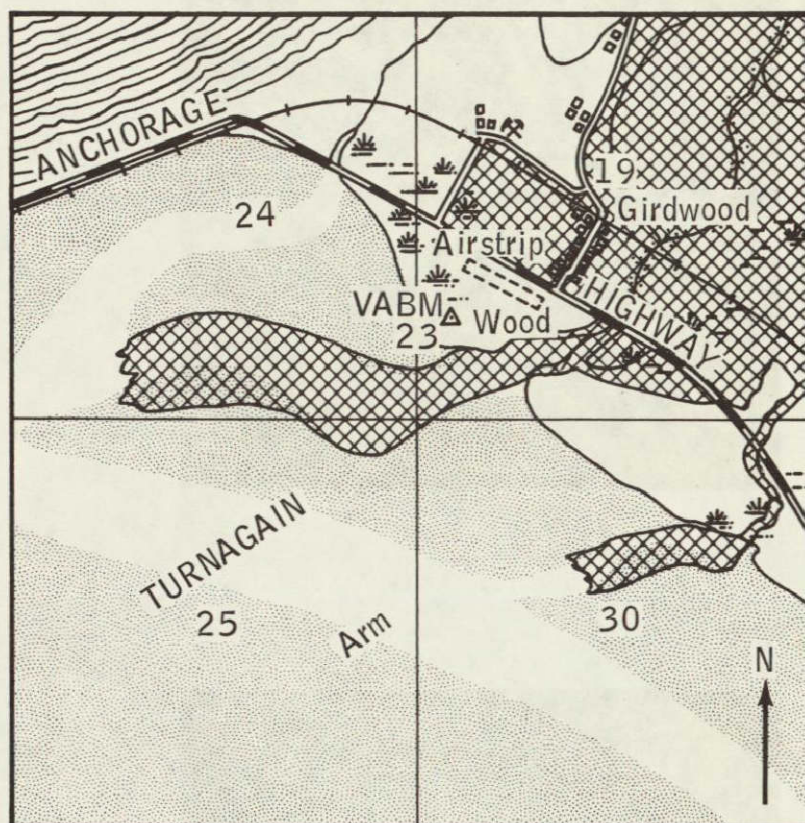


Figure 3.- Trace of infrared imagery showing relatively cold glacial-melt water flowing into warmer Turnagain Arm water (shaded and cross-hatched area is indicated as "cold" on the imagery).

0 1/2 1 Mile



Figure 4.- Color infrared photograph showing difference in color between silt-laden water (light, blue grey) and clear lake water (dark blue). Photograph of Palmer, Alaska area 50 miles northeast of Anchorage.



Figure 5.- Color infrared photograph of part of Anchorage lowland showing tonal differentiation of well-drained areas (light tones) from swampy, low-lying areas (darker tones).

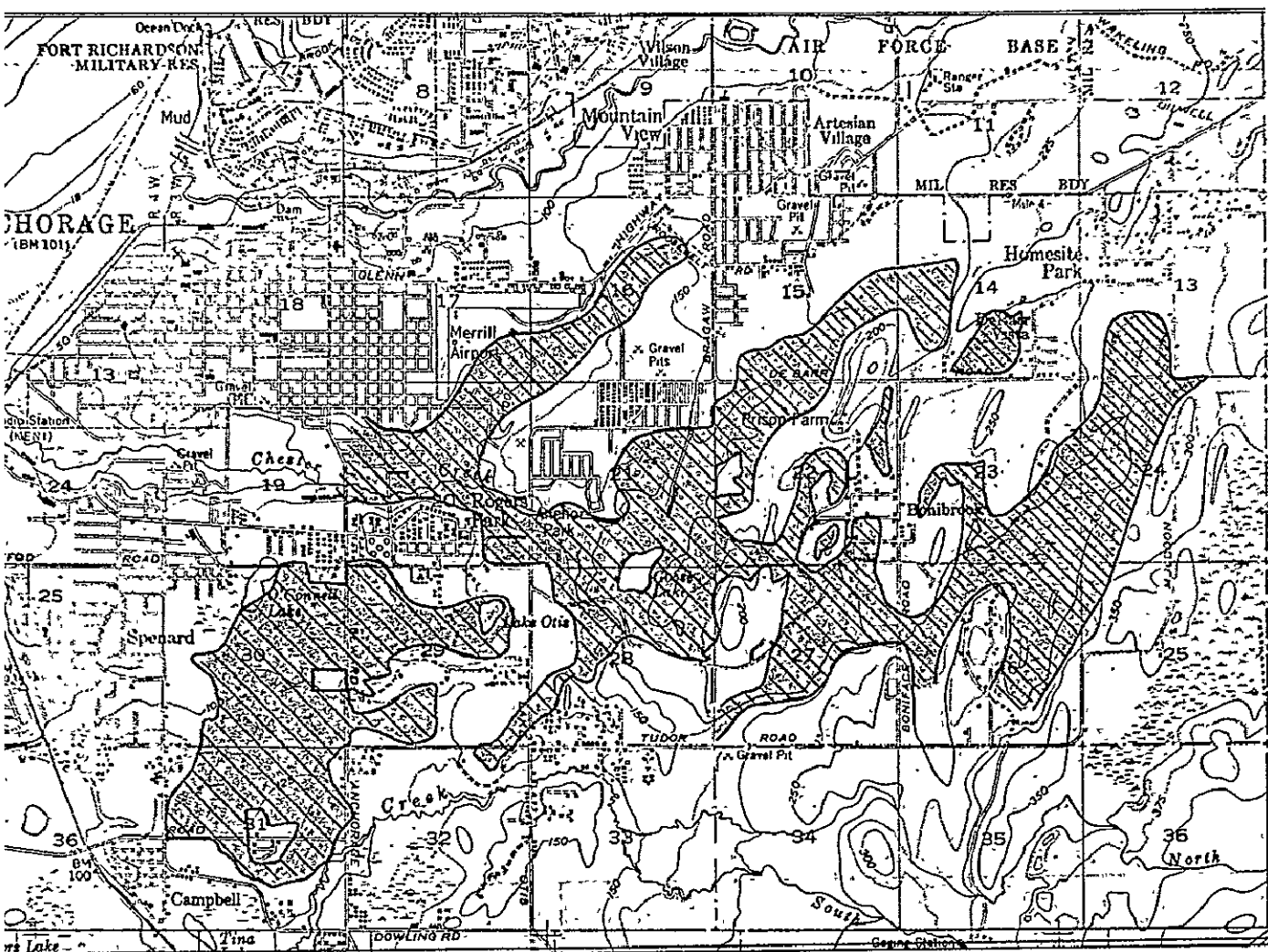


Figure 6(a) - Trace of the pattern of infrared imagery of a part of the Anchorage lowland, showing differentiation of swampy areas (dark on the imagery, cross-hatched here) from well-drained areas.



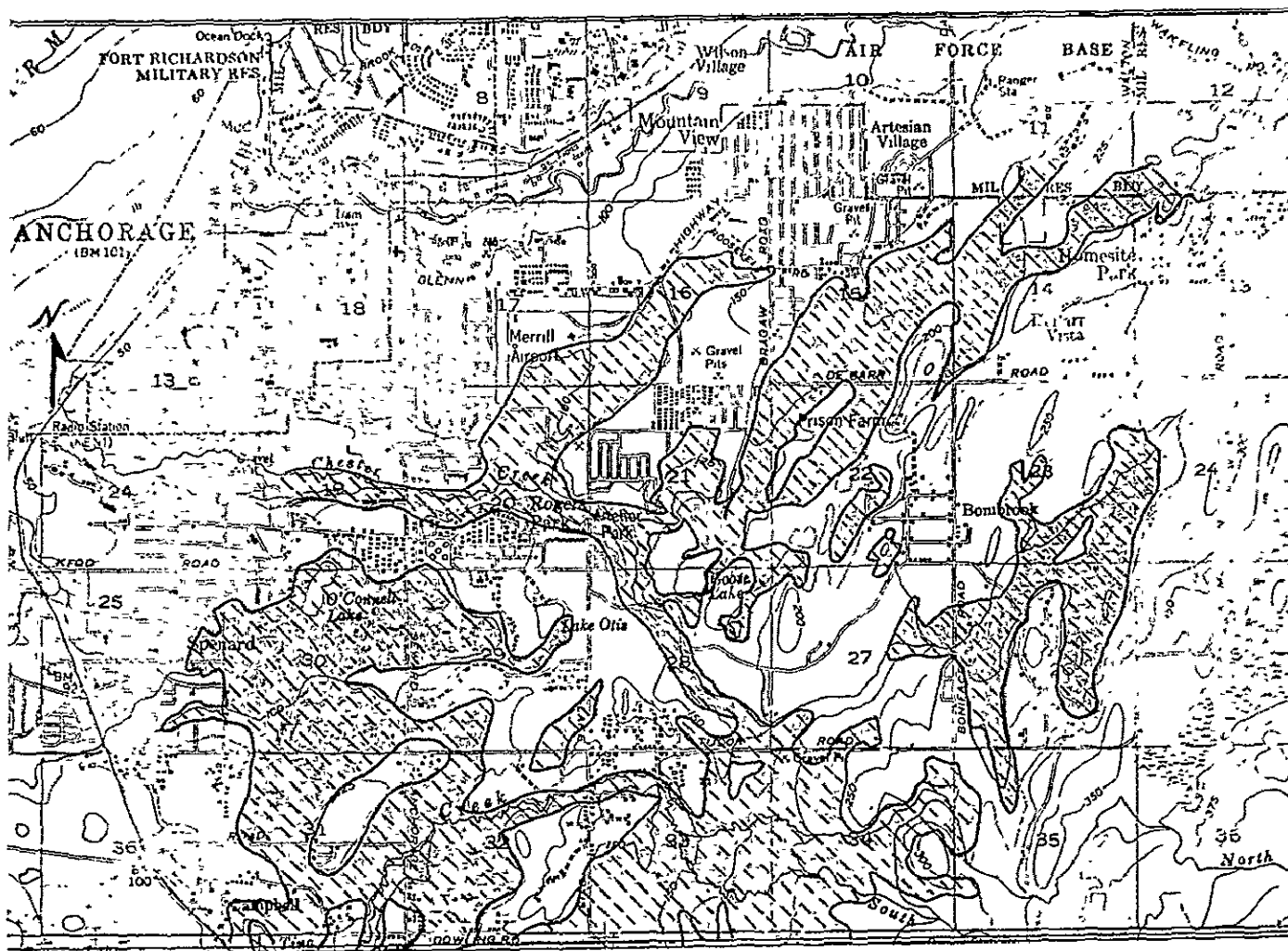


Figure 6(b) - Surficial geology of area covered in Figure 6(a), showing correlation of "swamp deposits"¹ with dark (= cold) areas on the infrared imagery.

1 0 1 Mile

¹ Miller, R.D. and Ernest Dobrovolsky (1959) - Surficial Geology of Anchorage and Vicinity, Alaska, U.S. Geological Survey, Bulletin 1093, Plate 1

SECTION 37
RELATION OF REMOTE SENSING TO TRANSPIRATION
OF FLOOD PLAIN VEGETATION

By Richard C. Culler and Raymond M. Turner
U.S. Geological Survey

Introduction

N71-11154

The amount of water vapor lost from plants through transpiration is in part a function of the volume of plant material covering a given area. If the variance in plant material through time and space is known, it should be possible to make certain inferences regarding the amount of transpiration through the same time period and over the same area. It is this varying plant volume that we have attempted to measure by the use of readily available aerial photographic techniques and materials.

Methods

We used Kodak Ektachrome Infrared Aero Film (Type 8443) in 9 inch format. The camera used was a K-17 equipped with a Metragon lens having a 6-inch focal length. The lens was equipped with the following Wratten filters: Number 12, CC20B, and CC30M. This filter combination was selected from a series of photographs of representative flood plain vegetation taken with 23 different filter combinations following a system described by Fritz¹. Choice of filter combinations was based on visual inspection of photos; final selection was made of the combination giving best discrimination among plant species. The wavelengths sensed by this equipment range from 0.5 to 0.9 microns. The photography was obtained from an elevation of 3600 feet above ground surface during 14 flights in 1968. All photography and film processing was done by the Phoenix Research Office, U.S. Geological Survey, Water Resources Division.

The film images were analyzed by use of a transmittance densitometer. The digital densitometer data were compared with ground truth information in the form of field estimates of plant volume.

The target area is 4,000 acres of the Gila River flood plain, San Carlos Indian Reservation, Arizona, and is part of the U.S. Geological Survey's Gila River Phreatophyte Project². This area has been divided into geographically defined quadrangles 2000 feet x 2000 feet in size. The quadrangles are subdivided into 25 plots, each having an area of 3.67 acres. The plot is the basic spatial unit for describing the variance of hydrologic parameters, vegetation, and for photo interpretation.

The surface cover of plants was divided into three vegetation types on the basis of dominant species. These types are: saltcedar (Tamarix pentandra), mesquite (Prosopis juliflora var. velutina), and mixed saltcedar and mesquite. A fourth category, bare ground, was also included. This discussion will be limited to but one of the vegetation types--saltcedar. The crown configuration of the saltcedar community was defined by four classes of canopy coverage and three height classes. (Black and white panchromatic photography was used in this assessment.) The plant volume of each 3.67 acre plot was described in terms of some combination of a height value and a coverage value. These measures of volume, expressed as cubic feet per square foot, represent the ground truth data. The volume we are dealing with can be viewed as the space occupied by a plant framework which seasonally supports transpiring organs.

The quantity and quality of leaves and branchlets is assumed to bear a direct relation to the volume of water transpired by the vegetation. If this is so, and if the volume and seasonal condition of plant material can be measured photogrammetrically, then aerial photographs or space sensing techniques may prove useful in estimating transpiration over large areas of the earth.

A Macbeth digital-readout transmission densitometer (Model TD-402) was used to measure the color densities of the transparencies. Measurements were made with Wratten filters 92, 93, 94, and 106. These filters correspond, respectively, to the red, green, and blue spectral bands plus a broad band through the entire visual range. A densitometer reading through each of the four filters was obtained for each of the 3.67 acre plots. Readings were made from aerial photographs taken on 14 dates from March through December 1968.

Results and Discussion

Stark differences exist in the amount of radiation that emanates from a dense saltcedar forest when leafless and from the same forest when in full leaf. The three film emulsion layers in color (infrared) film will be little sensitized in the former condition since the critical wavelengths of light are largely absent. Later when in leaf, the saltcedars actively reflect the wavelengths to which the film emulsion layers are sensitive and bright colors result.

The use of photographic film for remote sensing presents significant problems in maintaining uniformity. These problems, as identified in this study, can be classified as (1) differences among the photographic missions resulting from variance in film condition and processing, seasonal differences in sun angle, and differences in film exposure; and (2) variations within the same photographic frame from vignetting. Thus, seasonal differences in color density, due solely to changes in plant volume and condition, are confounded with differences due to lack of photographic uniformity.

The densitometer data have been manipulated by numerous methods in attempting to remove all or part of this unwanted variance. These studies are still in progress and the following methods of analysis have resulted in the best correlation between sensing and ground truth achieved to date. The unadjusted densitometer data are shown in Figure 1. The data points represent the means of densitometer readings for 364 plots covering 1320 acres where saltcedar is the dominate species. The figure illustrates the changes measured in film optical density on 14 dates. Each point represents the mean of 364 values obtained with one of the four densitometer filters. Our work to date has emphasized the portion of the spectrum sensed by the reds on the photograph. The intensity of red on the film is probably related to the volume of foliage¹, an environmental parameter closely related to transpiration.

Unadjusted values of red densities (Fig. 1) cannot be used, however. This is because variability in the densitometer readings from one date to the next is, in general, uniform for all filters, i.e., an increase in the density of blues on a given date is accompanied by a roughly equivalent increase in green, red, and visual densities. Because the values for all filters vary similarly, one suspects that the fluctuations in the important red values are somewhat influenced by conditions unrelated to plant volume.

An adjustment of the density readings was obviously desirable for making comparisons among the photographs taken on different flights. A concrete highway bridge, a short stretch of asphalt highway, and the roof of a building were the only objects in the target area suitable for use as controls. Density measurements of the control objects on all the flight dates were made using the four filters. These measurements indicate a linear relationship between the visual density values and the values with red, green, and blue filters. Density readings were therefore adjusted by expressing color densities as a percentage of visual density for all densitometer data. The normalized values obtained with the green, red, and blue filters are seen in Figure 2.

The variability in red density is assumed to portray the seasonal variation in foliage. From March 22 to April 5, the decrease in red optical density was in response to the flush of spring branchlet growth (Fig. 2). The increase in red density between April 19 and May 3 reflects a frost on April 20th which caused partial defoliation^{1/}. Following this, the red curve shows a sharp decrease in density to May 15 as the frozen leaves were replaced with new growth. The minimum density (or maximum foliation) was reached on August 13. The gradual change to fall dormancy is indicated by the increase in red density beginning in the latter part of August. This increase in red density continues until December when the trees are again leafless. We interpret the configuration of the last part of the red curve as resulting from the gradual aging and loss of branchlets and leaves.

^{1/} Optical density (\log^{-1} transmittance) is inversely related to foliage volume.

Figure 3 shows the seasonal variation in red density as a percentage of visual for each of four foliage volume classes of saltcedar. The highest volume class (13.0 cubic feet per square foot) was applied to a specially selected area when saltcedar was thought to be at its maximum density. As the standard error values show, the data points for the various dates are usually representative of distinct populations. Furthermore, the four curves show clearly that differences in the amount of energy reflected by areas dominated by different volumes of saltcedar can be discriminated by Ektachrome IR film. Thus, this readily available film can be used to describe the temporal and spatial variance of saltcedar.

Conclusions

The methods and interpretation of remote sensing as employed in this study are applicable to proposed remote sensing from earth resources satellites in four respects:

1. The spectral range of sensing is about the same in both.
2. Repetitive sensing is of fundamental importance.
3. The 3.67 acre unit of area sampled is probably within the resolution capabilities of proposed satellites.
4. The interpretive data are presented in digital form for computer storage and analysis.

The future objectives of this study will be to further refine the measurement of plant density by more consistent photography and through improved methods of interpretation. Methods of altering the infrared photography to simulate satellite sensing will also be investigated. Repetitive imagery sensing will be used as soon as facilities become available.

Some phreatophytes, such as saltcedar, are tolerant of drought; although under these conditions plant anatomy and morphology are altered. To monitor the varying structural and physiological condition of the plant is an important goal in inventorying this vegetation. The development of such capability will be a major concern once methods of identifying and measuring the aerial extent of phreatophytes are known. Realization of these goals will also improve the correlation between remotely sensed vegetation measurements and hydrologic parameters. The additional remote sensing needs for this project are primarily repetitive multichannel imagery.

References

1. Fritz, N. L., 1967, Optimum methods for using infrared-sensitive color film: Am. Soc. Photogrammetry, 33d Ann. Mtg., Washington, D. C., 18 p.
2. Guller, R. C., and others, in press, Objectives, methods, and environment--Gila River Phreatophyte Project, Graham County, Arizona: U.S. Geol. Survey Prof. Paper 655-A.
3. Knipling, E. B., 1967, Physical and physiological basis for differences in reflectance of healthy and diseased plants: Winter Haven, Florida Dept. Agr., Workshop on infrared color photography in the plant sciences, 25 p.

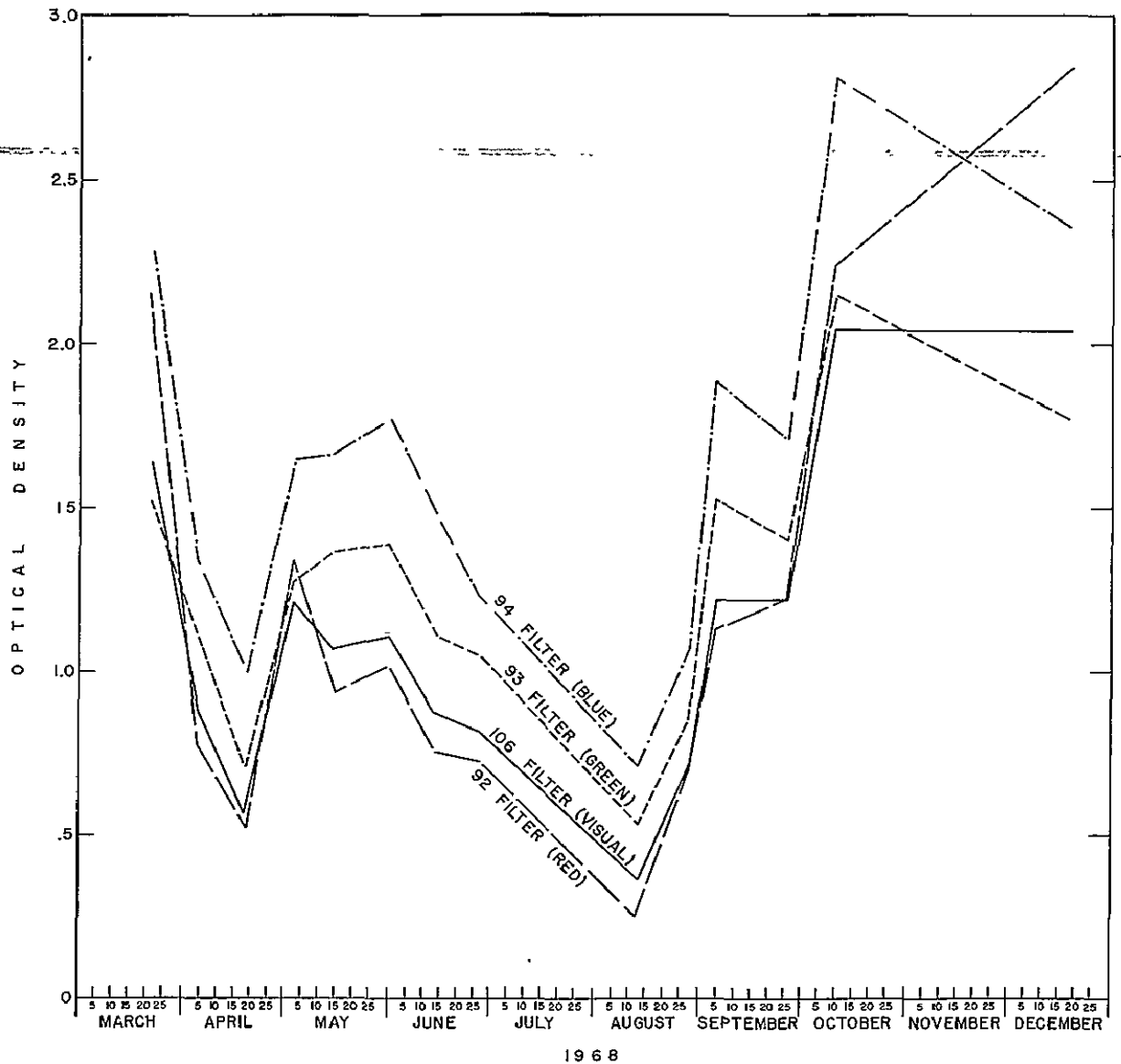


Figure 37-1.- Mean optical density values from Ektachrome IR images of a 1300-acre saltcedar forest, Gila River, Arizona. Data points are mean values for 364 forest plots imaged photographically on 14 different dates, 1968. Values obtained from photographs using four different densitometer filters.

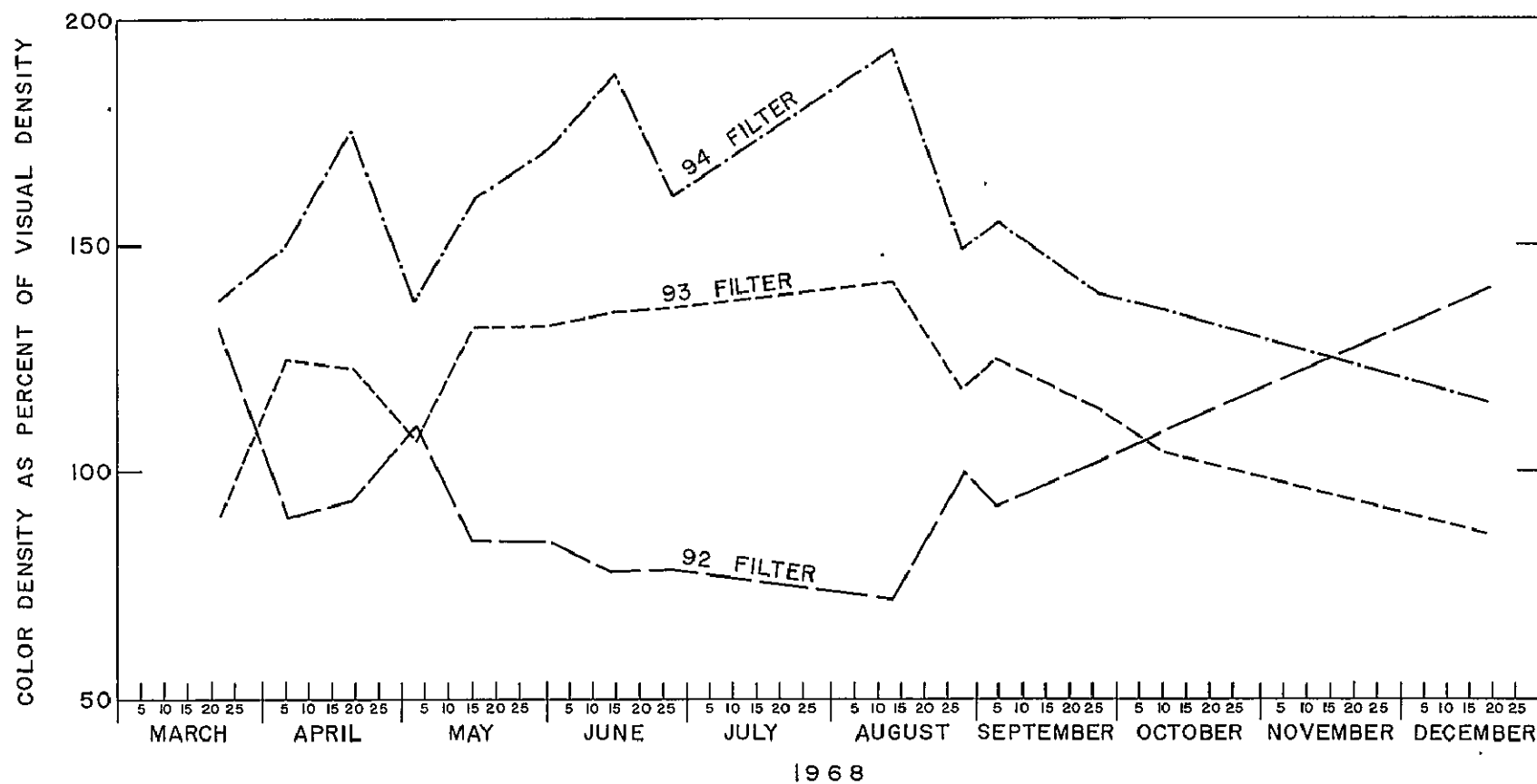


Figure 37-2.- Adjusted mean optical density values from Ektachrome IR images of 364 forest plots within a 1300-acre saltcedar forest, Gila River, Arizona. Normalized densitometer values computed by dividing the red, green, and blue filter by the visual filter for each of 14 dates, 1968.

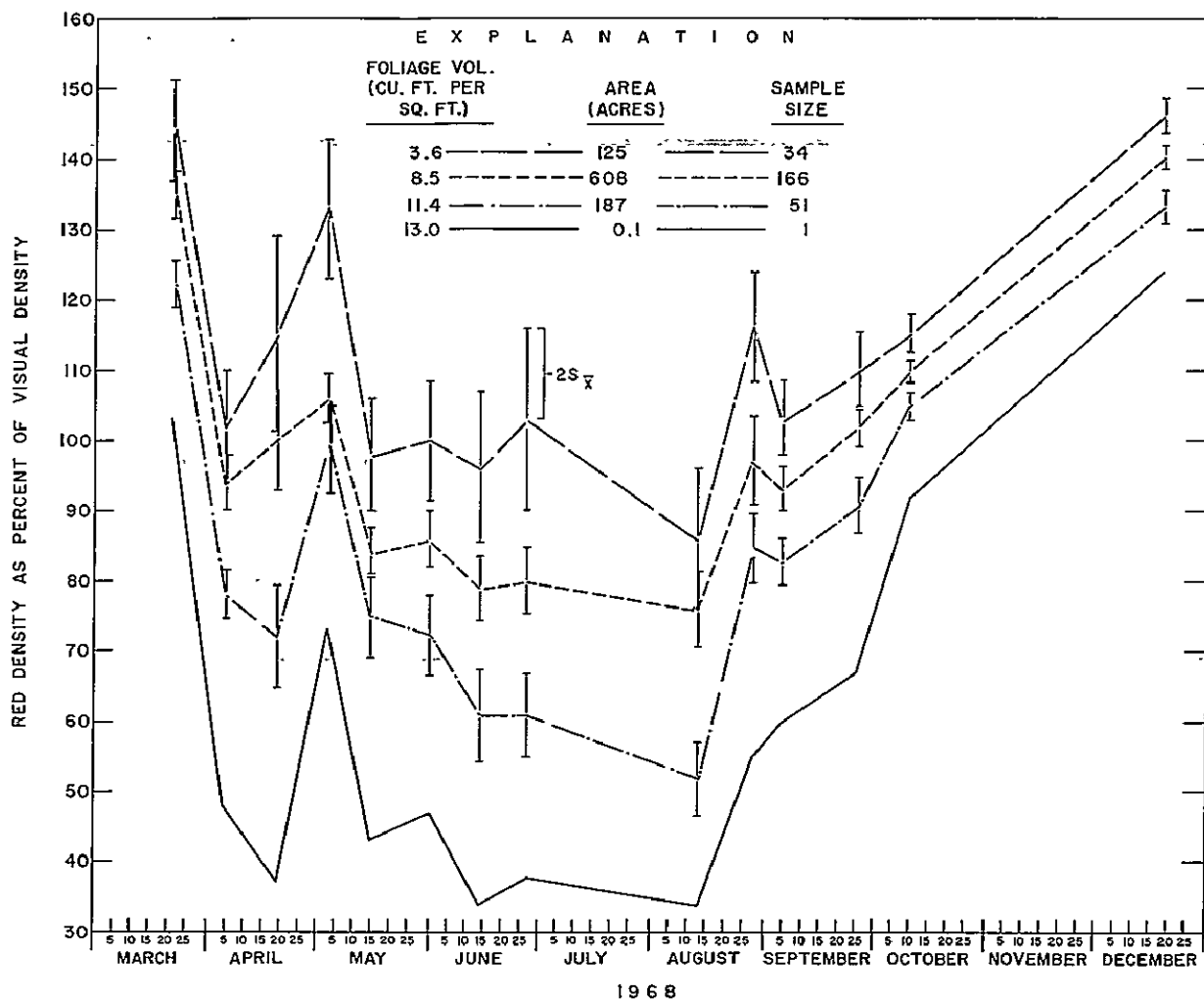


Figure 37-3.-Seasonal variance of adjusted red filter densities obtained from Ektachrome IR images of a saltcedar forest, Gila River, Arizona. Data points are mean density values for forest plots representing four different foliage volume classes. Where appropriate, confidence limits are shown by vertical lines equaling 2 standard errors about the mean.

UNITED STATES
DEPARTMENT OF THE INTERIOR
GEOLOGICAL SURVEY
WATER RESOURCES DIVISION

SECTION 38
SYNOPTIC REMOTE-SENSING SURVEY
OF LAKES IN WEST-CENTRAL FLORIDA

By

Joseph W. Stewart
U. S. Geological Survey

Prepared by the
UNITED STATES GEOLOGICAL SURVEY
in cooperation with
NATIONAL AERONAUTICS AND SPACE ADMINISTRATION

SYNOPTIC REMOTE-SENSING SURVEY OF LAKES IN WEST-CENTRAL FLORIDA

By

Joseph W. Stewart

INTRODUCTION

N71-11155

The overall purpose of this study is to determine the feasibility of effectively using remote sensors in the following problems in lake hydrology: (1) determination of the interrelations between lakes of different characteristics and their occurrence and effects on the hydrologic regimen of an area; (2) development of a classification of the shore features of lakes as a means of establishing average high water marks historically significant to the hydrology of an area; and (3) establishment of a classification of lakes in a karst topography which will have transfer value to other areas of similar hydrologic, geologic, and climatologic conditions. This paper is a summary of the first phase of the study. Items 1 and 2, listed above, have been emphasized.

This investigation was undertaken by the U. S. Geological Survey in cooperation with the National Aeronautics and Space Administration. The report is based upon data collected during NASA flights made in February and October 1968 (Missions 67 and 81, respectively).

The study area is in the west-central Gulf coast of Florida and includes parts of Hillsborough, Pasco, and Hernando Counties. The area surveyed is shown by the flight lines in figure 1. Flight lines 1-3 provided coverage of two distinct north-south chains of lakes in the terraced lowlands which extend from Tampa about 10 to 20 miles to the north, and lines 4-6 provided coverage of a northwest-southeast trending chain of lakes 20 miles long in an upland ridge between Dade City and Brooksville. Land elevations range from about 5 to 75 feet above msl (mean sea level) in the lowlands and from about 60 to 300 feet above msl in the ridges. The remote sensing data covers about 250 square miles.

The topography of the area is karst and contains a large number of lakes, ponds, sinks, and swamps. Most lakes throughout the area are classified as either water-table or sinkhole lakes. Water-table lakes exist in depressions that extend below the bottom of the upper surface of the zone of saturation; sinkhole lakes are connected with the underlying limestone which contains water under sufficient hydrostatic pressure to affect the level of the lakes.

Surface drainage patterns throughout the area are poorly developed and most drainage is internal through swamps, marshes, and drain sinks. Several small streams in the terraced lowlands terminate in sinkhole drains (Wetterhall, 1964).

Surface materials underlying the area range in thickness from 20 to 60 feet in the vicinity of the terraced lowlands and from 40 to 100 feet in the vicinity of the upland ridges. The material consists of interbedded sand, silt, and clay. A shallow water-table aquifer occurs in these sediments. The principal aquifer is the Floridan which underlies the sediments and consists of a sequence of sedimentary rocks, predominately limestone interbedded with dolomite, sand, and clay in the upper part and becoming dolomitic at depth (Menke, C. G., and others, 1961).

The terraced lowlands are characterized by intensive urban development and a shift of population north of Tampa into the lake complexes; the upland ridges are predominately rural and are devoted largely to cattle ranching and citrus farming.

The area was selected for the lake survey because of (1) the heavy concentration of lakes, swamps, and marshes of diverse origins and in various stages of development; (2) contrasting topographic and geologic settings having features related to problems of lake hydrology; (3) the contrast between the presence of rapidly expanding urban areas adjacent to that of predominately rural areas; (4) the diverse land use; (5) the changes in landform caused by sinkhole collapse; and (6) the presence of internal drainage through sinkholes.

Two types of remote sensors were used to collect data - aerial photography and thermal IR (infrared) imagery. The aerial photography was flown at altitudes of 2,000 and 6,000 feet in February 1968, and at an altitude of 2,000 feet in October 1968, using RC-8 metric cameras with black and white, color, and color IR film.

Pre-dawn thermal IR imagery was obtained at an altitude of 6,000 feet in February 1968 and at 2,000 feet in October and November 1968 using a Reconofax IV infrared imager to detect the relative intensity of electromagnetic radiation in the 8-14 micrometer part of the spectrum. The areas of highest radiance were from water surfaces and asphalt roads. The areas of lowest radiance were from sandy material dredged from lakes and canals or excavated in areas of rock mining.

DISCUSSION AND RESULTS

Thermal Infrared Imagery

The pre-dawn thermal infrared imagery (8-14 micrometers) provided tonal patterns on film that are useful for interpretation of lake hydrology. Thermal patterns of the water surface and surrounding vegetation indicate much about the past history and present condition of the lakes. For example, the thermal patterns of vegetation surrounding some lakes indicate relatively large declines in water levels. Also the thermal patterns within one lake and in a comparison of many lakes are indicative of their condition such as, eutrophication, depth, and drainage patterns to and from the water bodies.

The mottled pattern of light-to dark-gray tones on thermal IR imagery of the coastal lowlands was due to both the sedges and grasses growing on floatant and dense stands of woody plants, particularly cypress, growing on thick mats on the bottom of swamps and marshes. These "islands of vegetation" were cooler than the surrounding water and showed as dark tones against the light background of the water.

Figure 2 shows thermal IR imagery and IR photography of a swamp-marsh area about 20 miles north-northwest of Tampa. The predawn IR imagery was collected on October 10, 1968, at an altitude of 2,000 feet, and the IR photography on November 8, 1968 at an altitude of 2,000 feet, using a Wratten 15G filter. Although the two flights were made about a month apart surface features on both the imagery and the photography are comparable and show a sharp tonal contrast between water surfaces and vegetative areas. On the thermal imagery, water surfaces are warm and have a light tone because the water absorbs radiation during the day and releases the heat slowly during the night. However, vegetation has a relatively dark tone because it has a thin mass and loses its heat fairly quickly, becoming near ambient by pre-dawn. Similarly, sand grains on roads have a thin mass, lose heat quickly, and sand roads appear as dark streaks. Concrete roads have a large mass and probably would have appeared warm (light tone). On the infrared photographs, solar infrared radiation is absorbed readily by water, resulting in the green, blue or dark color for water. The chlorophyll in healthy vegetation reflects red on color IR (8443) film. The color, tone, and texture are clues to the density, size, and species of the vegetation. The sand roads reflect at all wave lengths and appear as thin, light bands on the color IR film.

Pre-dawn thermal imagery obtained October 10, 1968, for Lakes Iola (fig. 3) and Moody in the ridge uplands showed dark (cool) areas in the lake surfaces. At Lake Iola the dark area coincided with the deepest parts of the lake, which averaged 30-35 feet in depth. These dark areas in the lakes overlie the deep parts of the lakes to which cool water descends in large volume, causing those areas to appear cool on the imagery.

The effect of the automatic gain control adjustment to the average gain can be seen on the thermal IR image. Note that the scan lines have a gray tone when over land but the warm lake water caused the gain to adjust to a new average which resulted in the dark appearance of the land. An intermediate gain adjustment can be noticed near the extreme left edge of the lake by the very light tone over the lake and the slightly dark gray tone over the land. The changing gain makes it nearly impossible to make a quantitative thermal interpretation of the water body. This objectionable effect can be minimized by acquiring the data at a time when the land and water temperatures are nearly equal. This optimum time of equal temperature can be approximated by analyzing daily temperature curves of the water, land (dry and moist soils), and predominant vegetative types. for several days before a flight.

Thermal IR imagery and color IR photography of a large spring in north Tampa is shown in figure 4. The water in the spring boil has about the same chemical and physical properties as the water found in many artesian lakes in other parts of the area. Both the thermal image and color infrared photograph indicate a slight difference between the river and spring (artesian) water.

The thermal IR imagery obtained on October 10, 1968, of Sulphur Springs and the Hillsborough River (Figure 4A) resulted in a dark (cool) tone for both bodies of water with respect to the light (warm) tone of land surface. This probably was caused by the imager's automatic gain control averaging the gain so that the water appears virtually black and the land appears very light along the scan lines at the stream. The film is unable to properly record the entire range of the infrared signal which is compressed into dark and light tones at both ends of the dynamic tonal range of the film. This deficiency can be overcome by DC restoration and calibrating the imager to record in a specific, selected range of thermal interest (Lowe, 1968).

The imagery obtained on November 8, 1968 (Figure 4B) portrays a thermal difference between Sulphur Springs and the Hillsborough River. In this case, the land and water temperatures are similar and within the gray-scale range of the film. The discharge of the spring appears warmer (lighter) than that of the river or surrounding land and can be detected as flowing along the north shore of the river about 600 feet downstream from the spring outfall. The discharge of the Sulphur Springs was about 33 mgd (million gallons per day) at 24°C for both the October and November flights. During the November flight the Hillsborough River temperature was about 20°C and the air temperature was about 15°C. In addition to the temperature difference, the spring water is more highly mineralized than that of the river, although the mineralization probably is not detectable on the imagery. To be successful, infrared imagery should be obtained when maximum thermal differences exist, with preferably the stream of interest being warmer as it is in this case. If the spring were cooler, its water probably would sink to the bottom of the river immediately downstream from the outfall. Thus, the optimum time for study of enhancement of the spring water would be December through February. Consideration should also be given to diurnal temperatures, selecting the time of flight when temperatures are most favorable to enhance the item of interest, whatever that may be--springs, river, soil, or vegetative cover.

In figure 4B the scan lines are parallel to the river and several heavy lines crossing near the center of the bridge came close to obliterating the discharge plume in the river. It would seem advisable to fly the scanner so that the scan lines are oriented nearly perpendicular to a linear feature of interest, such as a river, to minimize the chance of obliterating a small important part of that feature.

Figure 4C is a color IR photograph of the area made February 28, 1968, showing the spring pool (dark green) and the discharge from the spring (light blue) into the Hillsborough River (dark green). The average depth of the spring flume was 2-3 feet, and the river depth was about 2-3 feet at the point of discharge of the spring water into the river. The bottom of the spring discharge channel is visible on the photograph as a deep blue plume that extended about 100 feet near the north bank of the river. During the overflight the river water had a dark brown organic coloring whereas the spring water was clear and the bottom of the spring channel was clearly visible. During a field trip on November 14, 1968, spring water was observed in the river for a distance of about 60 feet below its outfall into the river.

Color IR Photography

The results of the photography obtained at altitudes of 2,000 and 6,000 feet in February and November 1968 are briefly summarized in the examples that follow. These examples indicate the usefulness of color aerial photography in lake-hydrology studies.

A special color coding system was used to describe the lake surfaces shown on the color IR photographs of this report, realizing that color tones may vary on duplicate reproductions. The color index is based on the National Bureau of Standard Centroid color chips calibrated to National Bureau of Standards system of color designations. The color coding was obtained by comparing positive transparencies received from NASA with the Centroid color chips and selecting the number of the color chip which more nearly matched the color of the transparency.

Turbidity is the optical property of a suspension with references to the extent to which the penetration of light is inhibited by the presence of insoluble material and is reported in mg/l (milligrams per liter) silica.

Figure 5 shows the possible use of color IR photography in detecting the effect of dredging on the physical and chemical characteristics of water in a lake. Lake Sunshine is a small lake located in a cypress swamp about 15 miles north of Tampa and was reportedly dredged in 1963. Its average depth is about 15 feet. However, the southern part of the lake has several holes as deep as 24 to 27 feet. Lake Dosson, immediately north of Lake Sunshine is undredged and averages about 10 feet deep with several small holes about 15 feet deep at boat docks.

The turbidity of the water in Lake Sunshine (47 mg/l) was about seven times greater than that in Lake Dosson. To the eye the water had a muddy appearance, which probably was due to colloidal suspension of clay caused by dredging. Prior to dredging the water had a dark organic coloring similar to that which now occurs in Lake Dosson. On the basis of the color code used in this report to describe colors in color IR photographs, Lake Sunshine was assigned a medium blue green color, number 164 and Lake Dosson very dark blackish green, number 166.

Generally, the chemical quality of the water in both lakes was similar; however, the water from Lake Dosson contained high concentrations of aluminum, ammonia nitrogen, and organic nitrogen probably because the area around Lake Dosson supports more people and farming than does the area around Lake Sunshine.

Figure 6 shows two small lakes, Horse and Bonnie, that have similar settings on a wooded ridge near Brooksville. Horse Lake, the westernmost, has a surface area of 0.03 sq mi; a drainage area of 7.7 sq mi, comprised of woods, cattle ranches and a limestone quarry; and the lake averages slightly over 5 feet deep, including an 18-foot deep sinkhole located in the western part of the lake.

Lake Bonnie, located about 1,000 feet to the east of Horse Lake has about the same size surface area; a drainage area of less than half a square mile, comprised of sparse trees, grazing land, and some homes; and the lake depth averages about 3 feet, ranging from 0 to 5 feet. The dikes have been constructed to the east and south of this lake to restrict the drainage area size and to minimize pollution.

The sharp tonal contrast in color of the two lakes (Horse Lake, light green blue, number 172; and Lake Bonnie, slight blue green, number 160) is due to differences in turbidity of the water in the lakes probably caused by differences in drainage areas and land use. The turbidity of Horse Lake (47 mg/l) was more than double that of Lake Bonnie. Horse lake looked muddy while Lake Bonnie appeared relatively clear. Horse Lake had a sulfate content (16 mg/l) about four times that of Lake Bonnie, and the aluminum content (0.5 mg/l) of Horse Lake was the second highest of those determined for lakes of the ridge area. The organic nitrogen content (0.26 mg/l) of Horse Lake was less than that found in most lakes analysed. However, it appears that these chemical constituents probably did not affect the color of the water in the lakes.

Lake Zulu, in the northern part of the ridge area about five miles north of Brooksville, is an artificial lake formed by an earth dike to retain waste water from a mine quarry about a mile northwest of the lake (fig. 7). The lake is in a low area of less than 80 feet above msl.

The range of lake color from very light blue, number 180, to brilliant blue, number 177, is believed to be related to depth and turbidity. Shallow depths appear to have a lighter tone than the deeper parts of the lake, although the general light tone is probably due to the rather high turbidity concentration (23 mg/l). The concentration of lead (0.05 mg/l) is higher than for any other lake of the report area but probably does not have any effect on the tone. Other chemical constituents in the water are typical for lakes in the ridge area. The tonal difference from nearly white to light yellow pink, number 28, in the land area to the north of the lake is probably due to a combination of the near white reflectance of deposited fine material, predominately sand and clay from quarry operations, and reddish tone resulting from the vegetative growth of grass, sedges and small trees.

Figure 8 illustrates the temporal change in the stage of a small coastal lake about 25 miles northwest of Tampa. The lake is about a mile southeast of a large subdivision, where extensive land modification has occurred in the past few years. The area has a typical karst topography. Numerous small circular sinkhole lakes dot the landscape. Land elevations range from about 30 to 50 feet above msl.

The large decline in water level in the lake and the resultant splitting of the lake into five separate pools (1968) illustrates dramatically how rapidly the hydrology of an area may change. Such changes illustrate that a published map represents hydrologic conditions at the particular time the map was made. Because water is a dynamic resource, remote sensing can provide repetitive information on suburban development, land use, and other features that affect and relate to the hydrologic regimen of the area.

Figure 9 shows part of the U. S. Geological Survey topographic map of the Sulphur Springs Quadrangle dated 1956, a black and white reproduction of a color IR photograph, and a thermal IR image of selected parts of the area imaged on October 1968. This figure illustrates the dramatic temporal changes in land use and land form which have occurred since 1956. For example, much of the area designated as swamps and marshes in 1956 has been developed into citrus farms. Changes in land form include the appearance of a sinkhole lake and a water table lake in areas where neither existed in 1956.

The pre-dawn thermal IR imagery shown in figure 9 is an enlarged negative print; therefore, warm areas appear as dark tones and cool areas appear as light tones. Open water surfaces of lakes and ponds appear warm and dry sandy soils appear cool. Infrared imagery is useful to identify instances of thermal anomalies, such as the dried-up lake east of the merging "Y" road junction. The lake is of somewhat elliptical shape and of very light tone (cool), probably because the "bowl" of the lake is dry and the surface material quickly radiated its heat to the outer atmosphere.

The encroachment into swamps and marshes by subdivision developments and urban expansion is rapidly changing the drainage pattern and recharge to underlying aquifers throughout west-central Florida. Figure 10 shows a subdivision development in a typical swamp-marsh area in west-central Florida. Repetitive remote sensing information can provide urban planners, economists, hydrologist, and others with useful information on the hydrologic response to specific land uses. This information may be very valuable at a future time for maximum preservation and development of the water resources.

The development of a subdivision on lake front property about 15 miles north of Tampa is shown in figure 11. This figure illustrates a change in land use which is occurring with increasing frequency in the coastal area of west-central Florida as urban expansion moves northward. The physical characteristics of lakes are often changed by dredging silt from the lake bottom, depositing the material along the banks, and establishing the subdivision as depicted on the figure.

Lake Padgett, the lake near the center of figure 11, was partly dredged several years ago and Lake Saxon was dredged within the past few years. The distinct light banding which shows along the north shore of Lake Saxon, the lake to the east, is due to the deposition of fine to medium sand dredged from the lake bottom. The depth of Lake Saxon ranges from 0 to 35 feet and average about 20 feet. Lake Padgett averages about 15-20 feet in depth but is less than 5 feet deep at its narrow neck near the center of the lake.

The color of Lake Padgett is a deep black green, number 161 and Lake Saxon is a slight bluish green, number 160. The turbidity of Lake Padgett was 4 mg/l and that of Lake Saxon 10 mg/l. The lighter color of Lake Saxon is probably caused by its higher turbidity, although these concentrations are both relatively low. The low concentration is probably due to the low percentage of clay in the dredged soils. The chemical quality of the water in the two lakes was about the same.

It is significant to note that neither Lake Padgett nor Lake Saxon showed high turbidity even though dredging of both lakes has occurred fairly recently. Thus, color IR photography with Wratten 15G filter may be useful in determining areas where silt and clay occurs at shallow depth at or near lakes. A knowledge of the areal distribution of the shallow silt and clay layers would provide a basis for determining those areas where dredging may affect the turbidity of the water in the lakes.

Figure 12 shows a lake created in a borrow pit near the northwestern limits of Tampa. The dark red border around the lake is due to heavy infestation of water hyacinth, and the greenish-red clusters in the northern part of the lake are primarily thick stands of cattails. The depth of the lake ranges from 3 to 15 feet with the deepest holes occurring in the north half of the lake. Differences in the color of the main body of the lake (brilliant green blue, 168) and the isolated channel (very light green blue, 171) along the northeastern shore is due to differences in turbidity of the water. Because of the shallow depth (<5 feet) of the channel its bottom apparently ended in silt and clay beds causing the water to be more turbid than that in the main part of the lake. The turbidity of the water in the main lake was 16 mg/l in February 1968. No sample was obtained from the channel during the overflight and, at a later date, the reflectance characteristics were changed because of discharge into the channel from a nearby excavation. The turbidity of the water in the channel was 125 mg/l in August 1969. The chemical quality of the water in the lake was typical for most lakes sampled in the coastal lowlands.

Lake Pasadena, in the lower part of the ridge area near Dade City, has had a large decrease in storage during the past five years, largely because of below average rainfall. The lake now averages less than 8 feet deep. Shoreline features indicate the large decline which has occurred in the stage of the lake. (See fig. 13)

The three small islands shown in the southern part of the lake were about 100 feet in diameter and less than a foot above the lake level in October 1968. These islands probably were underwater and not visible during the flight made in February 1968, however at that time, both the thermal IR imagery and the color IR photography indicated differences in the

water surface for these parts of the lake.

Distinct radial patterns are visible on the transparent positives of Lake Pasadena; however, these patterns are indistinct in figure 13. These radial patterns resembled fracture patterns caused by land collapse in the lake. However, field examination and lake soundings showed the patterns to be cattle trails that had filled with black organic material in the lake bottom. The depth of the lakes between the islands was less than 2 feet. Thus, cattle moving from one island to another or around the islands disturb the lake bottom, and fine sediment would eventually settle in the trails. The material in the shallow parts of the lake is a very fine-grained light-gray organically-rich sand, which is overlain by black organic matter as much as three feet thick.

The most significant aspects of figure 13 are (1) the distinct vegetative banding around the shoreline of the lake showing the changes in water levels that have occurred within recent historical time, and (2) the fact that the radial patterns in the lake bottom can be erroneously interpreted as sinkhole collapses because of their similarity to such features.

The characteristic zonation of concentric rings of vegetation around many lakes and ponds provides historical record of significant changes in lake and ground-water storage throughout the area (fig. 14). The lakes shown in figure 14 best illustrate the zoning of plant communities. This concentric zonation is known to be associated with other lakes in the area which have shown large declines in water level.

A definition of these communities in other areas of the state may provide a means of establishing average lake levels in those areas where historical records are scanty or nonexistent.

Figure 15A is a color photograph and figure 15B is a color IR photograph using a Wratten 15G filter, of Lake Bystre, an undredged lake in the north-central part of the ridge area. The photographs were taken February 28, 1968, at an altitude of 6,000 feet.

The lake's drainage basin is largely restricted to a small area north of the lake, a gravel pit about half a mile east, and a quarry about a mile northwest of the lake. The lake averages about 4 feet deep and on February 28, 1968 the water surface was estimated to be less than 65 feet above msl. A sluice (which shows as a broad white strip west of the lake) discharges waste from the quarry to the west side of the lake. The dendritic patterns of the stream at the west-central shore was caused by water discharging from the sluice and flowing down the bank towards the lake.

Several sinkholes were reported to exist in the lake, but no exceptionally deep holes were found during sounding of the lake bottom. Both color and color IR photography show several circular features interpreted as sinkholes along the northern shore of the lake; however these holes

apparently were filled by sediments discharged into the lake from the quarry. The color IR photographs showed the circular sinkhole patterns in the lake more distinctly than the color photographs probably because the slightly deeper water over these areas produced darker tones on the color IR film.

A large number of dead oak trees are in the southern and eastern parts of the lake. The reason for the dead trees is probably related to flooding of the area in 1960-61, although the water in the lake had several constituents which were higher than those of any other lake in the ridge area. These constituents included calcium (43 mg/l), strontium (0.10 mg/l), and fluoride (0.4 mg/l). The color of the water on the IR photography is a slight greenish blue, number 169; its turbidity is 16 mg/l. Both the color and the turbidity of the water in Lake Bystre are comparable to the water in a borrow pit in the coastal lowlands. (See fig. 12).

Color infrared and natural color photographs often complement each other so that the combination may provide more information than each one interpreted independently. The color infrared photograph (fig. 15B) appears to contain more information than the natural color photograph on water boundary delineation, sink identification, determination of shallow depth areas, and vegetation. However, the natural color photograph provides an indication of the water color in the visible portion of the spectrum. Thus, the lake color can be combined with the features noted on the color infrared photograph to aid in the hydrologic interpretation of such features as the sinks and shallow depth areas.

The eutrophication of a small closed lake in the citrus farming belt of the ridge area is shown in figure 16. Drainage into the lake is restricted to agricultural runoff and to a small area around the lake, which includes a turkey ranch. Enrichment of the water is due largely to drainage from the turkey barns into the lake. The reddish pink color on the water surface in the southern part of the lake is due largely to duckweed (*Lemna minor*) intermingled with some watermeal (*Wolffia columbiana*). Both plants are characteristic of calm waters that contain high concentrations of dissolved nitrogenous materials and that have a pH less than 7.0. The lake water contained the greatest concentration of most chemical constituents of the lakes sampled including calcium, potassium, chloride, phosphates, zinc, and nitrogenous compounds.

Figure 17 is an example of a lake discharging into a drain sink. The lake is in the north-central part of the ridge area immediately west of State Road 41, and 0.5 mile south of U. S. Highway 98, about 6 miles southeast of Brooksville. The 1954 topographic map showed the area as a swamp. Overflow from the lake to the drain sink is determined by the elevation of the discharge outlet on the south side of the lake. The well-defined vegetative patterns around the shore of the lake on color IR photography may indicate that at one time the lake was at least three times as large as that shown on figure 17. The southeastern part of the lake (now known as Lake Zebra) was cut off from the drain sink by State Road 41.

The main part of the drain sink was about 100 feet in diameter when visited in August 1968. The lake stage was about the same elevation as the outlet and flow into the drain sink was less than 5 gpm. The lake level was higher in November than in August and discharge into the drain sink was proportionately greater.

Sinkhole lakes represent sources of rapid recharge of the underlying limestone aquifer. These sinks are also possible routes of ground-water pollution because surface water moves directly into the aquifer before it has had a chance to become purified by filtration through the soil. In some parts of the coastal and ridge areas drain sinks contribute substantial quantities of water to the aquifer. Thus, information on the location of sinkholes and their recharge potential may provide a means of aquifer management. Flood waters of good quality may be used to recharge an aquifer while contaminated waters may be diverted from the drain sink.

CONCLUDING REMARKS

Remote sensing from aircraft has useful application in lake studies of west-central Florida. Thermal infrared imagery and photography in the visible and near infrared range of the electromagnetic spectrum provide a detailed synoptic record over a large area during a near-instantaneous time interval and may be repeated later for temporal evaluation. The data are also useful for (1) water storage inventories, (2) determination of the type, source, and rate of water body eutrophication, (3) delineation of vegetative zones related to soil moisture and declining lake levels, and (4) providing an insight into subsurface drainage, such as sink drains and artesian springs.

Infrared imagery (8-14 micrometers) is useful to identify thermal anomalies that may be the result of artesian flow, water circulation, and water depth. The identification of ground-water discharge into a surface water body is dependent upon a temperature difference, which probably is maximum from December through February. At this time the ground water will be warmer than the surface water, therefore less dense, and will rise to the surface. Other thermal anomalies noted were related to the daily heat balance in that objects and vegetation of heavy mass tended to hold heat longer and appear warmer on the pre-dawn imagery than those of small mass. For example, an asphalt road appeared warmer than a sand road and moist soils tended to appear warmer than dry soils.

Both natural color and infrared color photography were obtained for this study. The color infrared photography was preferred (1) in hydrologic studies based upon vegetative indicators, (2) in delineation of shoreline boundaries, and (3) in qualitative evaluations of depth and turbidity. However, color infrared photographs appear unnatural because healthy vegetation is a shade of red and turbid water tends to be a shade of pale green or pale blue. Natural color photographs provide an image similar to that sensed by the human eye and are a helpful addition for proper interpretation of phenomena represented on the color infrared photographs.

The optimum time to use the Reconofax IV IR imager for lake studies in west-central Florida is from about mid-December through mid-February when maximum temperature differentials exist between surface-and ground-water bodies. The time of the flights determines to a large extent the degree of success achieved from this type of sensor.

REFERENCES

1. Wetterhall, W.S., 1964, Geohydrologic reconnaissance of Pasco and southern Hernando Counties, Florida: Florida Geol. Survey Rept. Inv. 34.
2. Menke, C. C., Meredith, E.W., and Wetterhall, W.S., 1961, Water Resources of Hillsborough County, Florida: Florida Geol. Survey Rept. Inv. 25.
3. Lowe, D.S., 1968, Line scan devices and why we use them. Proceedings of the Fifth Symposium of Remote Sensing of Environment, April 1968, University of Michigan, Ann Arbor, Michigan. p. 77-101.

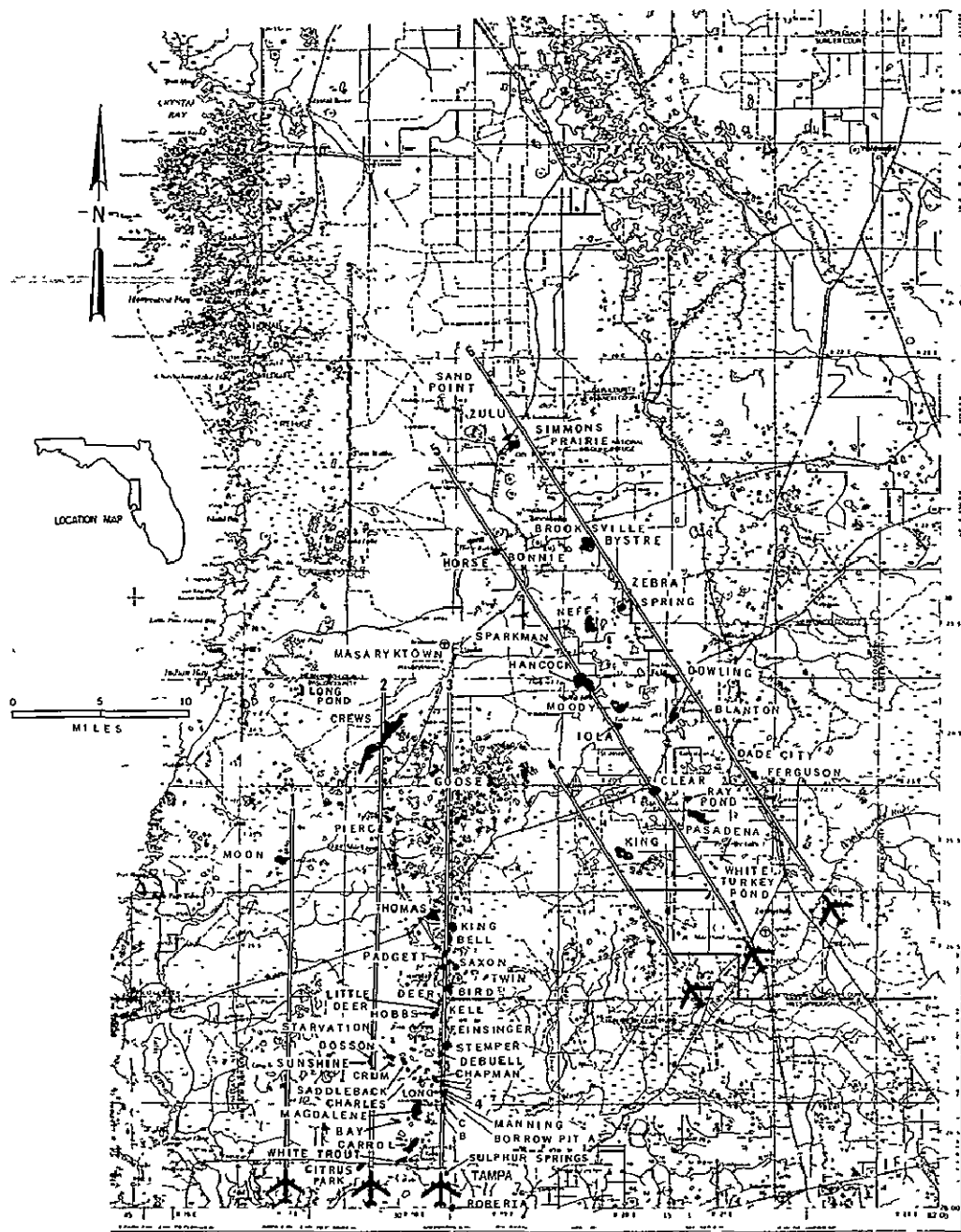
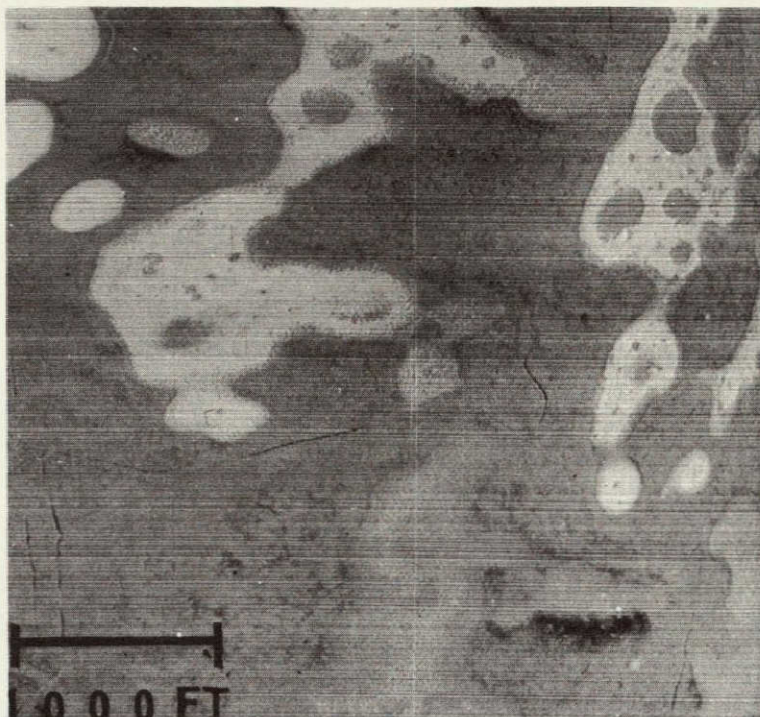
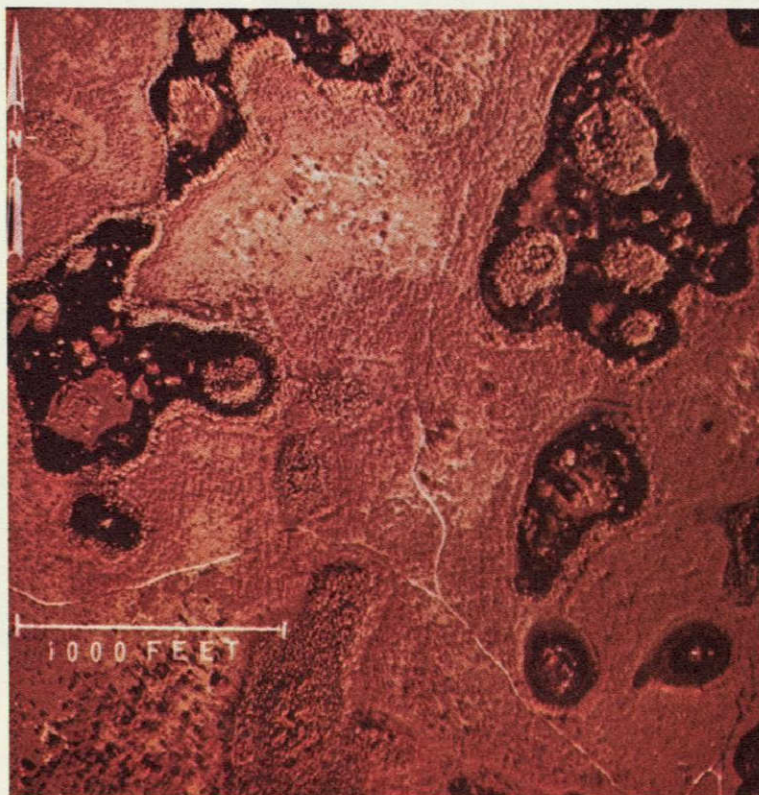


Figure 1. Map of west-central Florida showing study area - 1968.



a. Thermal IR imagery, October 10, 1968. Time, predawn; altitude 2,000 feet; line of flight due north. Imagery enlarged. 1 inch equals approximately 800 feet.



b. Color IR photograph, November 8, 1968. Altitude 2,000 feet; film, Ektachrome infrared with Wratten 15G filter.

Figure 2.- Thermal IR imagery and color IR photograph of a swamp-marsh area about 20 miles north-northwest of Tampa.

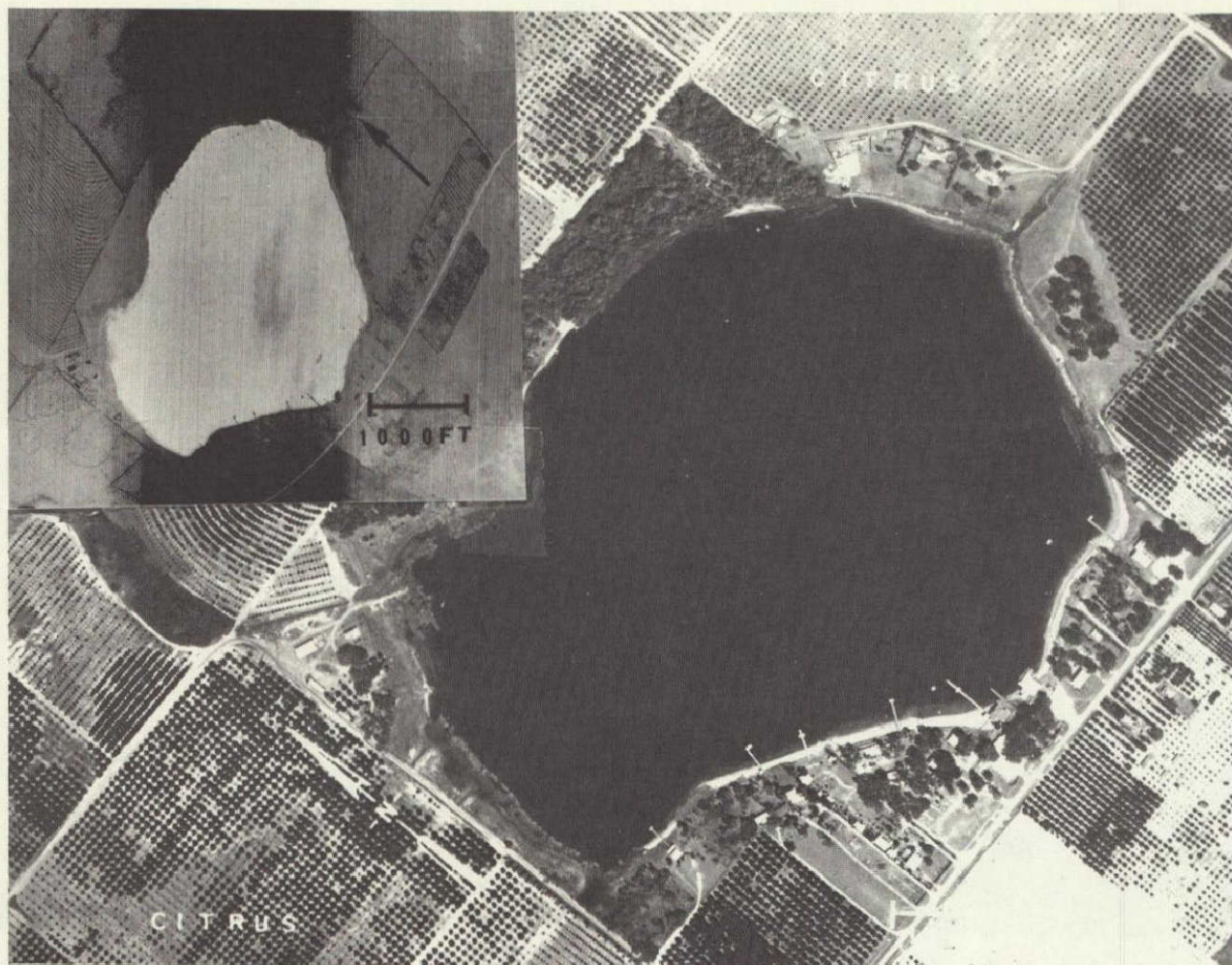
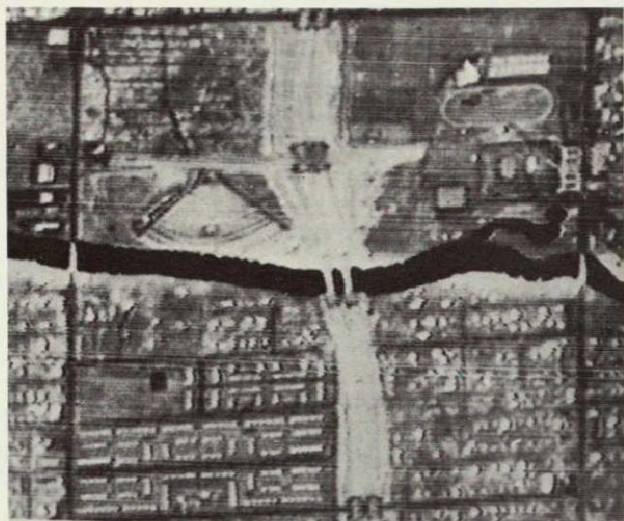
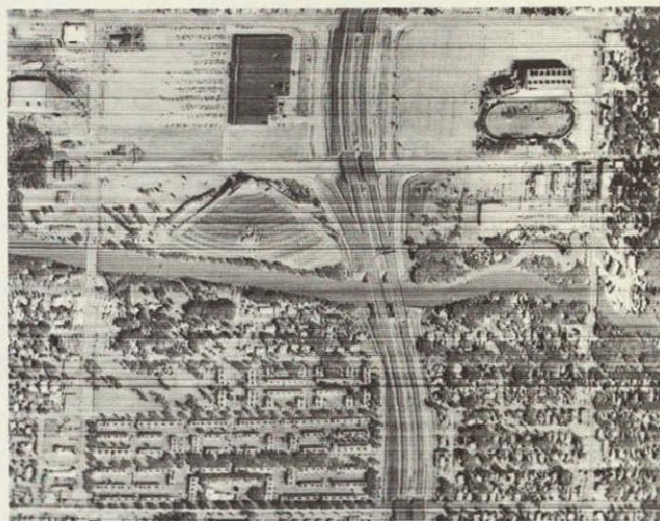


Figure 3.- A black and white print of color IR photograph and thermal IR image of Lake Iola. Color IR photograph obtained February 28, 1968 at altitude 6,000 feet using Ektachrome infrared film with Wratten 15G filter; thermal IR obtained predawn on October 10, 1968 at an altitude of 2,000 feet. The dark area in the southcentral part of the imagery represents a cool area overlying the deep part of the lake.



a. Infrared imagery, October 10, 1968; predawn. Altitude 2,000 feet; line of flight due north. Imagery enlarged. 1 inch equals approximately 1,000 feet.



b. Infrared imagery, November 8, 1968; predawn. Altitude 2,000 feet; line of flight due north. Imagery enlarged. 1 inch equals approximately 1,000 feet.



c. Color infrared photography, February 28, 1968. Altitude 6,000 feet; film, Ektachrome infrared; filter, Wratten 15G.

Figure 4.- Thermal IR imagery and color IR photography of an artesian spring discharging into a stream, Tampa.



SUNSHINE AND DOSSON LAKES - EFFECTS OF DREDGING ON THE PHYSICAL AND CHEMICAL CHARACTERISTICS OF WATER IN A LAKE: ALSO SHOWS DECLINES IN THE STAGES OF SEVERAL LAKES CAUSED BY HEAVY GROUND-WATER WITHDRAWAL FROM AN ARTESIAN AQUIFER. ABOUT 15 MILES NORTH OF TAMPA, FLA.

PHOTOGRAPHY: NASA, MISSION 67, SITE 147
 TIME: 1854, FEBRUARY 28, 1968
 FILM: EKTACHROME INFRARED AEROGRAPHIC, TYPE 8443
 FILTER: WRATTEN 15
 ALTITUDE: 6000 FEET
 WEATHER: CLEAR AND BRIGHT WITH SOME GROUND HAZE.

Figure 5.- Sunshine and Dosson Lakes.



LAKES HORSE AND BONNIE—DIFFERENCE IN THE PHYSICAL AND CHEMICAL CHARACTERISTICS OF WATER IN OPEN AND CLOSED LAKES IN A RIDGE AREA, NEAR BROOKSVILLE, FLORIDA.

PHOTOGRAPHY: NASA, MISSION 67, SITE 147
 TIME: 1708, FEBRUARY 28, 1968
 FILM: EKTACHROME INFRARED AEROGRAPHIC, TYPE 8443
 FILTER: WRATTEN 15
 ALTITUDE: 6000 FEET
 WEATHER: CLEAR AND BRIGHT

Figure 6.- Lakes Horse and Bonnie.



Figure 7.- Artificial lake near a mine quarry about 5 miles north of Brooksville.




1964



1954



1968

0 2000 feet


PHOTOGRAPHY: U.S. Geological Survey
 Water Resources Division
 TIME: May 1964
 FILM: Anscochrome, D200
 FILTER: HF-3
 ALTITUDE: 7,000

U.S. Geological Survey
 Topographic Division
 1954

NASA, Mission 67, Site 147
 February 1968
 Ektachrome Infrared, 8443
 Wratten 15G
 6,000

Figure 8.- Destruction of a small coastal lake, May 1964 and February 1968.
 Illustrates a dynamically changing resource (temporal change).

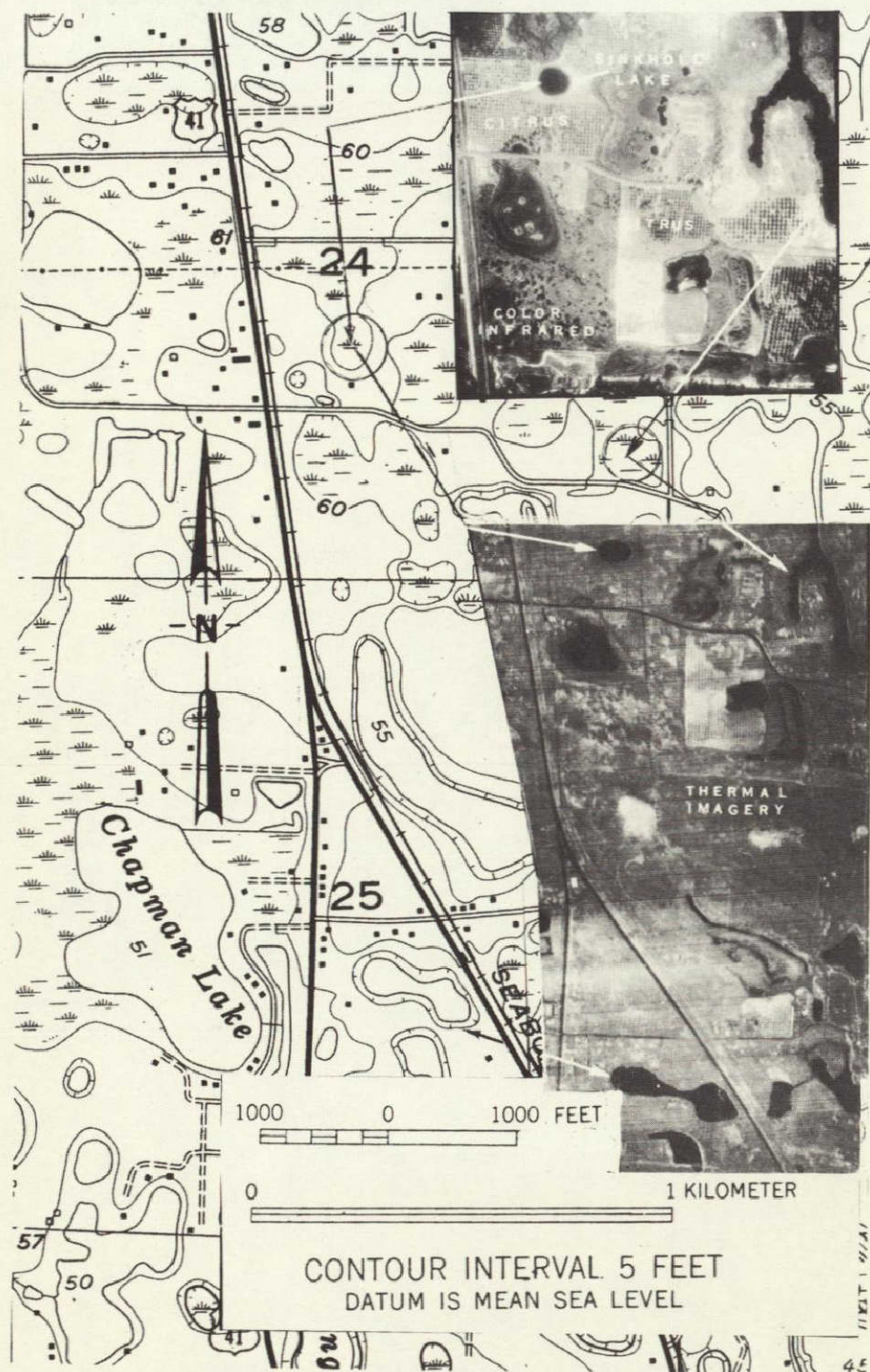


Figure 9.- Color IR photography and thermal IR imagery of an area north of Tampa illustrating the effects of changes in land use and land form on the hydrology of an area.

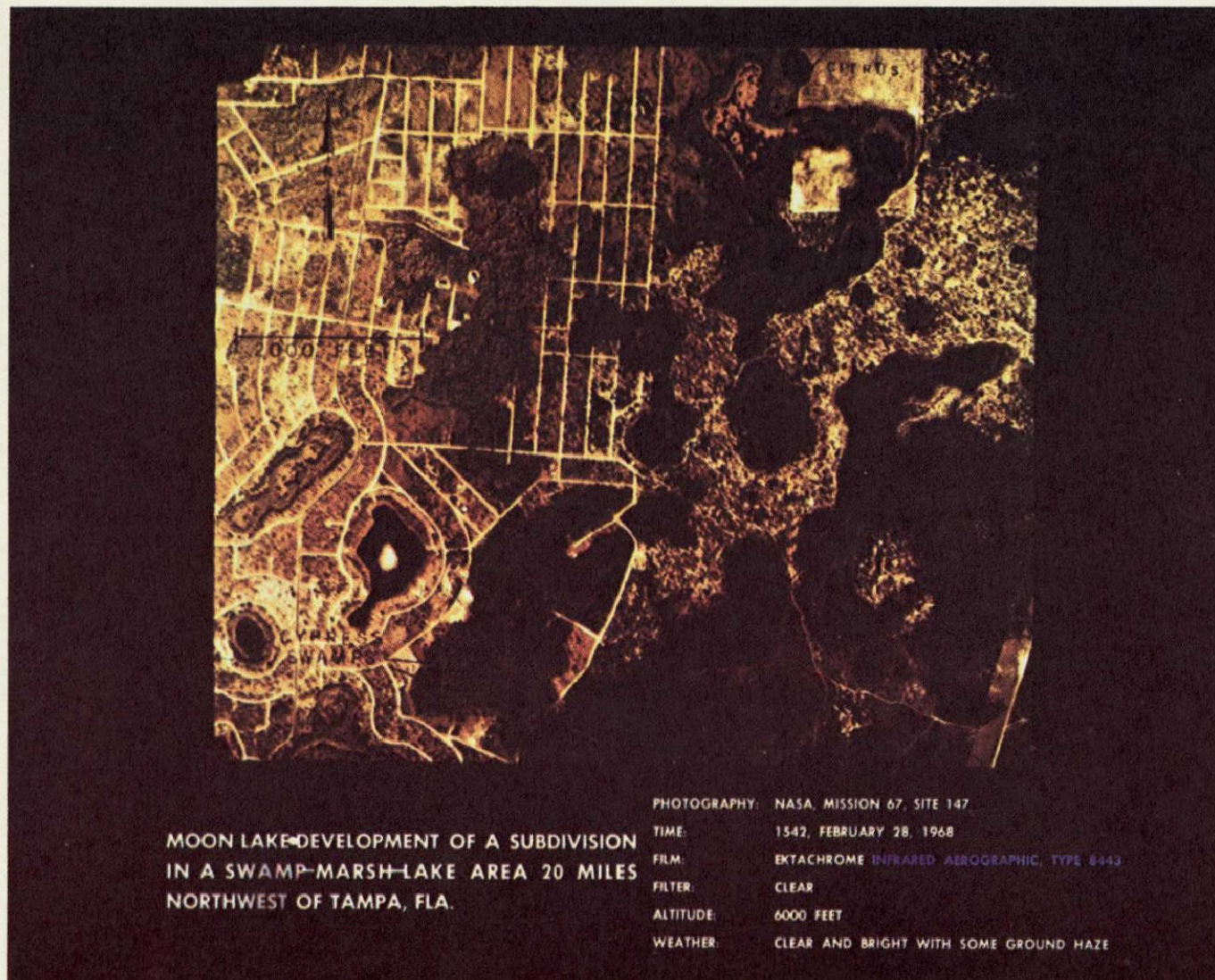
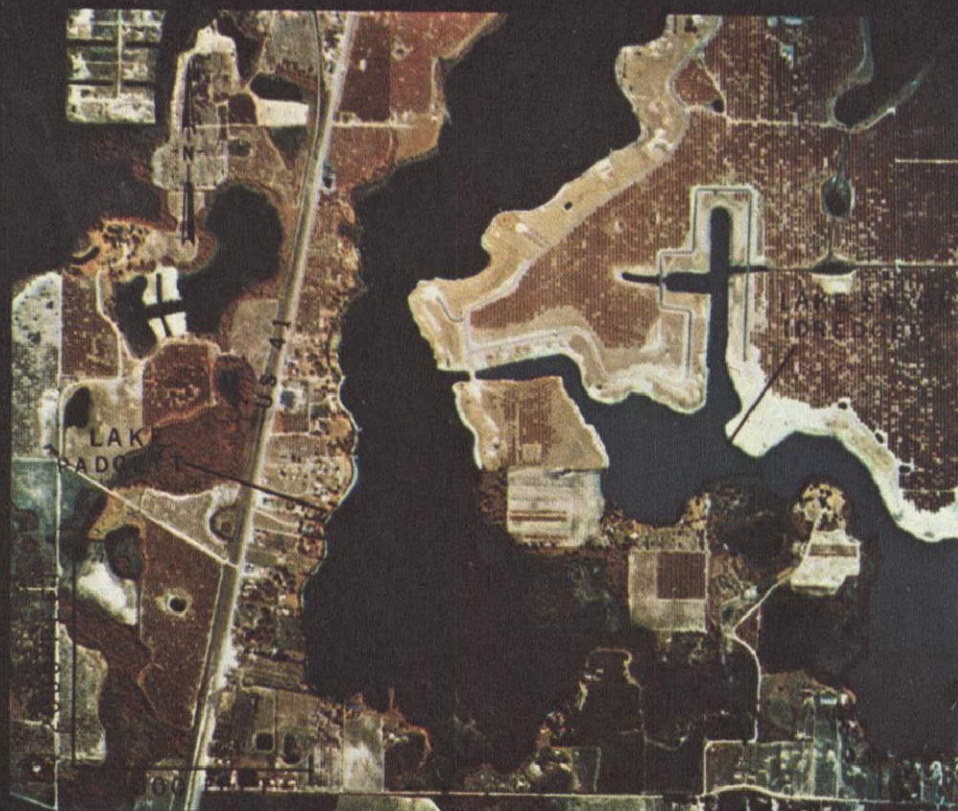


Figure 10.- Encroachment of a subdivision in a swamp-marsh-lake area, Pasco County.



**LAKES PADGETT AND SAXON—DEVELOPMENT
OF SUBDIVISIONS ON LAKE FRONT PROPERTY,
15 MILES NORTH OF TAMPA, FLA.**

PHOTOGRAPHY: NASA, MISSION 67, SITE 147
TIME: 1741, FEBRUARY 28, 1968
FILM: EKTACHROME INFRARED
AEROGRAPHIC, TYPE 8443
FILTERS: WRATTEN 15
ALTITUDE: 6000 FEET
WEATHER: CLEAR AND BRIGHT, EXCELLENT

Figure 11.— Differences in color of water surface in lakes dredged at different periods for subdivision developments.



**CITRUS PARK LAKE - WATER-FILLED
BORROW PIT, TAMPA, FLA.**

PHOTOGRAPHY: NASA, MISSION 67, SITE 147
 TIME: 1756, FEBRUARY 28, 1968
 FILM: EKTACHROME INFRARED AEROGRAPHIC,
 TYPE 8443
 FILTER: WRATTEN 15
 ALTITUDE: 6000 FEET
 WEATHER: CLEAR AND BRIGHT

Figure 12.- Borrow pit lake showing differences in color of water surface and infestation of parts of lake by water hyacinth.



Figure 13.- The development of shore-line features and offshore islands in a lake showing large declines in water level in the ridge area.

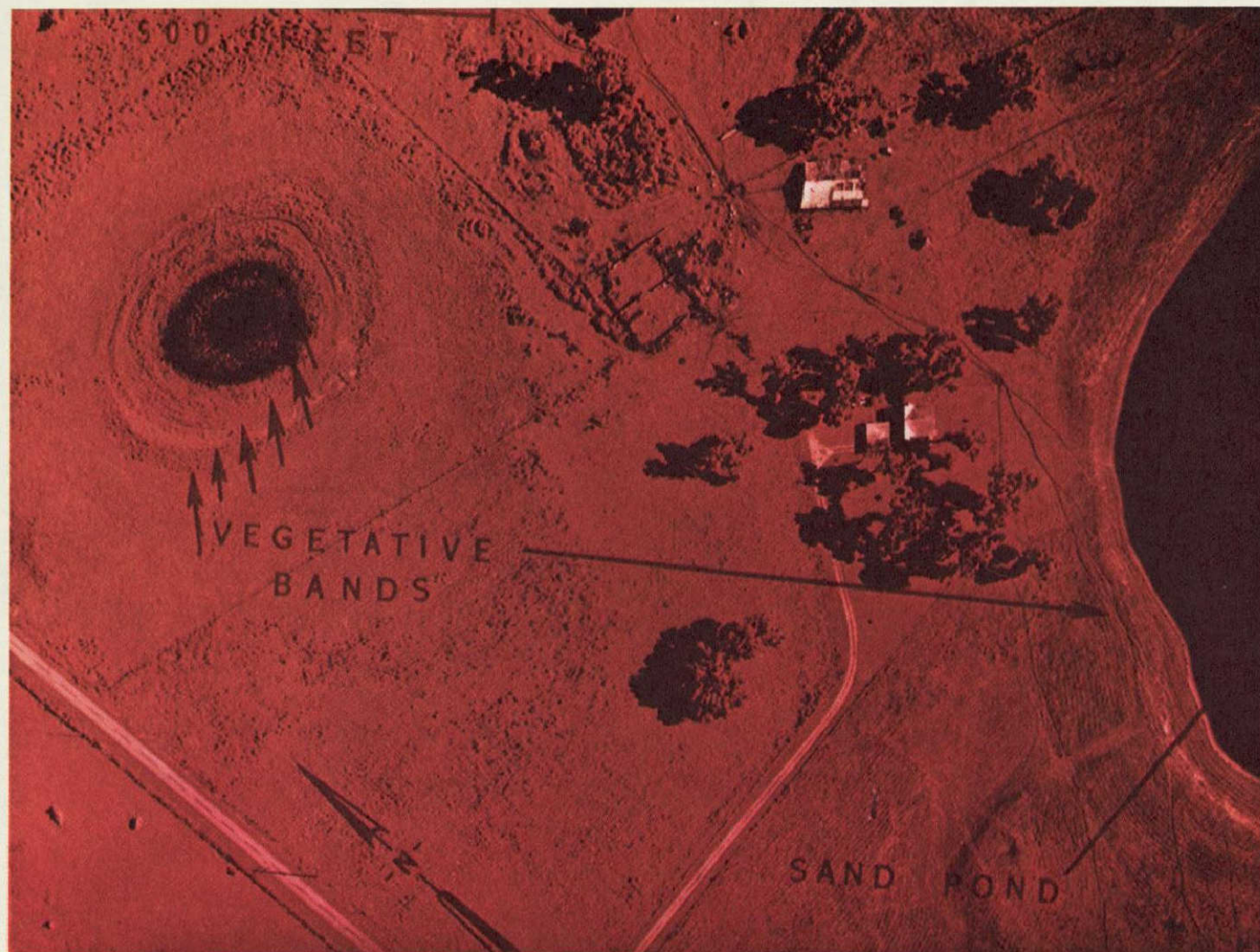


Figure 14.- Color IR photography of a pond and a lake in the ridge area showing concentric banding of vegetation. Photography obtained by NASA November 8, 1968 at an altitude of 2,000 feet using Wratten 15G filter.

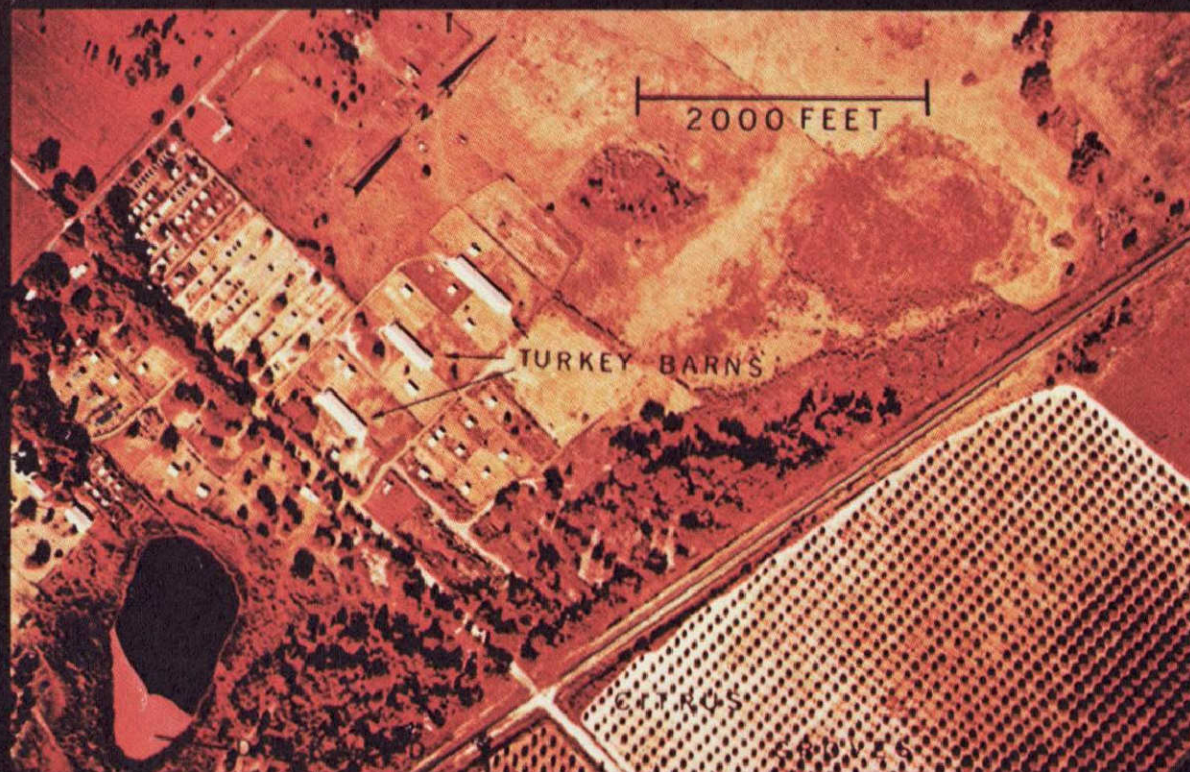


a. Color photograph of Lake Bystre.



b. Color IR photograph of Lake Bystre using Wratten 15G filter.

Figure 15.- Color and color IR photograph of a lake in the ridge area draining a limestone quarry. Photography made February 28, 1968, at an altitude of 6,000 feet.



WHITE TURKEY POND-EUTROPHICATION OF
A SMALL CLOSED LAKE IN A CITRUS FARMING
AND TURKEY RANCHING AREA, NEAR DADE
CITY, FLORIDA.

PHOTOGRAPHY: NASA, MISSION 81, SITE 147
TIME: 1427, OCTOBER 10, 1968
FILM: EKTACHROME INFRARED
AEROGRAPHIC, TYPE 8443
FILTER: WRATTEN 15
ALTITUDE: 2000 FEET
WEATHER: CLEAR, WITH ISOLATED
CLOUD COVER

Figure 16.- White Turkey Pond.



Figure 17.- Lake discharging into a drainsink in ridge area.
 Photography by NASA, November 8, 1968; altitude 2,000 feet;
 Ektachrome IR film with Wratten 15G filter.

SECTION 39

REMOTE SENSING OF OFFSHORE SPRINGS AND SPRING DISCHARGE ALONG THE
GULF COAST OF CENTRAL FLORIDABy J. D. Hunn and R. N. Cherry
U. S. Geological Survey

INTRODUCTION

Ground-water discharge is believed to occur from a limestone aquifer as submarine spring flow along the Gulf coast of central Florida. This aquifer, called the Floridan aquifer in hydrologic literature, underlies most of central and southern Florida and extends beneath the Gulf of Mexico. The aquifer supplies most of the water for the rapidly expanding population along Florida's central Gulf Coast.

Direct discharge of ground water from the Floridan aquifer to the Gulf of Mexico is possible wherever hydraulic pressure in the aquifer offshore exceeds that of sea water at the sea floor. A water-level contour map (fig. 1) shows artesian pressure in the aquifer expressed as water level in the aquifer, in feet above mean sea level. In the southern part of the report area, the zero water-level contour is located offshore. Direct discharge to the Gulf should be possible in this area.

As a result of a previous investigation (Wetterhall, 1965), sinkholes in the floor of the Gulf are known to occur in both the northern and southern parts of the study area. Wetterhall reports flow from one of two offshore sinkholes in the northern part of the area and from two sinkholes in the southern part. Flow from these sinks at low tide is not necessarily ground-water discharge. Water could enter the aquifer through the sinkholes at high tide and discharge again at low tide. Dredging of channels into the limestone in areas where the artesian pressure offshore is above sea level could increase the discharge of potentially useable fresh water into the Gulf of Mexico. Because part of the near-shore area is accessible only with difficulty by land, water-level data along the coast is scarce, and the accuracy of the zero water-level contour (fig. 1) is in doubt. The objective of the project is to detect thermal contrasts related to offshore ground-water discharge and to locate the offshore springs on photographs. If this objective can be achieved, 8-14 micron thermal imagery and aerial photography could become standard tools for hydrologic reconnaissance of similar coastal areas.

PROCEDURE

In order to detect ground-water discharge to the Gulf, 8-14 micron thermal imagery was obtained near low tide during times of temperature contrast between ground water and the Gulf. Ground-water temperature in the near-surface limestones of central Florida ranges from 23° to 25°C. Temperature in the Gulf near St. Petersburg

N71-11156

may range from 10°C in winter to 31° in summer, according to U. S. Weather Bureau data at Egmont Key, Florida.

Probable points of ground-water discharge were located by interpreting aerial photography, in order to interpret the thermal imagery of the test site. Known springs in the Gulf generally discharge from small nearly vertical sinkholes that range in depth from about 20 to 150 feet and range in diameter from about 15 to 50 feet. These springs occur generally on the Gulf bottom in shallow water 1 to 4 feet deep. Most of the light entering these sinkholes should be absorbed. The sinkholes should appear on aerial photographs as small, very dark areas surrounded by clearly visible bottom features. Color, color infrared, and multiband black and white photography were used to test the capability of these sensors to reliably detect submerged sinkholes. Feasibility of identification of sinkholes on the photographs was confirmed by field checking.

Thermal contrasts in the vicinity of known sinkholes can be interpreted as ground-water discharge, provided the contrast is the same as would be predicted from known differences between ground water and Gulf temperatures. Discharge from an offshore spring should appear on the imagery as a "hot or light spot" in the winter and as a "cold or dark spot" in the summer. No difficulties were anticipated as a result of mixing of spring discharge with the Gulf water, because of the very shallow general depth of water overlying the submerged springs.

RESULTS

All known offshore springs and four sinkholes in the Gulf not previously known to the investigators were identified on aerial photographs. Color photography (Ektachrome 8442, no filter) proved to be the most useful sensor tested for this purpose. Color infrared is equally satisfactory in very shallow water, but is not superior to conventional color photography.

Multiband black and white photography, using the Itek camera, did not show bottom detail as well as the color photography. Sinkholes in the floor of the Gulf appeared as small, round, or semi-round dark spots on the color film (fig. 2 and 3). Because of their small size, the sinkholes become more difficult to recognize with increasing altitude of the camera.

Thermal contrasts were observed near the two known offshore springs in the offshore area of positive artesian head. The spring discharge appeared to be warmer than the Gulf in winter and colder than the Gulf in late spring, as predicted (figs 2, 3, and 4). No definite thermal contrasts that could be related to spring discharge were noted in the area of negative artesian head, although sinkholes in this area are known to discharge some water at low tide. Interpretation of the May 15, 1969, imagery is more difficult because areas out of water at low tide have the same thermal contrast as the springs.

CONCLUSIONS

Color photography, using Ektachrome 8442 film and the RC-8 camera at altitudes of 3,000 to 5,000 feet, can be used to detect possible offshore springs submerged in shallow water. Identification of the possible springs and sinkholes on the photographs becomes increasingly difficult as their size on the image decreases. The photography taken at 5,000 feet represents the approximate altitude for the collection of interpretable data with the photographic equipment used.

The temperature contrasts, as indicated by the 8-14 micron imagery and observed spring discharge, occurred where predicted by the project hypothesis. The imagery showed the contrasting temperatures of sea-and aquifer-water and confirmed the existence of fresh-water discharge. The most easily interpreted results were obtained immediately before dawn on February 27, 1968, when ground-water temperatures were warmer than the Gulf of Mexico. When ground-water temperatures are colder than the Gulf, nighttime or early morning thermal contrasts related to offshore spring discharge could be mistaken for areas of the Gulf bottom exposed at low tide.

Detection of offshore spring discharge along the west coast of Florida and in areas of similar hydrology can be used to aid construction of water-level contour maps and to predict areas where dredging of channels into rock might result in increased submerged discharge of fresh water into the sea.

REFERENCES

- Wetterhall, W. S., 1965, Reconnaissance of springs and sinks in west-central Florida: Florida Geol. Survey Rept. Inv. 34.
- Cherry, R. N., Stewart, J. W., and Mann, J. A., 1970, General hydrology of the Middle Gulf area, Florida. U. S. Geol. Survey open-file report.

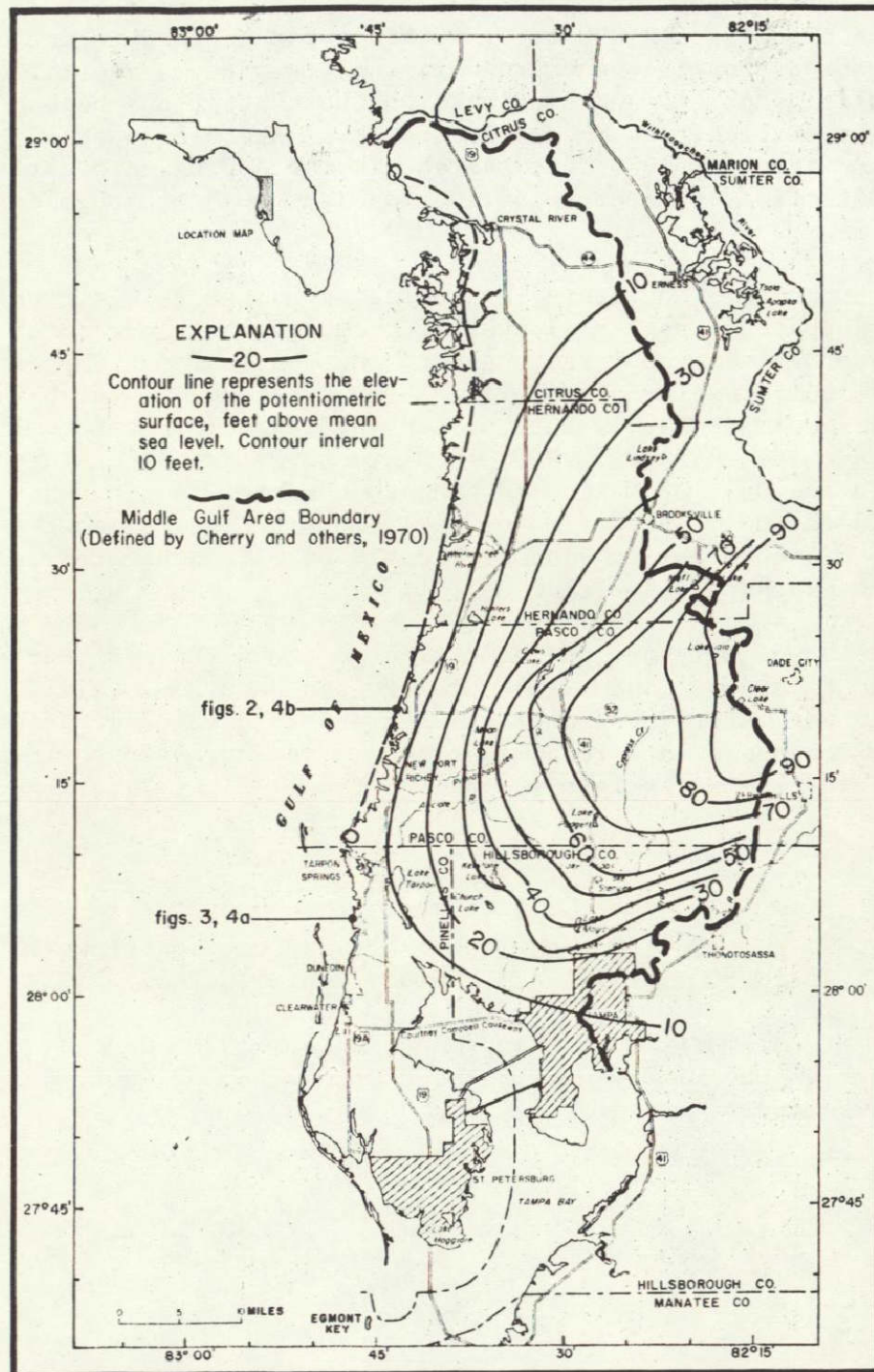


Figure 39-1.- Map of Middle Gulf area, Florida, showing location of zero water-level contour of the Floridan aquifer during August and September, 1965; project area between Clearwater and Crystal River, Florida, and sites shown on figures 28-2, 28-3, and 28-4.

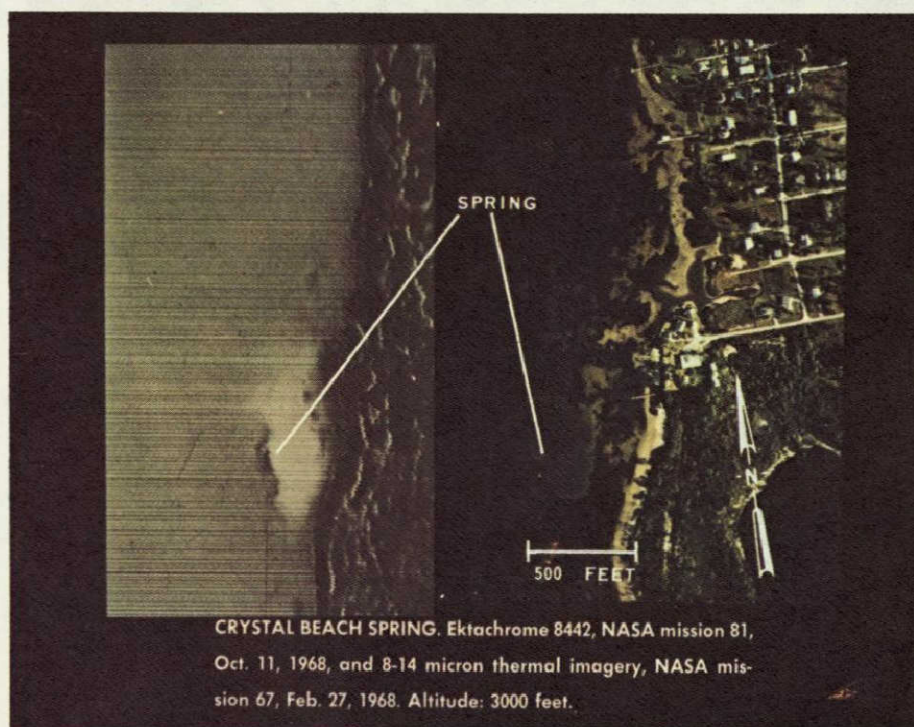


Figure 39-2.- The light area in the imagery (left) results from a temperature contrast caused by warmer ground water (about 25°C) discharging into the Gulf of Mexico (about 15°C) at Crystal Beach Spring (aerial photograph, right). The imagery shows approximately the same reach of coastline as the photograph, but the east-west scale of the imagery is considerably smaller.

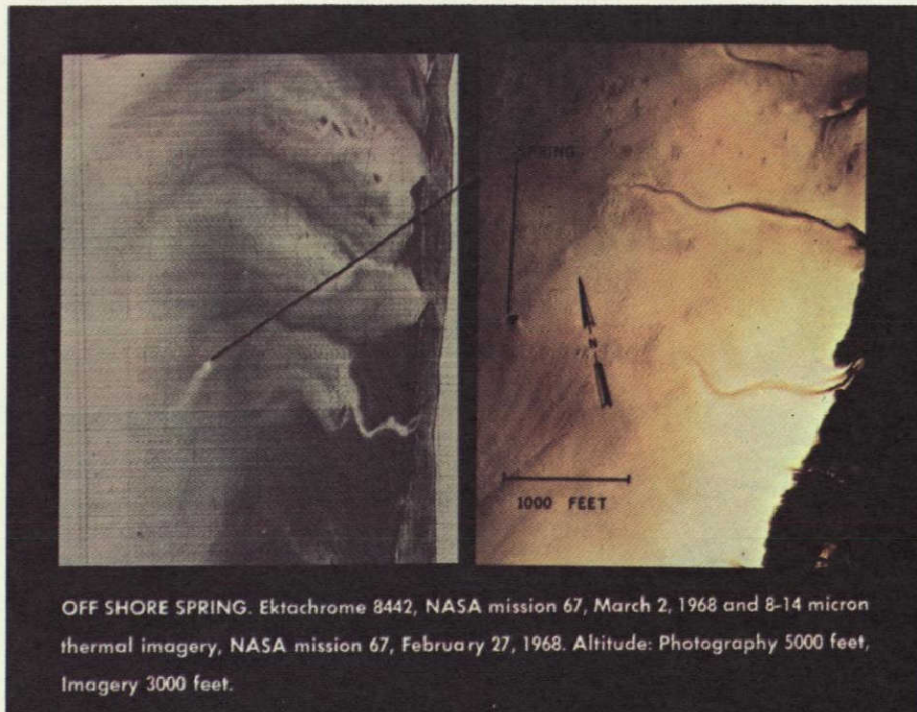
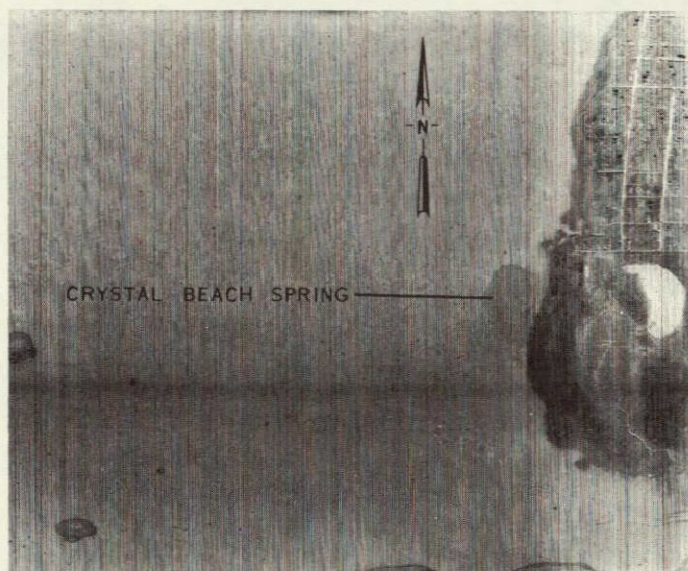
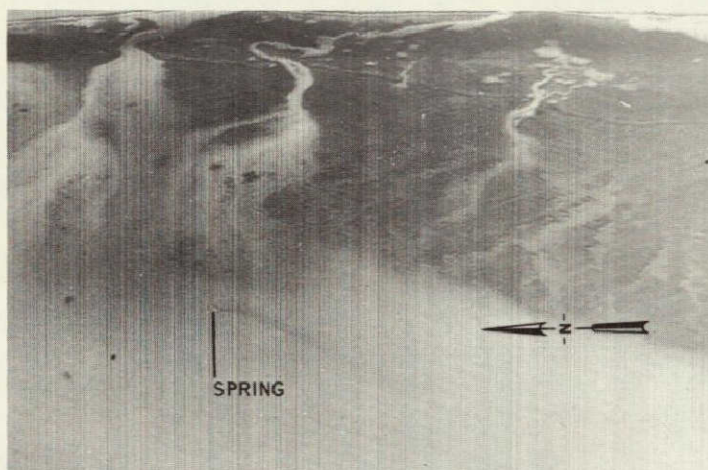


Figure 39-3.- Spring discharge, when warmer than the Gulf of Mexico, is shown by a light area on the thermal imagery (left). Parts of the Gulf bottom exposed at a low tidal stage are colder than the Gulf, if the imagery is flown at night or early in the morning. The resulting dark areas intensify the thermal contrast resulting from spring discharge. The small, semi-round, dark spring orifice (photograph, right) typifies the appearance of offshore sinkholes on color photography.



a. Island.



b. Tidal flat.

Figure 39-4.- Spring discharge shows as a dark area on 8-14 micron thermal imagery for May 15, 1969, when ground water was about 5° C colder than the Gulf of Mexico. Island (fig 28-4(a), lower left and bottom center) and tidal flats (fig 28-4(b)) were also colder than the Gulf during this evening flight. Foreknowledge of spring locations is necessary in order to interpret thermal imagery collected under these conditions.

N71-71157

SECTION 40

The Use of Color Infrared Photography
and Thermal Imagery in Marshland and
Estuarine Studies.

Dr. Richard R. Anderson
Biology Department
The American University
Washington, D.C. 20016

PRECEDING PAGE BLANK NOT FILMED

Introduction

This study is part of a larger effort conducted by the Office of Remote Sensing, U.S. Geological Survey, concerning hydrological applications of various remote sensing techniques. Research involving estuarine systems is receiving considerable attention, with projects in several areas of the United States funded, including this investigation.

The object of the work being reported herein is to test the feasibility of analyzing estuarine water quality and marshland vegetation, using imagery obtained from aircraft, and to establish qualitative and quantitative interpretive criteria by which these areas may be analyzed from spacecraft. This is a progress report and culminates the initial year of work.

Two overflights of the Patuxent River, Md. were obtained by Houston based NASA aircraft in June and September 1968. (Missions 74 and 79). Objectives of the flights were (1) test film and filter combinations for best delineation of plant communities and water pollutants. (2) determine change in imaging characteristics of marshland vegetation with growing season (spring and fall). (3) determine time of day when sunglint on the water could be avoided and still provide ample lighting for delineation of plant communities in marshes. (4) determine the usefulness of thermal imagery in marshland and estuarine studies.

Justification for Current Research

There is an increasing need for a rapid, relatively low-cost method for determining water quality in estuaries and general species composition of marshlands. Ecologists are concerned about the accelerated alteration and destruction of these little studied segments of the ecosystem which contribute both nutrients and shelter to aquatic animals and wildfowl.

If only commercially important species are considered, it appears that with the present rate of loss of wetlands, and increase in water pollution along the eastern coast of the U.S.A., one can expect a concomitant drop in harvestable crops of finfish and wildfowl. Juveniles of these groups abound in waters rich from nutrient additions from the marshes and where predators are not as prevalent. This early development is a very critical stage in the life cycle. Each species has very exacting requirements for food and shelter and the choice each species makes is instinctive and not open to arbitrary selection. Therefore any reduction in a habitat requirement for a given species will also ultimately result in a reduction of the population of that species.

Nearly 70% of the eastern coastal fishes are dependant in some stage of their life cycle on shallow waters bordered by marshes, intricately dissected by small creeks and inlets. Florida estimates about 85% of all fish and shellfish species depend on wetlands during part of the life cycle. In 1965, the commercial catch of all finfish in the South Atlantic and Gulf coast region dependant on wetlands amounted to 1.1 billion pounds, worth about \$32 million and constituted 28% of the Nations commercial catch of all finfish.

The dependence of finfish on estuarine areas for food stems from

the fact that few marine fish feed directly on planktonic organisms, but feed primarily on plants and animals higher up the "food chain" such as rooted aquatic plants, bivalves, worms and crustaceans which inhabit the river bottom (benthos). A generalized aquatic food chain would include the following:

1. Algae which grow on the nutrient rich marsh muds are capable of fixing atmospheric nitrogen into proteins and also photosynthesize sugars and vitamins. Marsh grasses and other plant species produce up to 10 tons of organic material per acre per year. (Compared to wheatfield which produces only 1 1/2 tons).
2. Marsh algae and higher plants die and through process of decay important nutrients and vitamins are released from the plants and washed into the water by tides and rainfall (up to 50% of organic material produced). Examples of important compounds contributed to the aquatic ecosystem are vitamins such as biotin, cobalanin, niacin and thiamin, also sugars, organic acids, amino acids, and polypeptides. The latter three are important in forming complexes with micronutrients such as manganese, zinc, copper, iron and phosphate and keeping them in solution for use by phytoplankton.
3. Much of the organic matter (about 45%) is washed from the marsh in a partially decayed form and settles to the bottom of rivers and estuaries where it is available for use by bottom dwelling organisms. Rees (14) reported on the highly diverse, rich bottom communities found in estuarine muds. He found a density of between 11 and 12 million animals per square meter, much of it concentrated in the top 1 centimeter where it is readily

available for use by higher aquatic animals.

4. The bottom communities as well as detritus from the marshes provide food for transient as well as permanent dwelling estuarine shell fish and finfish.
5. Man is at the top of the food chain and of course depends on shellfish and finfish for at least a portion of his food.

Submerged rooted aquatic plants also play an important role in the aquatic ecosystem. As well as supplying organic material to bottom animal communities they contribute to oxygen balance in the water, stabilize the bottom which reduces turbidity, provides a place of attachment for smaller plants and animals and a hiding place for young commercial fishes. They are also an important source of food for fishes, wildfowl and mammals.

Sculthorpe (16) has summarized the use of hydrophytes by various aquatic animals. Organisms which grow on rooted aquatic plants include algae, bacteria and protozoa. These serve as food for crustaceans, molluscs, worms and insect larvae on which carnivorous fishes in turn, depend. Up to 7.5 percent of the biomass of a rooted aquatic community may be consumed directly, each day. The fruits and seeds of many rooted aquatics provide the most important food of many types of waterfowl (coots, ducks, geese, grebes, and swans) and are eaten by marsh birds (bittern, and heron) and game birds (grouse, partridge and pheasant).

The justification for research in evaluation of marshlands and estuaries using remote sensing techniques is that there are pressures from various sources to dredge and fill in these areas for marinas, housing developments, etc. It is of utmost importance that marshlands and estuaries be inventoried, categorized and monitored in order to

ensure survival of many aquatic species for future generations. The most convenient, economical method for this type of study is through use of remote sensing devices.

Review of the Literature

Since little comprehensive research had been done on imaging characteristics of marshland vegetation and water pollutants prior to this research, much of the early work involved comparison of color and color infrared photography in remote analysis of these areas. It was concluded by the author that, although, natural color photography was extremely useful, Ektachrome IR photography would give, overall, the most information from low and especially high altitude (Anderson, 1969). Lukens (8) concluded that color photography is superior to Ektachrome IR in species identification of aquatic plants. Water chestnut was particularly well delineated. Recently Pestrong (13) reported the use of a variety of multiband imagery, including a nine-lens camera, panchromatic, Ektachrome and Ektachrome IR photography in evaluation of tidelands in San Francisco Bay. He concluded that nine-lens multiband imagery was excessive and could be reduced to four-lens imagery. Color IR photography was superior for the differentiation of vegetative types within saline marshlands, while natural color was most useful for general interpretation.

The use of remote sensing in delineation of gross aspects of water pollution has received some attention. Strandberg (17) and Scherz (15) have reported on photographic characteristics of some water pollutants. Thermal imagery has been used extensively to delineate distribution of heated water from power plants and other industrial sources. Van Lopik et. al. (18) and Lukens(9) are among those who have cited use of this sensor in pollution surveys.

Paulson (12) has demonstrated the use of thermal imagery in detecting various physical characteristics of estuaries, including the air-water interface, sources of sediments, velocity estimates and sources of petroleum pollution.

The ideal in any remote analysis of water pollution is to be able to arrive at a quantitative estimate of various pollutants from image quality on film, thus avoiding the expensive ground surveys usually employed for this purpose. Neumaier and Silvestro (10) have developed a method by which they believe qualitative measures of pollutant discharges such as paper mill waste, oil and sewage may be obtained from color photography.

It is becoming increasingly important to obtain information on spectral reflectance of ground targets. Olson and Ward (11) and Draeger (5) are among those who are utilizing this technique as a way of predicting what film-filter combinations may be useful in differentiating plant species. This technique will also be useful in analyzing multi-spectral imagery.

Results and Discussion

During June and September 1968, the Patuxent River, Md. was overflowed by Houston based NASA aircraft. RC-8 metric cameras with Ektachrome IR film (type 8443) fitted with one of three Wratten filters (15-G, 25-A, and 57) and a Reconofax IV infrared imager were utilized on the flights. An extensive data collection operation coincided with the times of flight for photography. Three boats were utilized to obtain information on turbidity, salinity and temperature of the estuarine water over the greater portion of the area being photographed. Radiometric quantities of water and marsh vegetation were obtained utilizing a PRT-5

Radiometer flown in a helicopter.

A. Color infrared photography

Results indicate that Ektachrome IR photography is a valuable tool in estuarine and marshland research. Tone and color rendition of the film is excellent and provides good definition of the identity and spatial distribution of important marsh plant communities. Characteristics of the estuarine water such as sediment content, current patterns, nutrient additions and distribution of small creeks in the marsh are more clearly differentiated than on natural color photography.

This study indicates that the Wratten 15-G filter will provide the maximum amount of information, although the 25-A and 57, with proper film exposure, may be superior in delineating certain important plant species and shorelines. (Figure 1, A,B,C,D,).

1. Plant species identification and wildlife biology.

Because ground investigation of marshlands are at best difficult, and at times impossible, an accurate remote sensing tool would be an invaluable adjunct to data gathering in these areas. There are several reasons why the knowledge of plant species composition in marshes may be important. One of these is that marshes containing certain types of plants are extremely important in the maintenance of some wildlife populations. Wildlife biologist are interested in locating and maintaining these areas of high value to wildlife.

The several characteristics of marshlands which can be used to identify them as important to wildlife such as wildfowl, muskrats, turtles, etc. are easily identified with Ektachrome IR photography. Important plant species such as reed, cattail, three-square, yellow pond lily and wild rice, which are used as food and protection, may be readily

identified on the film. Additionally, the degree to which the marsh is dissected by streams and inlets is easily ascertained due to sharp contrast between water and vegetation (blue against red). Thus the marsh may be quickly evaluated for its capacity to be used as protection and food sources for many of our commercially important fish which rely on these areas in the early part of their life cycle. (Figure 2)

Marshlands also contribute organic nutrients to the estuarine water which are utilized by plankton, benthic organisms and others which are important food chain animals. The extent of drainage from marshes may be easily estimated using Ektachrome IR photography (Figure 2).

2. Submerged vegetation: Fritz(6) has suggested that Ektachrome IR photography would not be particularly useful in delineating submerged vegetation due to the high reflectance properties of water. In this study submerged vegetation did not image well on film when, exposure, optimum for land vegetation was used. However, some frames, which were inadvertently overexposed, showed submerged species considerably better. Since marsh vegetation does not image well on overexposed film it may be necessary to make separate flights, if information about both habitats is required. (Figure 3)
3. Seasonal changes in vegetation: It is well known that marshland vegetation undergoes considerable change during the growing season from May through September. The changes are manifested in a decline of early appearing species, with a succession of later developing plants. If remote sensing techniques are to be utilized in monitoring marshland dynamics it is important that imaging characteristics of these areas, at

various times during the growing season, be known.

Preliminary indications are that Ektachrome IR photography will be useful in determining changes in vigor and species composition in marshlands. Figure 4 shows photographs taken in June and September over the same area. Most obvious is the change in tone signature of reed during the growing season and also that certain parts of the population are more vigorous than others. (Spectral analysis of this species is in progress to determine effect of plant vigor on spectral reflectance.) Also evident is the apparent decline in vigor of cattail and yellow water-lily.

4. Water Quality: The use of Ektachrome IR photography for estimates of water salinity and delineating sources, types and distribution of water pollutants has been discussed by this author in a previous paper (1). Salinity may be estimated using marsh plants as indicators. The number of plant species growing in fresh water is much greater than is the situation in more saline areas. Thus the vegetational tonal patterns as imaged on the film will be less complex and varied with increasing salinity. Sources and distribution of heavily sedimented water and algal blooms also image very well on Ektachrome IR photography for delineation of these water characteristics.

Sediment pollution is serious in the Patuxent River and one result of this has been the formation of large mud flats on both sides of the river. These mud flats and the progressive filling of the river channel eventually becomes navigation hazards and must be dredged out. One of the flights in Mission

79 coincided with a low tide and the extent of mud flat development along the river was clearly delineated, using Ektachrome IR photography (Figure 5).

5. Spectral Reflectance of Marsh Plant Species:

Research has begun on the nature of spectral reflectance curves of major marsh plant communities. This information is essential in choosing film-filter combinations which will best delineate certain marsh species. It will also aid greatly in tonal interpretation of multispectral imagery which will be obtained over the test site in the near future.

Current data analysis of spectral reflectance are incomplete. However, Graph 1 is an example of the kind of information being obtained from marsh species. The curves shown were obtained from two plants, Peltandra virginica (Pickerel weed) and Spartina patens (Marsh salt-grass). Spectral reflectance in the visible region indicates that these two species would be hard to differentiate on natural color photography, but the reflectance curves in the near infrared show that there is a rather large difference between the two species indicating that Ektachrome IR photography best delineates areal coverage. This seems to be true for many of the other plant species indicating the reason false color photography has been very useful in marshland studies.

B. Thermal Imagery

Results of this study indicate that thermal infrared imagery is an extremely useful tool in estuarine water temperature studies and also in delineation of certain marsh plant species. The Reconofax-4 system, used in the study, although not as sensitive as other imagers, appears to give adequate results. It has the added feature of not being clas-

sified instrument, hence the imagery may be published.

There are difficulties in interpreting IR imagery not encountered in interpretation of data from a photographic system. Gain setting of the IR imager (whether manual or automatic) plays a large role in determining the amount of information one will obtain from a particular environmental feature. This is particularly true in hydrological studies when the imager may be scanning both land and water. If information is desired from the water surface and the imager is set for the land temperature regime a degradation of data will occur. An averaging of land and water signal by the sensor may reduce the imaging quality of both environmental features. Hence the most ideal system for hydrological studies would be an imager with manual gain setting, along with the capacity to quantitatively analyze the water and land surfaces.

Both day and night imagery were obtained during Mission 74 and this report illustrates the relative merits of each in estuarine research. Although the conclusion reached is that the daytime imagery is much more useful than the night imagery, the author recognizes that this may not always be the situation, particularly if the imager gain setting was improperly set during the night mission. However, in this case, the day imagery was superior in tonal variations, interpreted as differences in water temperature and marsh vegetation. The night imagery was superior in delineating possible ground water seepage into the estuary.

1. Plant species: It is apparent in Figures 6 and 7 that some marsh plant communities may be delineated using temperature sensing devices. The daytime (morning) imagery was most useful in this respect. Those species which grow in large stands such as reed and salt reed grass were most discernable on the day imagery. These are the tallest

growing marsh species, (to three meters) and imaged as darker (cooler) tones. Lower growing species such as three-square and spike rush (sedge meadow) imaged as lighter (warmer) tones.

Radiometric quantities of the above species measured by the PRT-5 do not directly apply to the daytime imagery since these data were taken in relation to the night imagery. However, temperature differences among the above species were recorded and it can be assumed that these would hold at least into the morning hours. Phragmites (Reed) was measured at 6.8°C, Spartina (Salt Reed-Grass) at 8.0°C and the sedge meadow at 9.6°C.

Reflected energy becomes a complicating factor in interpretation of grey tone variation in day imagery and more work needs to be done on the effect of this on tonal signatures of various plant species. On a larger scale the relative usefulness of day and night imagery in plant species distribution needs considerably more research before definitive conclusions can be reached.

2. Water temperature: The use of thermal IR imagery in water temperature studies is well documented. Usually the imagery is taken in late evening or pre-dawn and the technique is very useable in delineating isotherms in a body of water.

Reconofax 4 imagery obtained during mission 74 was useful in defining water temperature characteristics of the Patuxent estuary. Pre-dawn imagery was less useful than the daytime imagery as was the case for plant species distribution in the marshes. Figure 6 show daytime imagery covering an eight mile section of the estuary. Change in temperature from 15 to 21°C is shown as a sharp change in grey tone. Figure 8 contrasts night and day imagery showing the sharper deli-

neation of cooler water entering the estuary from a creek on day imagery.

3. Ground water: An important use of thermal IR imagery is the detection of sources of ground water inflow to bodies of water. Ground water represents a significant contribution of fresh water to some estuaries.

The U.S. Geological Survey, had concluded, through geological evidence, that a considerable amount of ground water probably entered the Patuxent River near Upper Marlboro, Md. Night imagery from mission 74 presented evidence of significant contribution of ground water to the estuary in the area predicted by the U.S.G.S. Figure 10 shows the very dark (cool) tones in the marshes of this area. This has been interpreted as cool ground water seepage into the estuary. Marshes below this area (Figure 9) do not show these extreme dark tones in the marshes. Water temperatures were measured at a later date with a PRT-5 Radiometer and significant changes in temperature were noted going up the small creeks in the marshes (up to 5°C).

Conclusions

This report presents results obtained from data provided by two overflights of NASA aircraft on Missions 74 and 79 in 1968. The following conclusions may be made at this stage of data evaluation:

1. Color infrared photography was superior to natural color in marshland plant-community delineation, particularly with increase in altitude. This was primarily due to the superior haze penetration of the infrared color film.

2. There is considerable tonal change in marsh vegetation during the growing season, reflecting a decline of some species and a succession of others.

3. Color infrared photography is superior to natural color in detecting sources and distribution of sediment in estuarine water. This is particularly true in highly turbid water.

4. Sunlint from water may be avoided without undue degradation of the tone quality of the marshland vegetation.

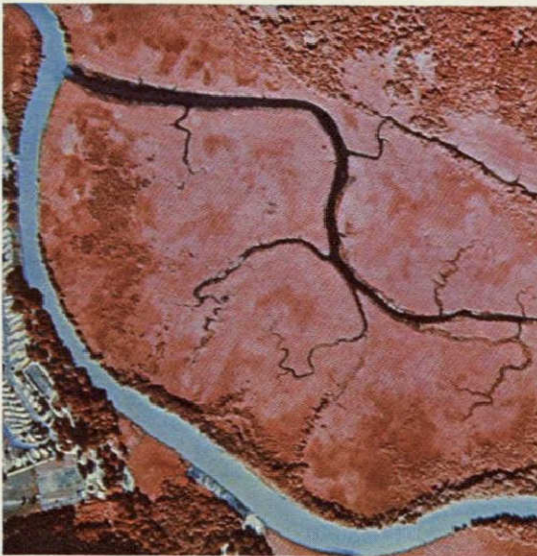
5. The Wratten 15-G filter provides the most information of any of the filters tested on color infrared film, while the 25-A and 57 filters are useful in delineating certain plant communities which are important in the maintenance of wildlife populations in marshes.

6. Infrared imagery of this area indicates that certain marsh species may be differentiated by temperature-sensing instruments. Sources of ground water and heated water from a power plant are also delineated.

Bibliography

1. Anderson, R.R. 1969. Remote Sensing of Marshlands and Estuaries using Color Infrared Photography. NASA, Earth Resources Aircraft Program Status Review, Vo. III.
2. Cochrane, G.R. False-Color Film Fails in Practice. Photogrammetric Engineering 34(ii):1142-1146.
3. Colwell, R.N. 1966. Thermal infrared imagery and its use in vegetation analysis by remote aerial reconnaissance. In: Selected Papers on Remote Sensing of Environment. American Society of Photogrammetry.
4. Concord, A., M. Kelly and A. Boersma. 1968. Aerial Photography for Shallow Water Studies on the West Edge of the Bahama Banks. Publication RE-42, Experimental Astronomy Laboratory, Mass. Inst. of Technology.
5. Draeger, W.C. 1968. Remote Sensing Applications in Forestry - The Interpretability of High Altitude Multispectral Imagery for the Evaluation of Wildlife Resources. Annual Progress Report, University of California.
6. Fritz, N.L. 1967. Optimum methods for using infrared sensitive film. Annual Meeting of American Society of Photogrammetry, March 10, 1967.
7. Jamison, D.W. 1967. Monitoring Water Quality with Aerial Photography. Regional Meeting, Pacific Northwest Pollution Control Association, Yakima, Washington.
8. Lukens, J.E. 1967. Monitoring Water Quality with Aerial Photography for Aquatic Vegetation Surveys. HRB-Singer, State College, Penn.
9. _____ 1968. Remote Sensing of Thermal Pollution. HRB-Singer State College, Penn.
10. Neumaier, G. and F. Silvestro. 1969. Measurement of Pollution Using Multiband and Color Photography. Proceeding, "New Horizons in Color Aerial Photography". A.S.P. and S.P.S.E. Joint Seminar, New York. p. 47-58.
11. Olson, C.E. and J.M. Ward 1968. Remote Sensing of Changes in Morphology and Physiology of Trees Under Stress. University of Michigan. Annual Progress Report.
12. Paulson, R. 1968. Preliminary Remote Sensing of the Delaware Estuary. NASA Technical Letter - 128.

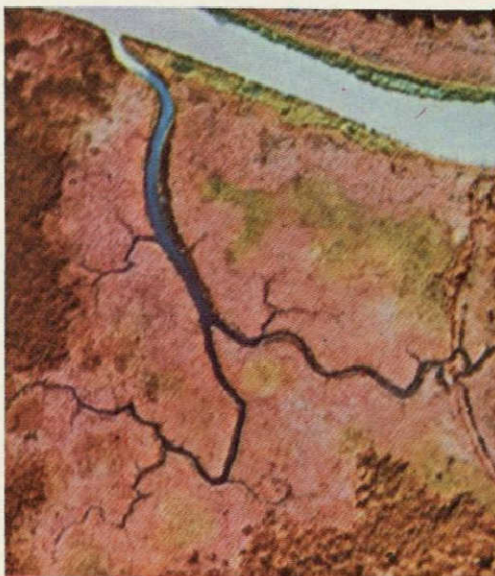
13. Pestrong, R. 1969. Multiband Photos for a Tidal Marsh. Photogrammetric Engineering. 35(5):453-472.
14. Rees, C.B. 1940. A preliminary study of the ecology of a mud-flat. J. Mar. Biol. Ass. 24:185-199.
15. Scherz, J.P. 1969. Photographic Characteristics of Water Pollution. Photogrammetric Engineering 35(1):38-44.
16. Sculthorpe, C.D. 1967. The Biology of Aquatic Vascular Plants. St. Martins Press. 610p.
17. Strandberg, C.H. 1964. An Aerial Water Quality Reconnaissance System. Photogrammetric Engineering 30(1):46-54.
18. Von Lopik, J.R., A.E. Pressman and R.L. Lundlum. 1968. Mapping Pollution with Infrared. Photogrammetric Engineering 34(6): 561-564.



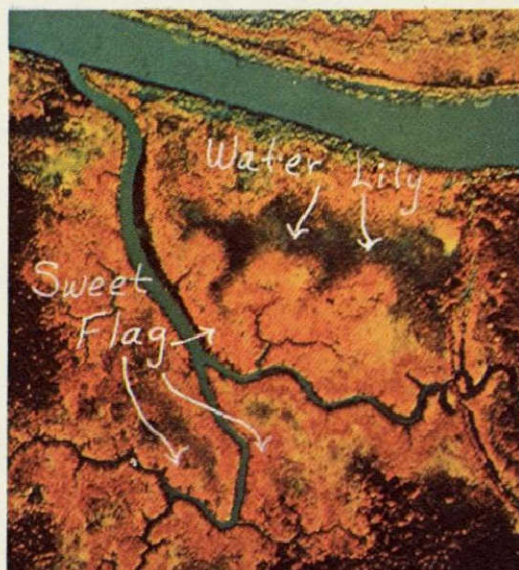
a. Wratten 15-G filter.



b. Wratten 57 filter.

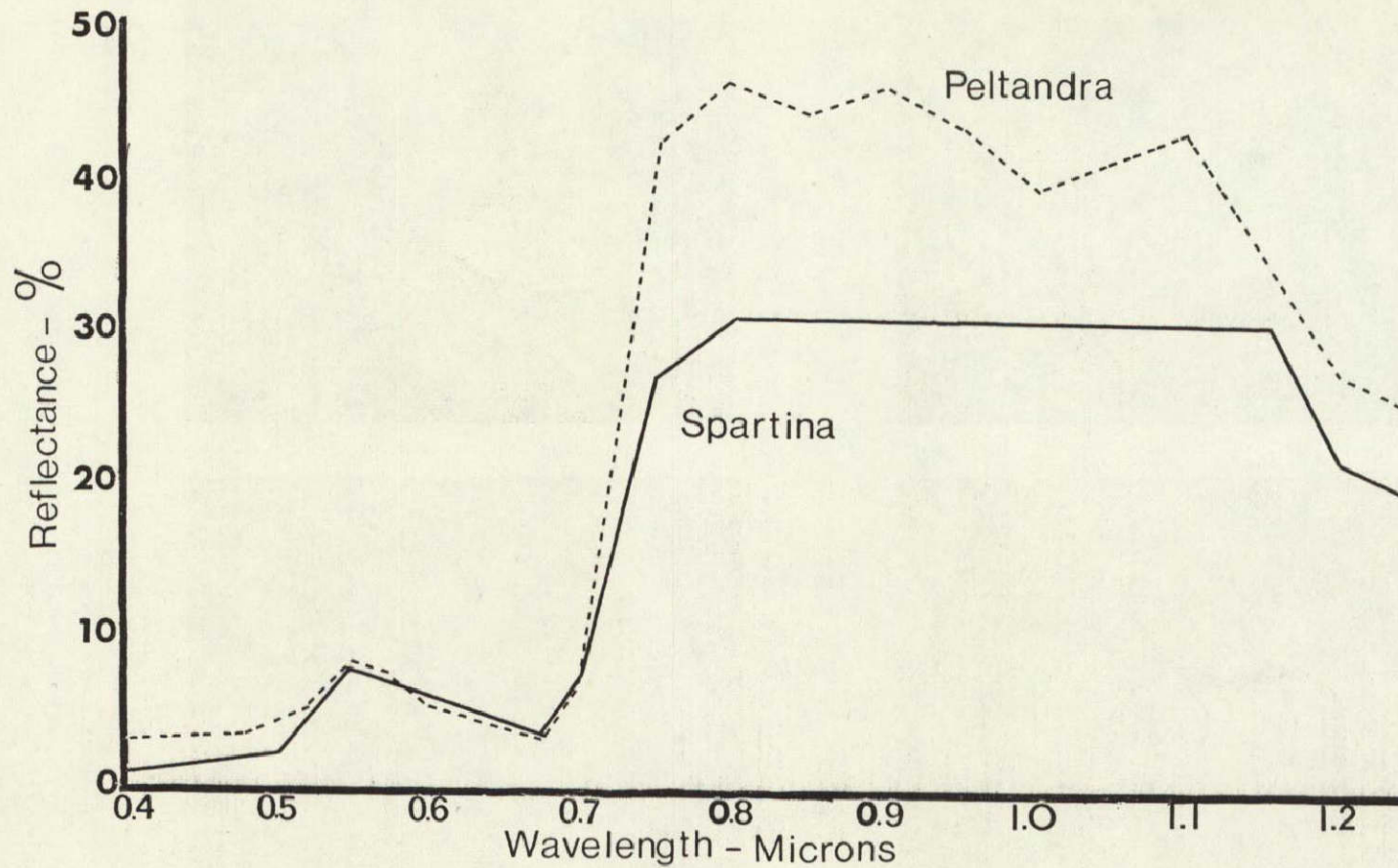


c. Wratten 15-G filter.



d. Wratten 25-A filter.

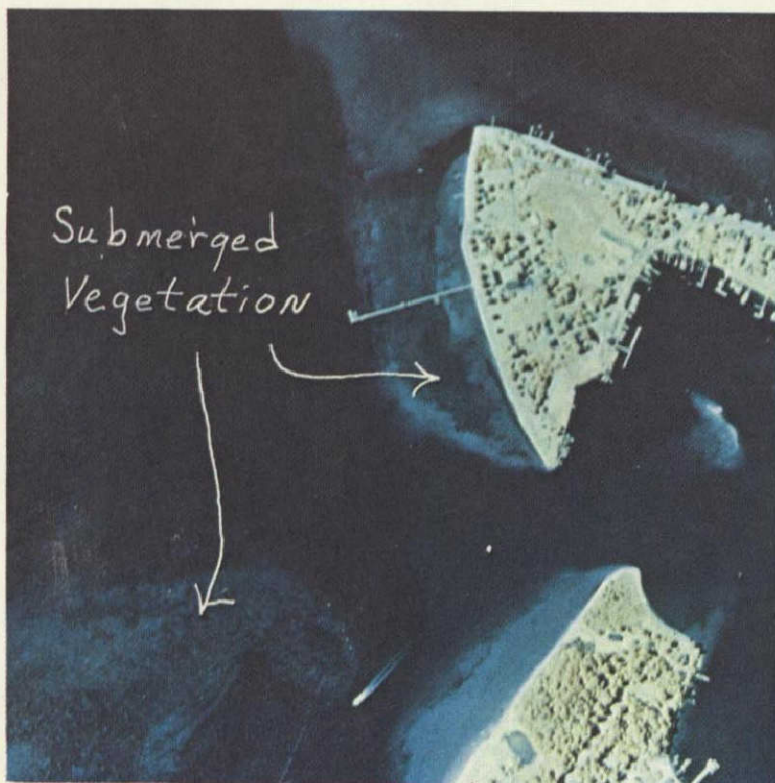
Figure 40-1.- (a),(b),(c),(d), shows imaging characteristics of marsh species with color IR film and selected filters. Note the imaging of only highly reflective species in (c) and the shift of color to orange and yellow in (d) with sharper tonal contrasts between species. (Scale: 1:6000. (a) and (c) Wratten 15-G filter; (b), Wratten 57 and (c) Wratten 25-A filter.)



Graph 40-1.- Spectral reflectance curves of two marsh plant species, *Peltandra* (Picheral Weed) and *Spartina* (Salt Reed-Grass). Note good separation of curve in region where color IR film is sensitive. (0.7 to 0.9 microns.)



Figure 40-2.- Shows ability of color IR film to delineate plant species important in wildlife ecology. (Scale: 1:12000. Wratten 15-G filter.)

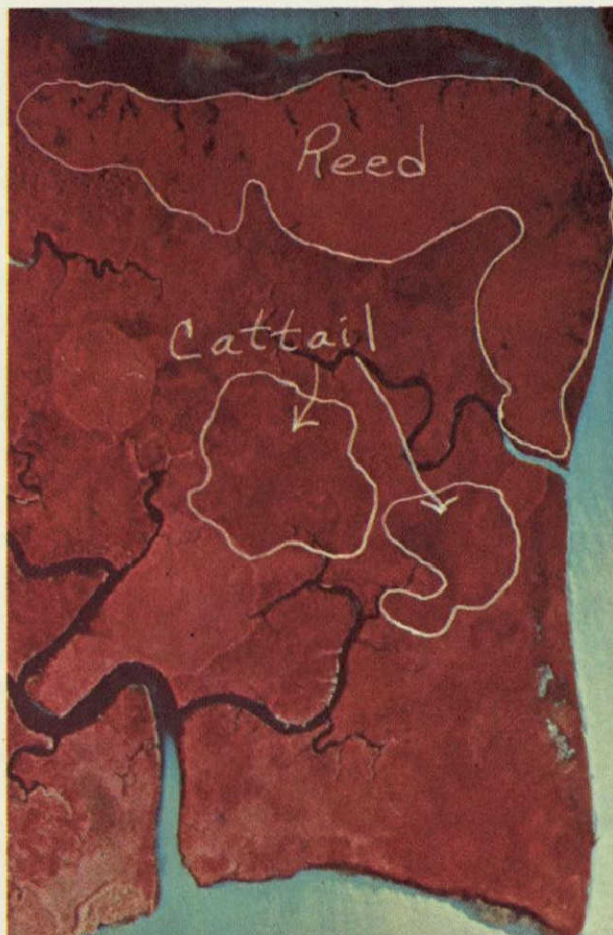


a.

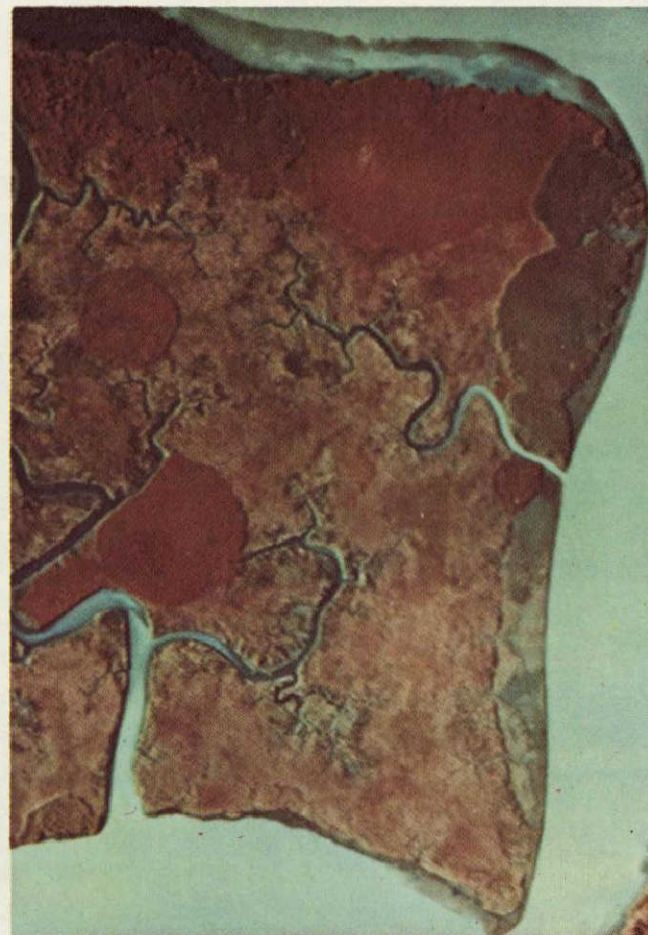


b.

Figure 40-3.- (a), (b), shows enhancement of image quality of submerged vegetation with over-exposure of color IR film. (a) overexposed, (b) normal exposure. (Scale: 1:12000.)

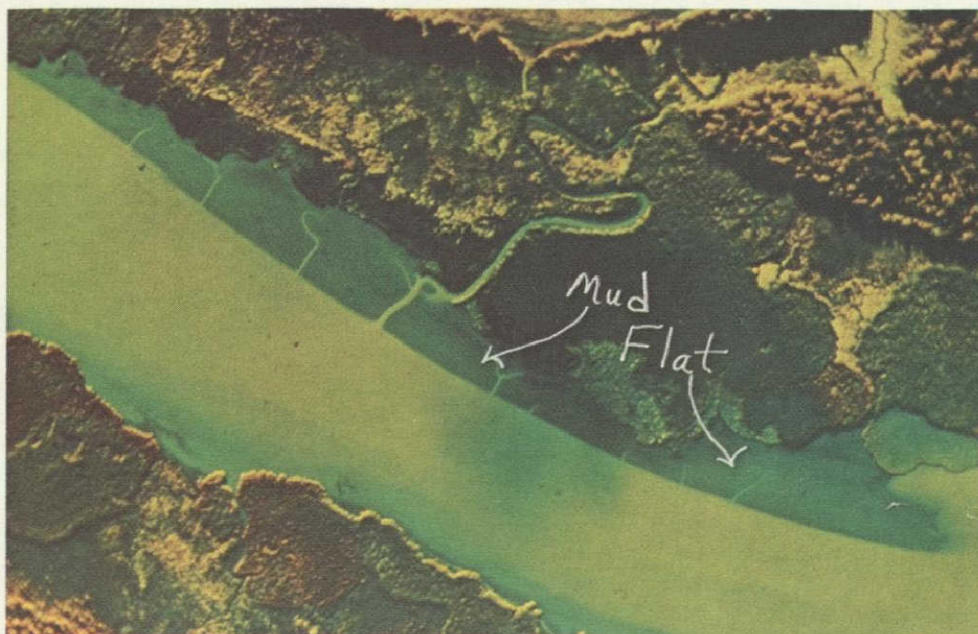


a.



b.

Figure 40-4.- Shows seasonal change in image characteristics of marsh vegetation using color IR film. Note apparent difference in vigor of reed, cattail and waterlily. ((a), spring; (b), fall. Scale: 1:12000.)



a.



b.

Figure 40-5.- (a),(b), distribution of mud flats along the estuary and light tonal quality of heavily sedimented water. Compare with Figure 29-3 showing darker water tones when little sediment is present. ((a),(b),Wratten 25, (a), and (b), Wratten 15-G filters. Scale: 1:12000.)



Figure 40-6.- Day thermal image showing water temperature variation and tonal characteristic of Phragmites (Reed).

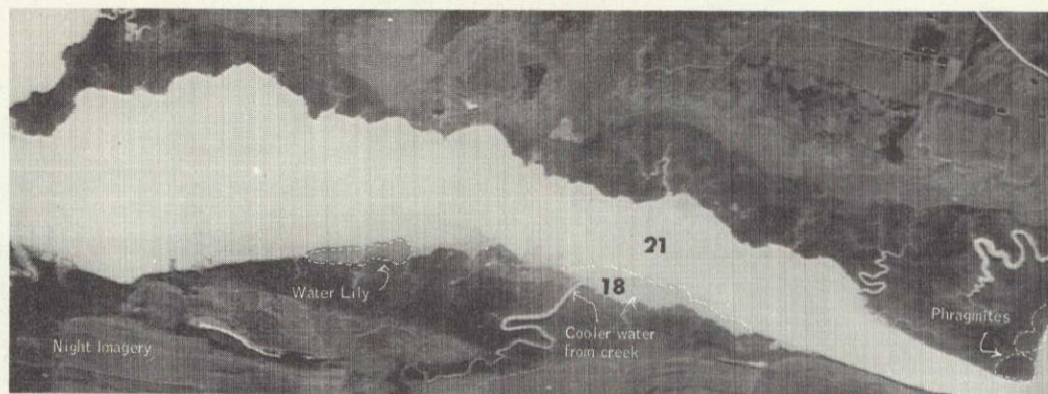
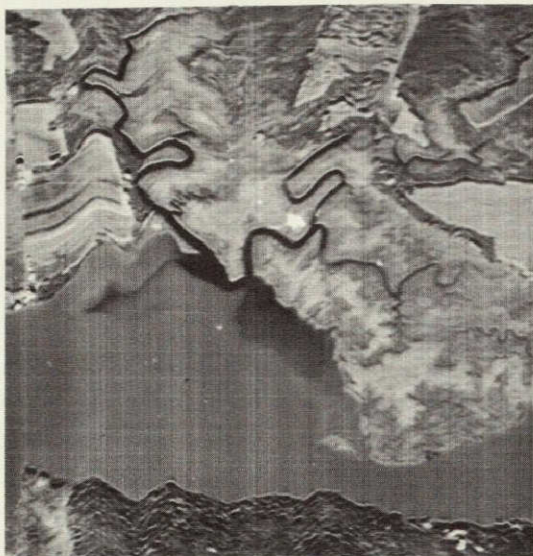


Figure 40-7.- Day and night time imagery compared. Shows tonal quality of water and vegetation, indicating day imagery is superior to night imagery.



a.

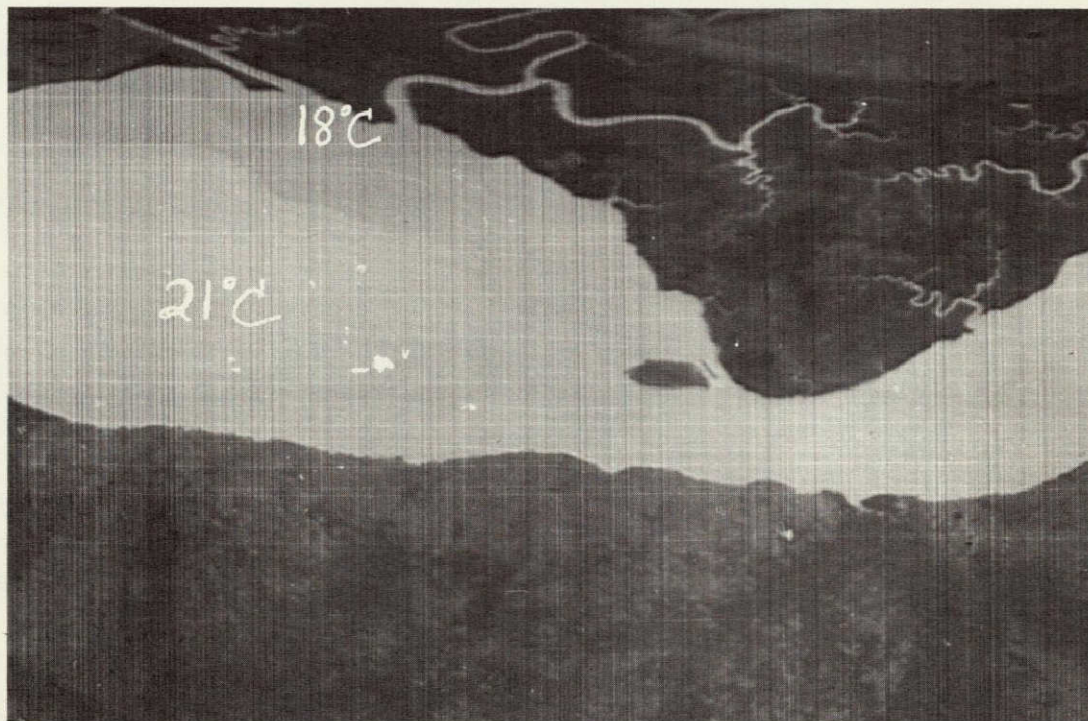


Figure 40-8.- Compares tonal variation of cool water entering the estuary from a creek. Note better delineation of cool water on day imagery. ((a), day: (b), night.)

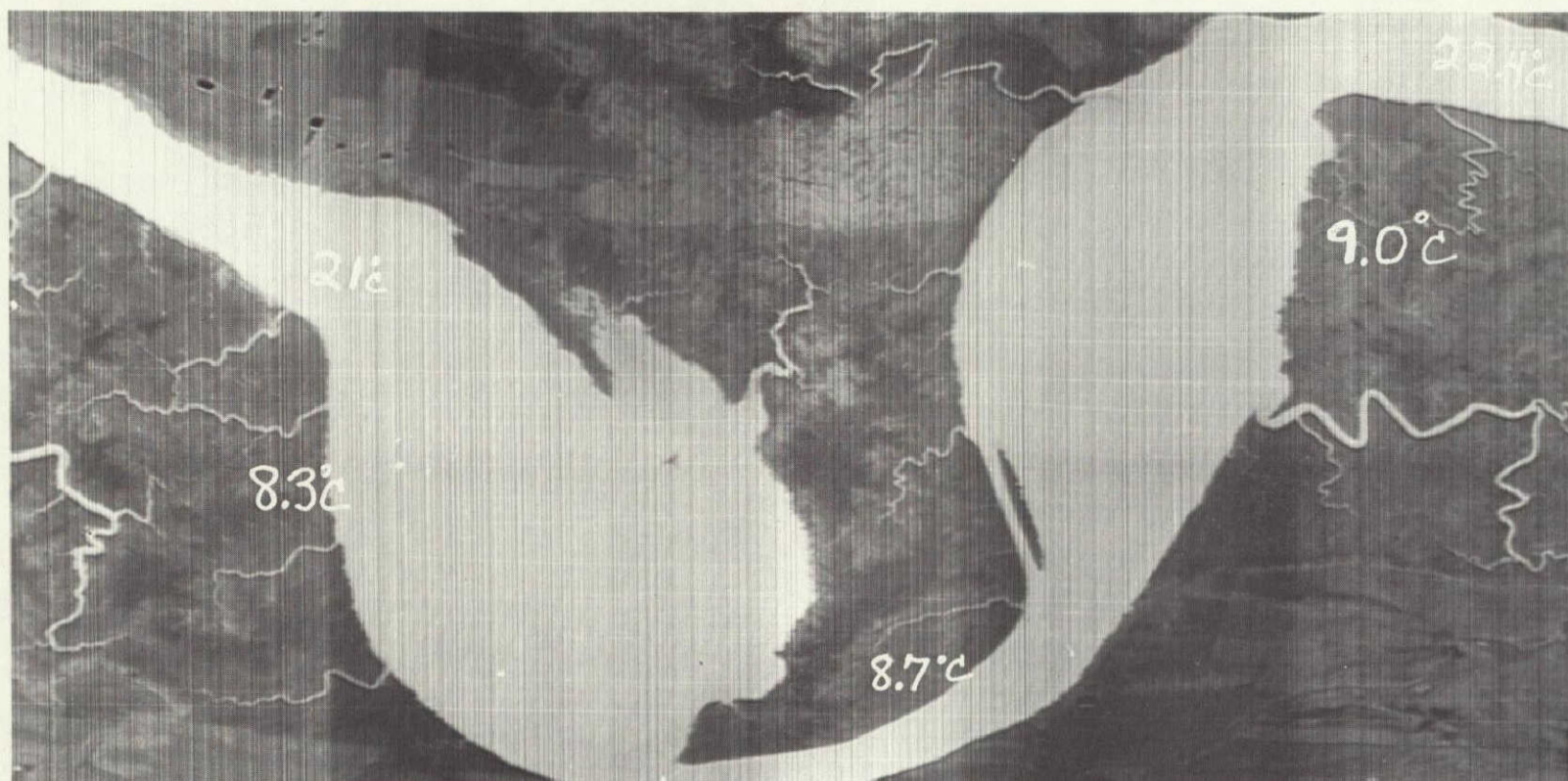


Figure 40-9.- Shows tonal variation and temperatures of marsh below area where ground water seepage occurs. (Compare with Figure 29-10.)



Figure 40-10.- Shows tonal variation and temperatures of marsh in area of ground water seepage. (Compare with Figure 40-9.)

SECTION 41 • • •

A THERMAL SURVEY OF THE CONNECTICUT RIVER ESTUARY

F. H. Ruggles, Jr.

N71 11158

INTRODUCTION

In October 1965, the U.S. Geological Survey undertook to compute tidal discharge and volume interchange in the Connecticut River estuary. Studies necessary to accomplish this were completed in 1966, and the techniques are now operational. Results of these studies were reported at the annual meeting of the American Geophysical Union in April 1969 by Lai.

At about the same time that the U.S. Geological Survey was able to compute tidal flow, the Yankee Atomic Power Plant at Haddam Neck was nearing completion. Controversy centered around the power plant, especially the effects its effluents would have on the Connecticut River estuary (see figure 1).

Because of this controversy, it became necessary to conduct studies to determine the effect of heated effluents on the marine life of the estuary. The U.S. Geological Survey was invited to observe and comment on the proposed studies to be conducted by the Travelers Research Corp. for the Connecticut Yankee Atomic Corp. Because the Yankee Atomic people agreed to make all their data available to interested parties, the Atomic Energy Commission and the National Aeronautic and Space Administration working in cooperation with the U.S. Geological Survey approved a coordinated thermal study wherein a free exchange of data would be effected.

In April 1968, it was agreed that the Travelers Research Corp. would conduct a thermal survey of the Connecticut River estuary in the vicinity of the Yankee Atomic Power Plant, utilizing submersible thermometers. At the same time the U.S. Geological Survey would conduct an aerial survey of the estuary utilizing the techniques of infrared imagery, and also furnish the necessary tidal discharge data.

This preliminary report was prepared under the direction of John Horton, District Chief, U.S. Geological Survey, Hartford, Connecticut. Daniel Hedden, Director, Environmental Science, NE Utilities Corp. provided the impetus and coordination necessary to make this study possible and without whose encouragement and advice this study would not have been possible. George Collins of Travelers Research Corp. directed the thermal survey of the river using submersible thermometers.

THE FIELD STUDY

Because of the complexity of the study, planning needed to be flexible enough to adapt to unforeseen occurrences, yet be rigid enough to insure a coordinated plan. To insure a maximum result, certain conditions of river flow and power plant operation were necessary. The following standards were adopted as the guidelines to be followed in selecting the day for the study:

- a. Minimum fresh-water inflow
- b. High river temperature
- c. A steady power plant operation for seven (7) days prior to the study
- d. Relatively clear weather with a minimum of low cloud cover.

The date selected was August 26, 1968. This day met all the conditions, except for power plant operation which became erratic. A secondary date was selected, and the test conducted on September 9, 1969. All conditions were met on this day except for a dense morning fog.

The Connecticut Yankee Atomic Power Company Plant at Haddam Neck, Connecticut was operating at a power level of 490 MW throughout the observation period on September 9, 1968. Weather during the period started with a dense fog in the early morning which burned off to a low stratus overcast by 0830 EST.

Air temperature ranged from 58.5°F to 72.0°F. Hourly dry bulb and wet bulb readings are shown on table 1.

Wind velocity, as measured at the power plant, varied from northeast at 3.5 mph to southeast at 3 mph. Hourly averages are also shown on table 1.

During the study period the lowest river stage at Haddam Marina occurred between 0730 and 0745 AM EST, and the highest river stage occurred between 1335 and 1400 EST. Maximum upstream flow occurred at 1130 and the maximum downstream flow was at 1700. The stage and flow data are shown on table 1 and figure 2.

The river temperature data were secured utilizing four 14 ft outboard-powered boats, three of which were responsible for patrolling an assigned reach of the river while the fourth boat was a "rover" charged with following the warm water plume and delineating its surface position. Temperature observations were scheduled over a two-hour period centered on the predicted time of low, incoming, high, and outgoing tides. Sampling simultaneously in each sector provided an essentially synoptic picture of a four mile reach. Observations were made by three boats along fixed traverses indicated

by previously placed buoys and show markers. Temperature measurements were made at the surface, 1 ft, 3 ft, 6 ft depths and then every 3 ft to and including the bottom. The thermocline, if present, was defined.

Each boat was equipped with a 2-way radio, a thermister and bridge with 50 ft lead, range finder, and a plough anchor for maintaining position. The shore command post was established at the Haddam Marina, where stage data was read and where discharge was calculated.

Infrared imagery data was secured by the H. R. B. Singer Co. under contract with the U.S. Geological Survey. The objective of which was to determine the capability of an infrared-thermal mapping system to delineate the extent of thermal patterns. In compliance with the objective, the contractor provided the necessary engineering and flight data collection services to gather the following data for the Connecticut River estuary.

- a. Preliminary imagery data on Sunday, September 8, 1968
- b. Predawn imagery data Sept. 9, 1968
- c. Mid-day imagery data Sept. 9, 1968
- d. Night-time imagery data Sept. 9, 1968
- e. The output of a radiometer recorded on an analog strip chart, correlated and annotated every 1/4 mile as to position with the imagery.

Accomplishment of this entire activity was a result of the cooperative attitude of each of the involved parties and the professional manner with which each group of men conducted their specific task.

INFRARED IMAGERY

The H. R. B. Singer Corp. was selected on the basis of a proposal to perform the specified field studies. The field data team consisted of an engineer and technician to operate and maintain the infrared-thermal mapping system, radiometer, and process the imagery; an environmental scientist to plan flights and analyze results; and the aircraft crew to manage flight operations. Flight operations were conducted from a twin Beechcraft G-185 aircraft.

The Infrared Mapping system met the technical requirements using an 8-14 micron GE: Hg detector. In addition, this equipment has been declassified by the Department of Defense and the resultant imagery is now unclassified. In addition to the mapping system, an infrared radiometer was boresighted to the centerline of the infrared scanner and was operated simultaneously in the 8-14 micron region.

The output of the radiometer was recorded on an analog strip chart and was correlated and annotated about every 1/4 mile as to position with the imagery. Daytime flights utilized a 8 uLP filter.

Flights were planned to be done at an altitude of 2,000 feet above the terrain, which would allow imaging the river from bank to bank within the central 80° of the line scan imagery. However, because of cloud cover, flight altitude was at 1,000 feet on September 9, 1968. The preliminary flight on September 8, 1968 was at the prescribed 2,000 feet.

The final flights and imagery secured were as follows:

Run No.	Date	Time	Quality
Test	Sept. 8, 1968	1430 to 1625	Excellent
1	Sept. 9, 1968	0424 to 0545	Poor
2		1320 to 1456	Excellent
3		1949 to 2118	Excellent

Analyzing the infrared data indicated a number of different patterns, each the result of a different impetus. Figure 3 is a composite showing the heated plume issuing from the atomic power plant for run numbers 2 and 3. The plume for run number 2 was secured during a period of upstream flow and downstream flow for run No. 3. The heated effluent seems to spread out but does not completely fill the cross-section of the estuary on an upstream flow, but fully occupies the estuary on a downstream flow. These data indicate that the heat plume is readily dispersed, especially on downstream flow.

Figure 4 is data recorded at the mouth of the estuary, and reveals many density differences as the river water flows into Long Island Sound. Figure 5 is data recorded at Hartford and records heat plumes from a fossil fuel plant, and river effluent from the Park River. Both of these warm water inflows are representative of local inflow conditions found elsewhere in the estuary.

In the center of the imagery is a dashed line. This line is a record of the time and location sequence of the temperature data as recorded using the radiometer. Clips of these recorded data are shown on figure 6. The response to temperature change is very rapid and illustrate changes recorded in the estuary from place to place.

Quantitative analysis of the imagery data is now in progress and will be presented together with the complete ground truth data in a later report.

CONCLUSIONS

It is possible to detect temperature differences at the surface of an estuary utilizing thermal mapping systems. The mapping system used in this study was supplied by the H. R. B. Singer Corporation. Further, the use of a thermal mapping system enables the user to delineate the extent of surface heat plumes in an estuary.

Quantitative analyses of the thermal loading of the estuary is in progress and will be reported in a final report.

REFERENCES

- Lai, Chintu, Ruggles, F. H., Weiss, L. A. (in preparation),
Flow Evaluation in Tidal Reaches of the Connecticut River by
Mathematical Model: Am. Geo. Union Trans.

Table 1.--Environmental data for Connecticut
River Estuary, September 9, 1969

Time (EST)	Air Temp.		River Temp. at CANEL dock (°F)	Wind (mph)	Haddam Marina Flow (cfs)
	Dry Bulb (°F)	Wet Bulb (°F)			
0700	58.5	58.5	75.5	SE 3.0	+19,790
0715	-	-	-	-	+10,480
0730	-	-	-	-	+14,180
0745	-	-	-	-	+14,660
0800	59.0	58.0	77.5	E 2.0	+13,810
0815	-	-	-	-	+12,450
0830	-	-	-	-	+9,524
0845	-	-	-	-	+4,082
0900	59.0	56.5	77.0	NE 3.5	-2,556
0915	-	-	-	-	-10,250
0930	-	-	-	-	-15,210
0945	-	-	-	-	-17,200
1000	58.5	56.5	77.5	SE 2.0	-18,970
1015	-	-	-	-	-19,790
1030	-	-	-	-	-21,040
1045	-	-	-	-	-22,590
1100	64.5	60.5	75.5	N 2.0	-23,700
1115	-	-	-	-	-23,610
1130	-	-	-	-	-24,530
1145	-	-	-	-	-24,442
1200	66.0	60.0	77.0	SE 2.0	-25,110
1215	-	-	-	-	-22,970
1230	-	-	-	-	-23,150
1245	-	-	-	-	-23,130
1300	69.0	63.5	75.3	SE 1.5	-21,290
1315	-	-	-	-	-20,620
1330	-	-	-	-	-18,640
1345	-	-	-	-	-16,500
1400	72.0	65.0	76.1	SE 2.5	-14,760
1415	-	-	-	-	-10,490
1430	-	-	-	-	-6,129
1445	-	-	-	-	-425
1500	69.8	64.5	75.6	SE 2.5	+6,929
1515	-	-	-	-	+13,820
1530	-	-	-	-	+17,270
1545	-	-	-	-	+19,160
1600	69.0	64.0	77.9	SE 3.0	+20,510
1615	-	-	-	-	+21,500
1630	-	-	-	-	+23,170
1645	-	-	-	-	+24,210
1700	69.0	64.5	75.3	SE 2.5	+25,790
1715	-	-	-	-	+24,410
1730	-	-	-	-	+24,650
1745	-	-	-	-	+23,550

- Upstream flow

+ Downstream flow

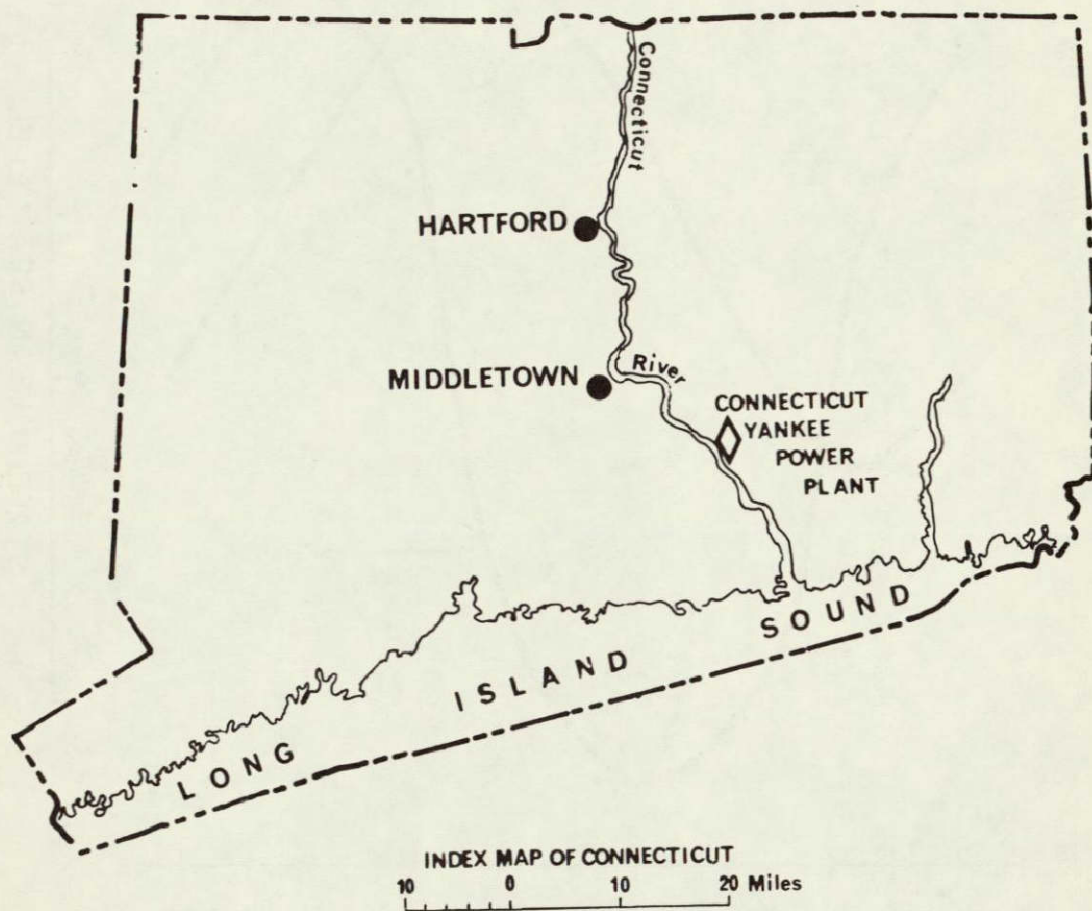


Figure 1.- Location map of the Connecticut River estuary.

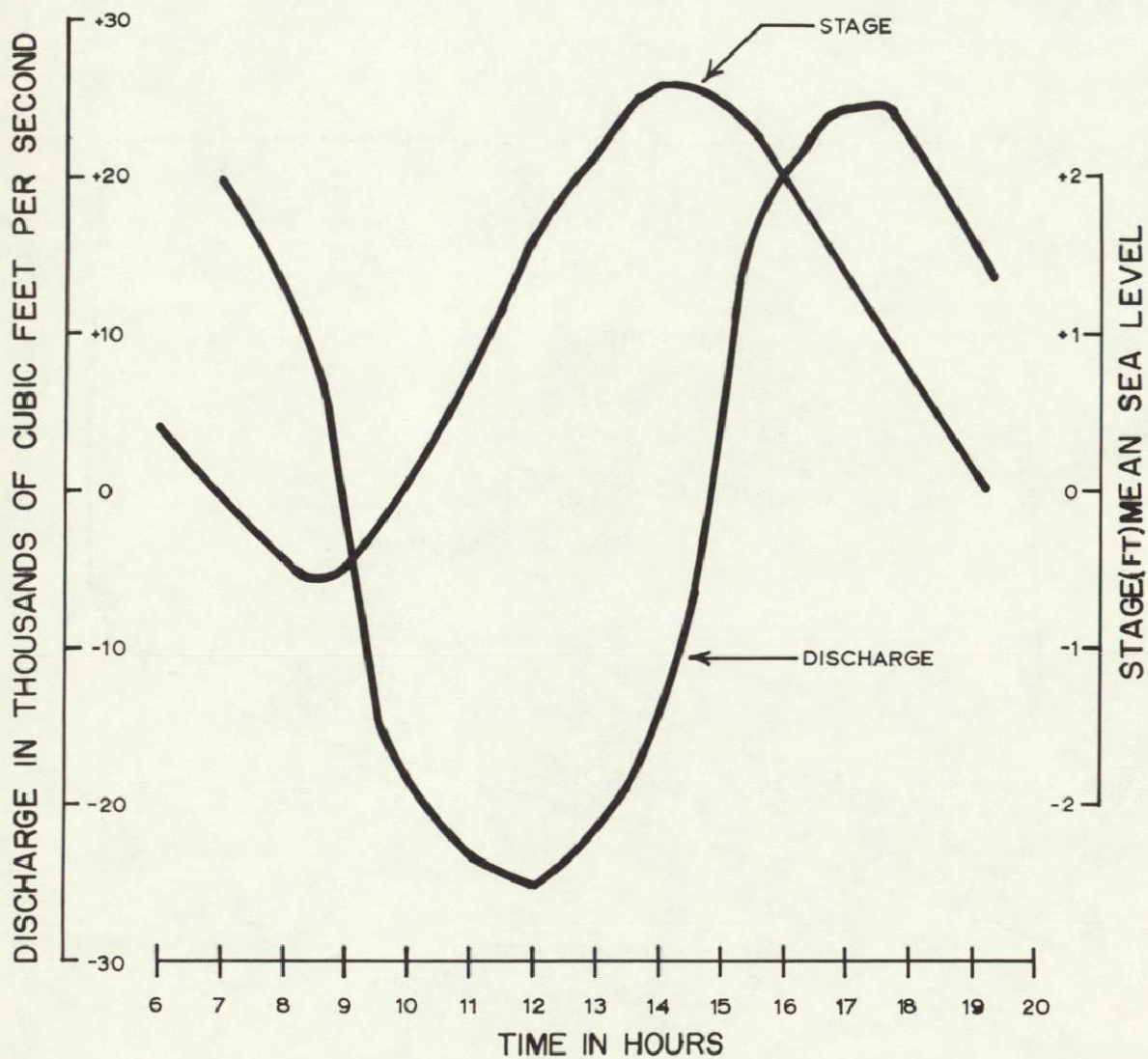


Figure 2.- Discharge and stage of the Connecticut River estuary at Haddam Neck, Connecticut on September 9, 1968.

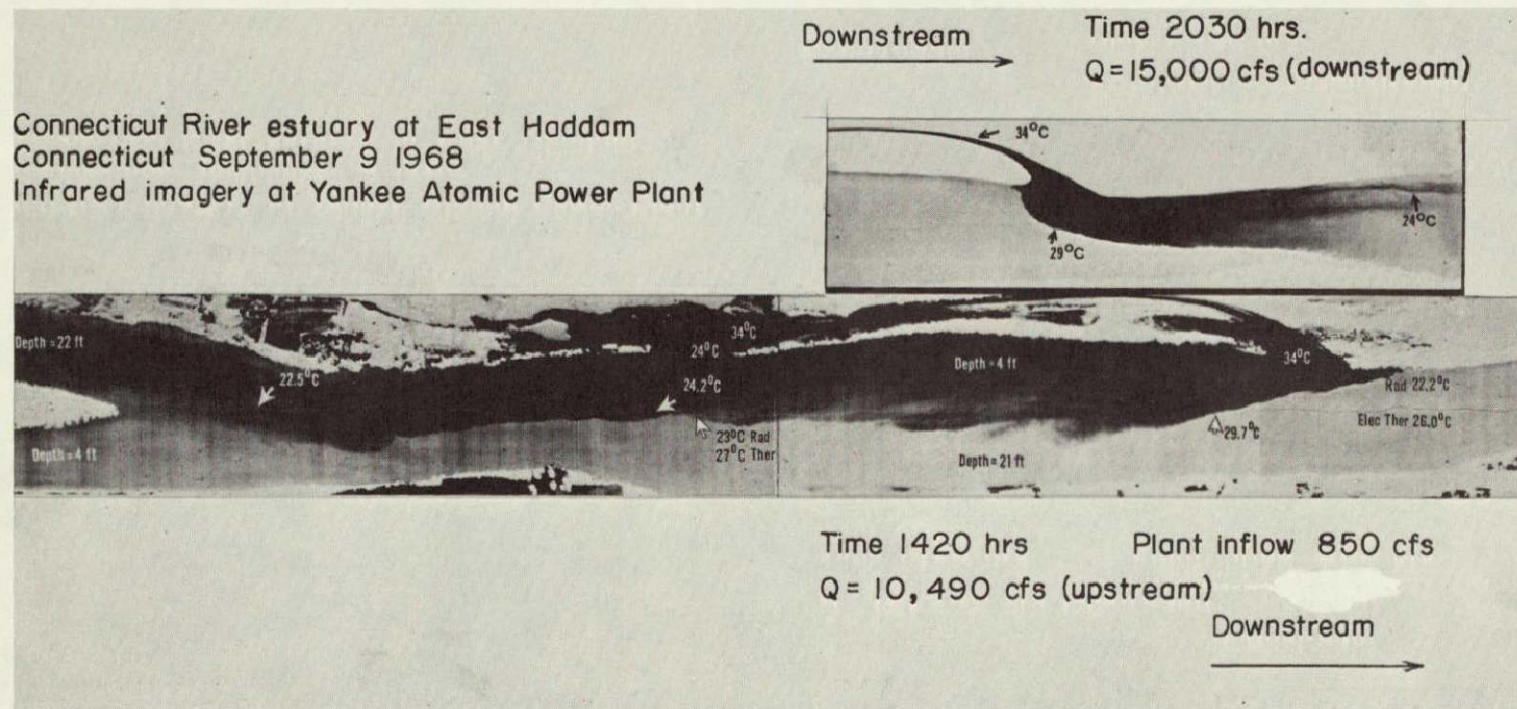
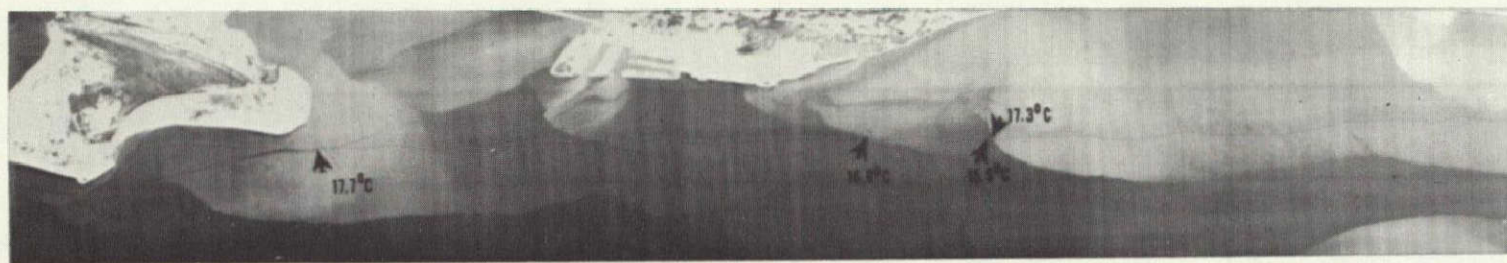


Figure 3.- Infrared imagery data for periods of upstream and downstream flow at the Connecticut Yankee Atomic plant, September 9, 1968.



Connecticut River estuary at Saybrook Point Connecticut September 9 1968 at 1408 E.S.T
Dark area is mostly in deep water (10-15 feet) Lighter areas are in shallow water (1-6 feet)
Dredged channel (15 feet) is delineated by narrow dark area at right of the picture.

Figure 4.- Infrared imagery data near the mouth of the Connecticut River estuary on
September 9, 1968.

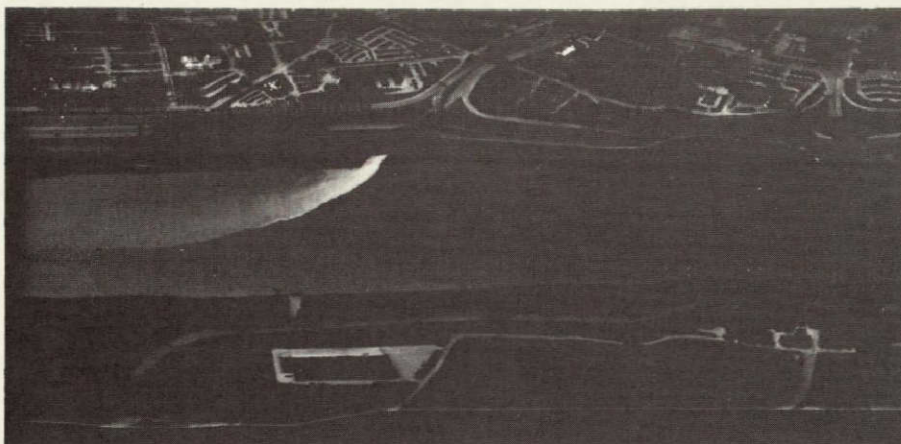


Figure 5.- Infrared imagery data for the Connecticut River estuary at Hartford Connecticut on September 9, 1968.



Figure 6.- Recorded radiometer data for the Connecticut River estuary September 9, 1968.

N71-11159

SECTION 42
APPLICATIONS OF MULTISPECTRAL DATA COLLECTION AND
PROCESSING TECHNIQUES APPLIED TO HYDROBIOLOGICAL
INVESTIGATIONS IN EVERGLADES NATIONAL PARK, FLORIDA

Aaron L. Higer
U.S. Geological Survey
Miami, Florida 33130

Norma S. Thomas
Fred J. Thomson
University of Michigan
Ann Arbor, Michigan 48107

Milton C. Kolipinski
U.S. Geological Survey
Miami, Florida 33130

BIOGRAPHICAL SKETCHES

Aaron L. Higer received his B.S. in Industrial Engineering from the University of Miami in 1959. Currently a hydrologist with the U. S. Geological Survey he conducts remote sensing and hydrobiological research in south Florida and has authored pertinent papers in his field. He is an adjunct professor of the Science Center at the University of Miami.

Norma S. Thomson received an A.B. degree in Education from the University of Michigan in 1958, and is currently working on a M.S. degree in Resources Planning and Conservation at The University of Michigan. Since 1965 she has been conducting research in the analysis of multispectral imagery and electronically processed multispectral data at The University of Michigan's Infrared and Optics Laboratory. She has published several articles and technical reports dealing with the application of multispectral remote sensing techniques to natural resource investigations. She is a member of the American Institute of Biological Sciences and the Ecological Society of America.

Fred J. Thomson received a B.S. degree in 1961 and a M.S. degree in 1963 in Electrical Engineering from The University of Michigan. Since 1961 he has been employed at the Infrared and Optics Laboratory of The University of Michigan's Institute of Science and Technology. He has been working for the last five years in the fields of multispectral data collection and processing for earth resource investigations and has published several articles on these subjects.

Milton C. Kolipinski is an aquatic biologist with the U.S. Geological Survey and his major interests lie in the ecology of the Everglades and in the application of remote sensing techniques to the solution of

ecological problems. He received a M.A. degree in Microbiology at the University of Buffalo in 1959 and a Ph.D. in Marine Science from the Rosensteil School of Marine and Atmospheric Sciences, University of Miami in 1964.

ABSTRACT

The Water Resources Division of the U.S. Geological Survey, in cooperation with NASA, as part of the EROS program is testing the applicability of remote-sensing techniques to the mapping and evaluation of water resources in the Everglades of Florida.

Mapping of hydrobiological features with multiband scanner imagery was tried for the first time in September of 1967 in the Everglades National Park on a strip of land eight miles long and 2,000 feet wide. This was done by electrically processing selected combinations of video signals in the narrow spectral bands between 0.4 and 1.0um (micrometers) to obtain recognition maps for tree islands, emergent aquatic grassland, and various surface-water depths.

The computer recognition maps of individual hydrobiological features were printed in different colors and superposed to provide a color composite map of the area. Periodic data collection and processing in this form would yield quantitative data concerning the direction and extent of plant successional changes in the park. This in turn would provide more accurate information for water management practices in the park.

This technique has potential for use in the hydrobiological evaluation of marsh, swamps and other shallow-water areas.

INTRODUCTION

Research objectives

For the first time, the advanced techniques of remote sensing and data processing (using a multispectral scanning system) have been applied to mapping aquatic vegetation and determining areal extent and general ranges of depth of water for a natural area. Similar techniques have been applied to the mapping of crop species by groups supported by the U.S. Department of Agriculture, and have resulted in successful identification of many of the common food plants in the midwest (ref. 1, 2).

The broad objective of the cooperative research effort between the U.S. Geological Survey's Miami office and the Willow Run Laboratories of the Institute of Science and Technology, University of Michigan has been to determine the capability of multispectral data collection and processing systems to provide means for classifying and mapping landscape site units in the Everglades National Park in south Florida. The purpose of the

research reported herein was to determine the feasibility of classifying and mapping plant, substratum, and water as indicators of surface-water supply conditions. Rapid techniques to inventory water supply are needed in the Everglades National Park for two major reasons: (1) to better assess the effects of seasonal and annual fluctuations in surface water levels on the stability of the ecosystem; and (2) to predict the consequences of water management practices on the biological populations within the park. The success of this study indicates that the multispectral scanning techniques employed in the Everglades have transfer value to other hydrological situations.

The Everglades situation

The Everglades National Park in southern Florida (fig. 1) encompasses a relatively flat fresh water marsh with tree islands that often shelter alligator holes. The alligator holes, important to the ecological balance of the glades, are ponds excavated and inhabited by alligators. As water levels decline in the dry season, the alligator holes serve as a vital, last-ditch water refuge for the fish and other animals in the adjacent open glades. Toward the coast the fresh-water marshes merge into brackish-water marshes. These marshes, in turn, merge into dense mangrove forests along the shoreline.

For centuries, alternate dry and wet seasons have created and maintained the ecological balance in the Everglades. However, water developments north of the park since the turn of the century have altered the natural surface flow of water. Water still enters the park, but part of the water that formerly flowed naturally southward is now impounded in large diked areas and directed by canals to the southeast Florida coast to sustain the aquifer system, and to inland agricultural areas.

The Geological Survey, in the cooperation with the National Park Service, has been investigating the water supply in and adjacent to the park since 1959. In 1964 the program was expanded to include ecological studies, in order to obtain additional facts on water needs of the plant and animal life. Knowledge of water needs is essential to the management and preservation of the park in perpetuity as a biological sanctuary. One objective of this program is to determine what changes in vegetation may occur or have occurred within the Shark River Slough (fig. 1), a shallow, slowly flowing river whose average width is 6 miles. The area of this slough within the park is about 125,000 acres. Selected parts of the slough have been studied in terms of the major vegetation types present, the general patterns of their distribution, and the broad characteristics of the habitats occupied by the vegetation types. The major plant communities which have been identified (fig. 2) are: (1) tree island communities, i.e., heads and hummocks; (2) sawgrass communities; and (3) wet prairie communities. Each community (characterized by a particular species composition) occurs in a habitat relatively uniform in substratum composition, elevation above mean sea level, period of inundation, and fire history.

Previously, conventional photographic interpretation techniques have been used to delineate the boundaries of the three major plant communities, using panchromatic, color, color infrared, and multispectral photographs (fig. 3). In September, 1967, in cooperation with the National Aeronautics and Space Administration, data were collected with The University of Michigan's multispectral scanner along the Shark River Valley Loop Road, a well-defined area of the Shark River Slough (fig. 1). Descriptions of the collection and processing of these data, a discussion of the results, and recommendations for future investigations follow.

MULTISPECTRAL DATA COLLECTION AND PROCESSING

Every object on the ground reflects solar radiation and emits long wavelength infrared radiation in a particular pattern called a spectral signature. The spectral signature may be used to identify a particular object. In the visible region of the spectrum, the spectral signature may be thought of as the color of the object. To identify objects or collections of small objects too small to be resolved by the scanner, data about the spectral signatures of these objects are collected. The data are then processed to determine when a particular spectral signature, representing an object of interest, is present.

Spectral signature data are collected with the multispectral scanning system. The scanning system samples the spectral signatures of objects being spatially scanned, converts the samples into electrical signals, and records the signals on magnetic tape. The spectral sampling is accomplished through the use of various optical filters or by a combination of a spectrometer and a fiberoptic bundle, and must be fine enough to preserve the distinctions between spectral signatures of different objects. After the radiation has been sampled by the filters or spectrometer, it is converted to electrical signals by detectors. The detector signals are amplified and recorded on magnetic tape for ease of storage and for compatibility with data processing devices described below.

The tape recorded data are processed in the laboratory by special purpose analog, digital, or hybrid computers to determine when a particular spectral signature selected by the operator is present in the data. Before the advent of computer implemented processing, human interpreters decided when a particular spectral signature was present in the data. This was inefficient because the amount of information that had to be recorded to adequately define a spectral signature was too much to handle. In computer-implemented processing, an operator selects a section of multispectral data known to contain the object of interest. The identification and location of the object are obtained from ground truth information. The computer stores the sampled spectral signature (training set) of this area and is programmed to recognize all areas with a similar spectral signature in other data presented to it for processing. From the data

supplied by the computer, a recognition map, which is a filmstrip or paper image of all areas having the same spectral signature as the training set, is generated.

Automatic data processing does not replace human interpretation; the investigator interacts with the computer by deciding which spectral signatures he wants it to recognize. He presents these data to the computer in the form of a training set, and the computer responds by reducing the data on any tape to a recognition map, which is more suited to human interpretation.

MULTISPECTRAL DATA COLLECTION

General discussion

The multispectral data collector consists of an optical-mechanical scanner mounted in an aircraft. As the aircraft flies over the terrain to be mapped, a rotating mirror scans the field of view of a parabolic mirror telescope across the ground perpendicular to the direction of flight. This action, in conjunction with the aircraft motion, covers a strip of terrain centered under the aircraft with a continuous scan (see photo in fig. 4). Two telescopes and one double sided (the two sides are rotated 90° with respect to each other) rotating mirror comprise the scanner. Two scanners are employed in the C-47 aircraft operated by the Willow Run Laboratories. Filtered detectors convert the radiation from the ground into electrical signals which are amplified and recorded on magnetic tape along with synchronizing signals necessary to reconstruct the images.

In the scanner system, multiple filtered arrays of detectors, filtered single detectors, and a spectrometer-detector combination are used to cover the visible and infrared spectra from 0.4 to $14\text{ }\mu\text{m}$ in as many as 18 different spectral bands. In the visible and near IR region (0.4-1.0 μm), the entrance slit of a prism spectrometer is placed at the telescope focus (see diagram in fig. 4). Photomultiplier detectors, coupled to the exit plane of the spectrometer by fiber optics, convert radiation from the scene (in narrow spectral regions defined by the prism dispersion and fiber optic bundle width) into electrical signals (fig. 5). The spectral regions of the spectrometer operation are shown in the lower part of figure 3; these may be compared with the spectral sensitivity of black and white, color, and multispectral photography which appear in the upper part of figure 3.

In order to get the spectral signature by which the processor recognizes distinctive objects on the ground, the scanner must collect simultaneous spectral information. As the scanner looks at each ground point, any spectral information about the point must be obtained instantaneously. The spectrometer-detector combination does this with twelve different photomultipliers which continuously convert radiation in narrow spectral

bands into electrical signals. The spectral signature of a ground point, which is the spectral radiance of the point seen by the scanner, may be constructed by sampling the twelve photomultiplier voltages at the instant of time that the scanner views the point. Signals from the other detectors in the system are not synchronized with the spectrometer data and cannot be processed with current technology.

A final remark on scanners concerns spatial resolution. The spatial resolution of the scanner is poorer than photographs on film for two reasons: Because the detector size is many times larger than the grain size of film, scanner spatial resolution in those wavelength bands covered by the filtered detectors is poorer than with photographic film. Similarly, because the entrance slit of the spectrometer must be large enough to pass a detectable amount of energy into the spectrometer, scanner spatial resolution for radiation in those wavelength bands covered by the spectrometer is also poorer than with photographic film.

The spatial resolution of the scanners of Willow Run Laboratories is 3 milliradians. Although the scanners have poorer spatial resolution than photographic film, the statistical accuracy of recognition maps made by computer is superior to manually interpreted photographs, because the computer defines boundaries between objects on a quantitative and unbiased basis, whereas human interpreters do not.

Data collection for the Everglades experiment

Flights were made over the Shark Valley Loop Road (fig. 1) at approximately 0930 hours on 7 September 1967, at altitudes of 500, 2,000, and 5,000 feet. Data were collected in 10 of the 12 spectrometer bands as follows:

Spectrometer Band	Wavelength Sensitivity, um	Color
3	0.40-0.44	UV-violet
4	0.46-0.48	Violet
5	0.50-0.52	Blue
6	0.52-0.55	Green
7	0.55-0.58	Green-yellow-orange
8	0.58-0.62	Orange
9	0.62-0.66	Bright red
10	0.66-0.77	Deep red
11	0.72-0.80	Deep red-infrared
12	0.80-1.0	Infrared

Supplementary data were collected as follows: a three-element array of indium arsenide detectors operating in the 1.0 to 1.4 um, 1.5 to 1.8 um, and 2.0 to 2.6 um regions. In addition data were collected by

three-element array indium antimonide detectors operating in 1.0 to 1.4 μm , 2.0 to 2.6 μm , and 4.5 to 5.5 μm bands and by a filtered mercury-doped germanium detector operating in the 8 to 14 μm band. Photographic data collected included panchromatic, color, and color infraed photography.

MULTISPECTRAL DATA PROCESSING

General discussion

The processing of scanner data depends upon the automatic recognition of objects by their spectral signatures. A spectral signature consists of the spectral radiance of an object, which is a continuous function of wavelength. The airborne spectrometer samples parts of the spectral signatures, and detectors convert the spectral samples to electrical signals proportional to radiance. The entire process of data collection consists of sampling the spectral signatures of ground objects, converting the data into electrical form, and storing it on magnetic tape. The spectral signatures of objects on the ground may be represented as sets of 12 video voltages, one from each of 12 spectrometer-detector channels.

The processing procedure consists of three steps:

- (1) Selection of a decision rule which states in mathematical terms the criteria to be used in determining the nature of the scanned objects.
- (2) Training of the computer by presenting it with a sample of data from the object to be mapped - a training set. The parameters of the decision rule are adjusted to this training set to optimize the detection process.
- (3) Presenting the computer with new data and asking it to recognize all objects similar to those in the training sets.

The data may be displayed in various forms, the simplest of which is a recognition map. This is a conventional black and clear filmstrip transparency. The black tones represent the objects recognized by the computer as having spectral characteristics similar to those of the training set objects. The clear areas of the recognition picture represent the objects which are considered by the computer to have spectral characteristics that are different from the training set objects.

The flow of processing operations is summarized by figure 6. Tape recorded data from the aircraft are edited by the operator to define the training set. The computer has previously been programmed to implement a particular decision rule. Then unknown data are processed by the computer. The computer output, an electrical signal, is printed on a cathode-ray-tube-camera filmstrip printer to yield a recognition map. A repetition of this

process with different training sets yields printouts of different object classes. These printouts are called recognition maps. Each recognition map is color coded and combined photographically with the others, producing a composite map in which each object class recognized appears in a different color.

Theoretical discussion of automatic processing

Deciding whether a sample of data contains the same object class as a training set may be done automatically, using various decision rules. A simple yet effective decision rule is the weighted Euclidean distance rule. This rule has also been referred to as the miss-distance or spectrum matching technique (refs. 2, 3).

A sample of spectrometer data known to contain a particular object is required for implementing the weighted Euclidean distance rule. This sample typically covers 1% to 2% of the total data to be processed. From this sample, also called the training set, the mean value (V_n) and standard deviation (σ_n) of the electrical signal in each spectrometer channel are determined. These data comprise the spectral signature of the training set. To decide whether data outside the training set contain the same objects as the training set, spectrometer voltages in each channel are compared to those of the training set. This is done by a special purpose analog computer which computes a discriminating function $L(t)$ defined by:

$$L(t) = \sum_{n=1}^{n=12} \left[\frac{V_n(t) - V_n}{\sigma_n} \right]^2$$

where $V_n(t)$ = video voltage in spectrometer channel n . This is a time-varying function, obtained from scanning the terrain.

V_n = mean value of voltage in spectrometer channel n for the area to be mapped. This is obtained from the training set.

σ_n = standard deviation of voltage in spectrometer channel n for the area to be mapped. This is obtained from the training set.

The equation shows that $L(t)$ will be small when the scanner sees an area similar to the area to be recognized, because each $V_n(t)$ will be close to V_n . The division by σ_n weighs the influence of spectral channels on $L(t)$ in inverse proportion to the variance of the signal from the training set. This variation may arise from two sources. First, all training-set areas in natural environments have some variability in composition, on a scale too small to be resolved by the scanner. These variations in

composition produce variations in the spectral signature. For example, variations in the percentage of cover of vegetation will produce changes in the spectral signature. Since individual plants usually cannot be resolved by the scanner, this variation appears as "noise". Second, the process of detection of radiation is noisy. This electrical noise is a source of variation added to the signals recorded on tape. Dividing by the standard deviation, σ_n , reduces the influence on $L(t)$ of noisy channels or channels where variation in the training-set signature occur. Thus $L(t)$ will be small when the area being scanned looks like the training set area, and large when it does not.

A threshold detector can be used on $L(t)$ to decide whether or not the area to be mapped is present. The threshold is represented mathematically as:

$$\begin{aligned} L(t) & K = \text{target object is present} \\ L(t) & K = \text{target object is absent} \end{aligned}$$

where K = threshold level.

The selection of the threshold level, K , is crucial to processor performance. If K is made too large, areas which closely resemble the target area will be recognized. If K is made too small, not all occurrences of the target will be detected. In practice, the threshold is set to recognize 90% of the training set.

Trial runs are made through the data to verify that the choice of threshold level is adequate. Upon examination of results, the threshold may be modified to give better results.

Not all spectrometer channels are used for forming $L(t)$; only those channels are used for which the target object radiance is different from the radiance of other objects to be mapped. A selection of these channels can usually be made quite easily from an examination of single channel imagery of each of the spectral channels. With some care, the selection may also be made from an examination of color and color infrared photographs. As with the threshold level choice, the success of a selection of a preliminary set of channels is determined from trial recognition maps. If persistent confusion of two objects occurs at all threshold levels, additional channels are used to form $L(t)$. The additional channels are selected by noting on the imagery those channels in which the contrast between the target object and the interfering objects is greatest.

Processing of the Everglades data

Previous studies in the Everglades have demonstrated that specific relationships exist among the ground elevation, mean period of inundation

at a given site, and the type of biotic community which the site supports (ref. 4). Although the recording of data at numerous locations throughout the Everglades would be a desirable approach to the study of fluctuating water supply, it would be impractical because of the size of the area, the restricted mobility within the area, and the time and manpower involved in handling recording instruments and analyzing the data.

Because ground altitude and mean period of water inundation are characteristics of the Everglades environment which cannot be remotely sensed by present scanning systems, selection of suitable indicators of water level conditions and ground elevations was necessary. From both the remote sensing and ecological viewpoints, the three basic components of the glades communities which seem to be most relevant as indicators of surface water conditions are: (1) depth of water, (2) vegetation types, and (3) substratum types. The purpose of the data processing was to delineate sites relatively uniform in water, plant, and substratum characteristics.

The data collected at 2,000 feet were selected for processing as the best compromise between high resolution (which is obtained at low altitudes) and broad area coverage (which is obtained at high altitudes). Only the spectrometer data collected simultaneously were used for processing because such data permit rapid processing by implementing the decision rule on a special purpose analog computer, SPARC (Spectral Processing and Recognition Computer). After initial setup, data may be rapidly processed, that is, data that took one minute to collect may be processed in one minute.

Ground-truth observations made on 8 September 1967 and aerial photographs and multispectral imagery collected on 7 September 1967 were studied to determine the probable number of sites which could be differentiated by automatic processing, suitable areas for location of the training sets representative of each of the site types, and suitable spectral channels for processing. Training sets for two different water depth sites, for a limestone site, and for five vegetation classes were selected for processing. Each training set was located in an area which appeared to be typical of the type to be mapped, was relatively uniform in composition, and was at least 20 feet in diameter in order to insure an adequate number of data samples.

The water depth training sets were located in two areas of known water depth: (1) an area downstream from a water control structure representing the deepest water in the scent, 5 to 15 feet deep, and (2) an area adjacent to a borrow pit representing shallow water of 3 to 5 feet deep. A pile of excavated limestone located near a borrow pit was selected for the limestone training set.

Training sets for five vegetation classes were selected using the criteria of physiognomy, dominant plant species, plant coverage, substratum type, and water depth. Physiognomy is defined as the gross external

appearance of vegetation, determined chiefly by the life-form of the dominant plants. A classification of vegetation based solely on physiognomic criteria would group all vegetation types, regardless of species composition or structure, into units based on the dominant life-form of the vegetation, e.g., all vegetation types having grasses or grasslike plants as the dominant life-form would be classified as grassland. The three different physiognomic types observed from the imagery were forest, emergent semi-aquatic scrub, and emergent aquatic grassland.

A dominant species is here defined as a plant which occupies the most space within a site (50% or more of the plant cover). The criterion of dominant plant species was used to select two different grassland training sets. One training set had sawgrass as the dominant species, and the other had spikerush as the dominant species.

Plant coverage is defined as the area of the ground covered by plants of one or more species, as viewed from above the plant canopy. The degree of cover for each physiognomic unit was estimated from the imagery within broad classes as follows:

<u>Cover Class</u>	<u>Coverage Description</u>
1	5%- 25%, vegetation very sparse
2	26%- 50%, vegetation sparse
3	51%- 75%, vegetation medium dense
4	76%- 100%, vegetation dense

Two broad categories of substrata occurred within the scene: one type composed of peat, marl, or limestone and covered with a benthic algal mat (periphyton), and the other composed of peat but not covered by periphyton. Plant cover and substratum were used as the criteria to select training sets representative of two different categories of sawgrass vegetation. One training set had an estimated cover range of 60% to 90% with a peat substratum, and the other had an estimated cover range of 35% to 45% with the bottom type covered by a periphyton mat.

Two different categories of spikerush grassland (wet prairie) were selected, using coverage and water depth criteria as follows: (1) spikerush grassland having 26% to 35% cover, and water 3 inches to 6 inches deep; and (2) spikerush grassland having 5% to 15% cover, and water 6 inches to 18 inches deep.

Different combinations and numbers of channels were selected for processing each site unit. Trial recognition maps were produced to verify that the choice of channels and threshold levels was adequate. A final recognition map for each site type was then printed on film. Each black and white recognition map was exposed on color print paper through

a different color filter, yielding a color composite recognition map with unrecognized areas rendered in black (fig. 7).

ANALYSIS OF THE EVERGLADES DATA

Introduction

The purpose of the data analysis was to determine how well the processor could delineate sites which were relatively uniform in water depth, vegetation type, and substratum type. Eight recognition maps were selected for producing the color-composite recognition map. A black-and-white photograph of the map is shown in figure 7. The display colors in each recognition map were chosen arbitrarily.

Evaluation of recognition success was made on the basis of the following data:

- (1) Color infrared photographs obtained at the time of the multispectral flight mission (7 September 1967).
- (2) Ground-truth observations made along the Shark Valley Loop Road on 8 September 1967 and on 17 February 1969.

Because of time and funding limitations, quantitative ground survey techniques were not used to determine the total area covered by each general site type, or to determine the boundaries of each specific site unit. The degree of accuracy of the processed recognition maps, therefore, was determined only in a qualitative manner, based chiefly on a comparison of the areas of each site type interpreted from color infrared photographs with those delineated on the recognition maps.

Using conventional photographic interpretation techniques, the boundaries of each site unit were drawn on mylar overlays of the color infrared photographs. The criteria used for delineating each site type are listed in table 1. Each descriptive element (i.e., water depth, substratum type, physiognomic type, etc.) for each site type was correlated with limited ranges of color, texture, and pattern on the color infrared photographs.

The areal distribution of each site type (as defined from color infrared photographs and ground observations) was compared with the areal distribution of the recognition-map units for each of the eight recognition types. The following is a discussion of the recognition results. The locations of the training set areas described below are indicated on the color-composite recognition map (fig. 7) by black outline boxes. Although some of the ground photographs illustrated in figure 7 were taken outside the training-set areas, they illustrate the typical appearance of the site types recognized.

The flight line chosen for this study covered a part of Everglades National Park centered on the Shark River Valley Loop Road. This road traverses a transitional region between the open Everglades at the north end and the Shark River Slough at the south end. The Shark River Slough is aligned in a northeast-southwest direction and intersects the flight line at a point very near the observation tower at Mile 7. Because the flight line covers this transition from the open Everglades to the slough, water conditions at the north end of the run are quite different from those at the south end. In general, the water at the south end is deeper by 1 or 2 feet than the water at the north end of the run. The water depth pattern is complicated by the presence of deeper water in borrow pits and the water control canal running east-west at Mile 0. In the canal and borrow pits, the maximum water depth was eight feet, and the maximum water depth at the control gate (Mile 0) was estimated at 15 feet at the time of flight.

DISCUSSION OF THE RECOGNITION RESULTS

Deep water (map unit 1)

The deep water training set was located at a water control structure at Mile 0, where the maximum water depth was 15 feet. Water less than 5 feet in depth was excluded from the training set. The deepest water in the moat at Mile 7 was detected with this signature. The deep water north (upstream) of the control structure (approximately 5 feet deep) was also detected. No other deep water measurements were available to permit verification of other deep water detections. The ground photograph of map unit 1 in figure 7 shows an alligator in a deep part of the moat at Mile 7.

Numerous small areas within the boundaries of tree islands and on their western sides were detected as deep water. In some cases, these detections of small areas were due to the presence of deep water in limestone-solution holes or in drainage channels within the tree islands. In other cases, tree shadows were detected as deep water. The false detection of tree shadows as deep water constituted approximately 1.5% of the total deep water recognition. The tree shadows occurred on the west sides of the tree islands because the data were collected early in the morning. In the spectral channels used for processing, tree shadows closely resembled deep water since both had low radiance values.

Shallow water (map unit 2)

The shallow water signature was obtained from a training set at Mile 4.50 having water 3 to 5 feet deep. The typical appearance of shallow water areas is illustrated by the water in the foreground of the ground photograph of map unit 2 in figure 7. The light colored substratum can be seen at the 3 feet water depth. Overlapping detections of shallow water

occurred in some areas having dense sawgrass cover and sparse sawgrass cover (table 2). On the original color-composite recognition map the former areas were pink and the latter were light yellow or white. These areas of overlapping detection had deeper water than was typical for the sawgrass vegetation classes.

Tree islands (map unit 7)

The tree island signatures were derived from two different training sets of known species composition. One set at Mile 0.5, was a young, even-aged stand of nearly pure willow (Salix amphibia); the other, at Mile 1.0, was an uneven-aged stand of mixed tree and shrub species, e.g., gumbo limbo (Bursera simaruba), strangler fig (Ficus aurea), cocoplum (Chrysobalanus icaco), dahoon holly (Ilex cassine), and myrtle (Myrica cerifera). The ground photograph of map unit 7 (fig. 7) was taken south of the moat at Mile 7 and shows willow as the dominant species of the tree island. Both sawgrass and spikerush grasslands can be seen adjacent to this tree island in the background.

Two separate recognition operations were performed, one on each training set, and the results were combined in a logical "OR" circuit before printing. The resultant recognition picture showed tree islands present when either of the two training-set signatures was matched by the data signature.

The boundaries of the tree islands, as observed on the ground and from aerial photographs, were more distinct than those of the other vegetation classes in the scene. Therefore, verification of the accuracy of the tree island recognition-map units was much simpler than for the other map units. It appears that all tree islands were detected. The boundaries of some tree islands delineated by the automatic processor were found to be more precise than could be delineated on the color infrared photographs.

Areas characterized by small scattered detections of trees and shrubs within a matrix of another vegetation type represent transitional regions of vegetation. Examples of tree and shrub vegetation mixed within sparse sawgrass grassland (map unit 5) and within dense sawgrass grassland (map unit 6) occur between Miles 1 and 2, and between Miles 5 and 6 on the recognition map (fig. 7). The subtle boundaries of such transitional areas are difficult to determine by ground survey techniques. It was not possible to differentiate these transitional areas on the color infrared photographs. However, even if the boundaries had been distinguishable on the photographs, accurately drawing the small scale boundaries by hand would have been impractical. The precision with which the transitional boundaries were mapped by the processor indicates that this technique may serve as a sensitive tool for assessing slight vegetation changes induced by changes in surface water conditions.

Medium dense to dense sawgrass grassland (map unit 6)

The training set for the dense sawgrass signature was located at Mile 6.75, in an area typical of the medium dense to dense cover of sawgrass (Mariscus jamaicensis). The ground photograph of map unit 6 (fig. 7) shows dense sawgrass in the background and a deer running through sparse sawgrass in the foreground. The photo was taken during higher water conditions than prevailed during the flight. The detection of medium dense to dense sawgrass throughout the scene was accurate. No detection failures were evident from the color infrared photographs and ground spot checks. However, field observations revealed that scattered small stands of dense herbaceous vegetation (e.g., solid stands of pickerelweed and cattail) were falsely detected with this sawgrass signature (table 2). This false detection constituted less than 1% of the total dense sawgrass detection. Other false detections occurred in areas having overlapping recognitions of dense sawgrass and shallow water (table 2). The water in these sawgrass areas was deeper than was typical for this sawgrass type. The dense sawgrass areas between Mile 0 and Mile 0.25 are a darker shade than the other dense sawgrass areas on the recognition map (fig. 7). This difference in shading occurred because the original black and white recognition filmstrip was a darker shade of gray in that area.

Sparse to medium dense sawgrass grassland (map unit 5)

The signature for sparse sawgrass grassland was obtained from a training set at Mile 6.5, in an area having approximately 40% sawgrass cover and 60% periphyton cover. The water in this portion of the slough was approximately 2 inches deep at the time of the flight. Areas in the scene having similar sawgrass cover, periphyton cover, and water depth were detected with this signature. The photograph of map unit 5 (fig. 7) shows sparse sawgrass in the foreground. The photograph illustrates a higher surface water level condition than existed at the time of the data collection flight. A few false detections for this signature occurred, where overlapping detection with shallow water occurred (table 2).

Spot checks on the ground between Miles 6.00 and 6.25 revealed that the unrecognized area coded in black in the original color-composite recognition map was sparse to medium dense sawgrass grassland that had been burned in recent years. The periphyton cover in the area was thus less than for the training set, and a darker substratum was exposed. The water on the east side of the road was a few inches deeper than on the west side of the road (table 2). A small area located at Mile 6.75 on the east side of the road (map unit 8 in fig. 7) also was coded black (unrecognized) in the color-composite recognition map. Field observations in this area showed that the vegetation consisted of sparse to medium dense sawgrass in clumps, interspersed with limestone outcrops too small to be resolved by the scanner. Sufficient exposed limestone was present,

however, to affect the spectral signature of the area so that it was not recognizable as sawgrass grassland (see ground photograph of map unit 8 in fig. 7). In addition to unrecognized areas, areas of excavated limestone were coded black in the original color-composite recognition map.

Sparse to medium sparse spikerush grassland (map unit 4)

The training set for sparse to medium sparse spikerush grassland was located near Mile 1.25 in an area having approximately 30% plant cover, 70% periphyton cover, and water 3 to 6 inches deep. Three species of Eleocharis were predominant in the training set area. The foreground of the ground-truth photograph of map unit 4 (fig. 7) shows a typical sparse spikerush grassland with both floating and submerged periphyton. Ground spot checks of this map unit type in the vicinity of Mile 4.50 indicated close agreement of plant cover, periphyton cover, and water depth in that area with those of the training set area.

Very sparse spikerush grassland (map unit 3)

The training set for very sparse spikerush grassland was located near Mile 1.60. The signature for this map unit was based on the integrated spectral radiance of the periphyton substratum (approximately 90% cover) and water ranging in depth from 6 to 18 inches. The plant cover varied within the training set from 5% to about 15%. Observations in the field near Mile 4.50 indicated that the computer recognition of this unit was correct. In the ground truth photograph of map unit 3, a small clump of sawgrass appears in the right mid-foreground, and very sparse spikerush grassland occurs in the mid-background.

RECOMMENDATIONS

Larger areas should be mapped with these techniques in future studies. This will require improvements in three phases of the effort: airborne data collection, ground truth data collection, and processing operations. More specifically, these improvements are:

A. Airborne data collection

- 1) Fly at 6,000 feet over terrain to achieve wider coverage. Some processing of 5,000 feet data indicates that automatic processor performance is not seriously degraded. If this is also true at 6,000 feet, data collected at this elevation would give a map scale of 1:12,000, or 1 inch to 1,000 feet. A reduction of this map scale to half size, 1:24,000 would produce a scale equivalent to that of the U. S. Geological Survey topographic quadrangle sheets, and would be a useful map size for the Everglades as well as for other investigations.

- 2) Measure aircraft altitude at time of flight (particularly yaw or crab angle) to permit partial rectification of images or recognition maps.

B. Ground truth data collection

- 1) Collect and interpret aerial photographs prior to the multispectral data flight to select training sets for the processor.
- 2) Concentrate ground truth measurements in the training set areas. These measurements, which are taken at the time of the multispectral flight, should include parameters likely to influence the spectral signature of the training set, e.g., quantitative species composition and water depth measurements.
- 3) Study methods of using data from existing ground instrumentation (reflectance, panels, color panels, spectrophotometers, radiometers, etc.) to assist in interpretation of the multispectral data.

C. Data processing operations

- 1) Evaluate a prototype processor for removing the geometrical distortion inherent in all scanning systems. When operational, this processor will produce a rectified image of the scene from raw scanner data.
- 2) Study the use of hybrid computers (combination of CDC 1604 digital and SPARC analog computers) to process data. The division of the processing work load should be defined since there are tasks which the digital computer can do more efficiently than SPARC and vice versa. The design criterion should be maximum processing speed.
- 3) Consider the use of a computer program, atmospheric-illumination and transmission model, developed by the Willow Run Laboratories for the Air Force. This program simulates the theoretical attenuation of energy reflected or emitted from a recognized target, given different altitudes.

REFERENCES

1. Purdue University, Laboratory for Agricultural Remote Sensing, Remote Multispectral Sensing in Agriculture, Volume 3, Report No. 844, September 1968.
2. P. G. Hasell et al., Investigations of Spectrum-Matching Techniques for Remote Sensing in Agriculture, Interim Report, March 1967 to December 1967, Report 8725-13-P, Volumes 1 and 2, Willow Run Laboratories of the Institute of Science and Technology, The University of Michigan, July 1968.
3. D. S. Lowe and J. G. N. Braithwaite, A Spectrum Matching Technique for Enhancing Image Contrast, Applied Optics, Volume 5, No. 6, June 1966.
4. M. C. Kolipinski and A. L. Higer, Some Aspects of the Quantity and Quality of Water on Biological Communities in Everglades National Park, U. S. Geological Survey open-file report, September 1969.

THIS PAGE INTENTIONALLY LEFT BLANK

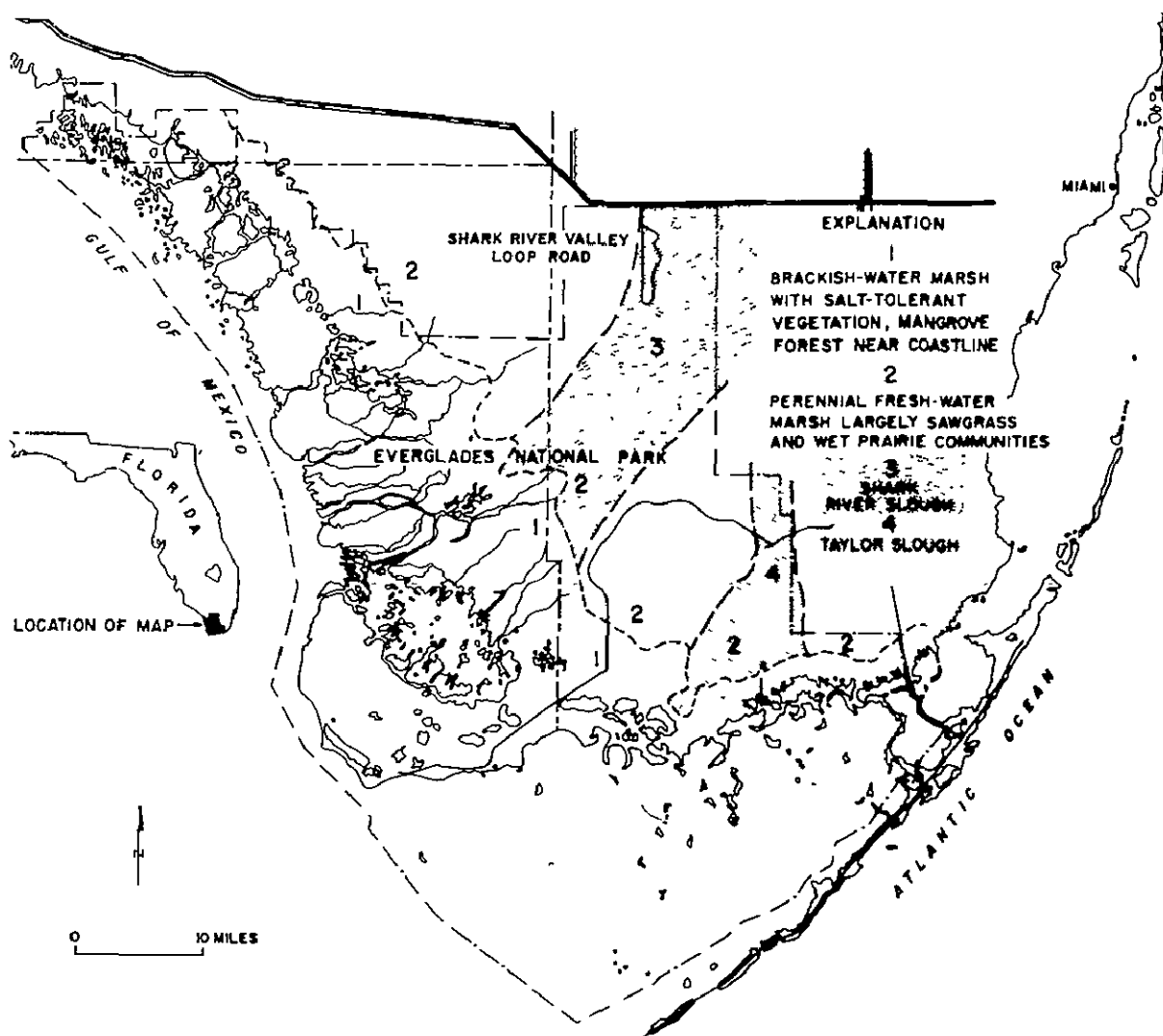


Figure 42-1.- Map of Everglades National Park indicating the location of Shark River Slough, Taylor Slough, and the approximate position of the interface between fresh water and brackish water along the coast.

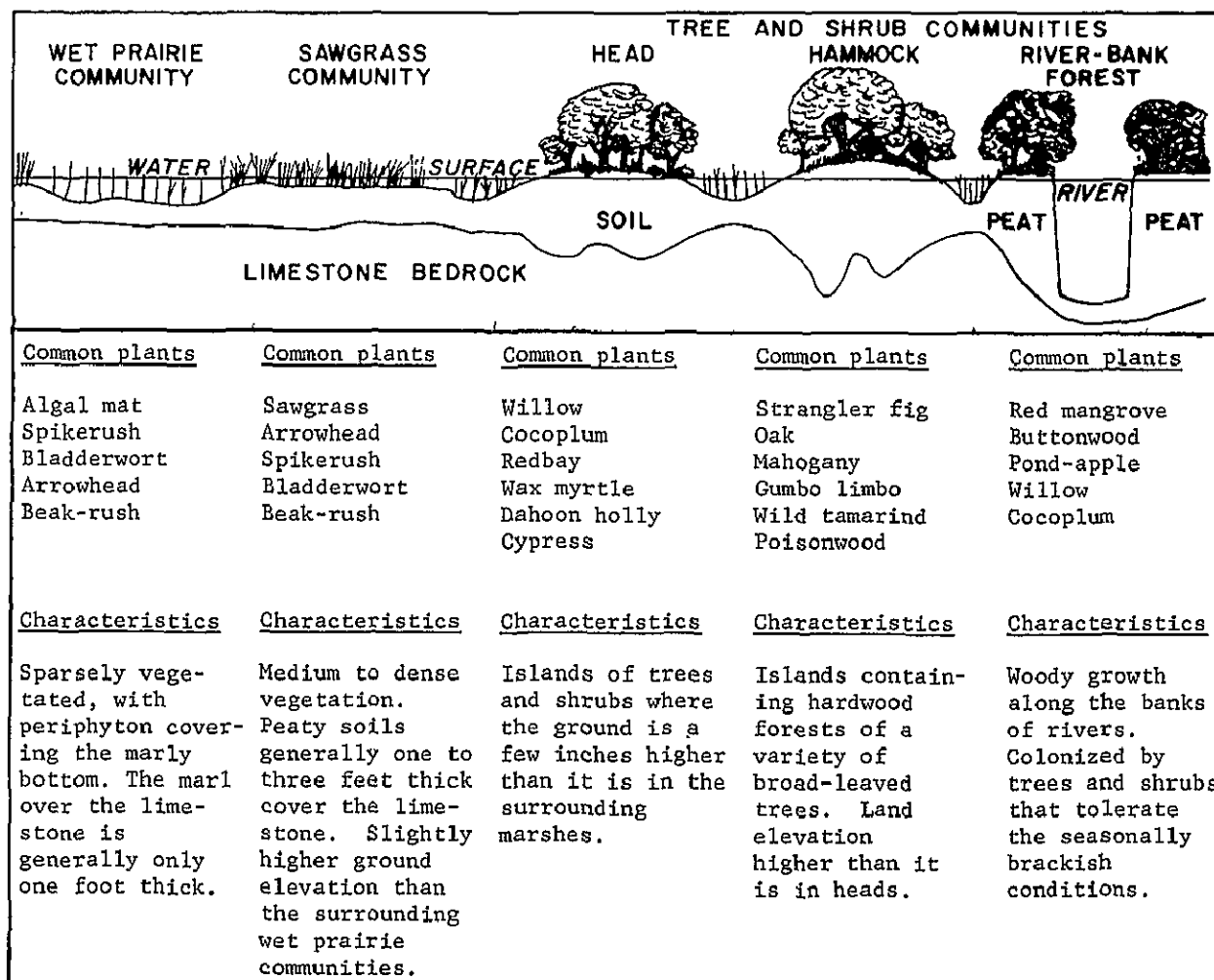


Figure 42-2.- Annotated diagram of the major plant communities in Shark River Slough. Note relation of communities to the position of the water surface and thickness of the soil.

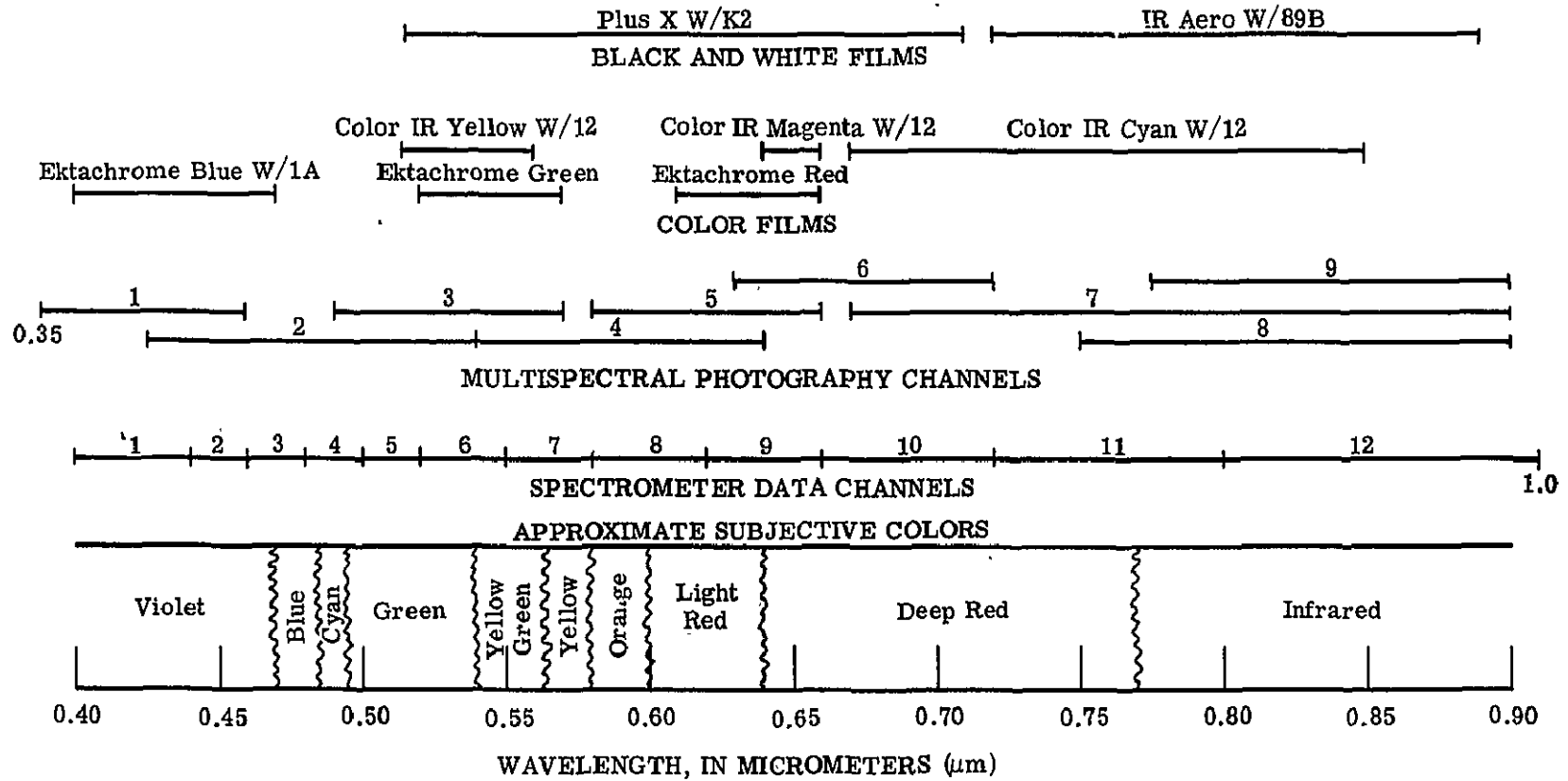


Figure 42-3.- The 50% sensitivity points of various film-filter combinations and of the 12-channel spectrometer.

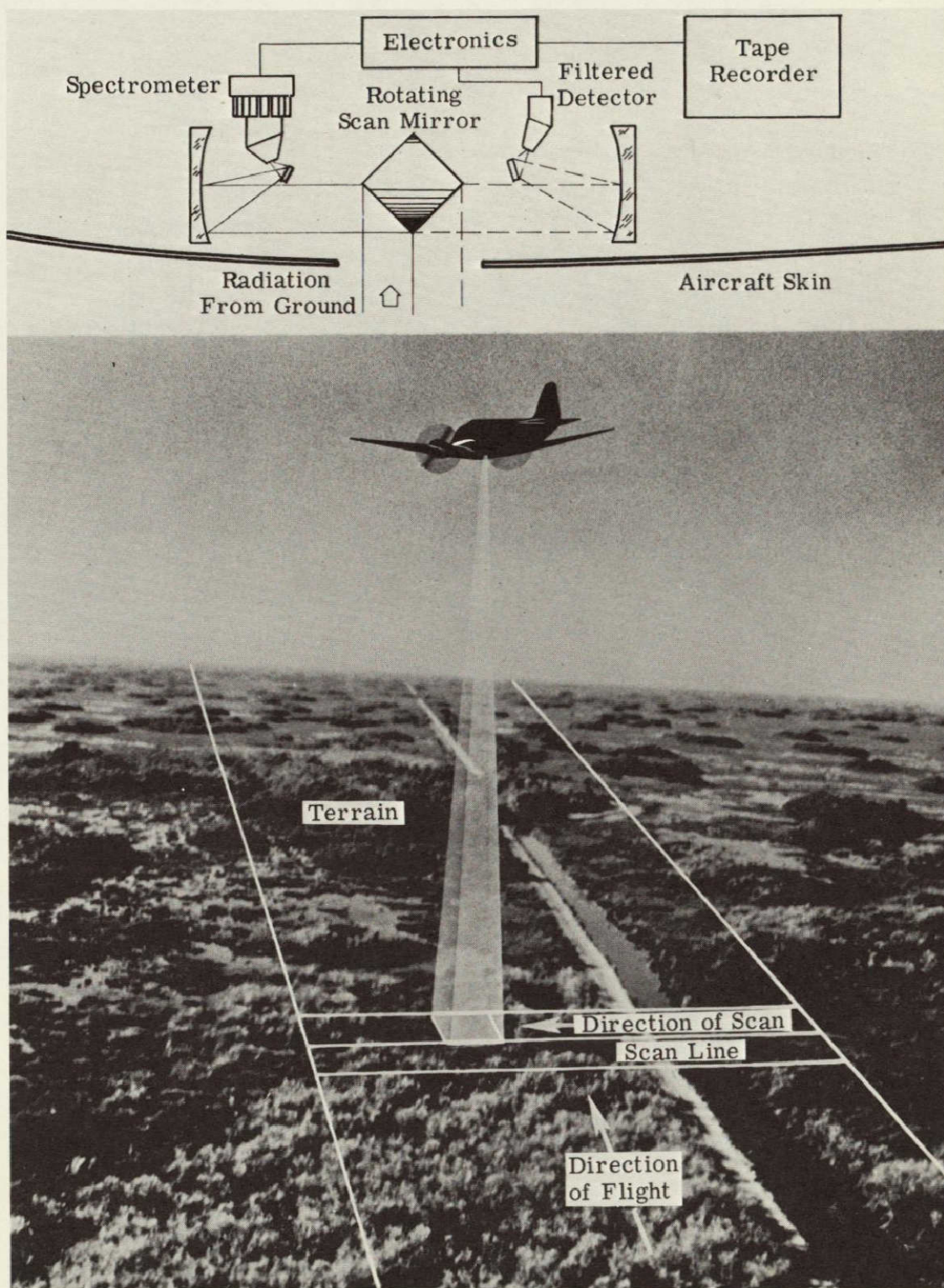
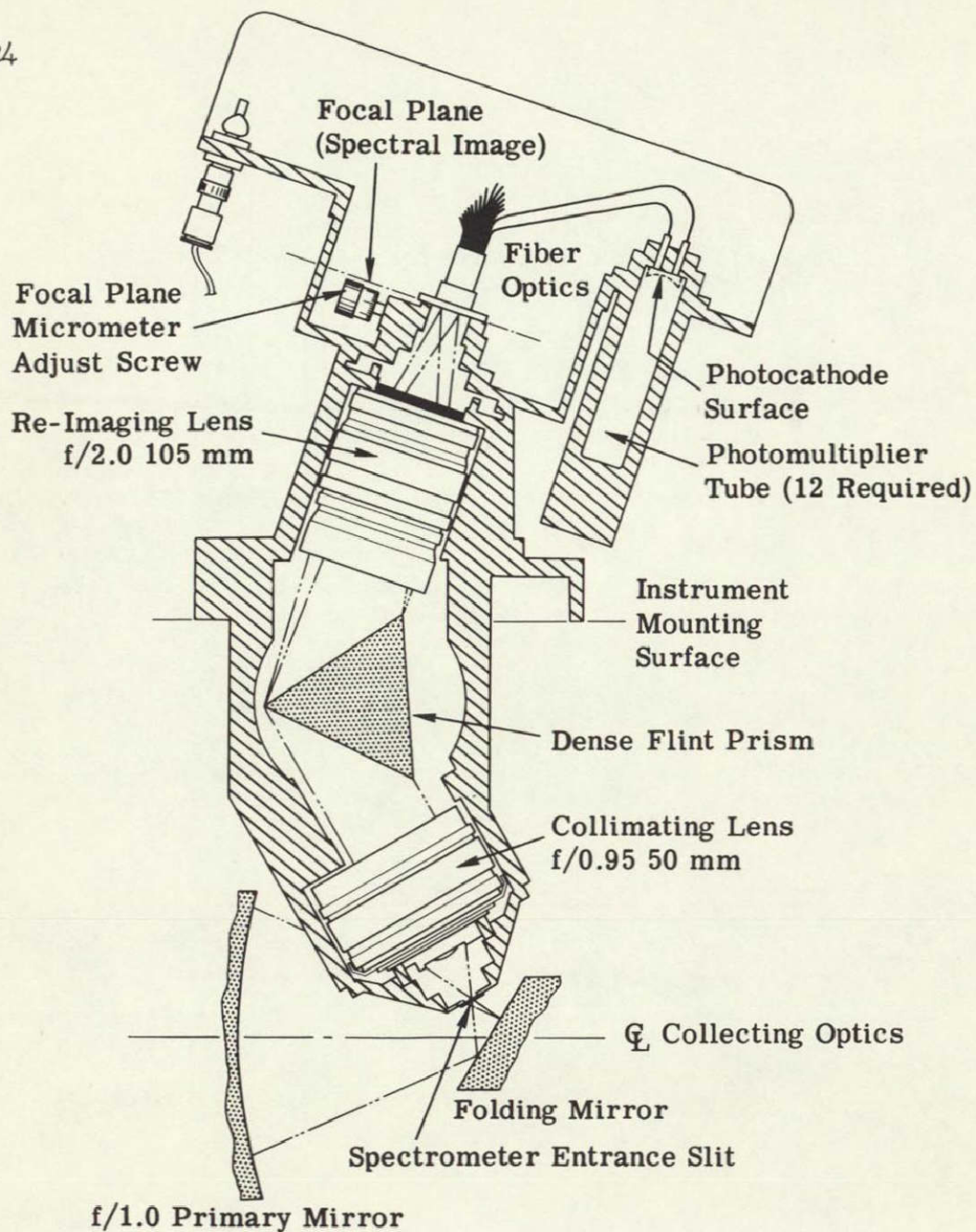
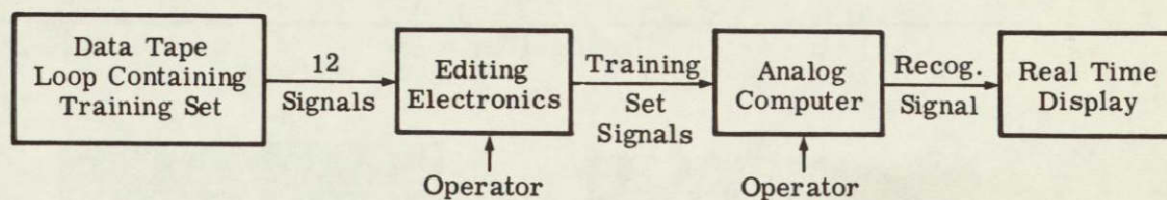


Figure 42-4.- Multispectral data collection operations.



12-CHANNEL SPECTROMETER
(0.4 μ To 1.0 μ)

Figure 42-5.- Conceptual sectioned view of existing spectrometer detector system.



Training Mode

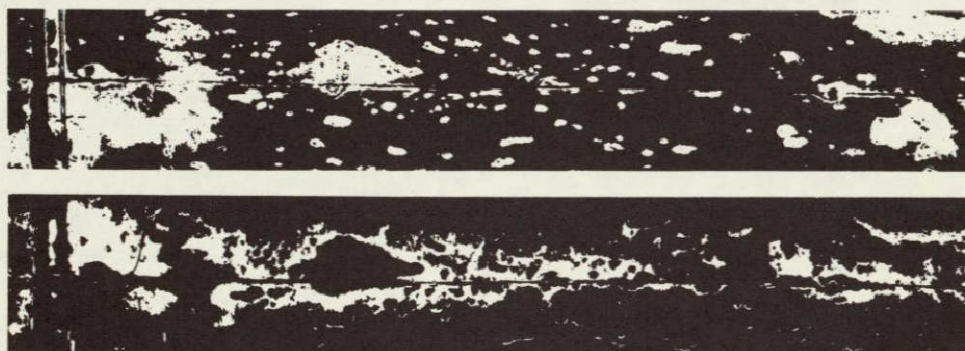
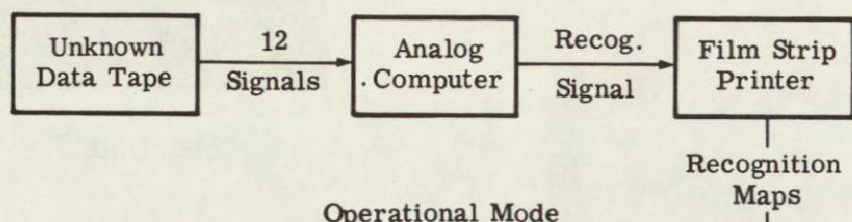
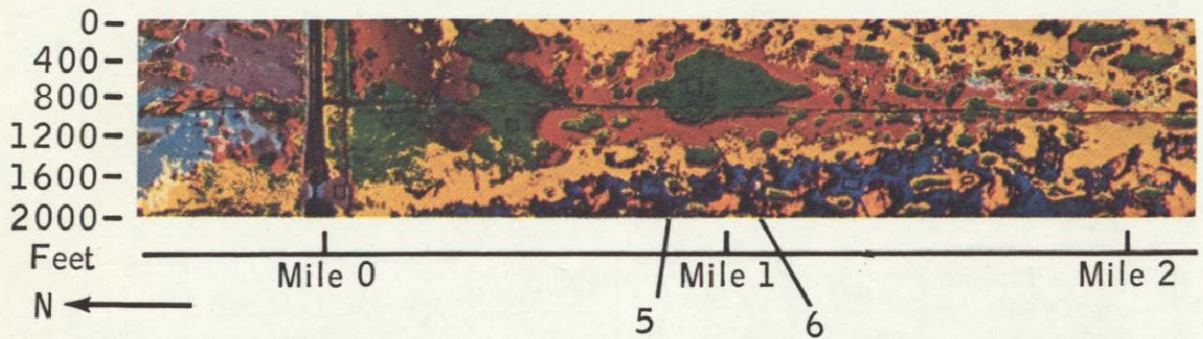
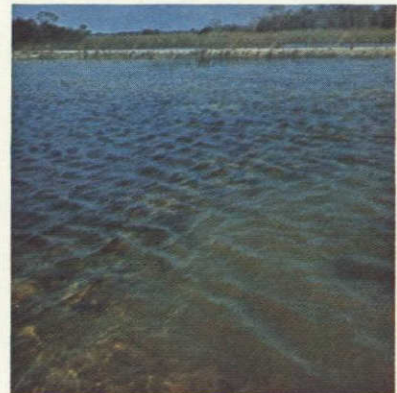


Photo Work

Figure 42-6.- Block diagram of multispectral data processing operations.



Map Unit 1



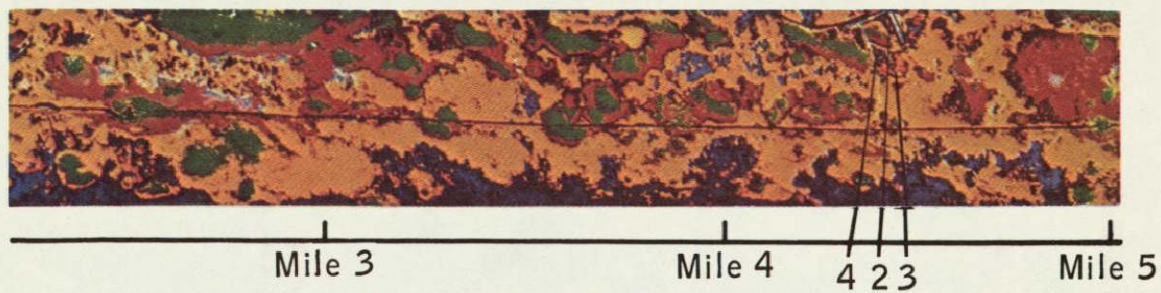
Map Unit 2



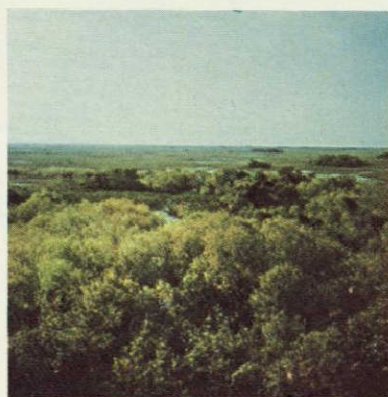
Map Units 3 & 4

Map Unit No.	Map Unit Color	Description of Recognition-Map Units
1	Violet	Water deeper than 3'
2	Cyan	Water shallower than 3'
3	Orange	Sparse spikerush grassland in deep water sites (6" to 3')
4	Dark blue	Sparse to medium dense spikerush grassland in shallow water sites (2" to 1')
5	Yellow	Sparse to medium dense sawgrass grassland in shallow water sites
6	Red	Medium dense to dense sawgrass grassland in shallow water sites
7	Green	Head and hammock islands composed of trees and shrubs
8	Black	Features not recognized (sparse sawgrass grassland in shallow water sites with exposed limestone, roads)

Figure 42-7.- Color-composite recognition map of hydrobiological features in a portion of the Shark Valley Slough in the Everglades National Park. Numbered leaders point to areas illustrated by ground photographs.



Map Units 5 & 6



Map Unit 7



Map Unit 8

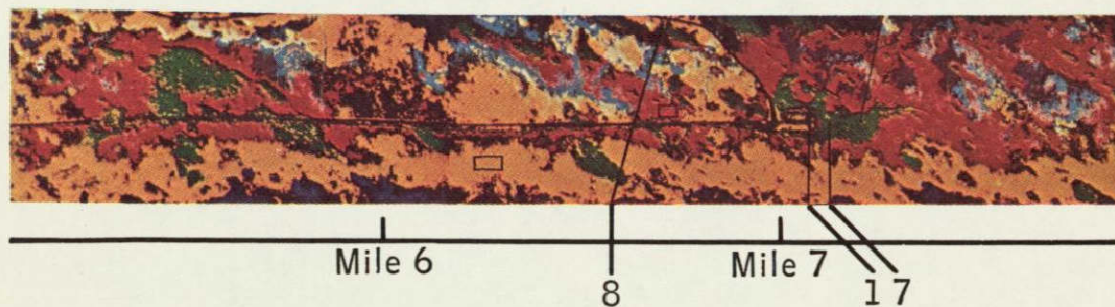


Figure 42-7.- Concluded.

SECTION 43

SNOW AND ICE SENSING WITH PASSIVE MICROWAVE
AND GROUND TRUTH INSTRUMENTATION:
RECENT RESULTS, SOUTH CASCADE GLACIER

by

M. Meier
U.S. Geological Survey
Tacoma, Washington

and

A. T. Edgerton
Aerojet-General Corporation
El Monte, California

N71-11160

SUMMARY

Passive microwave sensing holds considerable potential for synoptic monitoring of snowpacks and glaciers. It may be possible to determine melt rates, areal extent of snowpacks, and accumulation through the use of selected sensor wavelengths, antenna polarizations, etc. An experimental program, sponsored by the U. S. Geological Survey, is in progress to determine the microwave emission characteristics of snowpacks and to establish the feasibility of using microwave radiometry for monitoring meaningful hydrologic properties of snowpacks and glaciers. The study, performed by Aerojet-General Corporation, includes laboratory and field investigations combined with the development of theoretical prediction models.

Field experiments utilizing a multifrequency microwave radiometry field laboratory were conducted in the Pacific Northwest to assess the effects of melting, layering surface roughness, density variations, etc. on microwave emission and to determine effective penetration as a function of sensor wavelength. Laboratory studies involved measurement of the dielectric properties of snowpacks at microwave frequencies. Analytical modeling consisted of formulation of models to describe vertically structured media in which both the dielectric properties and physical temperature are permitted to vary with depth. During field studies, the investigators experienced difficulty in obtaining reliable ground truth measurements of snow moisture. To improve confidence in this measurement, a series of tests were conducted on the South Cascade Glacier where several techniques for determining snow moisture were compared.

The investigators are also analyzing 1.55-cm imagery of Mount Rainier where effects of terrain slopes parallel and perpendicular to the flight line are encountered. These data correspond to a variety of snow and ice conditions.

NASA P3V overflights of the South Cascade Glacier conducted during Mission 78 provided, for the first time, thermal infrared imagery of subfreezing snow. The 8- to 14-micron imagery indicates cold snow concentrated in very shallow valleys on the Glacier suggesting the existence of shallow, surface drainage winds.

FIELD OBSERVATIONS

Field studies were performed with Aerojet-General Corporation's microwave field laboratory, Figure 1. Radiometers tuned to wavelengths of 0.8, 2.2, and 21 cm were used along with considerable supporting ground truth instrumentation such as infrared radiometers, meteorological, geophysical and glaciological instrumentation. The microwave radiometers are dual-polarized and can be operated continuously in a fixed position or can be scanned in five degree steps between nadir and zenith. These operating modes enable the investigator to examine material as a function of sensor wavelength, polarization, and antenna viewing angle. Field investigations were configured to assess effects of diurnal variations, snow density, layering, and free water on microwave emission.

Diurnal Studies

Diurnal experiments were performed on sites near Mount Rainier, Washington and Crater Lake, Oregon. Significant brightness temperature changes were noted during each of these experiments. The variations were associated with varying melt conditions, changing weather conditions, snow accumulation, and moisture variations in the base material.¹

Snow Moisture

Snow moisture experiments were conducted under natural melt conditions and with melting induced by heat lamps. The resulting data indicate dramatic changes in the microwave emission at shorter wavelengths. Figure 2, representing earlier data taken of snow over lake ice, illustrates this point.² On this figure, free water content and thermometric temperature of the snow-ice system are compared with microwave brightness temperatures measured for antenna viewing angles of 10 degrees and 30 degrees above nadir. The striking features of this plot are the very cold 0.81 cm (37.0 GHz) nighttime temperatures which occur when free moisture content is very low and the fact that all brightness temperatures are very warm (255°K to 270°K) when the average free moisture content of the snowpack exceeds about two percent by volume. An additional point of interest is that no appreciable changes in brightness temperature occur when moisture values exceed about 2.5 percent by volume.

1. Edgerton, A. T. and Sakamoto, S., Microwave Investigations of Snowpacks, Interim Report No. 1, 30 July, 1969.
2. Edgerton, A. T. et al, Tech Report 4.

Research toward establishing a quantitative relationship between microwave emission and snow moisture has been impaired by uncertainties in the measured moisture values. To improve confidence levels in this measurement, a comparative study of snow moisture measuring techniques was performed on the South Cascade Glacier, Washington. Six measuring schemes, consisting of three types of calorimeters, two centrifuges, and a capacitive instrument, were evaluated. The snowpack used for the experiment exhibited a density of about 0.55 grams per cc, with grain sizes ranging from 1/2 to 1 1/2 millimeters. Table I shows the range and average moisture values in percent by weight obtained by each technique. Variations of more than one percent in snow wetness were obtained for readings taken at short intervals with the same instruments, and a comparison of different instruments and methods showed a much larger range of values. This large range in observed moisture values can be ascribed both to actual variations in snow moisture content and to sampling techniques. The Ambach meter (capacitance bridge) consistently gave the lowest readings and the combination calorimeter the highest. The freezing calorimeter was intended to serve as a standard for comparison and evaluation of other techniques; however, it exhibited as much variation as the other methods.

Snow Density and Thickness

Experiments were also conducted to assess effects of density and thickness variations on snowpack emission. The first of these was performed in an undisturbed, dry, 180-cm thick snowpack. In this experiment, Figure 3, a large aluminum plate (perfect reflector) was introduced at varying levels in the snowpack while brightness temperatures were monitored. These data, Figure 4, demonstrate a definite relationship between the water equivalent of cross-sectional mass of a snowpack and microwave response. In this experiment the 0.8 cm radiometer penetrated the 180 cm of snow (cumulative water equivalent of 0.35 meters). Emission at 2.2 cm and 21 cm was attenuated much less than at 0.8 cm. The 2.2 cm response ranged from 135°K with the plate situated at the snowpack base to 25°K with the plate at the surface. The corresponding 21 cm temperature variations were small, on the order of 40 degrees, and this was partly due to changing beamfill ratio of the plate. Of additional interest in this experiment is the discontinuity in the slope of the microwave temperature vs. water equivalent curves observed as the plate is moved across an ice layer situated near the middle of the snowpack. This effect was most apparent on short wavelength data.

A second experiment was conducted with the 2.2 cm radiometer wherein the attenuation of microwave energy as a function of increasing snow depth and density were observed. In this experiment an aluminum plate was measured as varying amounts of unstructured, dry, low-density snow were placed over the plate. The plate served to eliminate all but the radiation due to the snow cover and the reflected sky radiation. The plate was first observed with no snow cover and subsequently with snow cover of 20, 40, and 60 cm depth. The snow was then compacted to a depth of 51 cm and the measurement repeated. Figure 5 shows the observed antenna temperature variations. The measured temperatures

were substantially the same before and after compaction, illustrating a fundamental relationship between the transmission coefficient and the water equivalent or cross-sectional mass. Snow was added, following compaction, to increase the thickness to 60 cm.

LABORATORY STUDIES AND ANALYTICAL MODELING

A parameter found useful in characterizing substances electrically is the complex dielectric constant. From a knowledge of it, the reflectivity of a material can be determined as well as the absorptivity when conservation of energy is assumed.

The dielectric constant of most substances has been measured accurately at frequencies lower than 10 or 15 GHz while much less information exists at higher frequencies. This is particularly true for materials such as snow and ice. It is primarily for these materials that the free-space measurement method used in this study was developed. An ellipsometer essentially consists of a transmitter-receiver system capable of measuring the power reflected from a material's surface as a function of the angle of rotation of the receiver antenna about its axis. It can be shown that the ratio of minimum to maximum values of power, together with a "tilt" angle of the reflected elliptically-polarized wave, determines the dielectric constant.

In the experimental set-up, the ellipsometer and snow samples are situated in an "isothermal" chamber. The chamber temperature is controlled to near constant values of using large cooling fans which circulate the air in the chamber continuously.

Measurements have been performed at observational wavelengths of 0.8 and 2.2 cm. Preliminary measurements of a low loss sample indicate that the real part is relatively independent of the temperature as long as no melting occurs and that the imaginary part of the dielectric is too small to measure (0.01). Measurements of samples of varying density and moisture are now in progress.

A brightness temperature model has been developed for vertically structured media. The model enables calculation of brightness temperatures for media in which both the physical temperature and dielectric properties vary with depth. The model can handle variations in dielectric constant such as occur with density, snow moisture, and base material variations. Brightness temperatures are computed as a function of wavelength, antenna viewing angle and polarization. Dielectric constant values used for these calculations have been variously derived from the laboratory phase of the program, mixing formulas, and available literature.

Initial calculations, now in progress, are concerned with a layer of snow over soil. The effects of variations of snow depth, physical temperatures,

snow density, snow moisture, and base material are being considered. Calculations are in progress for sensor wavelengths of 0.3 cm, 0.8 cm, 2.2 cm, 6 cm, and 21 cm. These correspond to the sensors to be used in the field during the 1969-1970 snow season.

FUTURE PLANS

The study will continue during the forthcoming year. Field investigations will be performed with a much improved field laboratory, Figure 6, and additional observational wavelengths will be employed. A 6 cm radiometer is now in operation and an 0.3 cm instrument will be incorporated into the program about April 1970. Laboratory studies are expected to provide additional information on the dielectric properties of snowpacks. These data will be useful for refining prediction models.

The integrated study is expected to provide a better understanding of the physics of snowpack emission and to provide a sound basis for configuring aircraft experiments.

ANALYSIS OF MOUNT RAINIER IMAGERY

The investigators are also analyzing 1.55 cm imagery of Mount Rainier, Figure 7, where effects of terrain slopes parallel and perpendicular to the flight line are encountered.³ These data correspond to a variety of snow and ice conditions, Figure 8, but must be corrected for terrain slope before quantitative analysis can proceed. Figure 9 shows the associated geometry. The direction of flight is x (assumed to be horizontal), the nadir to the aircraft is z , and y is perpendicular to x and z . The microwave antenna scans over a broad cone of constant half angle θ , at certain specific scan angles β . The location (in x, y space) of each resolution element R_i on the ground is determined by the angles θ and β_i and by the local elevation h_i above a horizontal datum plane (such as sea level). Each resolution element represents a piece of terrain sloping at angles ψ_i and ξ_i in relation to the directions parallel and perpendicular to antenna polarization.

The heavy line on this drawing indicates one scan path over the terrain; the dashed line shows the scan path (a hyperbola) on a datum plane. This correction is necessary before meaningful comparisons can be made with known freezing levels and snow and ice types.

RECENT INFRARED RESULTS, SOUTH CASCADE GLACIER

Investigations of the possible utility of infrared imagery for measuring spatial variations of the heat balance on snow and ice surfaces are continuing. Although vital to many glacier-climatologic and mass-balance studies, the heat balance of a whole glacier has never been really measured. The heat balance has only been measured at selected points and can vary drastically from place to place.

3. 1968 Convair 990 Mission 8.

A key term in the heat balance is the long wave back radiation from the surface. Long wave radiation could be calculated if the surface temperature distribution of the glacier were known. The temperature distribution of the glacier could be obtained if a calibrated infrared image, in which gray scale could be related to temperature, could be obtained. However, no calibrated scanners have been flown over the test site. Attempts to make temperature inferences based on correlations of the scanner imagery, the radiometric measurements made with the airborne IR radiometer, the radiometric measurements made in the field at selected locations at the glacier and lake, and the contact temperature measurements made on the surface of the snow and ice have not been productive. However, some interesting qualitative results have been obtained, showing snow cooling first in irregular shallow valleys and flat areas (NASA NP3V Mission 78). Also, patterns of temperature change on the lake surface are clearly seen.

Table I
SNOW MOISTURE DATA

Technique Date	Freezing		Calorimeters				Centrifuge				Capacitive	
			Sakamoto		Combination (Yosida)		Loose		35 cc		Ambach	
	Avg.	Range	Avg.	Range	Avg.	Range	Avg.	Range	Avg.	Range	Avg.	Range
7 Aug. 1969	11.2	7.0-14.8	15.4	12.1-28.2	28.7	23.3-37.8	9.3	7.9-10.9	7.5	6.4-8.7	9.2	7.1-14.0
8 Aug. 1969	6.1	2.7- 8.7	9.3	3.7-28.0	15.7	7.3-22.7	2.3	1.4- 4.7	-	-	0.6	0.0- 1.5



Figure 43-1.-Microwave field laboratory.

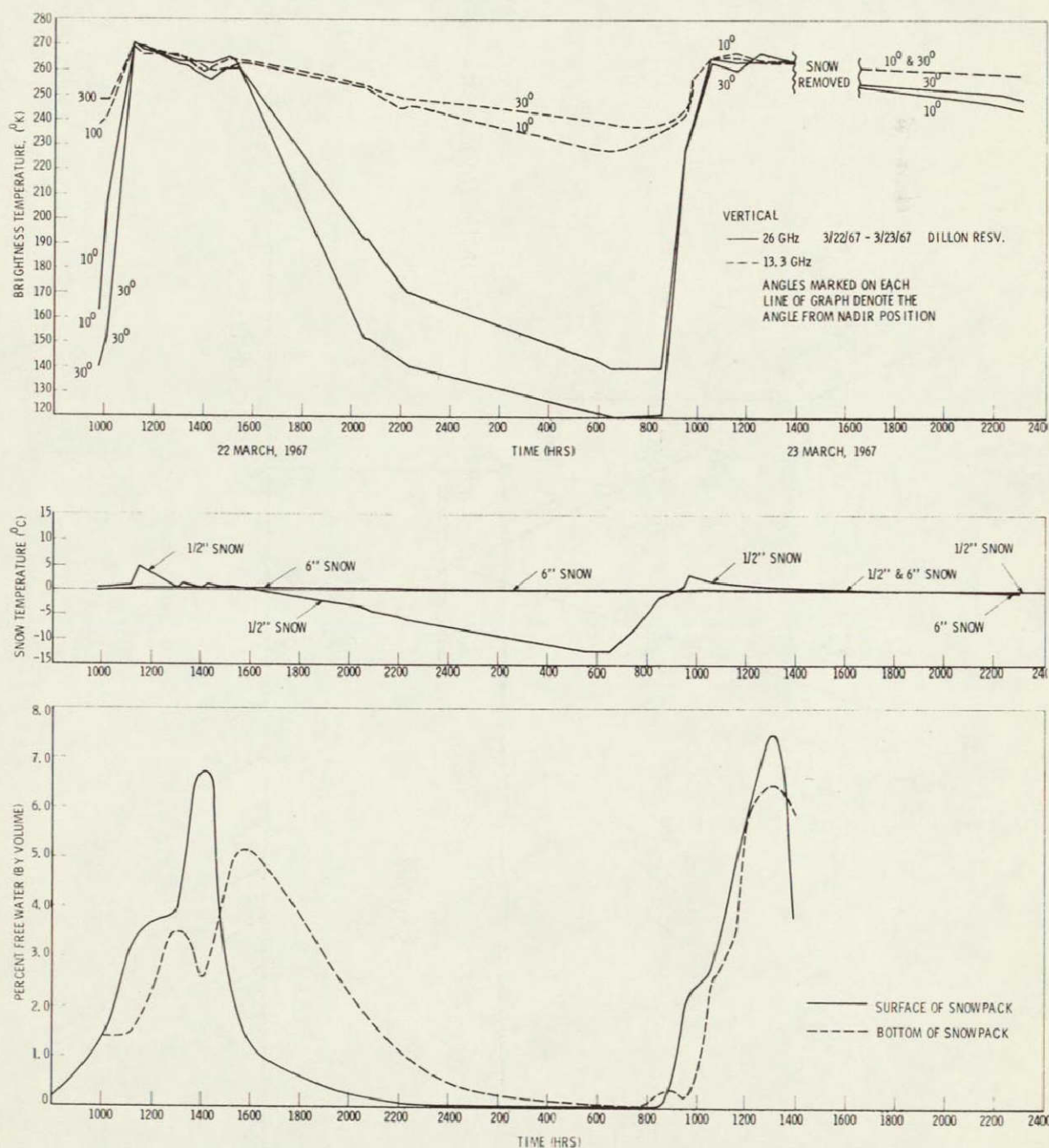


Figure 43-2.- Brightness temperature variations as a function of thermometric temperature and snow moisture.

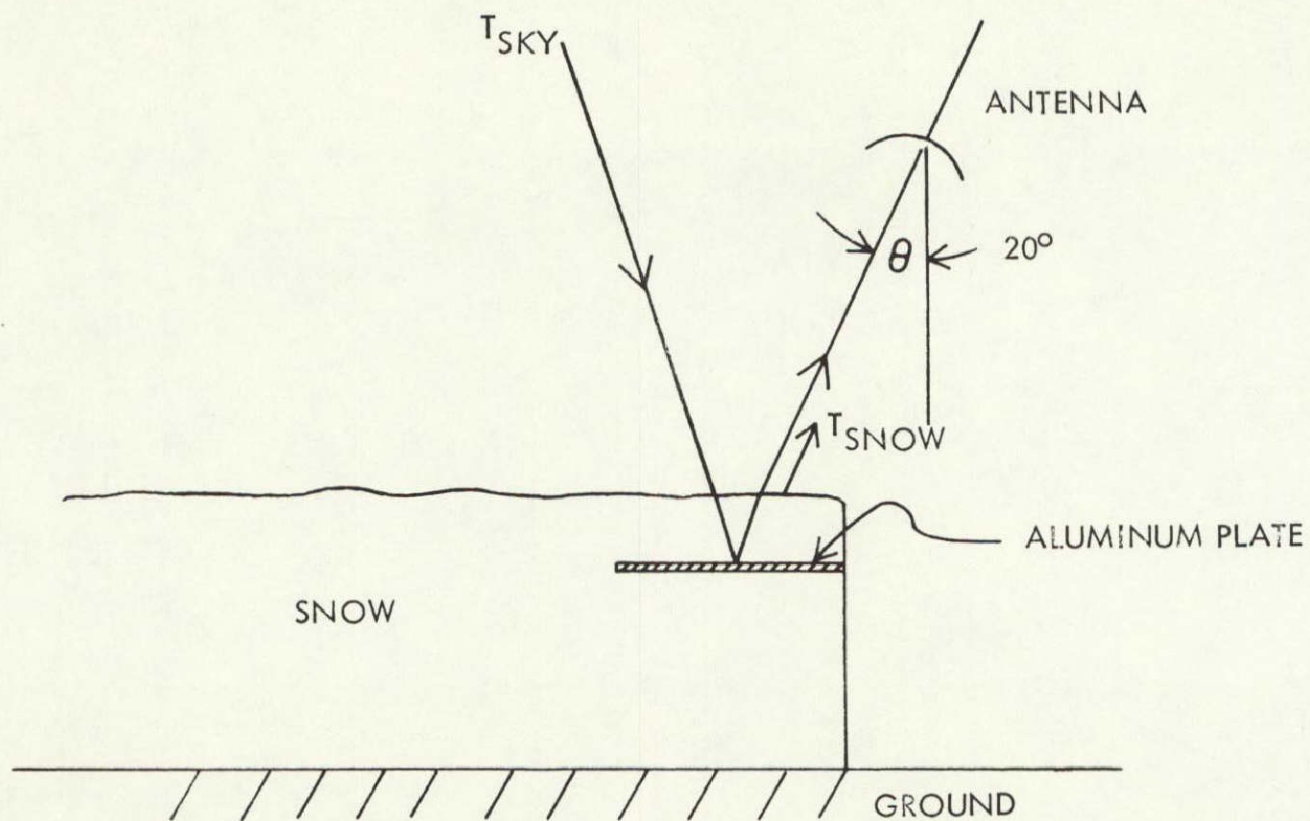


Figure 43-3.- Penetration experiment.

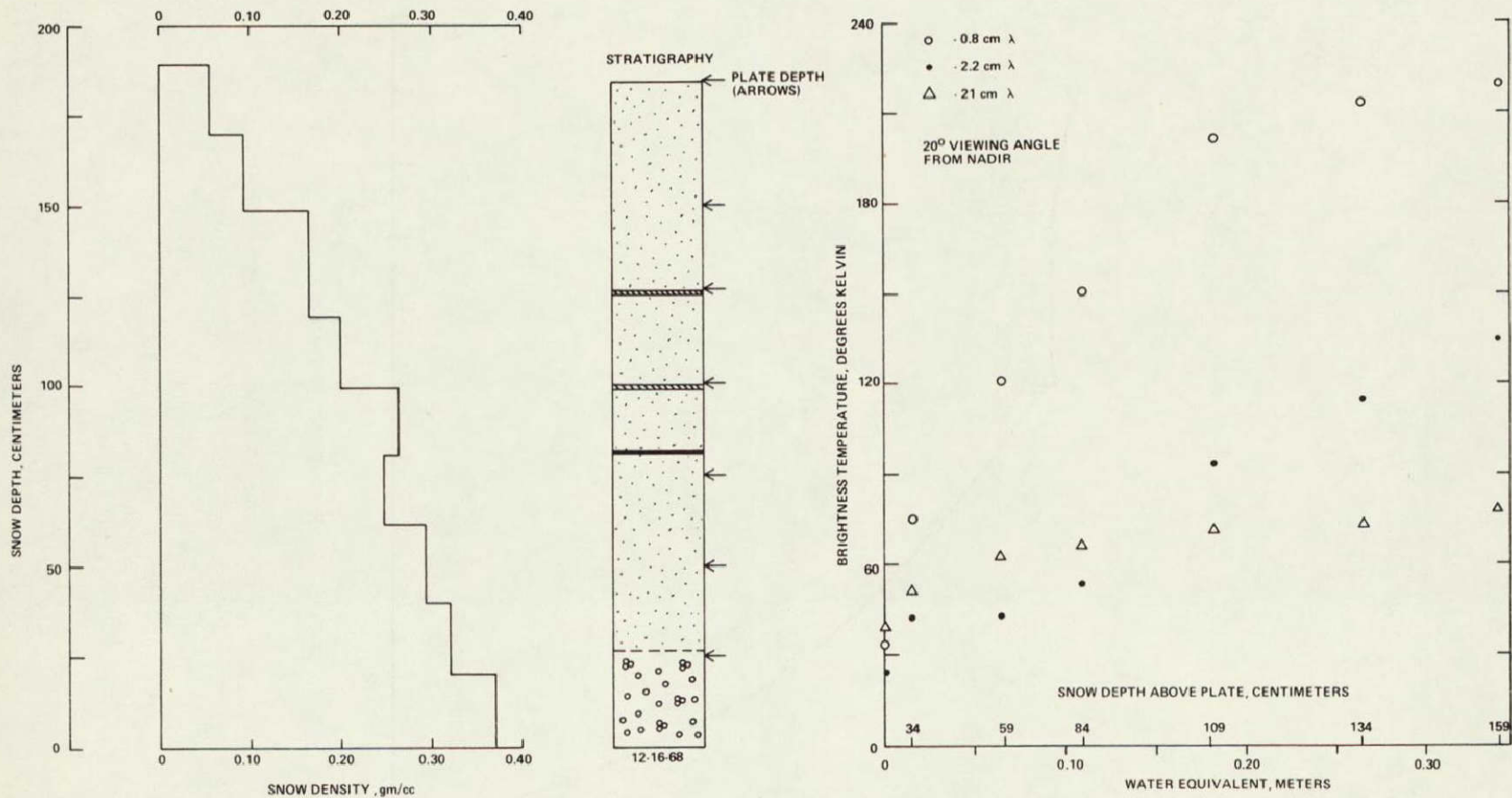


Figure 43-4.- Plate experiment to determine microwave penetration.

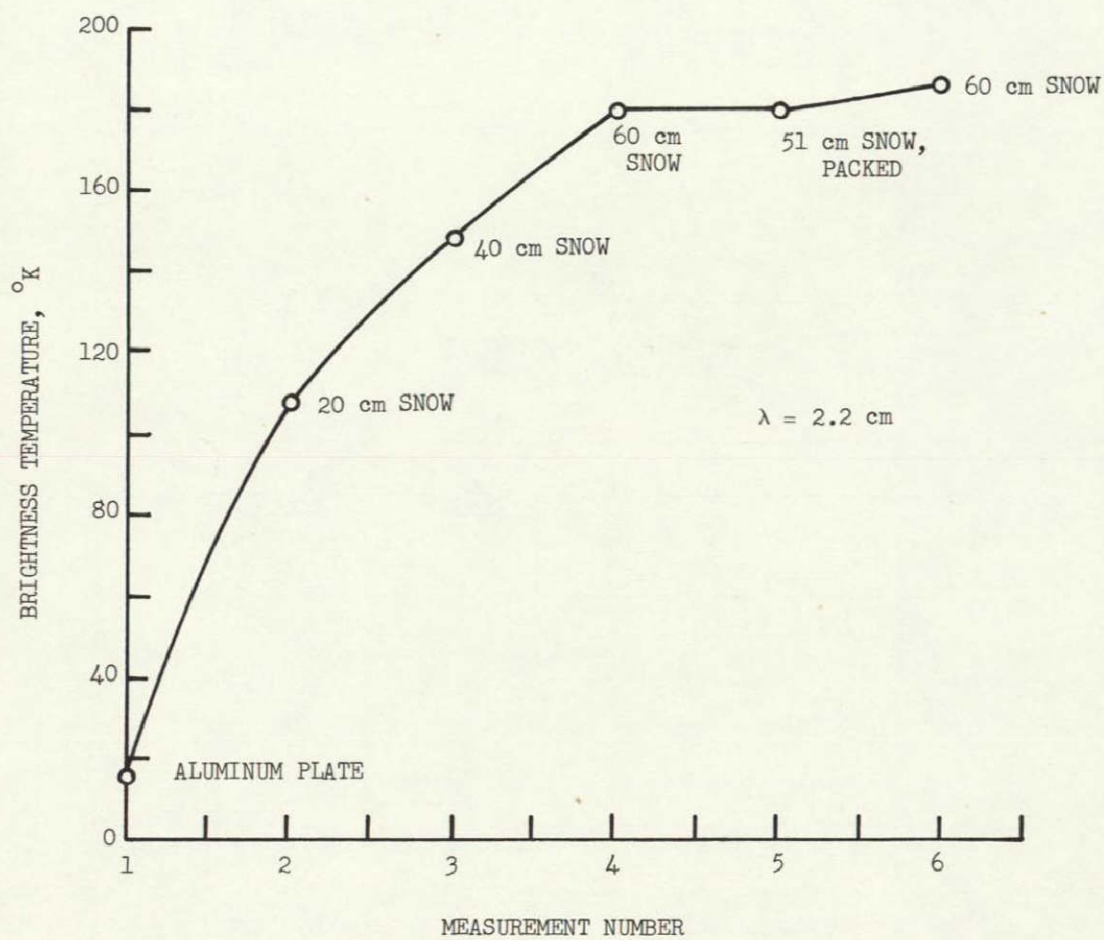


Figure 43-5.- Snow attenuation experiment.



Figure 43-6.- New microwave field laboratory.

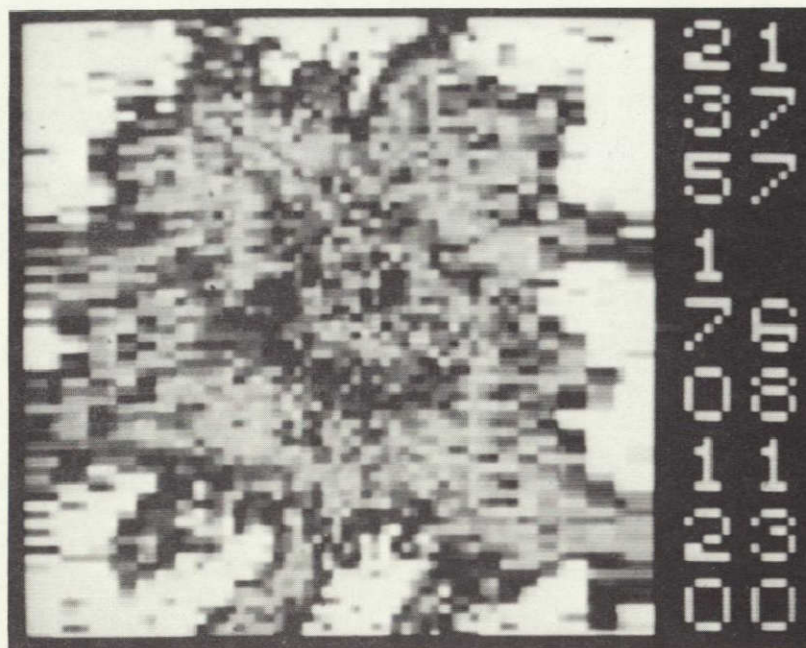


Figure 43-7.- 19.35 GHz microwave imagery of Mt. Rainier (white 281° K, 1-2° K per color step).

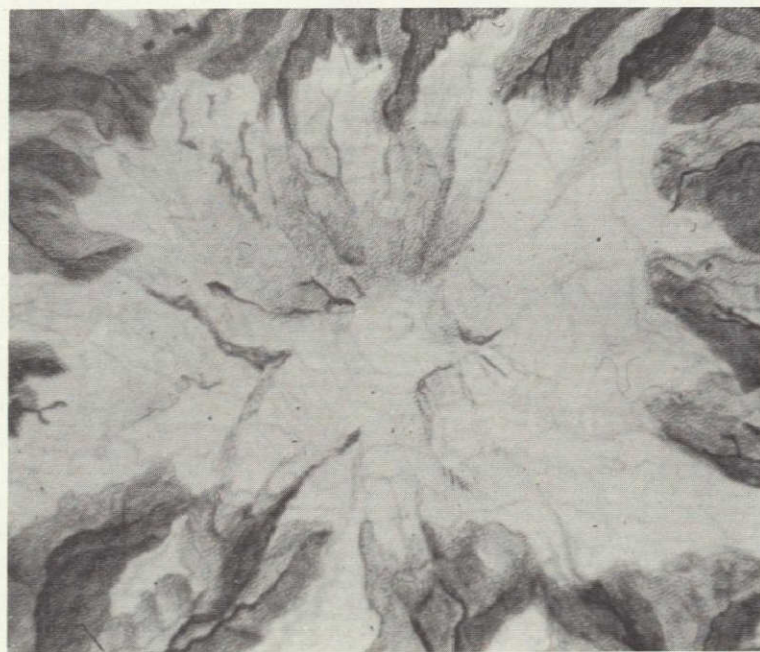


Figure 43-8.- Shaded relief sketch of Mt. Rainier.

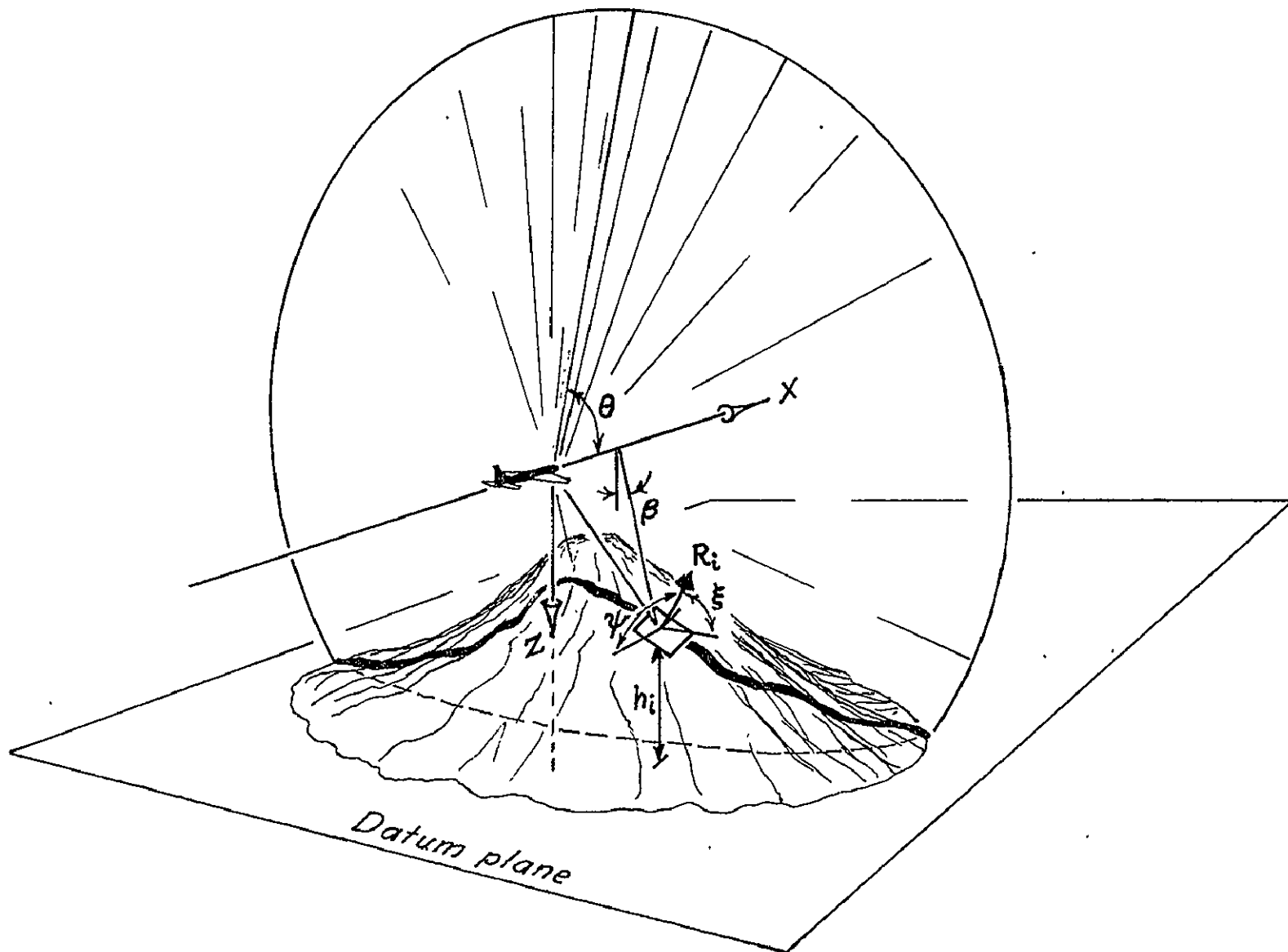


Figure 43-9.- Geometry of data obtained by a microwave imager flown over rugged terrain.

Hydrology

UNITED STATES
DEPARTMENT OF THE INTERIOR
GEOLOGICAL SURVEY

SECTION 44
USE OF INFRARED RADIOMETRY
IN MEASURING GROUND-WATER INFLOW TO STREAMS,
DELMARVA PENINSULA, MARYLAND AND DELAWARE

by

Este F. Hollyday ^{1/}
September 1969

Prepared by the Geological Survey
for the National Aeronautics and
Space Administration (NASA)

^{1/}Hydrologist, U.S. Geological Survey, Towsno, Maryland

PRECEDING PAGE BLANK NOT FILMED

44-3

SECTION 44

N71-11161

USE OF INFRARED RADIOMETRY
IN MEASURING GROUND-WATER INFLOW TO STREAMS,
DELMARVA PENINSULA, MARYLAND AND DELAWARE

by

Este F. Hollyday

ABSTRACT

A convective heat budget is used to calculate ground-water inflow to small alluvial streams. Stream temperatures are measured radiometrically from aircraft flying along a stream; upstream discharge and ground-water inflow temperature are measured by a ground team. Ground-water inflow and downstream discharge may be calculated for any desired subreach within the reach flown. Time required for data collection may be greatly reduced as compared with time required to make a seepage run. Ground-water inflow to a reach of Beaverdam Creek near Milton, Delaware, is calculated to be 5.7 cubic feet per second, which agrees within 11 percent with the inflow determined by standard stream-gaging techniques. Downstream discharge is calculated to be 9.1 cubic feet per second, which agrees within 7.5 percent.

INTRODUCTION

Knowledge of the quantity and location of ground-water inflow to streams aids in the design and testing of hydrologic models which are being used increasingly to plan the optimum development and management of the water supplies of the nation. The standard technique for determining the quantity and location of ground-water inflow to streams is a seepage run which involves on-the-ground measurement of stream discharge at a series of discrete stream cross sections. A seepage run is time consuming and is restricted spatially to those stream cross sections that are suitable for measurement.

The purpose of this paper is to present an application of remote sensing to hydrology that involves the use of 8 to 14 micron radiometry in measuring stream temperature and the use of stream temperature as a tracer for locating and quantifying ground-water inflow to streams. This preliminary investigation indicates that under suitable sensing conditions remote sensing can greatly reduce the time for data collection and can provide spatially continuous data without significant loss of precision compared with a seepage run.

The investigation was financed by the National Aeronautics and Space Administration. During the winter of 1968-1969, a helicopter and remote sensing equipment were provided by NASA, Wallops Island, Virginia. Technical support was provided by Mr. J. D. Pennewell of the Philco-Ford contractual remote sensing team stationed at Wallops Island.

HYDROLOGIC CONCEPTS

The test site (NASA Site 124) is in the middle of the Delmarva Peninsula and is entirely within the Atlantic Coastal Plain physiographic province. The site is mantled with about 100 feet of water-saturated sand and gravel. This shallow ground-water reservoir acts not only as a reservoir for water but also as a reservoir for heat. The shallow reservoir takes in precipitation, stores it, and slowly discharges it to streams, thereby maintaining streamflow during dry periods of the year. In addition, the shallow reservoir takes in solar heat, stores it, and slowly returns it to streams and the atmosphere.

Because many years are required for a drop of ground water to move from a watershed divide to a stream, seasonal fluctuations in temperature are dampened, and ground-water temperatures approach the mean annual air temperature for the site of about 14 degrees Celsius ($^{\circ}\text{C}$). In contrast, during mid-winter, stream temperatures commonly range between 4° and 7°C . Under these conditions ground-water inflow at a much higher temperature can be readily recognized with suitable instruments.

HEAT BUDGET

A simplified heat-budget model was developed in order to quantify ground-water inflow based upon the conjunctive flow of heat and water to streams from the shallow ground-water reservoir. Figure 1 is a block diagram of a stream reach showing heat flow and two equations defining the flow. Equation (1) simply states that the sum of the heat load entering a stream reach and the heat load from ground-water inflow equals the heat load leaving the stream reach. Heat load in equation (1) is expressed as the product of water discharge in cubic feet per second (cfs) and water temperature in degrees Celsius. Equation (2) states that the sum of water discharge entering the stream reach and ground-water inflow equals the water discharge leaving the stream reach.

The model assumes that there is no net heat exchange between the stream and the atmosphere resulting from an imbalance in solar and atmospheric radiation heat gains and back radiation and evaporation heat losses. This assumption can be satisfied approximately by careful selection of optimum weather conditions for data collection. Experience has shown that optimum daytime weather conditions are a complete high-altitude overcast combined with high relative humidity, no wind, and no precipitation in solid form during a period of very low air temperature. The model also assumes that there are no significant surface-water tributary inflows to the stream reach that can not be accounted for..

GROUND-CONTROL SURVEYS

A 1600-foot reach of Little Burnt Branch, Wicomico County, Maryland, was selected for testing and heat-budget model. This reach is instrumented with several shallow observation wells on the bank of the stream providing a means of measuring profiles of ground-water-inflow temperature. In addition, the reach is instrumented with three temporary U.S. Geological Survey stream gages providing a continuous record of stream discharge.

Figure 2 shows the results of a ground-control survey of this reach. The survey revealed that a 1.5°C rise in stream temperature in the downstream direction corresponded with a 60 percent increase in stream discharge between the middle and upstream gages. All water temperatures were measured with a Yellow Springs Instrument Company Tele-thermometer and thermistor calibrated to an accuracy of 0.1°C. Stream discharges were calculated from the stream-gaging station records by standard techniques to an accuracy of about 5 percent.

Figure 3 shows an example of the application of the heat-budget equations to a complete set of data (including ground-water-inflow temperature) collected in a subsequent ground-control survey. Ground-water inflow is calculated to be 0.7 cfs. Downstream discharge is calculated to be 2.1 cfs, which agrees within 3 percent with the downstream determined by standard stream-gaging techniques.

APPLICATION OF REMOTE SENSING

The ground-control surveys proved the feasibility of using the heat-budget model for measuring ground-water inflow, and the next phase of the investigation was to use the model for testing the accuracy of remotely sensed stream temperature in measuring ground-water inflow.

Uncalibrated infrared imagery was collected by NASA-Houston aircraft. The imagery provided a two-dimensional record of relative radiometric temperature of streams and surrounding terrain. The imagery proved useful in locating stream reaches that appeared to have anomalous temperatures (ref. 1). These stream reaches were selected for detailed survey and quantification of ground-water inflow.

Equipment and Calibration

Calibrated fixed-field infrared radiometry was used in the detailed surveys. The output from a Barnes Engineering Company PRT-5 Precision Radiation Thermometer was recorded on a Westronics D11E potentiometric strip-chart recorder. The signal from the radiation thermometer was fed to the recorder through a potentiometric voltage offset control that permitted use of the most sensitive span on the recorder. Recorder readings were calibrated in the laboratory by sighting the radiometer on a water surface. During laboratory calibration the water temperature was varied through a range equal to the range in stream temperatures to be sensed in the field.

In order to collect stream-temperature data from aircraft that is acceptably accurate for use in the heat-budget model, field calibration of the equipment is necessary in addition to laboratory calibration. McAlister and McLeish (ref. 2) have reported that a radiometer measures the temperature of a water body within the top millimeter of the water surface. During the usual conditions of heat flow of the top millimeter of the water body back to the atmosphere, a large temperature gradient occurs in this zone. As a result the temperatures measured by the radiometer are considerably cooler than the bulk water temperature that would be measured by a thermistor in a bucket sample. This "cold-skin" phenomenon has been documented by Campbell (ref. 3).

Figure 4 shows a correlation of radiometric temperatures of the Potomac River measured by radiometer from low-altitude helicopter with true water-body temperatures measured by thermistor at 1-foot depth from a boat. The river lacks thermal stratification, and temperatures measured at 1-foot depth agree with temperatures measured from near-surface to bottom within 0.2°C . The correlation shown in figure 4 was used to convert radiometric temperatures measured in subsequent surveys to true water-body temperatures using the ambient temperatures of the river and streams as a common reference datum.

Results of Remote and Ground Survey

Figure 5 shows a radiometric temperature trace as recorded from helicopter over a small narrow stream on the Delmarva Peninsula. Radiometric temperatures were picked from this trace at points of open water where the aerial view of the stream was not obstructed by tree limbs. The radiometric temperatures were corrected approximately to true water-body temperature, T_1 and T_3 , using the correlation in Figure 4 and assuming ambient temperatures as a common reference datum.

The heat-budget equations were applied to the corrected temperatures, T_1 and T_3 , to a ground-water-inflow temperature measured in a well by the ground team, T_2 , and to an upstream discharge also measured by the ground team, Q_1 . The ground-water inflow, Q_2 , was calculated to be 5.7 cfs, which is 11 percent less than the inflow determined by standard stream-gaging techniques. The downstream discharge, Q_3 , was calculated to be 9.1 cfs, which is 7.5 percent less than the downstream discharge determined by standard stream-gaging techniques.

Based upon the relatively small error obtained in this preliminary remote and ground survey, it is concluded that the remote sensing technique of measuring ground-water inflow warrants further investigation and refinement.

SIGNIFICANCE OF RESULTS

Knowledge of the quantity and location of ground-water inflow to streams aids in planning the optimum development and management of the water supplies of the nation.

A seepage run, the standard technique for measuring ground-water inflow, involves on-the-ground measurement of stream discharge along a single stream at a series of discrete stream cross sections that are

restricted spatially to sites suitable for measurement. Adjacent measurements in the series are then subtracted to determine the increase in stream discharge resulting from ground-water inflow between the two measuring points. In addition to the time required to gain access to the stream in areas lacking frequent road crossings and the time required to select a suitable measuring site, about .30 minutes to 1 hour is required to make each discharge measurement.

In the remote sensing technique, spatially continuous stream-temperature data may be recorded from aircraft at a rate of at least 25 feet per second. Application of the heat-budget equations could reduce the time and work on the ground to measurement of a single upstream discharge, a ground-water-inflow temperature, and several stream temperatures for field calibration of the radiometer. In addition the continuous temperature trace would allow calculation of ground-water inflow for an infinite number of incremental stream subreaches within the reach that was recorded. In contrast the seepage run allows calculation of inflow only between measuring sites in the series of discrete stream cross sections.

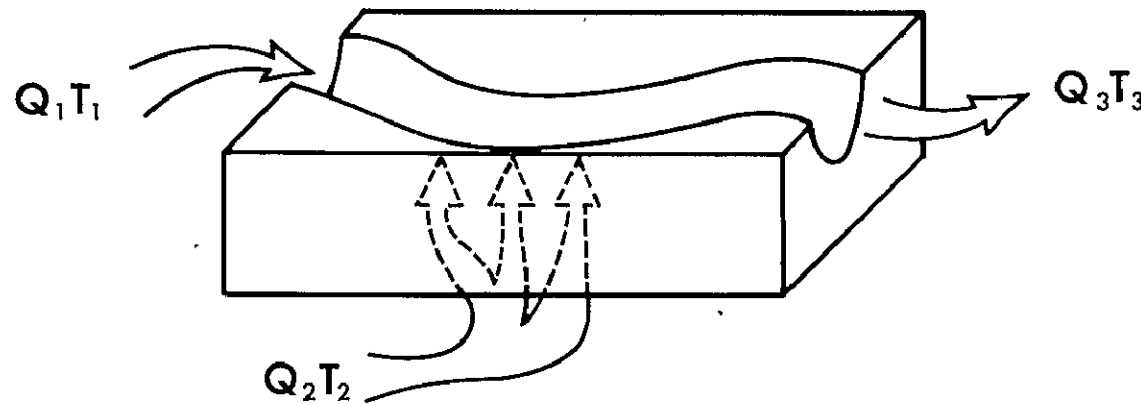
SUPPLEMENTAL INVESTIGATION REQUIREMENTS

To date the remote sensing technique of measuring ground-water inflow has been applied only during optimum weather conditions to small streams flowing over sand and gravel and having large ground-water inflows in relation to upstream discharge. Further investigation is needed to test the technique on streams with small ground-water inflows and in a variety of hydrogeologic terrains. Further investigation is also needed to determine the degree of refinement that may be introduced by taking into account heat exchanges between the stream and the atmosphere as part of the heat-budget model.

REFERENCES CITED

1. Hollyday, E. F.: Use of Infrared Imagery to Locate Surficial Aquifers, Delmarva Peninsula, Maryland and Delaware. NASA Earth Resources Aircraft Program Status Review, v. III, 1968, pp. 25-1 to 25-14.
2. McAlister, E. D., and McLeish, W.: Heat Transfer in the Top Millimeter of the Ocean. Journal of Geophysical Research, v. 74, no. 13, 1969, pp. 3408-3414.
3. Campbell, W. J.: Synoptic Temperature Measurements of a Glacier Lake and its Environment. NASA Tech. Letter 107, 1968.

HEAT BUDGET FOR DETERMINING GROUND-WATER INFLOW



$$Q_1T_1 + Q_2T_2 = Q_3T_3 \quad (1)$$

$$Q_1 + Q_2 = Q_3 \quad (2)$$

Where Q_1T_1 = Product of discharge and
temperature entering stream reach

Q_2T_2 = Product of ground-water inflow and
temperature to stream reach

Q_3T_3 = Product of discharge and
temperature leaving stream reach

Figure 1.- Heat budget for determining ground-water inflow.

GROUND-CONTROL SURVEY OF TEMPERATURE AND DISCHARGE,
LITTLE BURNT BRANCH, WICOMICO CO., MD., JANUARY 17, 1969

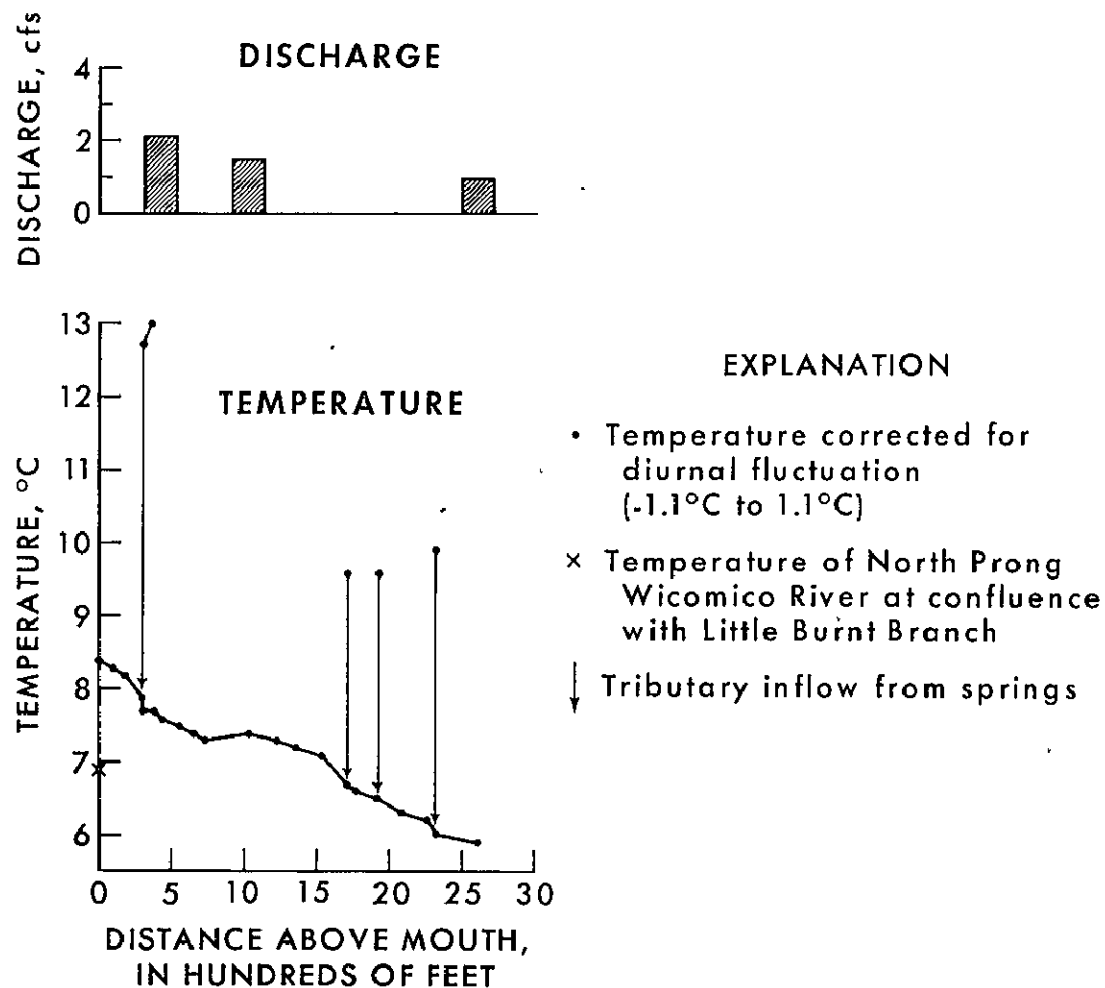
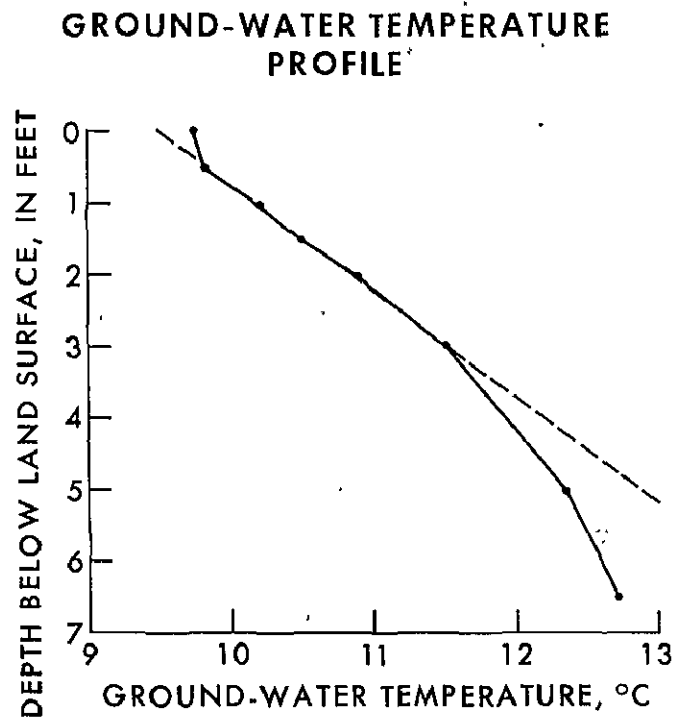


Figure 2.- Ground-control survey of temperature and discharge, Little Burnt Branch
Wicomico Co., Md., January 17, 1969.

GROUND CONTROL DATA



HEAT BUDGET CALCULATION OF GROUND-WATER INFLOW

Given:

$$Q_1 T_1 + Q_2 T_2 = Q_3 T_3 \quad (1)$$

$$Q_1 + Q_2 = Q_3 \quad (2)$$

T_1 , upstream temperature = 6.5°C

T_2 , ground-water inflow temperature = 9.5°C

T_3 , downstream temperature = 7.5°C

Q_1 , upstream discharge = 1.4 cfs

To determine:

Q_2 , ground-water inflow

Q_3 , downstream discharge

Calculations:

$$1.4(6.5) + Q_2(9.5) = (1.4 + Q_2)7.5$$

$$9.1 + 9.5Q_2 = 10.5 + 7.5Q_2$$

$$2.0Q_2 = 1.4$$

$$Q_2 = 0.7 \text{ cfs}$$

$$Q_3 = Q_1 + Q_2 = 2.1 \text{ cfs}$$

Check:

Q_3 , downstream discharge = 2.11 cfs,
determined by standard
stream-gaging techniques

Figure 3.- Ground control data.

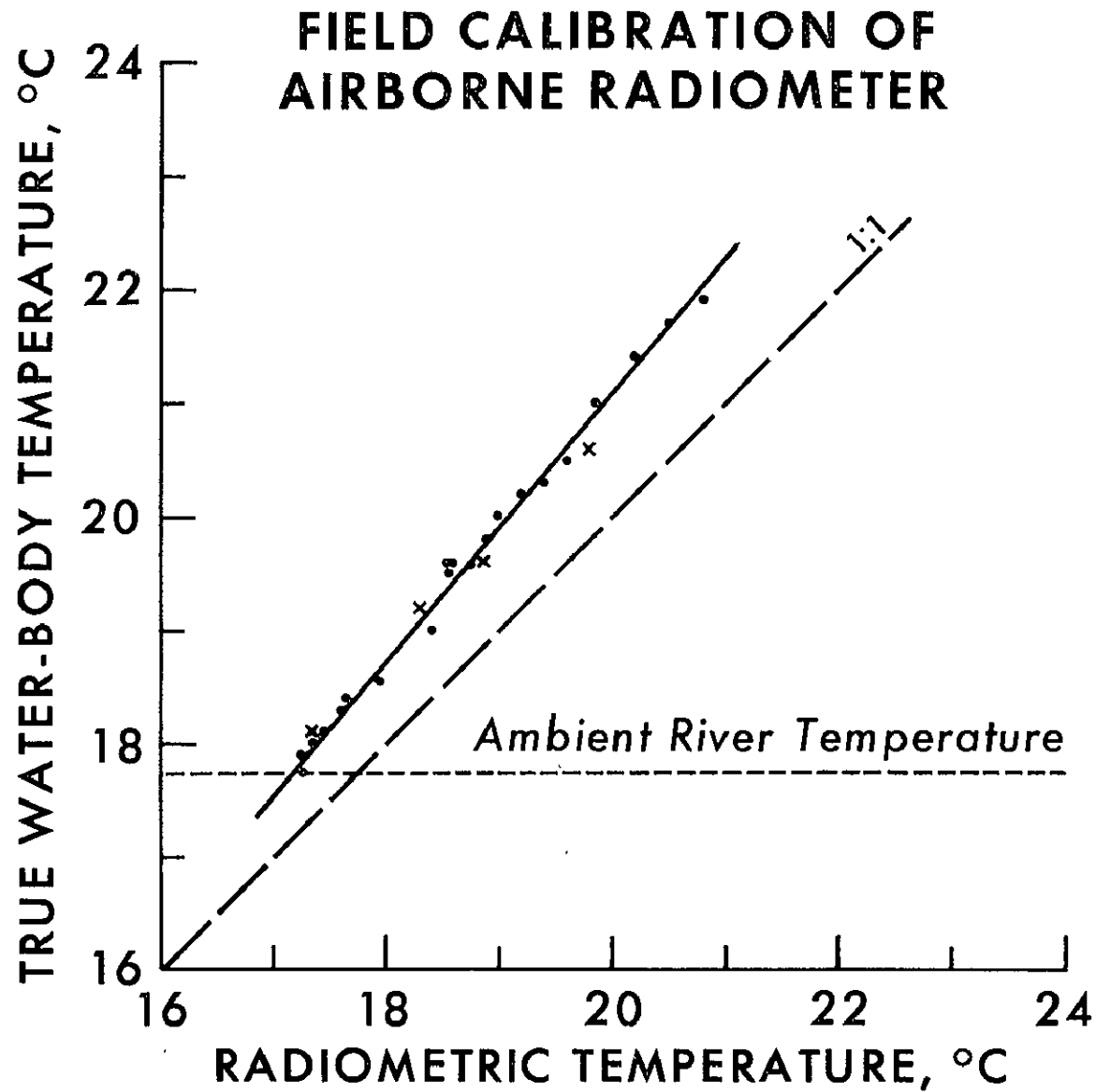


Figure 4.- Field calibration of airborne radiometer.

AIR AND GROUND SURVEY OF BEAVERDAM CREEK NEAR MILTON, DELAWARE

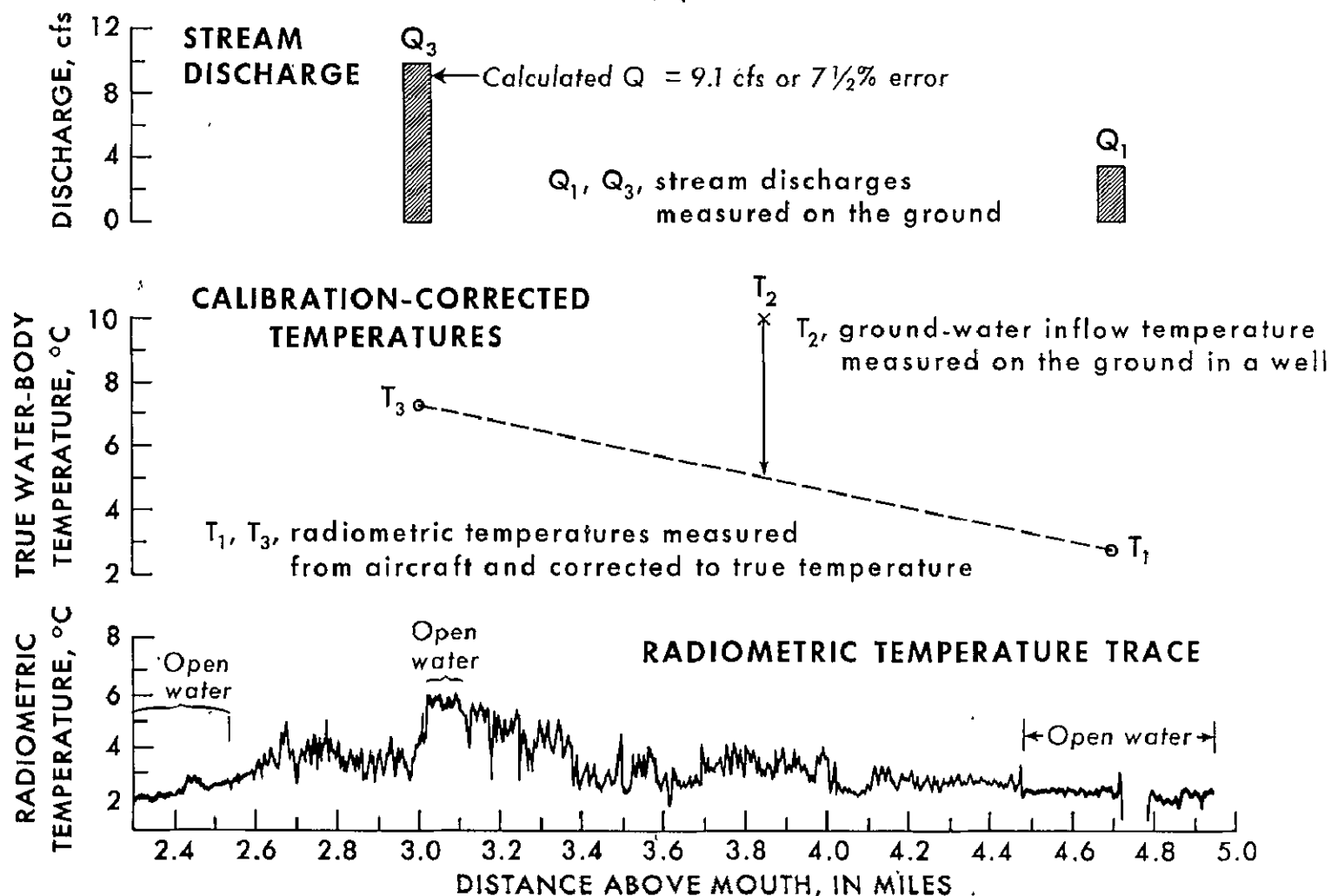


Figure 5.- Air and ground survey of Beaverdam Creek near Milton, Delaware.

SECTION 45

UNITED STATES DEPARTMENT OF THE INTERIOR
GEOLOGICAL SURVEY

Preliminary report on remote sensing in water-resources studies in
Yellowstone National Park, Wyoming

by

Edward R. Cox

Prepared in cooperation with the
National Aeronautics and Space Administration

October 1969

PRECEDING PAGE BLANK NOT FILMED

N71-11162

Preliminary report on remote sensing in water-resources studies
in Yellowstone National Park, Wyoming

by Edward R. Cox

Abstract

Data obtained from remote sensing should be useful in locating bodies of cool ground water near thermal-water areas in Yellowstone National Park. Remote-sensing data, particularly infrared imagery, from aircraft missions in August 1966 and September 1967 are being studied, and methods of interpretation are being developed to correlate remote-sensing and ground-truth data. Test areas are being established where hydrologic ground-truth data can be obtained to correlate with imagery.

Areas that show promise for correlation of imagery and ground-truth data are near Old Faithful, Fountain Paint Pot, Shoshone Lake, Norris Junction, and West Thumb. Patches of snow observed in April 1969 near Old Faithful and Fountain Paint Pot correlated exactly with relatively cool areas interpreted from infrared imagery. A snow line across Nez Perce Creek valley near Fountain Paint Pot correlates with a boundary between cool and warm ground water that was determined from augered test holes. In June 1969, traverses were made with a portable radiation thermometer, and temperature measurements were made in the upper 6 inches of the soil zone with a thermistor-type thermometer. These traverses show the boundary between cool and warm ground water in Nez Perce Creek valley.

Additional remote-sensing data, particularly low-altitude infrared imagery and infrared photography, are needed in areas where hydrologic ground-truth data are available.

PRECEDING PAGE BLANK NOT FILMED

Preliminary report on remote sensing in water-resources studies in
Yellowstone National Park, Wyoming

by Edward R. Cox

Introduction

The U.S. Geological Survey is making a water-resources study, begun in September 1966, in Yellowstone National Park for the U.S. National Park Service. This study involves a search for water supplies, preferably ground water, near thermal-water areas. The search for potable ground water, therefore, must delineate the boundary between the thermal and the cold-water areas. The presence of thermal ground water often is obvious by noting the occurrence of hot springs, geysers, and other surface features. At places, however, thermal ground water is discovered only from information obtained by test-hole construction. The use of remote-sensing techniques, particularly infrared imagery, should be a valuable tool in a reconnaissance of ground-water conditions near thermal areas, and it could, in places, eliminate the need for or reduce the number of test holes to be constructed.

The main purpose of the investigation described in this report is to evaluate the usefulness of remote-sensing data in hydrologic studies in Yellowstone National Park. Remote-sensing data, including infrared imagery, have been collected in Yellowstone National Park for use in this and other remote-sensing studies.

In order for remote-sensing data to be useful in the hydrologic study in Yellowstone, the effects of warm ground water must be expressed at the land surface and be detectable by remote sensors. These conditions are most likely to exist when warm or hot ground water occurs at very shallow depths. In parts of the Park, ground water occurs at very shallow depths, often less than 10 feet and occasionally less than 5 feet below land surface. The effects of warm shallow ground water on land-surface temperatures may be noticeable in infrared imagery. The thickness of the material through which the temperature of ground water can affect the land surface temperature may be related to the type of material overlying the ground water body as well as the temperature of the ground water. These factors will be considered during the study.

The temperature of shallow ground water may affect the type and vigor of vegetation. Dead trees near thermal-water areas are common in the Park. The temperature effects of ground water on vegetation may be discernible by remote-sensing data, particularly infrared color photography.

Remote-sensing data, particularly infrared imagery, are being examined in detail in areas where hydrologic data are available from test holes to find key indicators that aid in correlating imagery and field data. Also, in areas where remote-sensing data are available, additional test holes will be made to collect additional ground-truth information. Areas in the Park where hydrologic field data have been or will be collected and where remote-sensing data are available from aircraft flights are being selected for intensive study.

Procedure

Black, white, and shades of gray on the infrared imagery indicate relative temperatures of land-surface features. An examination of infrared imagery from Yellowstone National Park shows clearly the areas of thermal-water discharge and nearby relatively hot terrain. Ground water is undoubtedly hot under areas appearing on the imagery as hot land surface. An interpretation of cool terrain, however, does not rule out underlying warm ground water because warm ground water may or may not warm the land surface.

Slight differences in shading on the imagery may represent differences in temperature of ground water. Correlation of shading of imagery and temperatures of ground water can be done only after much data have been collected on ground-water temperatures in areas covered by imagery.

Remote-sensing data that have been most useful to date for this project are 3-5 micron thermal infrared imagery from an August 1966 mission by HRB-Singer, Inc. and multi-channel scanner imagery from a September 1967 mission by the University of Michigan. The August 1966 mission covered a larger area of the Park than the September 1967 mission, but the September 1967 mission was flown at a lower altitude and shows more detail. Both missions were flown for the Geological Survey as part of extensive studies on geology, geophysics, and thermal waters in the Park in cooperation with NASA (National Aeronautics and Space Administration). Recently, two missions have been flown in Yellowstone by NASA aircraft but data are not yet available. One mission was flown at high altitude (60,000 feet) and the other was flown in late August 1969 specifically for this project at low altitude (13,000 feet).

Brief studies were made in April 1969 near Fountain Paint Pot and Old Faithful to observe the effects of relatively warm and cool land areas on snow-pack conditions. These were ground-truth observations to be correlated with the imagery.

In June 1969, ground-temperature surveys were made at Fountain Flats and Nez Perce Creek valley near Fountain Paint Pot, near Norris Junction, and near West Thumb (fig. 1). The temperature data will be correlated with imagery from the August 1966 and September 1967 missions, depending on coverage and detail of imagery, and with imagery from recent aircraft flights. Ground-temperature data were also collected in August 1969.

Most of the ground-temperature data were collected from a 3-mile reach of Nez Perce Creek valley where warm and cool ground water are known from augered test holes. A Barnes Engineering Company PRT-5 portable radiometer (8-14 micron) was used to monitor point radiation along cross-section lines in the valley. In addition, temperatures were measured by inserting the probe of a portable thermistor-type thermometer into the upper six inches of soil.

Ground-truth information to correlate imagery and field data also is being collected from test holes. Most of the test holes to date have been made for the water-resources study of the Park and not for the remote-sensing evaluation study. Most of the holes were made by a truck-mounted power auger and a portable power auger. Test-hole construction in much of Yellowstone, however, can be done only by a hand-operated auger because of the inaccessibility of most parts of the Park to motorized equipment.

Unfortunately, the area covered by the low-altitude September 1967 mission does not coincide with many areas where test holes have been augered (fig. 1) for the general water-resources study in the Park. Test holes will be augered in some areas covered by the September 1967 mission. Although a much larger percentage of the Park is covered by the high-altitude August 1966 mission, some test-hole areas were not covered in the mission.

Results

Test holes augered prior to August 1969 for the water-resources study of the Park are outside of the areas covered by the September 1967 low-altitude mission except for test holes near Canyon Village, Mammoth, and Mud Volcano. Neither warm water nor warm ground was penetrated in the test holes at the first two sites mentioned. The effects of warm water at a depth of 72 feet, overlain by cool water, in a hole augered near Mud Volcano, as expected, do not show on infrared imagery collected during the September 1967 mission. The August 1966 high-altitude mission covered some areas where test holes have been augered, but the imagery does not show sufficient detail to correlate well with the data from the holes.

Areas covered by imagery and underlain by both cool and warm ground water that show promise for correlation of imagery and ground-truth data are near Old Faithful, Fountain Paint Pot, Shoshone Lake, Norris Junction, and West Thumb. Most promising of these areas is Nez Perce Creek valley about 2 miles north of Fountain Paint Pot.

Patches of snow as much as 2 feet deep were observed in places as near as 50 feet to hot springs in geyser basins near Fountain Paint Pot and Old Faithful during field studies of snow-pack conditions in April 1969. These patches of snow correlate well with relatively cool areas interpreted from infrared imagery.

The lower 2-mile reach of Nez Perce Creek valley, an east-west trending valley about 2 miles north of Fountain Paint Pot, was completely free of snow during the April 1969 studies. A definite snow line across the valley separated the upper snow-covered part from the lower snow-free part. This snow line corresponds to a boundary between cool and warm ground water that was determined from augered test holes. The part of Nez Perce Creek valley that has the boundary between cool and warm ground water was not covered in the September 1967 mission; therefore, correlation with imagery will be deferred until the August 1969 imagery is available.

A snow line was also noted in the valley of the West Fork of Iron Spring Creek near Old Faithful. This snow line seemingly correlates well with a cool-warm boundary interpreted from infrared imagery from the September 1967 mission.

These brief field studies of snow-pack conditions and infrared imagery indicate the possible usefulness of similar more detailed studies. Aerial photography taken during early stages of spring snowmelt should supplement infrared imagery for this particular application.

Ground-temperature surveys in June 1969 were made, at times, under adverse weather conditions. The changeable weather in June, however, allowed the gathering of information under a variety of conditions. Frost, rain, and snow occurred during the surveys and soils in places were nearly saturated. The radiometer was greatly influenced by soil moisture and the type of ground cover (bare soil, needle insulation, or grass). Despite these background interferences, temperature trends could be determined that compare favorably with observed spring snow-pack conditions and information from augered test holes. The temperature surveys show the boundary between cool and warm ground water in Nez Perce Creek valley. Dry-soil temperature data were obtained in late August and more data will be collected this fall. When the August 1969 imagery is available, it will be studied to see if these ground observations can be correlated with the imagery.

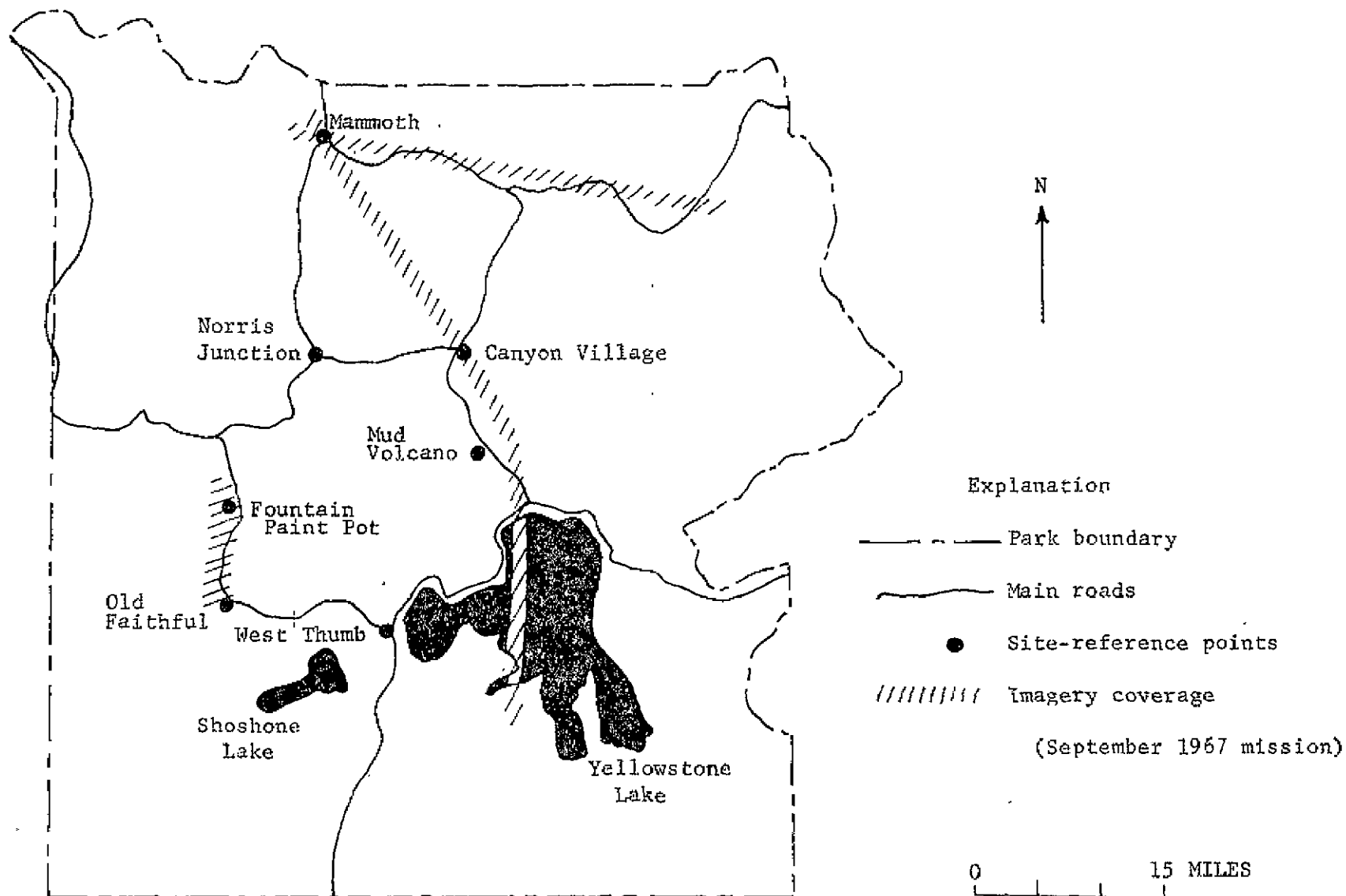


Figure 1.--Map of Yellowstone National Park, Wyo., showing locations of site-reference points and approximate coverage of infrared imagery from the September 1967 mission.

SNOWFIELD MAPPING WITH K-BAND RADAR

William P. Waite
Harold C. MacDonald

N71-11163

Center for Research in Engineering Science, Remote Sensing Laboratory
University of Kansas

ABSTRACT

Analysis of K-band imagery from several geographic areas in the United States where snowfields occur has provided evidence that the distribution of perennial snow results in an anomalously high signal return. In contrast to normal snow survey methods, it appears feasible to map the areal extent of old snow areas irrespective of most weather conditions, and even when covered with new fallen snow.

Because snowfields are an important source of stream flow in many parts of the world, this study has particular significance for the hydrologist; however, the anomalously high return signal attributable to the snowfields is extremely pertinent to instrumentation studies conducted by the radar engineer. The anomalously high return from the snowfields seems largely independent of incidence angle. This factor tends to suggest that the backscattering mechanism is something other than the common smooth multilayer model used by most previous theoretical studies. In the past, the measured differences between old and new snow have been primarily attributed to differences in the moisture content of each snow type. In this study, the observed differences in signal return between the metamorphosed snow and the surrounding terrain do not seem explainable simply by moisture content.

It is suggested that the significant increase in signal return is actually due to volume scattering. As such the structure of the metamorphosed snow plays a much more important role than just that of effecting the form factor of the dielectric mix of ice and air. This of course, means that a considerably more complex model must be assumed for the interpretation of microwave return from snowfields.

The additional complexity of the surface model does not merely increase the complexity of data interpretation; but actually adds a dimension to the measurement. The use of additional sensor frequencies and the relative penetration of each should certainly be investigated as a possible means of monitoring the volume and quality of snow and ice fields.

INTRODUCTION

The radar-geologic studies conducted at the University of Kansas are concerned with determining the value and effect of polarization, look-direction, depression angle, and frequency in the geological interpretation of radar images. This study is an outgrowth of these instrument-oriented investigations. Even though the radar imagery analyzed was not collected during the past year, the results of this study have relevance to the NASA-ERS program, particularly future mission planning and instrument acquisition.

In recent years the potential of imaging radars for ice investigations in polar environments has been well documented. In the alpine environment of the United States, radar has been cited as being capable of distinguishing glaciers from the surrounding terrain (Meier, et al., 1966); even when covered by thin snow; however, the feasibility of mapping the distribution of snowfields has not been previously investigated. Because snowfields are an important source of stream flow in many parts of the world, this study has particular significance for the hydrologist; however, the anomalously high return attributable to the snowfields is extremely pertinent to instrumentation studies conducted by the radar engineer. The primary objectives of this preliminary study were to: 1) present the results of data analysis; 2) attempt to define the parameters affecting the radar return signal from snow; and 3) evaluate the applicability of imaging radars as a practical snow survey technique.

RADAR PARAMETERS

The general operational parameters of a side-looking airborne radar system (SLAR) have been presented in another investigation also included in this Second Annual NASA Program Review (see MacDonald, Radar-Geologic Studies). Because of the interaction of the radar signal return and the physical character of the snow itself, several specific radar parameters should be examined in somewhat more detail than discussed in the above mentioned article.

Radar signals are normally returned from the terrain, to the receiver, by a scattering process (reradiation). The signal strength (or intensity of this terrain return) received at the antenna determines the relative degree of brightness of a resolution cell on the imagery. Taylor (1959) measured the backscatter from many different types of terrain (using three frequencies with vertical and horizontal polarization), and concluded that the fundamental parameters which affect terrain return are: surface roughness, incidence angle, polarization, frequency, and complex dielectric constant.

Surface roughness and dielectric properties are functions directly related to the terrain and may be collectively expressed as the scattering coefficient, (scattering cross-section per unit target area per unit solid angle in the direction of the receiver). The scattering coefficient contains a major part of the geoscience information about the illuminated terrain that the radar is capable of sensing, except for location (Rouse, et al., 1966). Frequency is a function of the transmitted signal and the frequency dependence of the electromagnetic properties of the terrain. Incidence angle depends in part on the position of the transmitter and in part on the geometry of the local terrain, while polarization is both a function of polarization of the incident signal and the depolarizing effects of the terrain (Ellermeier, et al., 1966).

Angle of Incidence

The angle of incidence, θ , is the angle formed by an impinging beam of radar energy and a perpendicular to the incident surface at the point of incidence. The angle between a line from the transmitter to a point on the terrain, and a horizontal line passing through the transmitter is the depression angle (Figure 1C). The geometric parameters of SLAR imaging systems are such that along the swath width of an area imaged (near to far range), there is a continuous change in the angle of incidence (Figure 1A,B). When imaging homogeneous flat terrain, for any constant depression angle along the flight path, the angle of incidence will remain constant. Under more typical natural terrain conditions, however, local variations in terrain slope can change the effective angle of incidence. The consequence of terrain slope on the incidence angle, at a constant depression angle, is shown in Figure 1C. The slope of the terrain is expressed in the measurement of the aspect angle; the complement of the incidence angle. Note on Figure 1C that if the terrain is flat, the aspect angle equals the depression angle.

If terrain slopes are inclined at an angle toward the imaging radar and the effective angle of incidence decreases (with increasing terrain slope angle) to a point where the angle of incidence equals the angle of slope, vertical incidence (maximum reradiation) is the result. Conversely, if terrain slopes are inclined away from the imaging radar, the angle of incidence increases (with increasing terrain slope angle) to a point where grazing is the resultant.

Surface Roughness

Surface roughness is a geometric property of the terrain and is the most important influence upon the return signal as it dictates the extent of scattering which forms the reradiation pattern field. Surface roughness is not an absolute roughness, but the relative roughness expressed in wavelength units. Terrain surfaces may be divided into two major categories according to surface roughness, depending upon the relationship of the root mean square (rms) surface roughness to the signal wavelength ($\lambda/10$) the surface appears "smooth" to the imaging radar, while for surface roughness on the order of a wavelength or more, the surface appears "rough." For a more general example, a terrain surface can be classed according to roughness between the extremes of a perfect specular reflector (no scattering), where backscatter exists only near verticle incidence, to an isotropic scatterer, where the scattering coefficient is independent of the angle of incidence.

Polarization

In the traditional SLAR configuration the electric vector is radiated and received horizontally, and thus receives the designation "like-polarized." Independent of the transmitted polarization, the return signal will be depolarized as a function of certain terrain parameters. The orthogonal or cross-polarized return can be displayed simultaneously with the like-polarized signal, if the system is capable of receiving both polarizations. The radar system (AN/APQ-97) which produced imagery for this study was capable of recording dual-polarized signals.

SNOWFIELD DETECTION

Snow Terminology

In those geographic environments where the winter snowfall exceeds summer snow melt, patches of perennial snow or "old snow" are evident. Although snow as it falls on the landscape is commonly flaky and dry, the combination of snow accumulation, melting, compaction, and refreezing can produce a granular texture most often referred to as névé or firn. Such granular snow or firn is in reality a haphazard heap of ice crystals which comprise the major portion of the snowfields in the alpine environment. Because these snowfields contribute significant amounts of water for stream flow, the volume and areal distribution of these snowfields is of particular importance to the hydrologist.

Recognition on Radar

The first indication of snowfield detectability with an imaging radar was revealed by a CRES geologist investigating the loss of interpretive data due to variance in depression angle in high relief areas. The imagery initially examined was AN/APQ-97 imagery acquired in October 1965 by Westinghouse under contract from NASA. The region concerned was the Sonora Pass area of California (Figure 2). Close scrutiny of the imagery disclosed a number of anomalously high return areas (see white area just north of area A on radar cross - polarized imagery, Figure 2) which appeared to be totally independent of the areal distribution of geologic formations and vegetation. Similarly, these areas of anomalously high return were discovered on terrain slopes facing both toward and away from the radar, indicating a relative independence of radar incidence angle and look-direction.¹ The appearance of the return on the radar imagery was much like snow would be expected to appear on ordinary aerial panchromatic photography. Upon consulting with radar engineers, the preliminary interpretation was that whatever the explanation for the anomalously high return, the most unlikely would be return from snow. It was reasoned that if the microwave radiation did not penetrate the snow, the return, if anything, should be lower than that from the surrounding terrain. Theoretically, a dielectric mixture of ice and air should be lower than that from the background signal from rock, soil, and vegetation.

In late summer two years after the imagery was collected, the University of Nevada conducted field work in the Sonora Pass area, and gathered a number of photographs in conjunction with our studies at the University of Kansas. Comparison of the 1965 imagery and subsequent photography (1967) is illustrated in the lower portion of Figure 2. The distinctive high return area on the radar imagery (north of Area A) is obviously correlative with the snowfield on the photograph. Ground investigations provided evidence that the snowfield was composed of a tightly packed granular snow more commonly referred to as firn.

¹ Radar look-direction is the direction orthogonal to the ground track of the aircraft.

Analysis of radar imagery in other alpine environments where snowfields also have been mapped has provided confirmation that the anomalously high returns from snowfields were not confined to the Sonora Pass area. Figure 3 illustrates radar imagery and simultaneous 35mm photography collected within the Yellowstone Park region of Wyoming during October, 1965. Radar #1 corresponds to photo #1, and identical locations A and B have been inserted on each inset. Because the radar imagery must be viewed in an opposite direction from the radar look-direction (to avoid topographic inversion), some interpretive difficulty may be encountered by the reader when matching either radar #1 with photo #1 or radar #2 with photo #2. For example, on photo #1 the small slope segment devoid of snow (just above area A) corresponds with the same area on radar #1 just below location A. Careful comparison of radar and photography reveals that every snow covered area not in shadow provides an extremely high return on the radar image.

Although the radar imagery tends to suggest a preferential slope orientation with respect to the radar² look-direction, this appearance is actually a combination of radar shadowing² and dominance of snow accumulation on north facing slopes. Comparison of the range of incidence angle across the imagery swath width (Figure 1B) with the slope of the terrain itself, provides evidence that the return signal from the snow is actually the highest return recorded on the imagery.

The greater tonal contrast provided by the cross-polarized imagery is preferable over the like-component for both interpretive and illustrative purposes. With a normal gain setting, the excessively high return signal from the old snow areas results in signal saturation or blossoming on the like-image. The reduced gain setting on the cross-polarized component produces a relatively better contrast, thus improved detectability of high return areas. Whether this increased detectability on the cross-component is attributable to the reduced gain setting or increased depolarization (by the snowfields) cannot be determined at this time. Obviously, polarization is another radar parameter that must be investigated with a well defined field experiment. Although areas of extensive snowfield coverage have been accurately outlined on the radar imagery of Figure 3, the question naturally arises as to radar's capability of detecting comparatively smaller areas of old snow. Figure 4 shows a comparison between radar imagery and aerial photography where extremely small snowfields have been detected by both sensors. The lack of ground data precludes any accurate definition of snowfield size, but detectability down to several acres in size appears feasible.

Penetration of New Snow

The imagery of the Yellowstone Park area has also provided limited evidence that radar systems in the Ka frequency band appear to provide a capability of penetrating new fallen snow. Although ground data were not available,

² Radar shadowing always occurs on that side of the terrain feature most distant from the transmitter, but only when terrain back-slope exceeds depression angle.

35mm slides (Figure 5) taken simultaneously with the radar imagery clearly show an area of new fallen snow in the Lewis Lake region. Area B located on both radar images and the photograph represents the approximate center of the snow area. At relatively higher elevations east of Lewis Lake, bright radar returns dominate the north facing slopes where accumulations of perennial snow have been detected. To the west of Lewis Lake, the radar imagery appears to have produced a faithful reproduction of the terrain configuration, whereas the photograph shows this region to be masked by new fallen snow. Inadequate ground information relating the amount of snow accumulation precludes estimating the depth of penetration.

While image (a) provides a look-direction to the west, image (b) provides a look-direction to the east. On both images, from different look-directions, the new snow cover has been penetrated, but the regions of old snow display a characteristically high return. In previous studies concerned with the influence of radar look-direction in geological interpretation (MacDonald, et al., 1969), it has been found that certain terrain features are preferentially enhanced on radar imagery depending on radar look-direction. Obviously there is some data loss (caused by radar shadowing) on both radar images Figures 5a and b; however, in those areas not masked by radar shadow, the slope orientation has little influence on the detectability of the snowfields. In this particular case (Figure 5a and b), two opposing look-directions would provide near optimum data retrieval.

Detection of Glaciers

There is an additional step in the metamorphism of snow to ice that has not yet been mentioned in this study. With increased volume of firn granules, the firn itself undergoes a physical transition. Continued pressure forces out most of the air between the granules, and reduction of pore space ultimately results in a true solid of interlocking ice crystals, called glacier ice. The volume, areal distribution, and movement of this glacier ice is the prime concern of the glaciologist.

A series of radar flights in the Glacier Peak area of Washington, and the Three Sisters area of Oregon have provided imagery over regions where glaciers have been previously mapped. Figure 6 represents the mapped snowfields and glaciers in the Three Sisters area (Three Sisters Quadrangle, USGS Topographic Map, 1959). On the topographic map there is no distinction between snowfields or glaciers, thus the actual distribution of glacier ice is not known. The upper image on Figure 7 illustrates radar imagery of a portion of the area shown in Figure 6. Area A of Figure 7 represents the east slope of south sister (Figure 6), while area B on Figure 7 outlines the east slope of middle sister (Figure 6).

The crater located in the center of south sister (Figure 6) has not been mapped as either an area of perennial snow or as a glacier. The same area appears on Figure 7 (above A upper image) as an area of high return, characteristic of those old snow areas previously examined (Figures 2-5). Similarly, on the west slope of south sister, there is an extensive area of high return; however, several anomalously low return areas are also distributed on this slope. The geometric shape of these low return areas coincides quite accurately with the areal extent of the larger mapped glaciers of Figure 6. Similar low returns areas are evident in the Glacier Park area of Washington (lower radar image Figure 7). In this region near-simultaneous photography can be compared with

the radar imagery. Although some high return areas on the radar imagery are evident, the dominant imagery tone is indicative of low return and correlative with the snow covered areas of glacier ice.

QUALITATIVE EXAMINATION OF RETURN

The radar imagery previously presented in this study provides in a qualitative fashion, the magnitude of the backscattered radar return from three distinct stages in the metamorphosis of snow to ice. The virtual transparency or exceedingly low return of fresh, low density snow and the relatively low return from glacier ice is not particularly surprising; however, the most striking feature of this data is the magnitude of the return from areas of old snow or firn.

As previously discussed, cursory imagery analysis suggests that the high return areas attributed to old snow have a preferential slope orientation with respect to the radar. However, close examination shows this to be an illusion fostered by a combination of the loss of return from back-slopes due to radar shadowing and the concentration of old snow upon north facing slopes common to an Alpine environment. More significant is the lack of variation of the return with angle of incidence. From the range of incident angles across the imagery combined with the slope variation of the terrain itself, it is possible to show that old snow remains the highest return on the image throughout a range of at least 20 to 70 in incident angle.

As a first step in interpreting these returns let us consider the dielectric properties of the surface and their effect upon the reflection coefficient at the interface.

Dielectric Properties of Surface

The surfaces appearing on the imagery may be roughly divided into four categories: snow, ice, soil, and vegetation. Unfortunately, absolute measurement of return is impossible from this imagery and we shall confine our attention to qualitative changes across boundaries. The snow and ice returns previously illustrated are almost exclusively from nonvegetated areas, hence the properties of vegetated areas will not be considered.

An excellent review paper on the dielectric properties of ice and snow by Evans (1965) shows the relative dielectric constant of ice to have an essentially constant value of 3.17 ± 0.07 for frequencies from 1 MHz to well above the microwave region. The dielectric constant used here is the real portion of the complex permittivity, ϵ given by

$$\frac{\epsilon}{\epsilon_0} = \epsilon' - j\epsilon'' \quad (1)$$

where ϵ_0 is the dielectric constant of free space, ϵ' is the relative dielectric constant based on free space as unity, and ϵ'' is the relative loss factor. The ratio ϵ''/ϵ' is frequently used as a measure of dielectric properties and is called the loss tangent, $\tan \delta$. The temperature dependence of the relative dielectric constant of ice is also shown to be negligible so long as it is maintained below the freezing point.

The variation of the loss tangent of ice with both frequency and temper-

ature is shown in Figure 8. From these values it may be seen that the contribution of the loss factor to the reflection coefficient of an air-ice interface will be negligible throughout the microwave range.

The Weiner theory of dielectric mixtures is almost universally used to describe snow as a mixture of air and ice. This rather simple formulation enable one to describe the dispersion of one medium within another by a single parameter called the Formzahl. The Weiner formula with ϵ_m , ϵ_1 , and ϵ_2 the relative permittivities of the mixture and the two separate media respectively is given by

$$\frac{\epsilon_m - 1}{\epsilon_m + u} = p \frac{\epsilon_1 - 1}{\epsilon_1 + u} + (1 - p) \frac{\epsilon_2 - 1}{\epsilon_2 + u} \quad (2)$$

where p is the proportion of the total volume occupied by medium 1 and u is the Formzahl. Equation (1) includes the effect of losses if the complex values of ϵ_1 and ϵ_2 are used and the result separated into real and imaginary parts. If losses are sufficiently low ($\tan^2 \delta < 1$) the above expression may be used to describe the behavior of the real portions alone with no modification.

The Formzahl characterizes the structure of the mixture, and Figure 9 illustrates the type structure associated with different values of u . The relative dielectric constant of dry snow as a function of density and differing Formzahl is likewise shown in Figure 9. The dielectric constants of ice and air were taken as 3.2 and 1.0 respectively for these calculations. The measured values shown as points on the Figure 9 are due to Cumming (1952) and were made at a frequency of 9,375 MHz. The limiting value for the loss factor of dry snow will be that assigned the ice portion of the mixture. As both constituents of the mixture are nondispersive over the frequency range of interest the mixture (snow) is likewise nondispersive.

While both ice and snow may be considered essentially independent of temperature, so long as the constituents are solely ice and air, the addition of free water to the mixture has a pronounced effect. The Debye dispersion formula may be used to describe the frequency dispersion of polar dielectrics such as water and is given by

$$\epsilon_r = \epsilon' - j\epsilon'' = \epsilon_\infty + \frac{\epsilon_s - \epsilon_\infty}{1 + j\omega\tau} \quad (3)$$

where the subscript s refers to the static value and the subscript ∞ refers to the optical relative dielectric constant. The angular frequency is represented by ω while the molecular relaxation time is τ . The ordered orientation is disturbed by thermal agitation, hence the relaxation time, τ , is frequency dependent. The relaxation time for water is approximately 2×10^{-13} sec at a temperature of 0°C . With so short a relaxation time it is apparent that frequency and temperature effects will be important in the microwave region.

The effect of free water upon the dielectric properties of a mixture such as snow may be considered by extending usage of the Weiner formula to consider a mixture of dry snow and water. Curves of the dielectric constant of wet

snow of specific gravity 0.5 as a function of percent water content are shown in Figure 10. The dielectric constant of the dry snow was taken as 2.0 and that of the liquid water as 80.0 for these calculations. As might be expected, these curves show that for a mixture with widely differing dielectric constants the Formzahl has considerably more effect. Again the loss factor of the mixture will approach that of the water as the percentage water is increased.

The dielectric constant of the soil surrounding and underlying the snow-fields must be estimated due to the wide variety of soils involved and the lack of ground truth in the areas. While identification of soil type could be performed even at this late date (four years after imagery was flown); the even more important determination of moisture content must be made at the time of the overflight.

Return from Fresh Snow

Assume that the return from areas of fresh snow may be represented by a homogeneous plane layered model. We may then compare the estimated percent energy return at normal incidence from the air-snow and snow-soil interfaces of the model. From Figure 8 the dielectric constant of relatively fresh dry snow is estimated to be approximately 1.4. Further assume that the apparent dielectric constant of the soil at Ka band is 4.5. The apparent dielectric constant used here is that obtained by neglecting losses and attributing the reflection at the boundary to be due solely to the change in relative dielectric constant of the two media.

Since losses are likewise negligible for snow the reflection coefficient at normal incidence is given by

$$r = \frac{\sqrt{\epsilon_1} - \sqrt{\epsilon_2}}{\sqrt{\epsilon_1} + \sqrt{\epsilon_2}} \quad (4)$$

where ϵ is the apparent relative dielectric constant.

With the above rather gross assumptions the percent energy reflected at each boundary is as shown in Table I. From these values it may be seen that the return from the snow surface is negligible in comparison to that of the ground and further that the snow cover will not seriously attenuate the return for normal depths. It may be argued that the use of dry snow is unrealistic for this calculation; however, any increase in moisture content of the snow will cause a corresponding increase in the moisture content of the soil in the immediate area.

TABLE I

Interface	Percent Engery Reflected
air-snow	0.62
snow-soil	8.1
air-soil	12.9

Return from Old Snow

The return from old snow might at first appear to be the result of increased

moisture content. While the addition of considerable free water might explain the increase of return between fresh snow and old snow, it does not explain the huge difference in return between old snow and the surrounding soil. It hardly seems reasonable to postulate a large free water content for the snow without likewise assuming a significant increase in the water content of the soil in the immediate vicinity of the snow pack. As the dielectric constant of both surfaces increases it may be seen from equation (4) that the difference between returns will decrease. Change in dielectric constant thus does not seem sufficient to account for the magnitude of the return from old snow.

Another factor which could conceivably account for the difference in return between the old snow and the surrounding soil would be a substantial change in surface roughness scale, near that of the incident wavelength. Recent observation of old snow packs confirm that any change in the roughness of old snow in comparison to soil at Ka band wavelengths is toward a smoother surface. The behavior of a relatively smooth surface is in direct contrast to the observed near isotropic behavior of the old snow with variations in incident angle.

Two possibilities come to mind in attempting to rationalize the observed behavior of the return from old snow. The structure of old snow is granular with the size of the individual granules or crystals ranging to above 3mm in diameter depending upon temperature conditions (Shumskii, 1964). This size range is comparable to the sensing wavelength and the basic assumption of the Weiner theory that the geometry of the electric field is not a function of the relative proportion of the two media is definitely violated. A volume scattering model based on a random distribution of spheres could conceivably produce the increased return noted and would likewise be insensitive to angular variation.

Another possible explanation involves the behavior of moisture in the granular old snow. The free water existing in such a structure is predominately a coating on the surface of each crystal. The entire surface might then be considered as an almost continuous water film with a roughness in the sensing wavelength range due to the size of the snow granules. This degree of roughness would likewise produce the angular insensitivity noted.

Return from Glacier Ice

The return from mapped glaciers in the Three Sisters area is significantly lower than the surrounding areas of both old snow and bare soil (Figure 7). A slight decrease between ice and soil might be predicted from the difference in dielectric constant; however, the difference predicted at Ka band does not appear to be sufficient to completely explain this behavior. Again difference in surface roughness might partially account for the difference observed at angles considerably off normal.

CONCLUSIONS

To draw any quantitative conclusions regarding the nature of radar return from snow and ice as a result of the rather qualitative data analysis presented in this study would be extremely naive. An extensive and well calibrated ground measurement program is a necessary requisite for determining the relationship between radar return and snow type.

It is apparent that two extremes in radar signal return result from the

microwave irradiation of snow and ice; the relatively high signal return from old snow or firn, and the very low return from glacier ice. Equally significant is the fact that microwave energy of Ka band frequency is capable of penetrating an appreciable depth of new fallen snow.

While the exact mechanism of the radar return may remain undefined for some time, a heuristic approach to the application of imaging radar systems for snow surveying could be implemented immediately. Similarly, radar imaging systems other than Ka band frequency should be used to investigate the possibility of estimating both the areal extent and volume of the snow pack. Simultaneous flight coverage with available multifrequency radar imaging systems that could be correlated with accurate ground truth measurements would provide the hydrologist, glaciologist, and radar engineer with excellent working data to evaluate the snow-mapping capability of a multifrequency radar system.

REFERENCES

1. Meier, M. F., R. H. Alexander, and W. J. Campbell, 1966, Multispectral Sensing Tests at South Cascade Glacier, Washington: Proc. Fourth Symp. Remote Sensing of Environment, (April 1966), University of Michigan, Ann Arbor, pp. 145-159.
2. Taylor, R. C., 1959, Terrain Return Measurements at X, Ku, and Ka Bands: IRE Nat'l. Conv. Rec., pt. 1, vol. 7, pp. 19-26.
3. Rouse, J. W., W. P. Waite, and R. L. Walters, 1966, Use of Orbital Radars for Geoscience Investigations: Proc. Third Space Congress Canaveral Council of Technical Societies, pp. 77-94.
4. Ellermeier, R. D., A. K. Fung, and D. S. Simonett, 1966, Some Empirical and Theoretical Interpretation of Multiple Polarization Radar Data: Proc. Fourth Symp. Remote Sensing of Environment, University of Michigan, Ann Arbor, pp. 657-670.
5. MacDonald, H. C., J. N. Kirk, L. F. Dellwig, and A. J. Lewis, 1969, The Influence of Radar Look-Direction on the Detection of Selected Geological Features: Proc. Sixth Symp. Remote Sensing of Environment, (October 1969) University of Michigan, Ann Arbor (In press).
6. Evans, S., 1965, Dielectric Properties of Ice and Snow — A Review: Journal of Glaciology, vol. 5, no. 42, pp. 773-792.
7. Cumming, W. A., 1952, The Dielectric Properties of Ice and Snow at 3.2 Centimeters: Journal of Applied Physics, vol. 23, no. 7, pp. 768-773.
8. Shumskii, P. A., 1964, Principles of Structural Glaciology, Dover Publication Inc., New York, 497 pp.

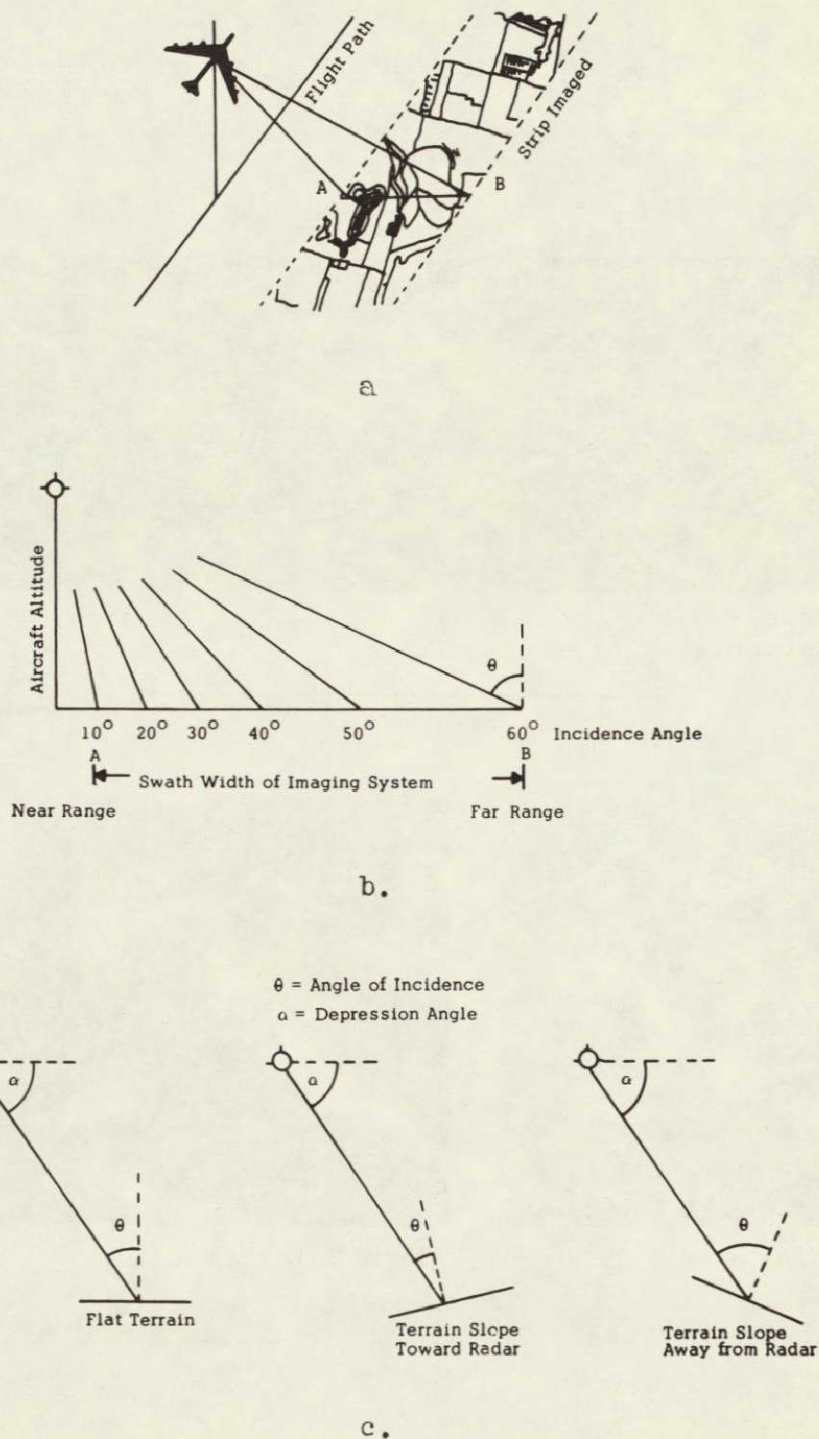
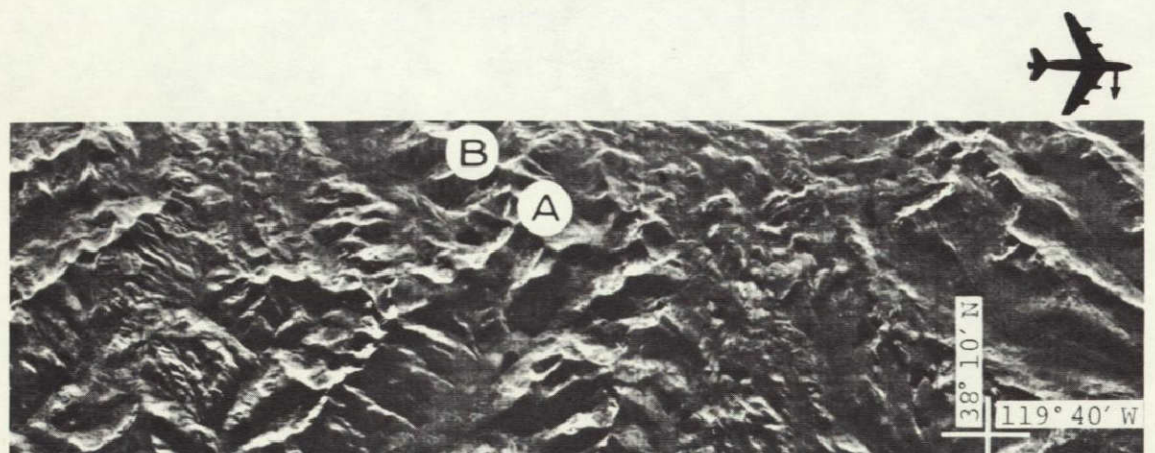
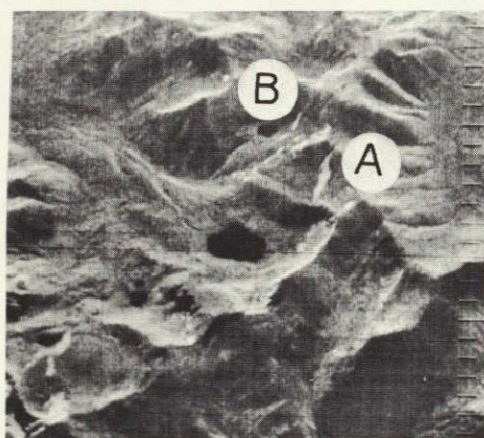


Figure 46-1.- SLAR imaging system. (a) Ground coverage. (b) Hypothetical swath width and respective incidence angles. (c) Effect of terrain slopes on incidence angles.

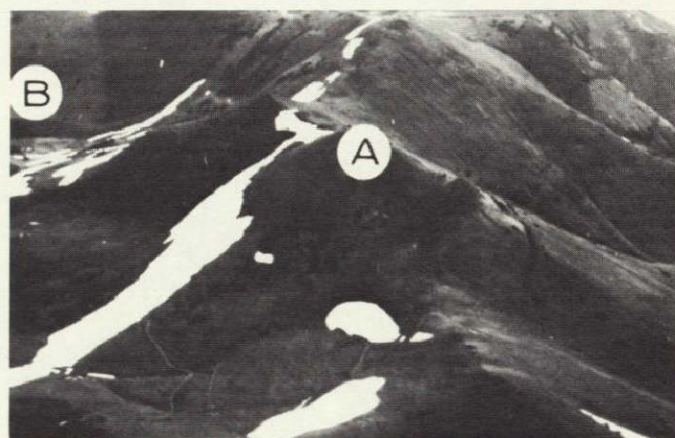


Radar Cross-Polarization

0 5 10 15 Km.
Approx. Scale

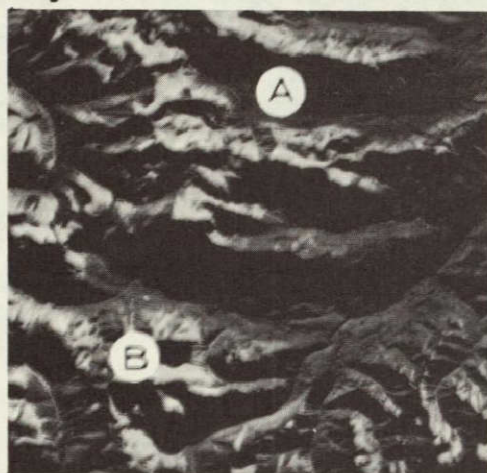


Radar Enlargement 2x



35mm Enlargement 2x

Figure 46-2.- Radar imagery and photography, Sonora Pass area, California.



RADAR 1 - Cross Polarization

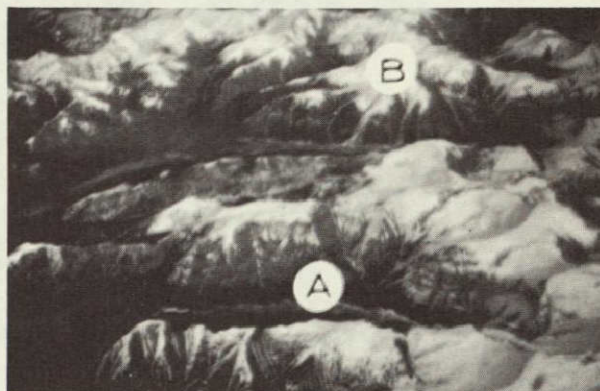
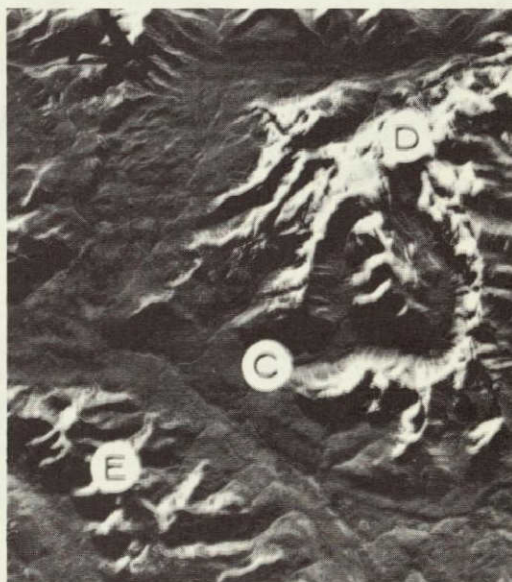


PHOTO 1

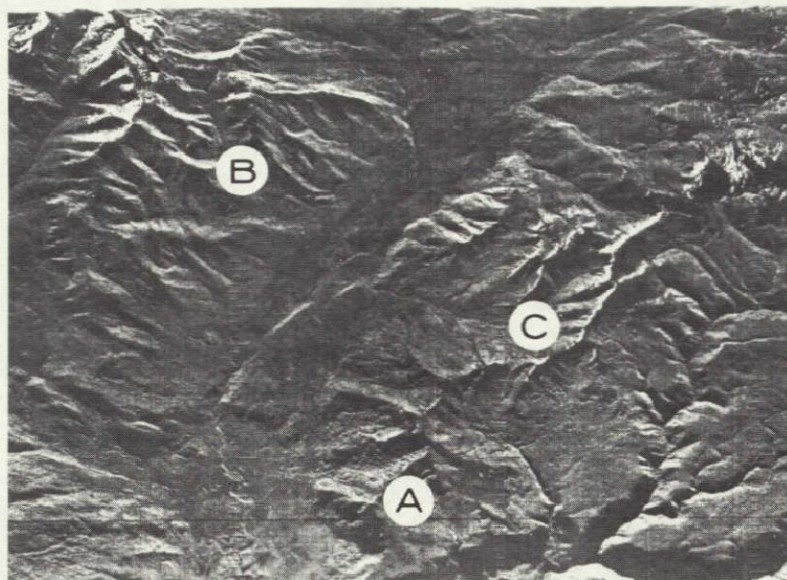


PHOTO 2

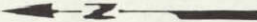


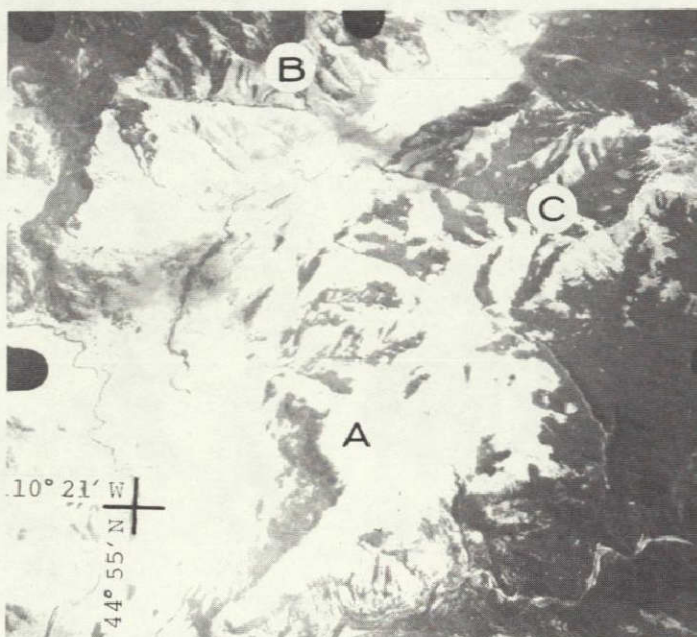
RADAR 2 - Cross Polarization

Figure 46-3.- Radar imagery and photography comparison, Yellowstone Park area, Wyoming.



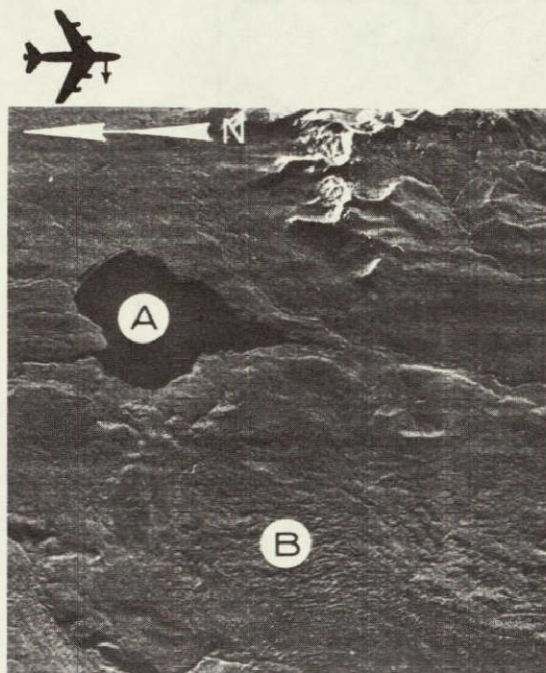
Cross-Polarized Radar Imagery

0 5 Km. 
Approx. Scale

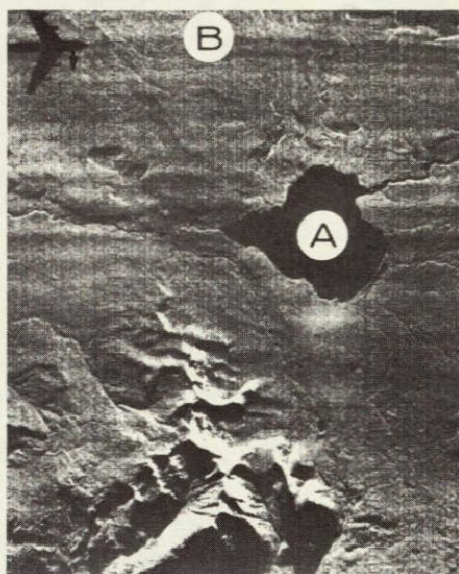


KA-30 Oblique Photography

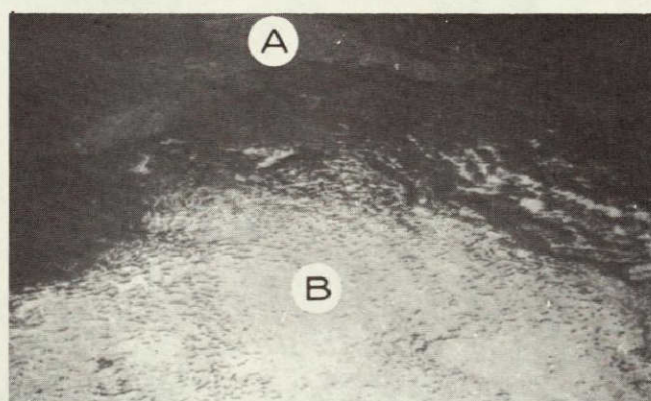
Figure 46-4.- Radar - photo comparison,
Yellowstone River area, Wyoming.



a. Radar look-direction, west.



b. Radar look-direction, east.



c. Simultaneous photograph.

Figure 46-5.- Effective snow penetration by radar. (a) Radar look-direction, west. (b) Radar look-direction, east. (c) Simultaneous photograph.

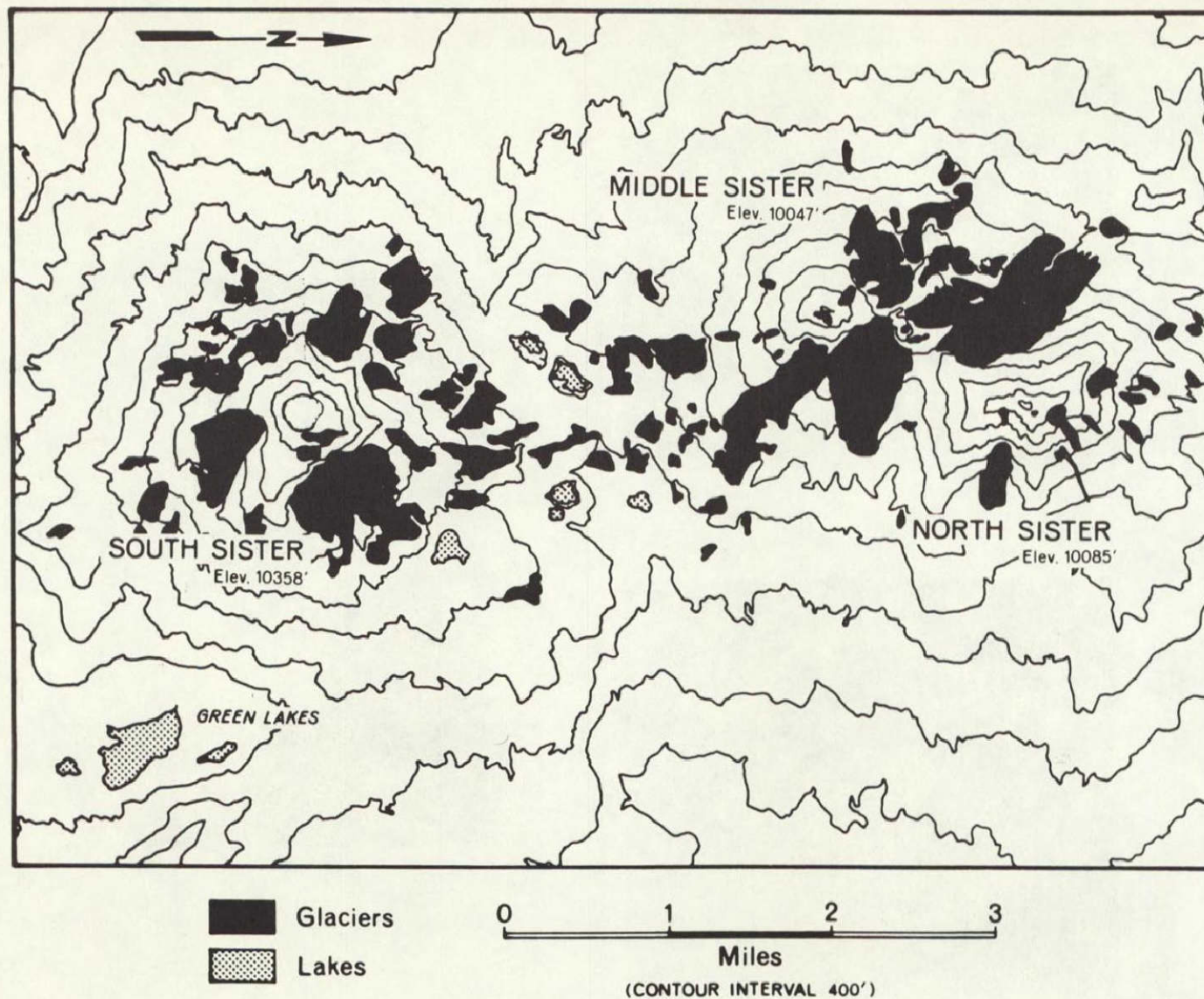
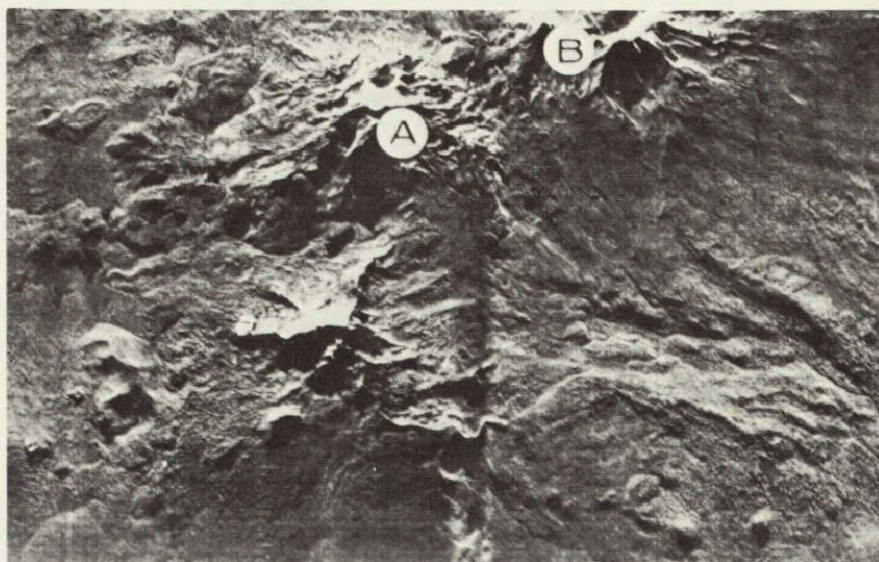


Figure 46-6.- Mapped glaciers, Three Sisters area, Oregon.

THREE SISTERS AREA, OREGON

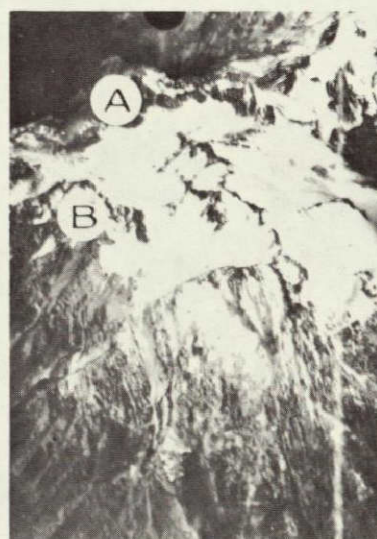


Cross-Polarization Radar

GLACIER PEAK AREA, WASHINGTON



Radar Imagery



KA-30 Photography

Figure 46-7.- Radar imagery at Three Sisters area, Oregon, and Glacier Peak area, Washington.

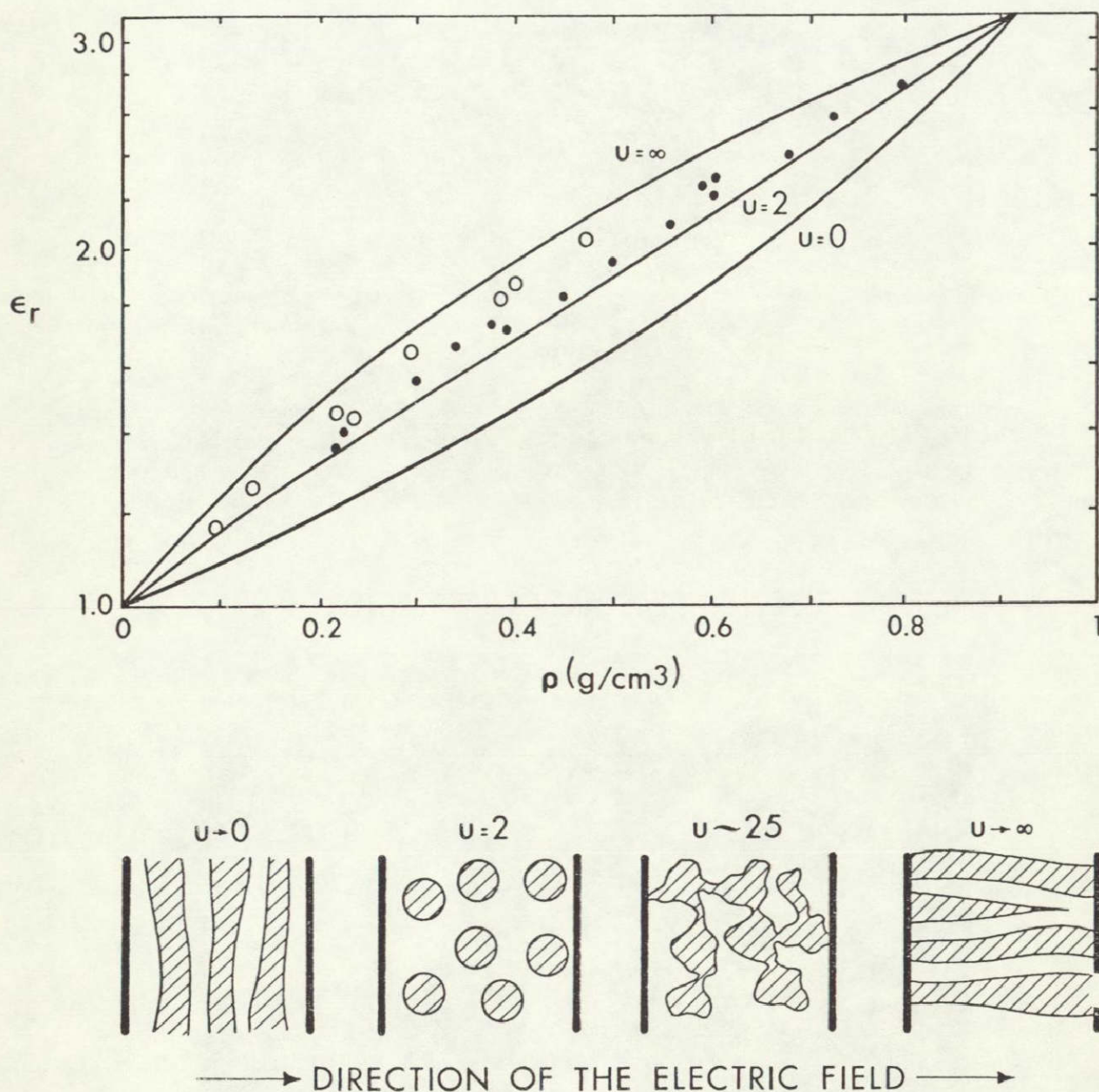


Figure 46-8.- Relative dielectric constant of snow versus density (after Evans, 1965).

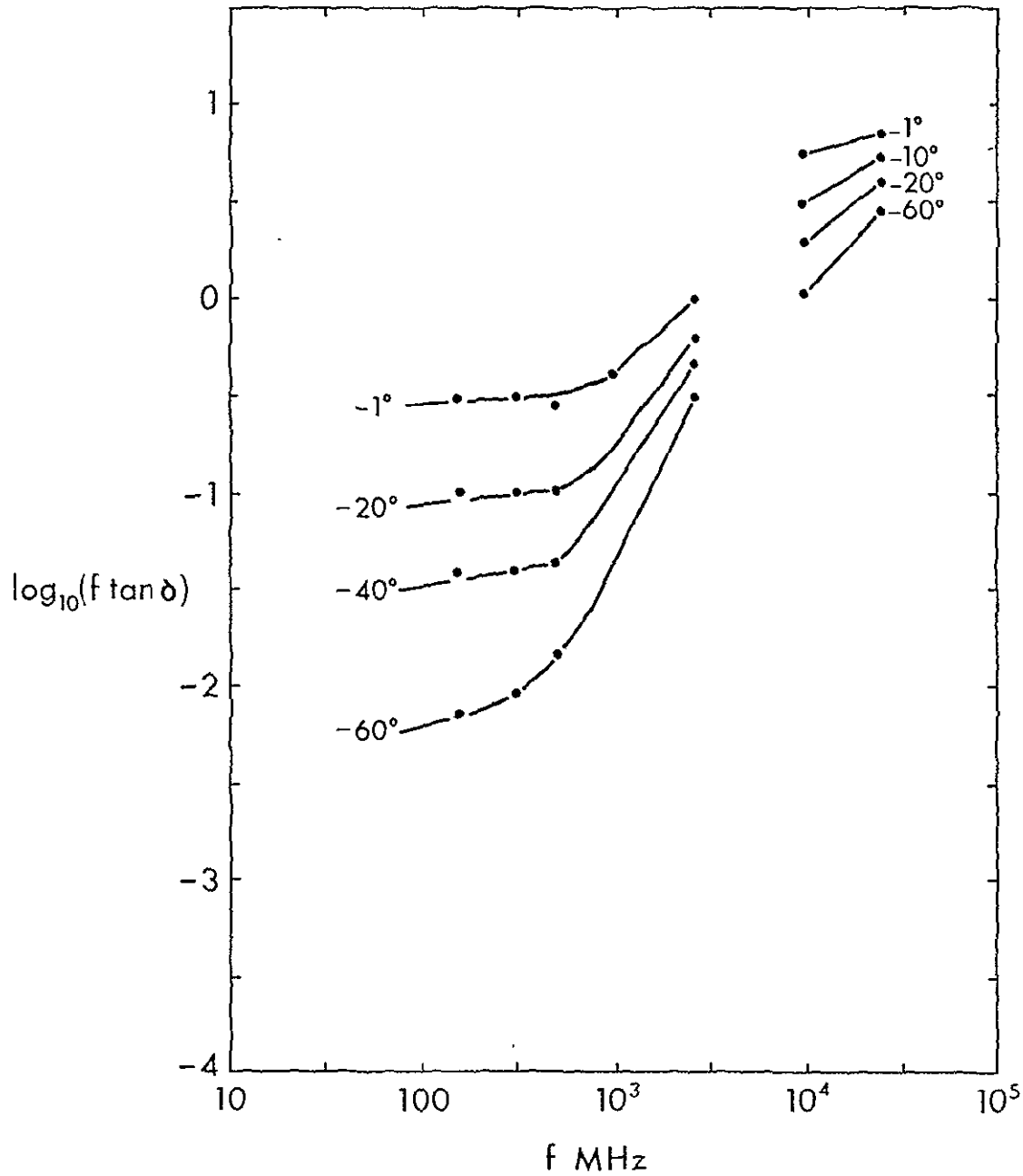


Figure 46-9.- Loss tangent of ice versus frequency and temperature (after Evans, 1965).

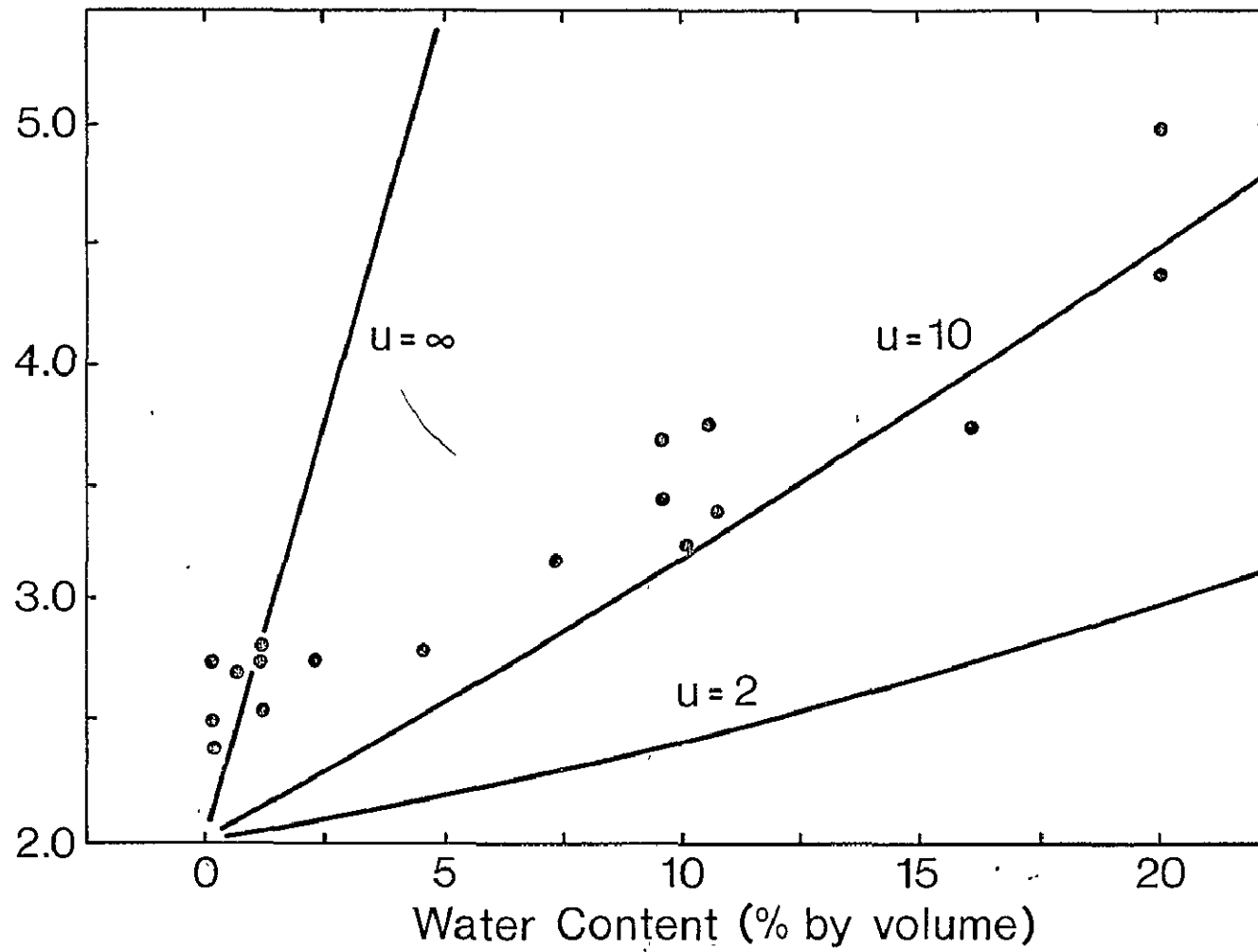


Figure 46-10.- Dielectric constant of wet snow versus volume percentage of liquid water (from Evans, 1965).

SECTION 47

PASSIVE MICROWAVE STUDIES

N71-11164

James P. Hollinger
E. O. Hulburt Center for Space Research
Naval Research Laboratory
Washington, D. C.

INTRODUCTION

The microwave oceanography project is supported by Spacecraft Oceanography (SPOC), NAVOCEANO. Our ultimate goal is to determine the system parameters and measurement techniques required to obtain unambiguous, all-weather information about the sea surface by means of passive microwave measurements from a satellite.

The measurement program began in October 1968 with the construction of two microwave radiometers and polarimeters at 8.35 and 19.35 GHz instrumented for observations from a fixed ocean platform. The ocean platform was chosen for the initial measurements because the excellent ground truth and high spatial resolution of the sea surface it provides facilitates the correlation of microwave antenna temperature and sea surface conditions. In addition it is easier and more convenient to calibrate, adjust and manipulate the microwave equipment on a fixed platform, as well as being cheaper, than it is to construct, install and operate the radiometers in an aircraft. Sea state measurements were made from Argus Island Tower in March-April 1969 and measurements of artificially generated foam and rain were made in July 1969. No aircraft observations have been made to date. However aircraft borne measurements are essential to our program and two missions using the NASA P-3 are planned for November 1969 and January-February 1970.

The Argus Island measurements and results will be presented first. Then the planned P-3 missions will be discussed along with comments on the future aspects and approaches of the passive microwave program.

ARGUS ISLAND OBSERVATIONS

Argus Island Tower is located 28 miles southwest of Bermuda in 195 feet of water. The radiometers were mounted on a loading platform 65 feet above the mean sea surface. Both the 3.6 and 1.6 cm systems consist of a parabolic antenna, circular feed, and dual-mode transducer followed by a conventional Dicke-type crystal-mixer superheterodyne receiver. The

RMS noise output fluctuations with a one second time constant are $1/4^{\circ}\text{K}$ at 3.6 cm and $1/2^{\circ}\text{K}$ at 1.6 cm. The half-power beamwidths are 3.4 and 2.7 degrees providing a half-power spot size on the sea surface at nadir of 4 feet and 3 feet at 3.6 and 1.6 cm respectively. The polarimeters can operate in either of two modes. In one mode, the absolute antenna temperature of linearly-polarized radiation incident upon the antenna is measured. In the other mode, the difference in absolute antenna temperature between two orthogonal linearly-polarized components is measured. Since the antennas can be rotated about their electrical axes, any plane of linear polarization may be selected. In practice the vertical, 45 degree and horizontal components were measured. This allowed complete determination of the linear polarization. The antennas can be scanned in incidence angle between nadir and zenith.

The results of observations made from Argus Island in March and April 1969 are given in Figures 1 through 6. Figures 1 and 2 give the results of a typical observation at 1.6 and 3.6 cm respectively and show the form and range of the measurements. The solid dots are the antenna temperatures measured by integrating for about one or two minutes, to obtain statistical stability, at successive incremented incidence angles. The upper and lower curves are the vertically and horizontally polarized components respectively. The solid curves have been calculated for a specular sea with the measured values of salinity and temperature and for a plane atmosphere using the opacity determined from atmospheric emission measurements between zenith and the horizon. The open circles are the derived main-beam brightness temperatures of the sea after correction for reflected sky radiation and for radiation entering the side and back lobes of the antenna. The emissivity of the sea surface is given by the ratio of this brightness temperature to the temperature of the sea. The absolute errors in the measured antenna temperatures and the relative errors in the derived main-beam brightness temperatures range from 1 to 3°K . The absolute errors in the main-beam brightness temperatures are approximately 5 to 10%. The measurements are probably not reliable between nadir and about 15° incidence angle because of the effects of the tower structure or between about 75° incidence angle and the horizon because of the large correction for reflected sky radiation required, especially at 1.6 cm.

The sea states encountered during the March-April series of measurements ranged from calm with about 2 foot swell to winds of 20 to 22 knots with 6 to 8 foot waves. To facilitate the analysis of the results over this limited range, the data

were divided into two groups comprising the highest and lowest sea conditions and averaged together. The two groups represent average sea conditions of about 3 knot winds with 3 foot waves and 15 knot winds with 6 foot waves.

Figures 3 and 4 show the average derived main-beam brightness temperatures of the vertical and horizontal components for these two groups at 1.6 and 3.6 cm as a function of incidence angle. The general agreement of the data and what is expected for a specular sea (solid curves) is gratifying and shows that the rough form of the variation in microwave brightness temperature with incidence angle is given by simple calculations for a specular sea. Qualitatively, the results show that the vertical component is independent of sea state at about 50 to 60 degrees incidence angle and increases below and decreases above this angle with increasing sea state. The horizontal component increases with sea state over the range of incidence angles from 15 to 75 degrees. These results are experimental verification of the theoretical predictions of A. Stogryn (1).

Figure 5 shows the measured percentage polarization, defined as the difference between the vertical and horizontal components divided by their sum, as a function of incidence angle. The error in the measured percentage polarization is about 1% and is independent of calibration errors. Again the solid curves are calculated for a specular sea. The percentage polarization is seen to be dependent upon sea state, decreasing with increasing sea state. The rate of decrease with sea state increases with increasing incidence angle.

Figure 6 shows individual measurements at 1.6 cm and at 50 degrees incidence angle of the vertical and horizontal components of the brightness temperature and of the percentage polarization as a function of wind speed. A least-squares straight line has been fitted to the data in each case. The vertical component of the brightness temperature is sensibly independent of wind speed as expected from the average data shown in Figure 3. The horizontal component increases with wind speed at a rate of $0.60 \pm 0.12^\circ\text{K}$ per knot in good agreement with Stogryn's theoretical prediction at 1.55 cm of about $1/2^\circ\text{K}$ per knot (1). The polarization decreases at a rate of 0.26 ± 0.06 percent per knot of wind speed. An even greater dependence of the polarization on wind speed occurs at incidence angles above 50 degrees because the vertical component is decreasing, instead of constant with increasing wind speed, at the same time that the horizontal component is increasing. Therefore, even though the polarization is sensitive to errors in the correction for atmospheric attenuation, at large incidence angles the errors in the derived

wind speed are only about half those incurred by using the horizontal brightness temperature alone. Most important the polarization is independent of absolute calibration and therefore is independent of errors in absolute calibration whereas the horizontal brightness temperature is not.

Complete linear polarization measurements showed that the plane of polarization was always vertical within the error of measurement of 3 degrees. This is not in agreement with the theoretical prediction of V. A. Sirounian (2). His results predict a rotation of up to 12 degrees at 1.6 cm wavelength for the range of sea conditions observed.

In July 1969 measurements of the effects of artificially generated foam and rain were made from Argus Island Tower. The foam generator consisted of two manifolds with ten garden hoses strung between them and over all dimensions of 10 feet by 25 feet. The generator was floated two feet below the sea surface and air forced through 1/10 inch holes drilled to form a square grid with a one foot spacing. The presence of foam greatly enhanced the emissivity of the sea as expected on the basis of work by Williams (3) and by Nordberg (4). The artificial foam increased the emissivity at 15 degrees incidence angle from about 0.42 to greater than 0.67. This corresponds to an increase in brightness temperature of from about 130°K to over 200°K. Within the experimental error of about 10 to 15°K this lower limit was the same at 1.6 and 3.6 cm. Because of experimental difficulties in positioning the foam generator measurements at larger angles of incidence are not reliable. The effects due to the surface disturbance of rain were relatively small, only about 1/5 or less that of foam.

The results of the Argus Island Tower measurements at 1.6 cm and 3.6 cm over a range of incidence angles from about 15 to 75 degrees and for a range of sea states up to 20 knot winds and 6 to 8 foot waves may be summarized as follows:

(1) General form of the dependence of vertical and horizontal components of the brightness temperature of the sea on incidence angle are given by simple calculations for a specular sea.

(2) Vertical component independent of sea state between about 50 to 60 degrees incidence angle.

(3) Vertical component increases below and decreases above about 55 degrees incidence angle with increasing sea state.

(4) Horizontal component increases with increasing sea state.

(5) Horizontal component at 1.6 cm and at 50 degrees incidence angle increases about 0.6°K per knot of wind speed.

(6) Polarization decreases with increasing sea state at rate which increases with increasing incidence angle.

(7) Polarization at 1.6 cm and at 50 degrees incidence angle decreases about 1/4 percent per knot of wind speed.

(8) Plane of linear polarization always vertical to within experimental error of 3 degrees.

(9) Foam greatly enhances the emissivity of the sea.

(10) The surface disturbance due to rain has much less effect on the emissivity of the sea than does foam.

(11) All of the above conclusions are sensibly the same at 8.35 and 19.35 GHz.

FUTURE PLANS

Certainly a great deal of work remains to be done and in particular measurements over a greater range of sea states are needed. On the basis of the experimental results to date, the percentage polarization is an attractive sea state indicator to pursue because of its independence of absolute calibration. Sea foam has a very great effect and must be taken into account. Further measurements of foam as a function of frequency, polarization and incidence angle are needed. If the increase in the horizontal component and hence polarization saturates at wind speeds above about 30 to 40 knots, the increasing foam coverage with increasing wind speed may still allow passive microwave determination of sea state. If saturation does not occur, corrections for foam and atmospheric attenuation may be possible by measurements of the vertical component at about 55 degrees incidence angle. Atmospheric effects and very likely those due to foam decrease greatly with increasing wavelength and measurements at L or S band are needed to determine if more reliable sea state measurements can be made at these wavelengths.

The future observational program must include aircraft borne measurements. The aircraft will allow a greater range of sea states to be investigated as well as providing an environment more nearly comparable with a satellite as regards

atmospheric attenuation, spatial resolution and data acquisition rate. We feel that the most productive course to follow is to make aircraft borne measurements in conjunction with observations from an ocean tower. Joint measurements with the tower will benefit by the excellent ground truth available from the tower, a better calibration of the instruments and the comparison of greatly different spatial resolutions. The different spatial resolutions will allow an experimental test of the assumption that the time average of sea state effects as measured from the tower is identical to the spatial average as obtained from an aircraft or satellite.

At present two aircraft borne experiments are planned using the NASA P-3 aircraft. The first, Mission 113, in the Gulf of Mexico November 10-15, 1969 will be used to become familiar with the aircraft, flight procedures, radiometers, data handling and aircraft measurement techniques. It should also provide good sea state information but is intended primarily as preparation for the second and main mission. This second mission is tentatively scheduled in January-February 1970 between the east coast and Bermuda. This experiment will be part of the Joint Ocean Surface Study (JOSS) being planned by SPOC and will include passive microwave measurements from Argus Island Tower. We hope to obtain information over a large range of sea states and further explore the possibilities of polarization, foam and longer wavelength measurements as means of obtaining a reliable determination of sea state.

REFERENCES

- (1) Stogryn, A., IEEE Trans. Ant. and Prop., vol. AP-15, p. 278, 1967.
- (2) Sirounian, V. A., Douglass Report #DAC-60786, Sept. 1967.
- (3) Williams, G. F. Jr., J. Geophys. Res., vol. 74, p. 4591, 1969.
- (4) Nordberg, W., Microwave Review Meeting, NASA, Washington, D. C. 1969.

1.6 cm RUN #5 12 KNOT WIND
 4-6 FOOT WAVES
 SALINITY 34/1000
 SEATEMP 291°K

• - - • - - • MEASURED ANTENNA TEMPERATURE
 ○ ○ ○ DERIVED MAIN-BEAM BRIGHTNESS TEMPERATURE
 ——— CALCULATED BRIGHTNESS TEMPERATURE OF
 SPECULAR SEA & PLANE ATMOSPHERE OPACITY 0.060

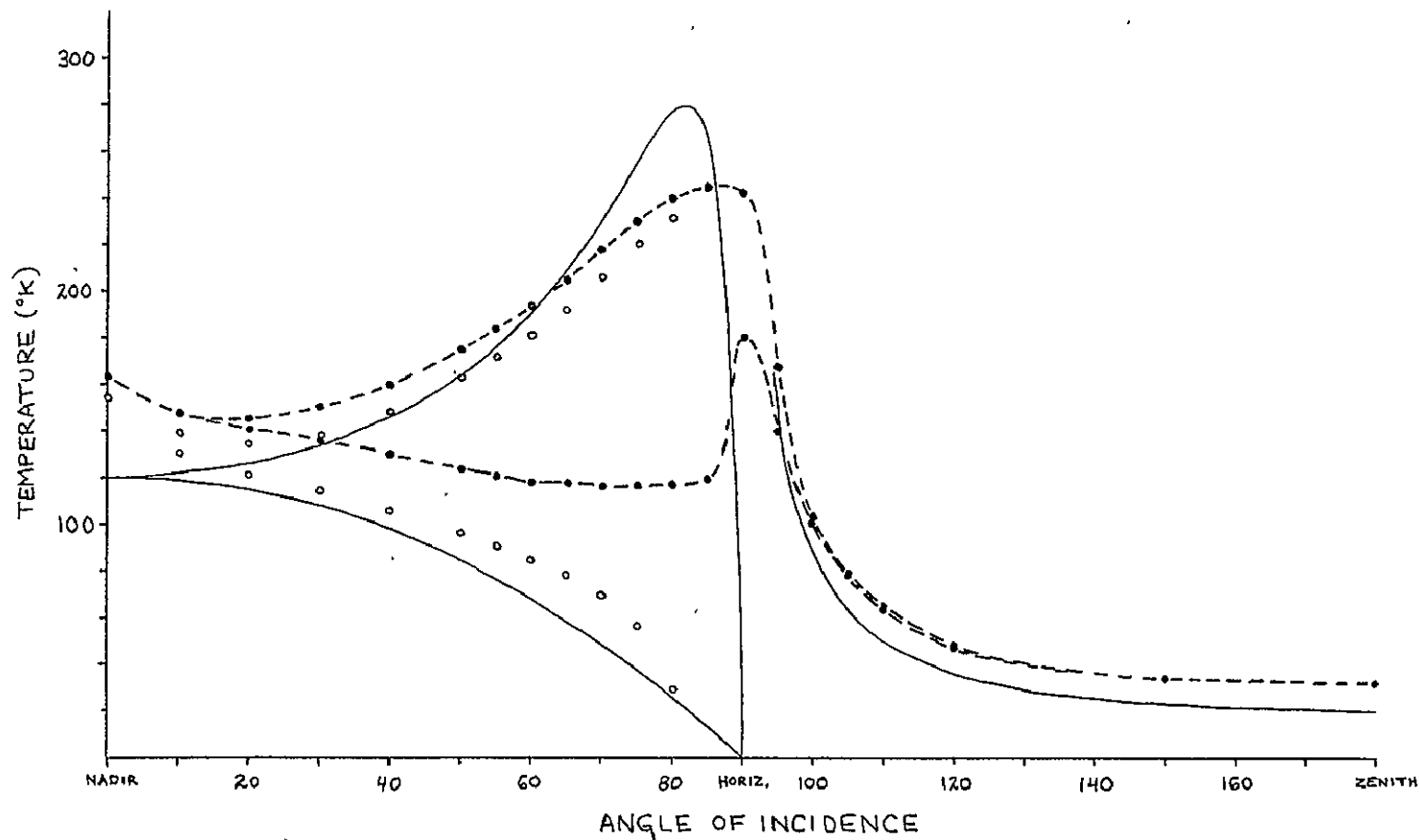


Figure 47-1.- Temperature data versus angle of incidence, run no. 5, 1.6 cm.

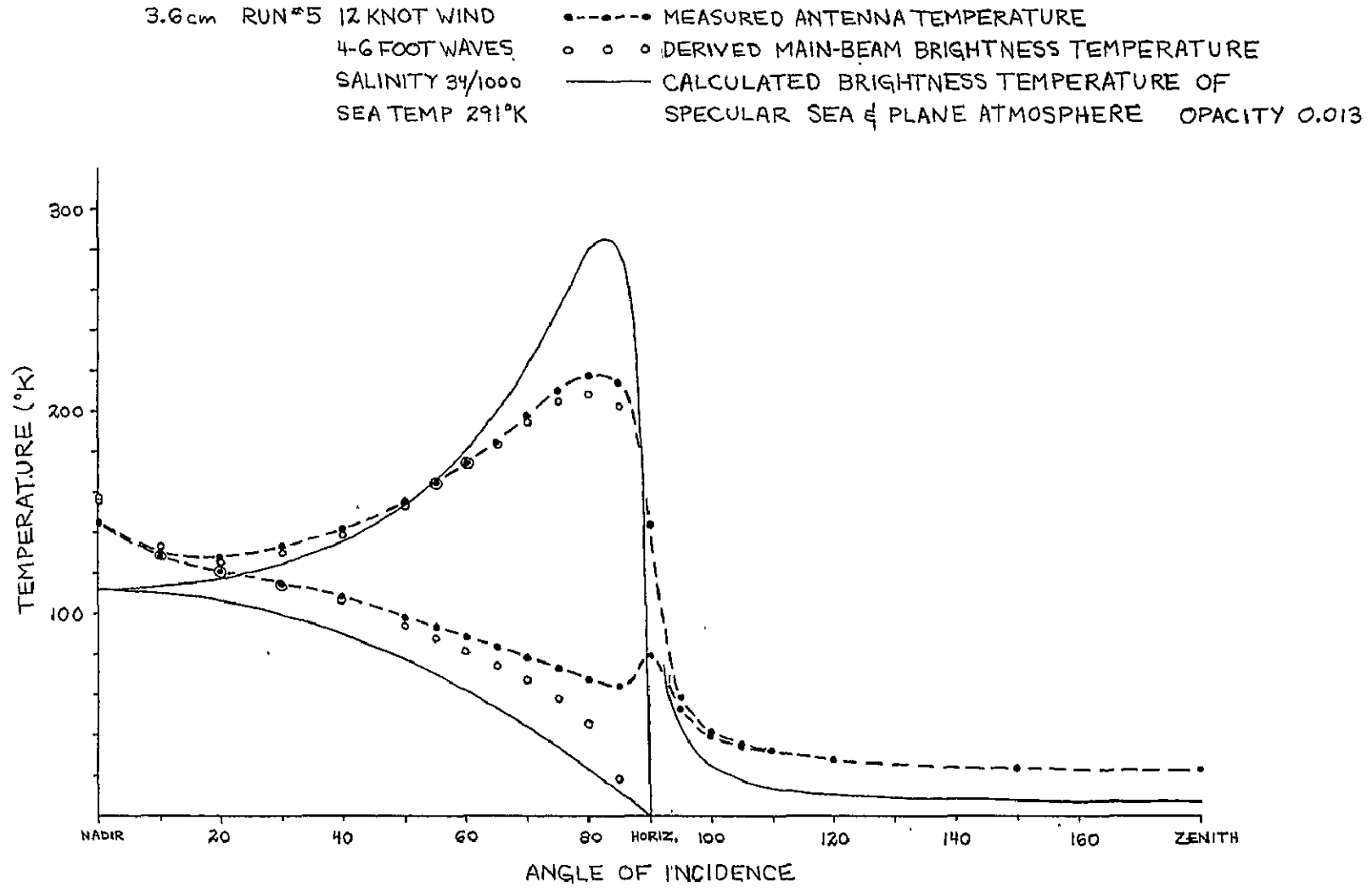


Figure 47-2.- Temperature data versus angle of incidence, run no. 5, 3.6 cm.

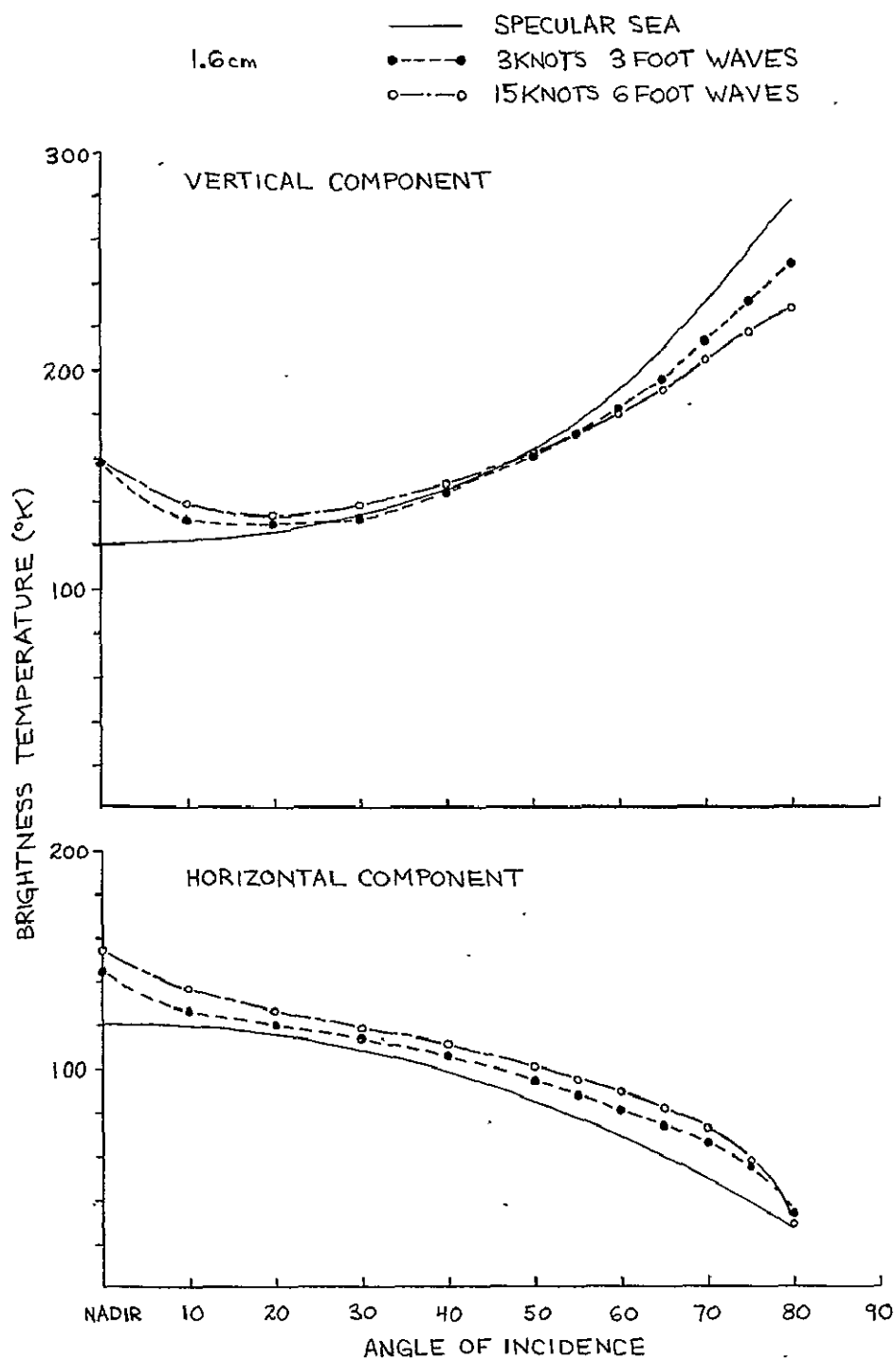


Figure 47-3.- Brightness temperature data versus angle of incidence for horizontal and vertical components, 1.6 cm.

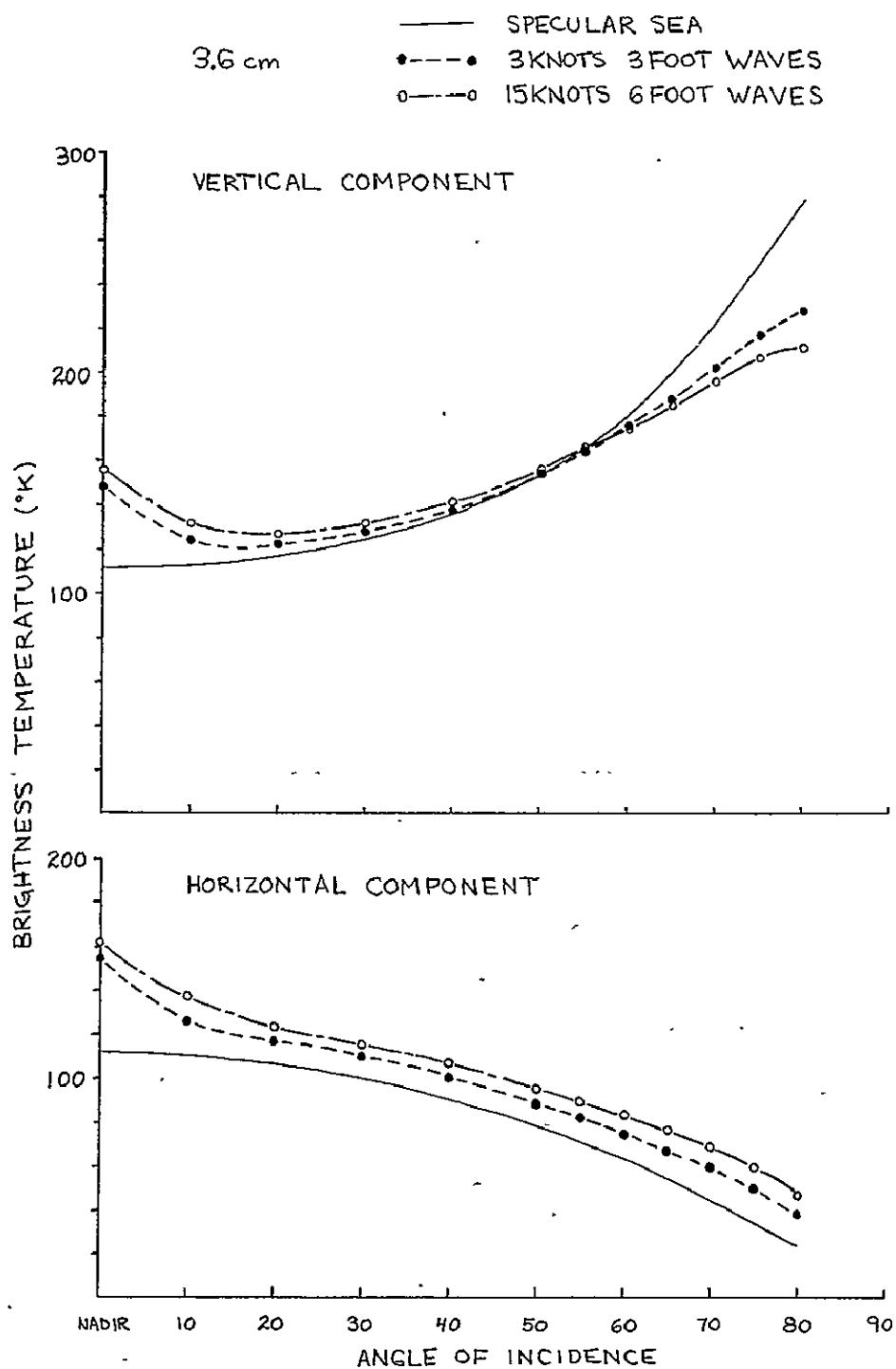


Figure 47-4.- Brightness temperature data versus angle of incidence for horizontal and vertical components, 3.6 cm.

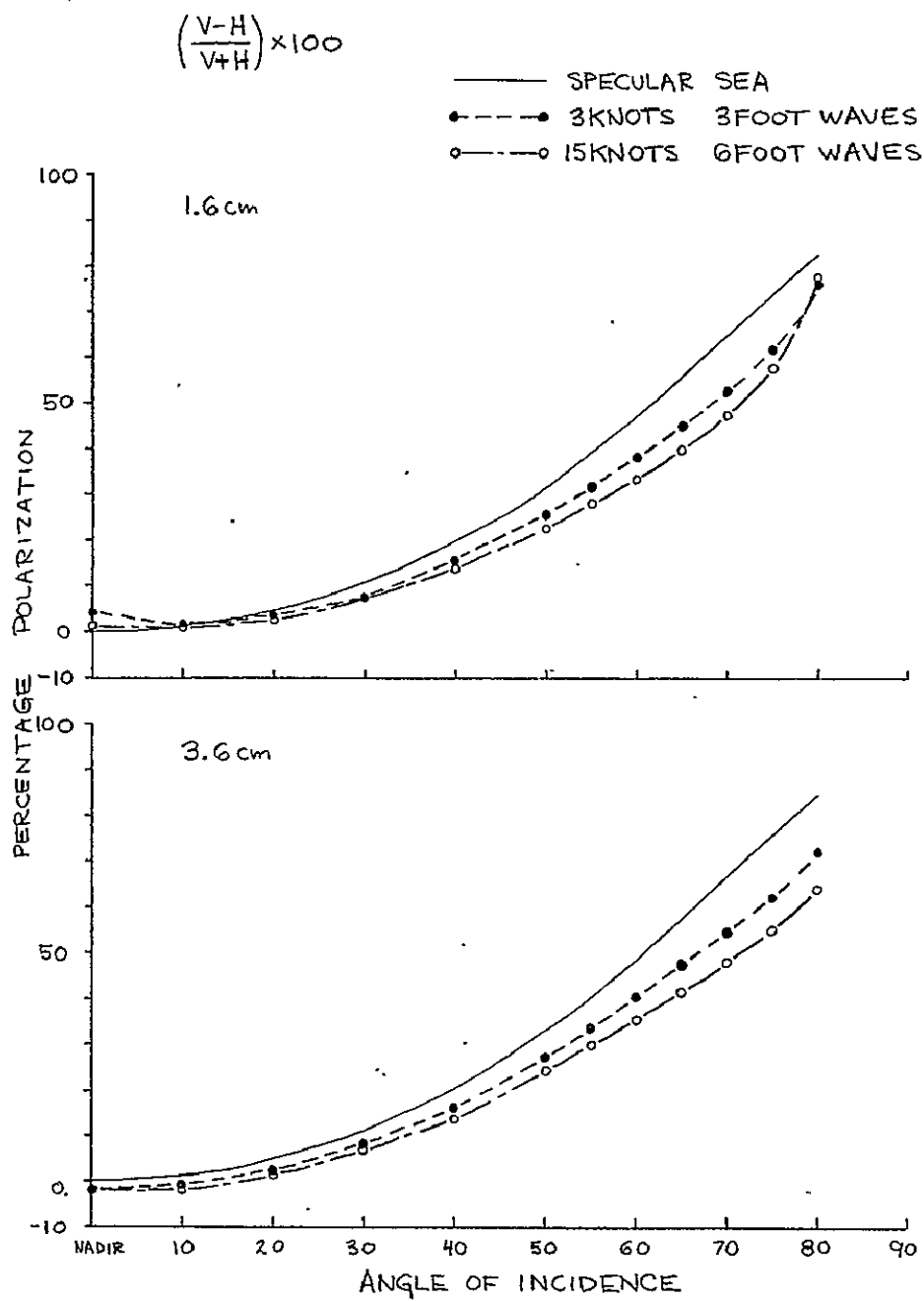


Figure 47-5.- Percentage polarization data versus angle of incidence, 1.6 cm and 3.6 cm.

47-12

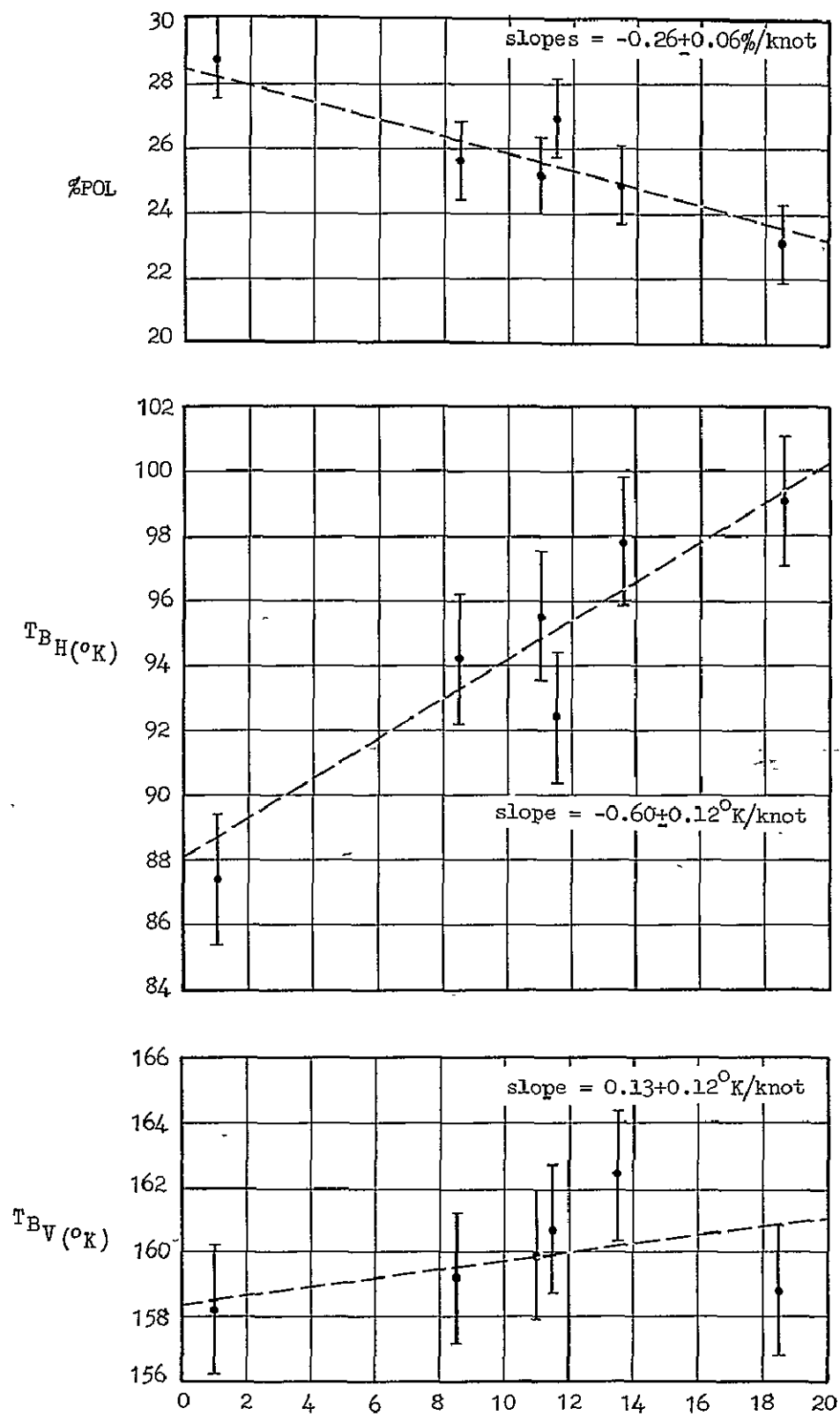


Figure 47-6.- Fifty degree incidence angle, 1.6 cm.

SECTION 48

RADAR AND OCEANOGRAPHY

by Richard K. Moore
and Gerald Bradley

The University of Kansas

N71-11165

INTRODUCTION

Spacecraft radars have several potential applications related to remote measurements of significant characteristics of the ocean. Radar instruments available for these measurements include the scatterometer, which measures radar reflection coefficient as a function of incidence angle, the radar altimeter, which measures the mean sea level, and the radar imager, which measures the radar signature of specific areas of the ocean and ocean-land interfaces. Ocean characteristics that can be determined using these instruments include predicted ocean wave spectra using scatterometer data, variations in mean sea level using the radar altimeter, and sea ice conditions using the scatterometer and the radar imager. In addition, monitoring functions can be performed using spacecraft imaging radars to catalog worldwide shipping operations, to measure coastal changes due to storms and to monitor small scale ocean wave patterns.

Recent studies of radar oceanographic applications conducted at the University of Kansas have been directed toward a further understanding of the relationship between measured radar response and ocean surface characteristics. These studies have included the analysis of differential scatterometer coefficient data measured with two scatterometers (at radar frequencies 13.3 GHz and 0.4 GHz) and the variation of these data with sea state and wind conditions. Associated with the scatterometer study has been the analysis of the accuracy and calibration of scatterometer systems in addition to an examination of methods available to implement such systems in space.

The first stage has been completed of a continuing study of the accuracy of radar altimeters operating over the ocean from spacecraft. Theoretical work has continued on radar backscatter with some of the emphasis placed on scatter from the ocean. In this connection modeling experiments using electromagnetic waves at the Naval Research Laboratory and in the U. S. S. R.

Scatterometer measurements over the North Atlantic in the last two years clearly demonstrate the strong correlation between the shape of the scattering coefficient curves at 13.3 GHz and wind speed. Comparable measurements by Naval Research Laboratory at about 9 GHz show a much smaller variation in the scattering coefficient curves than observed at 13.3 GHz. In our own measurements at 0.4 GHz we show little variation with wind speed. Because of difficulties in calibration of the 13.3 GHz scatterometer on the NASA MSC aircraft it is not possible to make strong statements at this time about the absolute level of the scattering coefficient variation with wind speed, but the statements about the curve shape can be made with a high degree of confidence.

Studies of a technique for constructing spacecraft scatterometers using radiometer-like receivers show that this technique can yield precision measurements with less power than would otherwise be required for the transmitter. Measurements by Bell Telephone Laboratories indicate that a microwave radiometer can indeed be used to calibrate the atmospheric attenuation for the scatterometer.

Analysis of the tracking errors for a split-gate radar altimeter show that such a system can theoretically have accuracies of the order of a few tens of centimeters or better.

Both our own work and that of others indicate that the primary cause of radar return from the sea at angles away from the vertical is very fine structure whose height is of the order of the radar wave length.

SEA-STATE MEASUREMENTS

The discussion of sea-state measurements is in three parts: description of the results from Missions 70 and 88 of the NASA Earth Resources Aircraft Program, description of the scatterometer system used in that program at 13.3 GHz, and discussion of the problems in validating the data obtained with this scatterometer.

Results of Missions 70 and 88

Mission 70 was conducted in the spring of 1968 from a base in Keflavik, Iceland, to points in the North Atlantic near several weather ships. Mission 88 was conducted during the spring of 1969 from a base in Shannon, Ireland, to weather ships in both the North Atlantic and the Irish Sea. The highest winds on Mission 70 were about 38 knots in the North Atlantic; the highest winds on Mission 88 were about 50 knots in the Irish Sea.

During Mission 70 only the vertically polarized 13.3 GHz scatterometer was used. On Mission 88 this instrument was supplemented by a 1.6 GHz scatterometer and a multipolarization 0.4 GHz scatterometer. Operation of the 13.3 GHz system was not as good on Mission 88 as on Mission 70 because of high noise levels. A technique was developed, however, that permitted correction of most of the data for the effect of these high noise levels. The 1.6 GHz system was not used because it created strong electromagnetic interference to other systems in the aircraft and at the same time was itself susceptible to EMI. This EMI appeared to originate from problems associated with a heating element necessary in the scatterometer rather than from the scatterometer itself. The 0.4 GHz scatterometer appeared to perform satisfactorily on Mission 88. Only preliminary analysis has been made of the data from this system because it appears that the scattering coefficient does not vary significantly with wind speed as originally expected, even though the data appear good.

Figure 1 shows a representative collection of scattering coefficient curves for different wind speeds from Missions 70 and 88. These curves have been corrected to remove, as nearly as possible, the effect of noise on the data.

The shapes of the curves from the different missions for comparable wind speeds are quite similar, but the absolute level is not consistent either from one mission to the other or within a single mission. Apparently there are errors in absolute level calibration of the order of ± 3 db. This judgment is based upon the clustering of the curves in the 5 to 10° region, and upon both theoretical and experimental observations by other observers that indicate a crossover should occur in the curves for different wind speeds in the neighborhood of 10° . Fundamental characteristics of the theory upon which all investigators agree indicate that curves having higher σ° values at large angles of incidence should have lower values of return at small angles of incidence (1). Thus, the steeper curves should cross over the less steep curves and no curves should be parallel with different amplitudes. Because of this, we have proceeded to analyze the data from these missions in terms of the shapes of the curves, rather than their absolute level.

Figure 2 shows a collection of normalized scattering coefficient curves for the upwind condition with both Mission 70 and Mission 88 represented. Normalization has been achieved by assigning a common value to the scattering coefficient at 10° . Such a normalization permits comparing the shapes of the curves without concern for their absolute amplitudes. It also shows the way in which comparing values of scattering coefficient from 10° with those from any other angle shown on the curve permits determination of wind speed from such measurements. Although normalization could have been achieved by bringing the returns at any angle to a common level, 10° was chosen because it is close to the value of crossover predicted by all of the theories and observed in many measurements earlier involving wind speeds less than about 20 knots (2).

Figure 2 shows that the curves for lower wind speeds are indeed steeper than the curves for higher wind speeds. The Mission 70 and Mission 88 curves are consistent with each other except for the difference between the two 12.5 knot curves. Plotted this way, the curves get closer together, for increasing wind speeds, meaning that there appears to be some kind of saturation when the scattering coefficient is expressed in decibels — but, of course, the decibel is a logarithmic measure. Comparison of the scattering coefficient in decibels with the log of the wind speed is more appropriate. Figure 3 shows that the apparent saturation effect may be simply a consequence of the scales used. Although the curves appear to bend over somewhat above 30 knots, evidence of saturation is mission. For upwind data the experimental values show $\sigma_{12.5}^\circ = (u/12.5)^{2.7}$ below 29.5 knots and $\sigma_{29.5}^\circ = (u/29.5)^{2.15}$ above 29.5 knots, where u is the wind speed in knots.

Figure 4 shows a comparison between upwind and crosswind measurements for Mission 88 data. Clearly, the signal received across the wind is considerably less than that received upwind. Thus any operational system must have a means for determining wind direction to overcome this effect; otherwise high-wind-speed measurements made across the wind direction would be confused with lower wind speed measurements made in the upwind-downwind direction. Figure 3 shows the cross-wind variation of σ° with wind speed.

Figure 5 compares the results at 0.4 GHz and at 13.3 GHz. Only the extremes for the higher frequency are shown, with three sample curves for the

lower frequency. The data of Figure 5 show that the effect of wind speed on scattering return is much less at the lower frequency. In fact, for these three curves the effect is reversed; that is, the curve for the higher wind speed is steeper than that for the lower wind speed. They are so close together that this may not be a significant factor. This result is similar to measurements at the same frequency by the Naval Research Laboratory.

Scatterometer System

Scattering coefficient is measured on the MSC aircraft using a scatterometer that depends on Doppler frequency to separate the returns from different angles and uses a fan beam antenna to permit simultaneous measurement of signals from many angles. This is illustrated in Figure 6 where the illuminated region on the ground is shown beneath the aircraft with a sample Doppler frequency cell. The Doppler frequency changes with angle because the relative velocity between the aircraft and a point on the ground is a function of the angle. The relative velocity is greatest directly ahead of and behind the aircraft and is zero directly beneath the aircraft.

The scatterometer used is shown in the block diagram of Figure 7. A klystron supplies the transmitted signal to one antenna; the signal is received on a different antenna and split into two components. One of these is phase shifted by 90° , and the other is transmitted without phase shifting. This technique is necessary so that the positive Doppler frequencies from ahead of the aircraft can be separated from the negative Doppler frequencies from behind the aircraft. The direct and phase shifted signals are mixed with a greatly attenuated sample of the klystron signal, and the resulting audio outputs are amplified in the two channels called redop-1 and redop-2. The two outputs are recorded on separate channels of a tape recorder in the aircraft. An audio calibrate signal is inserted in one channel at a frequency higher than the highest Doppler frequency received. It is used to modulate the incoming signal, and the resulting sidebands pass through the same mixer and audio amplifier as the non-quadratured incoming signal. Thus, the calibration signal, which is proportional to the transmitter power level, experiences the same overall attenuation as the received signal, and any changes will be reflected in changes in the amplitude of the calibrate signal. In this way, the radar range equation parameters are continuously monitored and the system operation is 'normalized' during the digital data processing of the recorded scatterometer measurements to compensate for variations in these parameters.

In the data processing procedure the data tapes are subjected to a preliminary analog spectral analysis used to evaluate data quality and general characteristics of the scatterometer measurements. The data tapes are then digitally processed, dependent of course on a sufficiently high data quality indicated by the analog preliminary analysis. The tapes are digitized and further analysis is accomplished in the Computation and Analysis Division at MSC. Figure 8 shows the basic procedure presently in use for digital analysis. It is completely different from the system used prior to December of 1968, but should achieve comparable results. Mission 70 data have been reprocessed using this program.

The digitized information in each channel is passed through a complex fast-Fourier-transform program. Proper combinations of the real and imaginary components of the in phase and quadrature complex transforms produce outputs proportional to the positive and negative Doppler frequencies in the original received signal. The output of the digital program is about 4,000 separate complex numbers representing frequencies whose spacing is only a few Hertz. The final filtering operation consists of combining enough components to represent the bandwidth desired, with suitable weighting to adjust the filter passband shape.

Figure 9 shows a sample spectrum obtained for returns from the ocean at 49 knots. In this particular spectrum, the calibration signal does not appear since it was obtained under conditions where the aircraft was bouncing so much that the calibrate signal frequency apparently was being shifted by vibration of the calibration oscillator. This occurred only on the 1,500 foot run of Mission 88. The actual received spectrum is a maximum of zero frequency, corresponding to minimum range at the zenith angle and decreases with increased Doppler frequency according to the radar equation and the decrease of σ° with incident angle. To improve the performance of the system for the weaker signals and still remain within the dynamic range of the recorder, the gain characteristic of the amplifier is shaped so that small signals at high frequencies are amplified more than the weak signals at the lower frequencies. Because of this, a peak occurs in the spectrum shown at about 4,000 Hertz, and the signal decreases for lower frequencies. With the steeper scattering coefficient curves associated with lower wind speeds, the peak in this spectrum is at a lower frequency, but it always has a shape similar to this because of the extreme gain reduction at frequencies below 2,000 Hertz.

Figure 10 shows a scatterometer power spectrum obtained over agricultural terrain. It appears flatter than that over sea and is also a closer representation of the spectrum at the input because the gain of the amplifier is reduced less for the low frequencies over land than over sea. The calibrate signal can be seen in this figure at about 10 kHz.

Data Validation Study

Table I shows the various items presently being considered in the data validation study.

TABLE 1: SCATTEROMETER DATA VALIDATION STUDY

Analysis of calibrate signal variations and the effect on the absolute level of the σ° vs θ curves.

System noise analysis and the effect of noise source location and level on data validity.

Analysis of overall system transfer response (including data tape recorder) and the prediction of data validity versus operating point.

Analysis of the effects of saturation on scatterometer data.

The largest remaining problem with sea return scatterometry involves the effect of calibration signal variations on data validity. Recent studies have been performed on the effects of signal-to-noise degradation on data validity with a resultant modification in the digital data processing program which compensates for signal-to-noise level variations. In addition, we have completed an analysis of saturation effects in the receiver-tape recorder subsystem and the effects of saturation on data validity. Unfortunately, all over-land scatterometer measurements have been subjected to one or more of these three effects (i.e. calibration variation, excess noise, saturation) and the validity of the data is questionable. However, for all over-sea scatterometer measurements, the data in past missions appears to be subject only to calibration signal variation and the excess noise problem. As mentioned, we have devised a technique to compensate for the latter effect.

Calibration variations are an unknown for past mission data, and force interpretation of the sea data on a relative rather than an absolute basis. The shape of the scattering coefficient curve measured by this system appears to be correct (for noise compensated data) for incidence angles up to 35 or 40° for the oceanic data. The consistency of the results taken in separate years has been demonstrated and the basic problem of obtaining the curve shape is independent of the absolute calibration problem.

The absolute calibration, or 'bias' problem, is related to the method used to sample any variations in the scatterometer system parameters. In concept, the calibration signal recorded on tape is designed to be proportional to the transmitter output power, the receiver gain, and any variations in component operation. An injected calibration signal, at an audio signal higher than the maximum Doppler frequency, is used to modulate the incoming rf receive signal. The magnitude of the calibration signal at rf is then directly proportional to the amplitude of the calibrate oscillator as well as the amplitude of a sample of the transmitter output coupled into the receive channel. Any variations in mixer conversion loss or any changes in receiver amplification are reflected by corresponding changes in the amplitude of the recorded calibration signal. The correct operation of this method is dependent upon knowing accurately the amplitude of the calibration oscillator output, the coupling constant of the transmitter sample, and the calibration modulator characteristics.

In the old system the calibration signal was provided by a standard Hewlett Packard audio oscillator. In the new system it is provided by an internal oscillator. In either case the amplitude of the oscillator signal must be monitored on an electronic voltmeter with a presentation for the operator. The voltmeter used in the past has been calibrated at regular intervals by the Central Calibration Laboratory at MSC. However, we have no record as to the amount of change necessary to bring it into calibration at these regular intervals. Thus we do not know whether the voltmeter remained calibrated during any particular sequence of measurements.

Perhaps the most critical problem associated with the calibration of the scatterometer involves the use of a ferrite modulator to introduce the calibration signal into the receive channels. Because ferrite devices are especially

temperature and vibration sensitive, use of a ferrite modulator can severely limit the stability and reliability of the calibration method and consequently decrease the confidence in the measured scatterometer data. We have recommended that the ferrite modulator be subjected to controlled environmental testing to determine the relation between calibration signal injection accuracy and variable operating conditions. In addition, we have begun an intensive study of alternate methods of calibrating the scatterometer which promise to improve the stability and reliability of the system. Of special interest in the use of alternate methods is the elimination of the ferrite modulator now placed directly in the return signal path. The use of the ferrite device in the signal path, in addition to the instability inherent in the device, may produce presently unknown temperature-dependent phase shifts on the rf signal. These phase shifts result in errors in the separation of positive and negative Doppler frequencies and consequently errors in the scattering coefficient calculation.

This problem is eliminated in the scatterometer being constructed for the Navy at the University of Kansas by modulating the calibrating signal on an attenuated version of the transmitter signal with the resulting signal and its sidebands being coupled into the received signal path through a directional coupler. By making the amplitude of the calibration signal strong compared with the sample of the transmitted signal on which it is modulated, the amplitude of the sidebands becomes proportional only to the amplitude of the transmitter signal. In this system the calibrate signal provides an actual measure of the overall performance of the radar since its input amplitude is proportional to the transmitter signal strength and it undergoes the same attenuation and amplification in the receiver as the received signal. If at all possible, the MSC system should be modified to work the same way.

During Mission 88 strong signals that appeared to be harmonics of the 400 Hz power supply frequency of the aircraft appeared in the data. Figure 11 shows a spectral plot versus time indicating the presence of these lines in the spectrum. Initial analysis of the data was with arbitrarily set filterband centers and some of the bands (probably including the calibrate band) contained these undesired signals. Subsequent reworking of the data has been based on moving the filters to points between these lines in the spectrum so that they could not affect the amplitude at any particular Doppler frequency and angle.

The noise level during Mission 88 was high. A measurement of the noise prior to the mission showed that it was essentially uniform across the passband of the amplifier. Since the signal is integrated for many independent sample periods, it is possible to correct the output of the receiver which contains both signal and noise power by subtracting the noise power from the signal power, just as a radiometer determines the signal by subtracting noise from the sum of signal and noise. In the case of the radiometer, this is achieved by switching from a known source to the combined signal and noise and examining the difference between the output in the two positions of the switch. For the scatterometer it is achieved by measuring the noise level at a frequency beyond the maximum expected Doppler frequency and subtracting the results noise power from the output of the receiver. Figure 12 shows this technique. A similar correction is made for the calibrate signal.

Although saturation apparently has not been a problem over sea, it has been evidenced in several over-land missions. Accordingly, an analysis was made of the effect of saturation on the spectrum. When the signal is saturated, cross modulation products between strong amplitude components in the low frequency part of the spectrum change not only that part of the spectrum, but also the high frequency part. Actually the effect is greater on the high frequency part of the spectrum as shown in Figure 13. Clearly such a change in the shape of the spectrum can cause serious errors in interpretation of the data. In-flight procedures now being established should eliminate this problem.

Over land it is very important that the signals received from ahead of the aircraft be correlated with those from the same location after the aircraft has moved closer to it. Thus the problem of proper alignment of the flight direction and the pointing angle for the antenna is significant. Fortunately, over the ocean the statistical properties of the sea somewhat to the side of the flightpath should be the same as those directly along the flightpath. Consequently, the alignment problem should not affect the oceanic data.

SPACECRAFT SYSTEMS STUDIES

Use of the radio telescope principle in active microwave systems has been studied during the year. The basic principle of a radio telescope, or a microwave radiometer, using the Dicke technique involves switching between a known noise source that is used for calibration and the noiselike signal due to thermal radiation and receiver noise combined. Integration of the noise over a long enough period reduces the variance to a small amount. Thus when the variance is small enough, a signal causing only a very small increase in the receiver noise can be separated from the combined signal and noise by subtracting out the receiver noise calibration obtained by like integration of the signal from the calibration noise source. With the radar, the noise-like signal consists of the radar return whose noise-like property is established by the differing Doppler frequencies from different parts of the illuminated cell. The signal that must be determined separately consists of a combination of the receiver noise and the noise coming in through the antenna, which would be signal for the microwave radiometer. Although the Doppler bandwidth of a radar signal, even for a radar on a vehicle traveling at low-altitude orbital velocities, is quite narrow compared with the typical radiometer, use of a relatively large resolution cell permits sufficient averaging to reduce the variance significantly. For a practical example at 3 cm wavelength, this means that a signal to noise ratio of the order of unity permits very precise measurements. The principle is illustrated in Figure 14. Actually, unlike the radiometer, no switch is involved at the input. The signal is transmitted for a short period and the receiver is left on for a longer period than that required to receive all echoes from the ground. The output is switched so that the signals received while the echoes are returning to the radar are processed by one integration channel and the signals received during the time when no echoes are present are processed by another channel. If the same number of independent samples is integrated in each channel, the output signal to noise ratio is as given on the figure, where r is to number of samples and $(\text{SNR})_1$ is the signal-to-noise ratio prior to integration. (3)

Because a receiver operated in this fashion need have only about unity signal-to-noise ratio, less transmitter power is required for a system of this sort since the transmitter need not establish a higher signal to noise ratio.

Combination of the 13.3 GHz information obtained in the NASA program, the 9 GHz data obtained by Naval Research Laboratory, and the 0.4 GHz data obtained by both agencies indicates that the higher frequencies are desirable for measuring winds at sea by the use of related variations in radar return; however, precipitation and cloud attenuation may be of some significance in a space radar used for sea-state measurement. Accordingly, a proposal has been made to fly a combined radar and radiometer, with the radiometer being used to establish the attenuation which can be applied as a correction to the radar signals. Fortunately, communications people have recently been conducting research leading toward the use of microwave radiometers to determine attenuation along communication paths, thereby obviating the need for establishing a transmitter at one site and a receiver at another. In one such measurement reported by Bell Telephone Laboratories (4), the attenuation calculated from the "sky brightness" measured by an upward looking radiometer was compared with attenuation measured by a radio telescope tracking the sun. The success of the technique at 16 GHz is indicated by Figure 15. Clearly attenuations up to about 6 db can be determined this way quite accurately, at least under the conditions of the experiment. The dispersion appears to be only about 2 db even for attenuations of 10 db.

Combination of the results obtained from Missions 70 and 88 with the use of a radiometer-like receiver and a radiometer for measuring attenuation indicates that it should be possible to measure wind speeds at sea within an along-track scatterometer made of a scanning radiometer-radar. If the absolute level measurements made in the future verify our expectations, such measurements will also be possible with a crosstrack system which can, of course, obtain more data with each orbit. Figure 16 shows how the along track system might work. It is based upon using radar returns at two angles, 10° and 35° from the vertical. Figures 2 and 3 indicate that this technique should work for conditions where the wind and the flight track are in the same direction. Since the data of Figures 2 and 3 have been normalized to 10° , the system would work by taking the ratio of the signal observed at 35° to that observed at 10° for each point on the ocean. In Figure 16 the 35° point for the spacecraft position at the left is the same as the 10° point for the spacecraft position at the right. In essence, this is the same as the along track scatterometer used in the aircraft program except that a scanning pencil beam would be used for this system rather than the fan beam with Doppler separation of angles, as in the aircraft system.

ALTIMETER ACCURACY

The applications of an accurate radar altimeter carried in a spacecraft to both oceanography and geodesy have been previously documented (5). Such a system could work effectively over the oceans. It could not work effectively over the land because of inaccuracies in radar altimeter measurements where the height variations of the illuminated pattern patch are large.

Many accuracy calculations for radar range measurement are based upon

signal-to-noise ratio. Unfortunately, the signal from an area-extensive surface such as the ocean, fades in such a way that the effective signal-to-noise ratio can never be more than a few dB, even though the actual signal-to-noise ratio can, in the mean, be very high. The trouble is that the radar return comes from many facets, and the difference in path length from different facets to the radar is enough that many revolutions of phase may occur even though the total difference in distance is small compared with the required measurement accuracy. The result is that the signal amplitude is governed by the Rayleigh statistical distribution.

One technique that is used to overcome the effects of noise and fading is the split-gate tracker. With this system the energy received in two different time intervals is compared. Moving the gates until the energy in each gate is equal means that the gates are positioned on the center of the pulse of the return comes from a point target (6). For a satellite altimeter operating over the ocean, however, the pulse extends for many microseconds because of scatter from angles away from the vertical. Thus, a split-gate system should be designed so that the gates center on the leading edge of the pulse. Received power in an average pulse increases linearly for a time equal to the duration of the rectangular transmitted pulse. Thus, to make the energies equal the first gate must be longer than the second one since the first one is associated with smaller return power. Analysis has shown that best results are obtained when the duration of the combined gates is equal to that of the transmitted pulse. There is a high probability that even for properly positioned gates the signal during the first gate will be greater than the mean while that in the second gate is less than the mean, so that an error signal is given when none should appear. Of course, there is also a probability that the signal in the first gate fades down when the second fades up, again giving a faulty error signal. To compensate for this effect, the feedback gain in the tracker that moves the gates must be reduced. If this gain is reduced far enough, the gate movement cannot be large enough to follow actual changes in altitude. Use of a simple prediction scheme, however, permits a much smaller gain to be used, with a resulting improvement in accuracy of range measurement. Errors as low as 10 cm can be achieved by integrating a 5,000 pulse per second altimeter return for a period of 10,000 pulses (two seconds), using a transmitted pulse duration of 0.1 microseconds (7). Figure 17 shows an example of the type of error obtained with an unambiguous pulse rate of 100 pulses per second as a function of the number of pulses averaged. The random error is reduced by averaging more pulses. The prediction error shown is based upon a linear extrapolation of past measurements over the period indicated. The error increases with the length of time involved because, of course, orbital altitude does not vary linearly as the prediction assumes. A more elaborate prediction system would permit reduced total error. Even in this case with a 0.1 microsecond pulse, an accuracy is achieved even though the "resolution" associated with such a pulse is 15 meters.

This sort of calculation assumes that the measurement is made with respect to a smooth ground plane. Phase differences that are actually caused by height differences, must be caused on a smooth ground plane by some sort of impedance difference. The problem with the ocean is to modify this analysis to determine exactly what surface is being measured with this precision. Is it

the crest of the waves? Or the trough? Or the mean sea level? The answer to these questions depends to some extent on the signal-to-noise ratio and to some extent on the type of tracker used. It is the next analysis that must be undertaken (8).

THEORY AND FUNDAMENTAL EXPERIMENTS

Theoretical developments at Naval Research Laboratory (9), in the U. S. S. R. (10) and at the University of Kansas (11) within the past several years all tend to show that most of the scatter appears to come from extremely small wavelets riding upon the larger waves of the ocean. Wright's theory, which is much like that of the other investigators, is based upon an approximation that is not valid when the height of the phenomenon involved is significantly greater than a sixth of a wavelength. We believe that the actual theoretical description is more complicated than this, but that this is a good first-order approximation to the actual scattering response. There are, however, disagreements about what the actual spectrum of wavelets of this size may be on the ocean under conditions in which waves are breaking, foam is present, and drop-lets from breaking waves are falling back on to the surface.

Ultrasonic experiments at the University of Kansas, electromagnetic experiments in the swimming pool at Naval Research Laboratory, and both ultrasonic and electromagnetic experiments in the U. S. S. R. confirm that, at least for small waves, this theory comes close to explaining the experiment.

Conclusions

Several conclusions pertinent to the space program can be drawn from the results of the research of the past year:

1. At 13.3 GHz the shape of the scattering coefficient versus angle curve is truly dependent upon wind speed, with a difference in the ratio of 35° scattering coefficient to 10° scattering coefficient of more than 10 db for the wind speed range from 12 to 50 knots.

2. Experimental error is sufficient that the absolute level of the curves must be established by better experiments. Hopefully, these can be conducted during the spring of 1970. Even with the error of measurement, however, the measured "absolute" value of scattering coefficient at 35° increases with increasing wind speed.

3. The difference between the measurements made by the Naval Research Laboratory at 9 GHz and the NASA MSC aircraft at 13.3 GHz must be resolved. The Naval Research Laboratory measurements indicate a variation with wind speed of about 3 db over the same range where the NASA measurements indicate a variation of more than 10 db. Although it is possible that part of this may be due to differences in technique and calibration, a real difference due to this relatively small range of frequencies (a 50% increase over the 9 GHz) may exist. Professor Pierson now believes he has a theoretical explanation for this.

4. The use of a radiometer-like radar receiver will permit a scattering coefficient measurement from space with lower signal-to-noise ratios, and consequently lower transmitter power, than would be possible with a more conventional radar receiver. Furthermore, the measurements by Bell Telephone Laboratories and other communications researchers indicate that calibration of the attenuation through the atmosphere by a radiometric measurement should be feasible. Such calibration would be used to correct the scattering coefficient of the ocean measured from a satellite.

5. Radar altimeters with accuracies of the order of a few tens of centimeters seem quite feasible for carrying on satellites.

6. Both theory and controlled experiment indicate that the major contribution to scattering from the ocean from angles away from the vertical is due to extremely small components with sizes of the order of the wave length of the incident radar radiation.

References

1. Skolnik, M., A Review of Radar Sea Echo, NRL Rpt 2025, July, 1969.
2. Beckman, P. & A. Spizzichino, The Scattering of Electromagnetic Waves from Rough Surfaces, MacMillan Co., New York, 1963.
3. Gerchberg, R. W., "Sensitivity Enhancement of a Limited Power Earth Sensing Radar", CRES Tech Memo 118-14, The Univ. of Kansas, August, 1969.
4. Wilson, R. W., "Sun-tracker Measurements of Attenuation by Rain at 16 and 30 GHz", B. S. T. J., vol. 48, no. 5, pp 1383-1404, 1969.
5. Greenwood, A. T., et. al., "Radar Altimetry from a Spacecraft and Its Potential Application to Geodesy and Oceanography", NYU Geophys. Sci. Lab. Rpt. TR-67-3, 1967.
6. Barton, D. K., Radar System Analysis, Prentice-Hall, Inc., Englewood Cliffs, N. J., 1964; p 365.
7. Lee, H. L., "The Range Error Statistics of a Satellite Radar Altimeter", CRES Tech. Rpt. 112-3, The Univ. of Kansas, Sept. 1969.
8. Lee, H. L., "Determination of the Level of Measurement on Sea Surface by Radar Altimeter", CRES Tech Memo 112-6, The Univ. of Kansas, March, 1969.
9. Wright, J. W., "A New Model for Sea Clutter", Trans. IEEE, vol. AP-16, pp 217-223, 1968.
10. Bass, F. G., I. M. Faks, A. I. Kalmykov, I. E. Ostrovsky, and A. D. Rosenberg, "Very High Frequency Radiowave Scattering by a Disturbed Sea Surface", Trans. IEEE, vol. AP-16, pp 554-568, 1968.
11. Fung, A. K., and H. L. Chan, "Backscattering of Waves by Composite Rough Surfaces", Trans. IEEE, vol. AP-17, Sept., 1969.

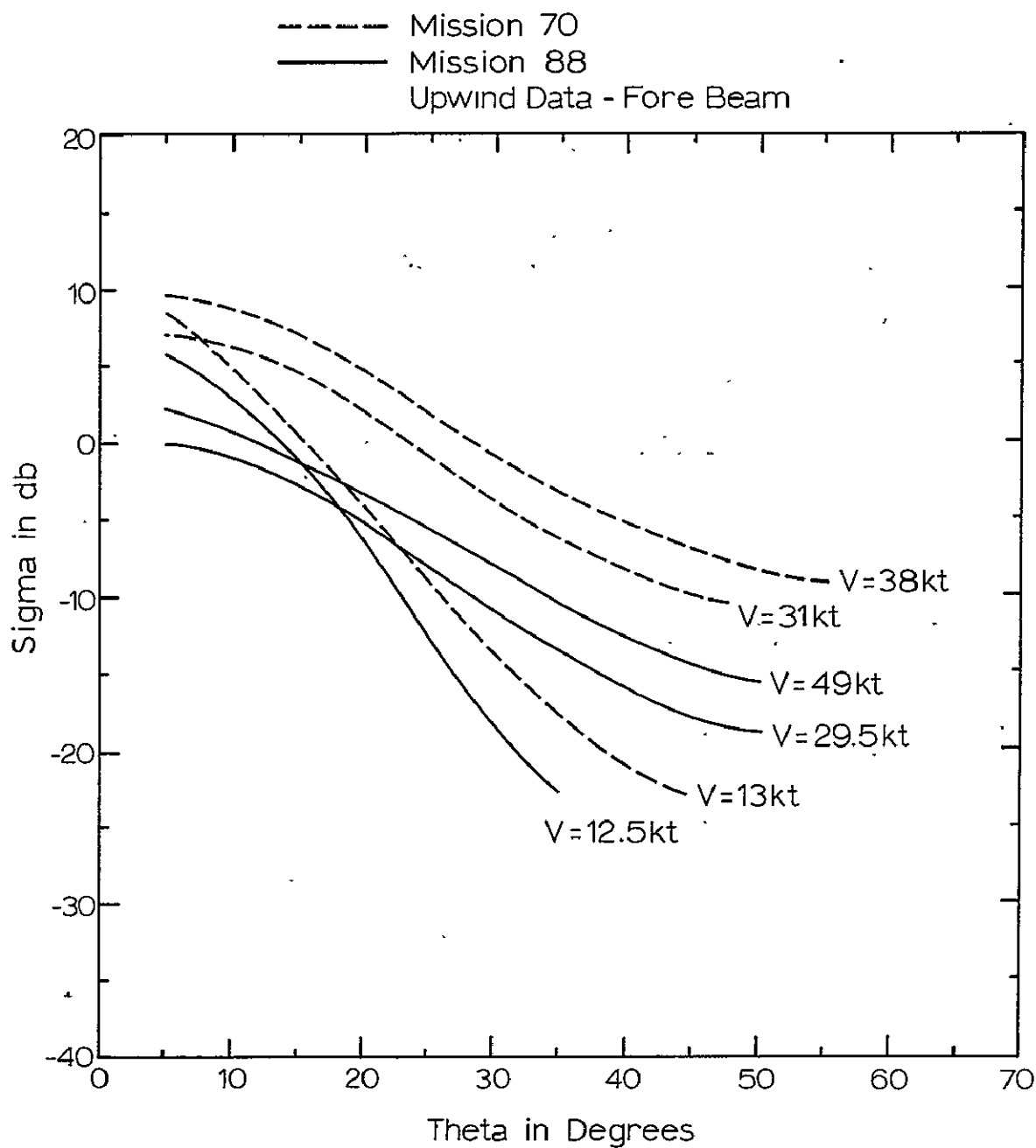


Figure 48-1.- Summary of sea-state scatterometry data.

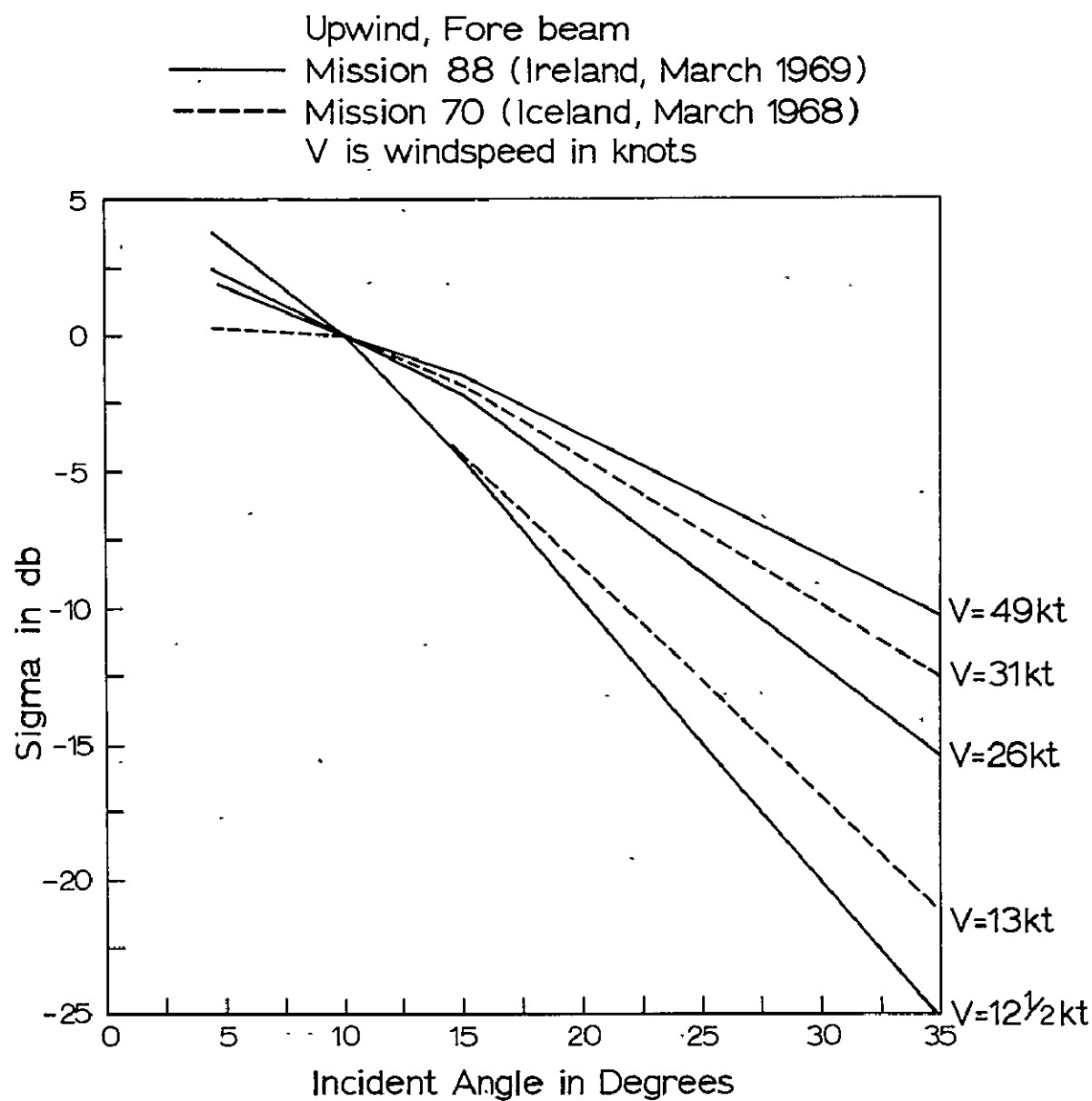


Figure 48-2.- Differential scattering coefficient of ocean at 2.25cm wavelength. Normalized to 0 db at 10°.

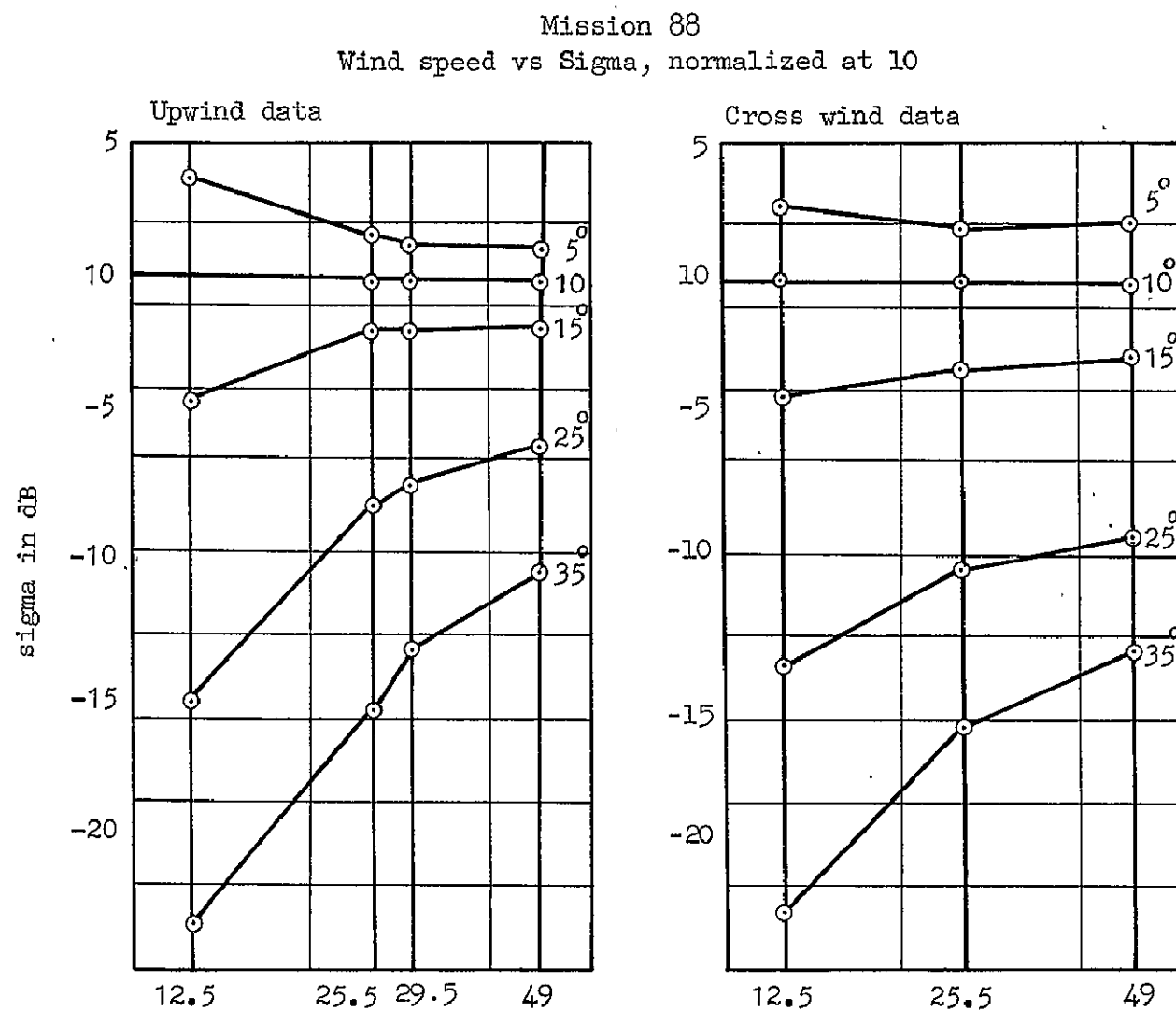


Figure 48-3.- Wind speed in knots.

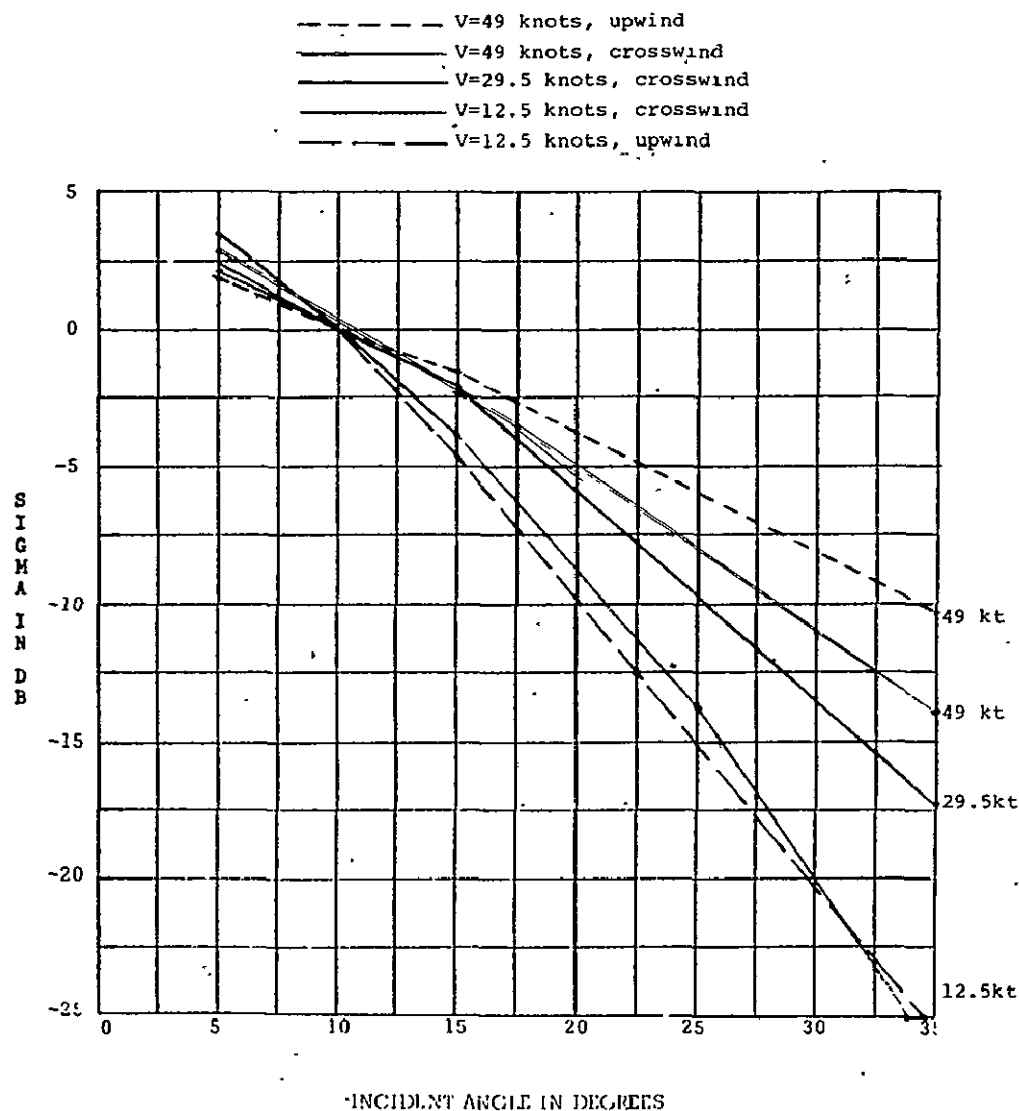


Figure 48-4.- Comparison of crosswind and upwind data
(Mission 88, Ireland, March 1969).

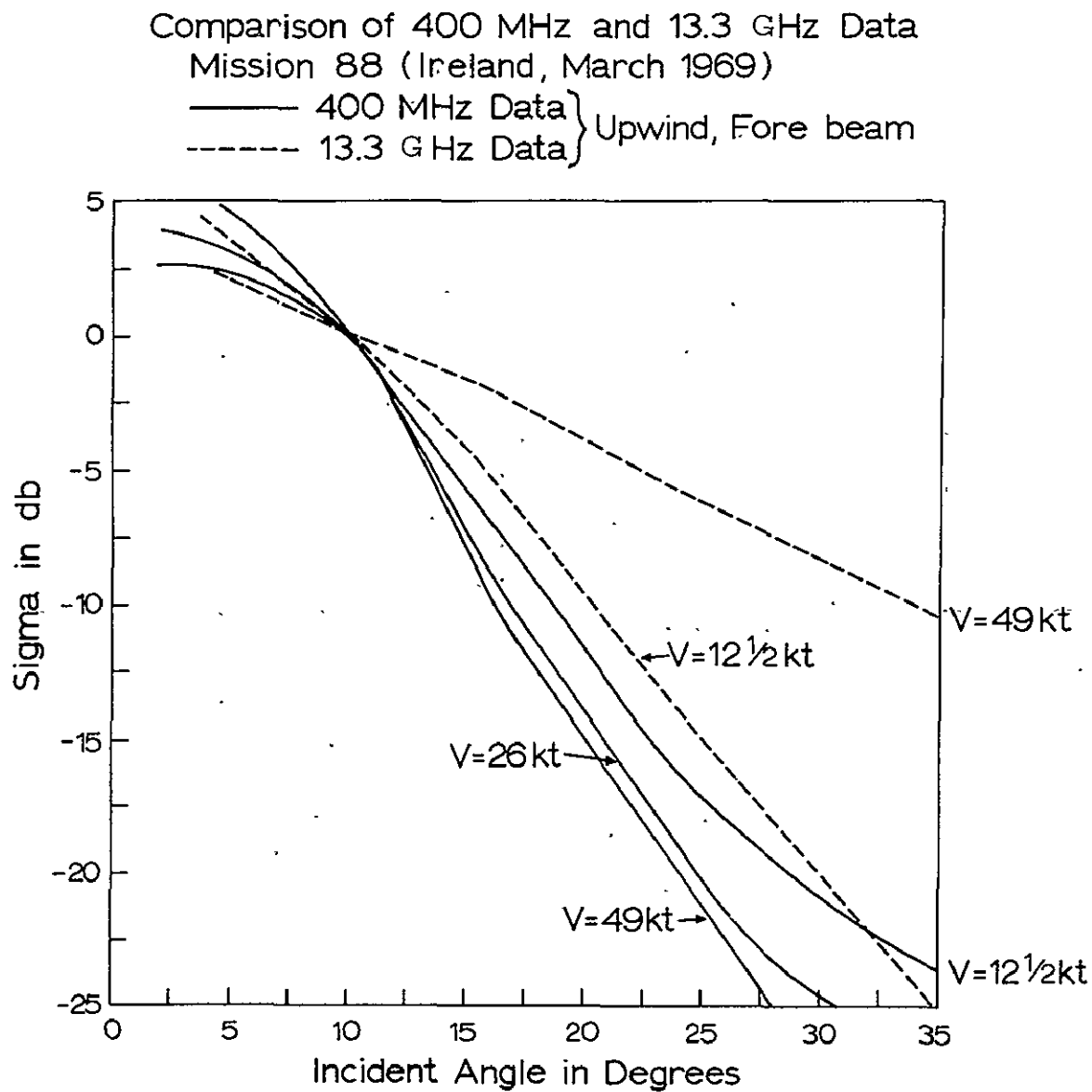
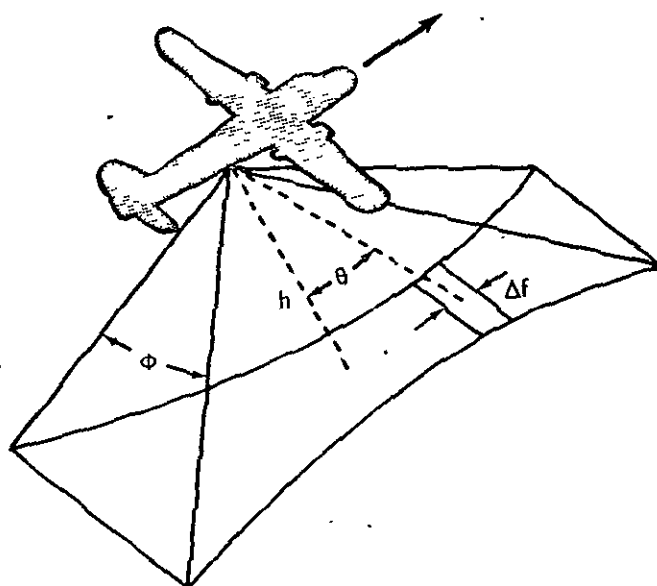


Figure 48-5.- Differential scattering coefficient of ocean.
Normalized to 0 db at 10° .

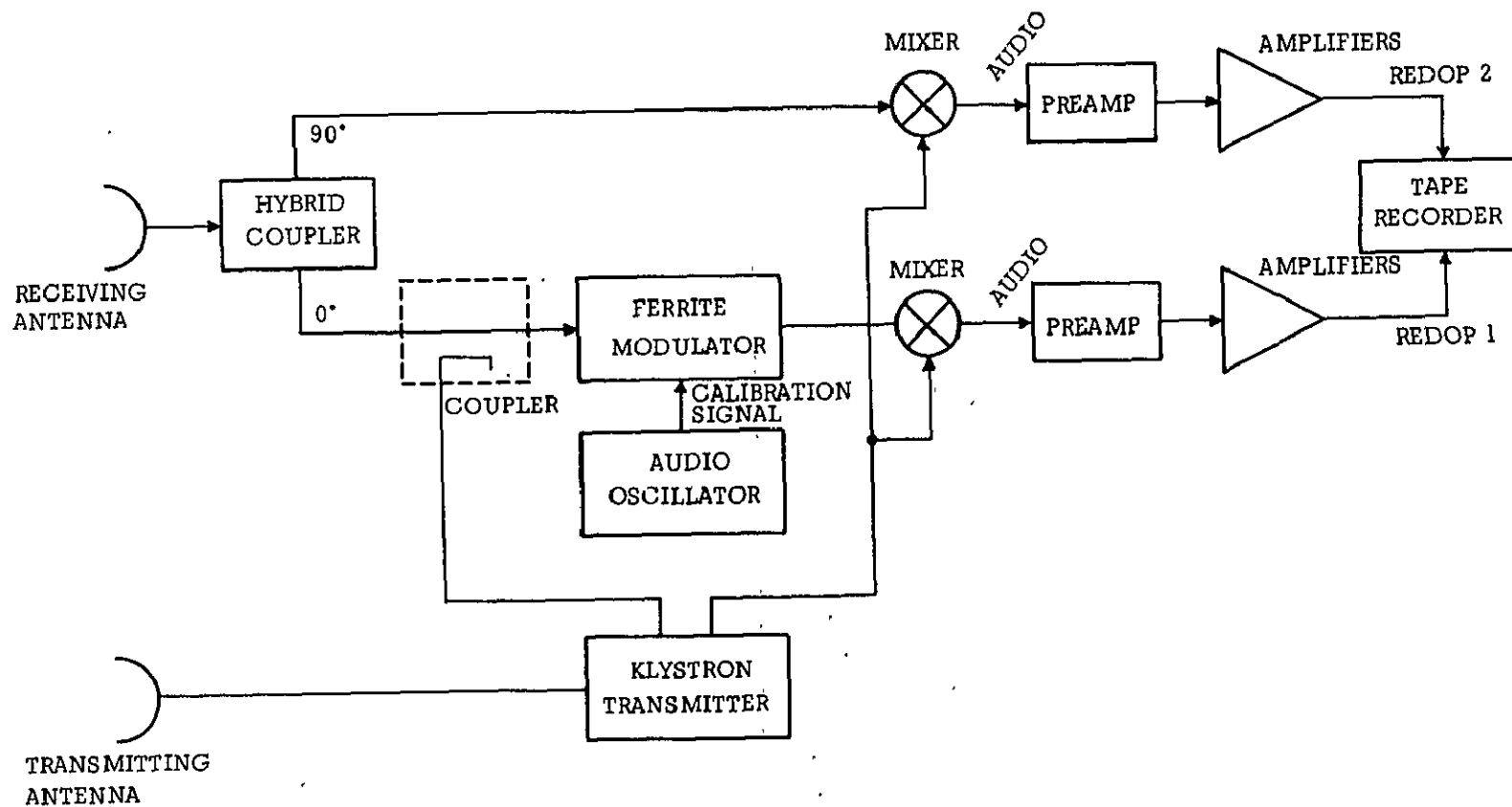


$$F_d = \frac{2V}{\lambda} \sin \theta$$

here: F_d = Doppler frequency
 V = True ground speed
 λ = Wavelength
 θ = Incidence angle,
 measured from nadir

ϕ = Lateral beam width angle
 h = Altitude above terrain
 Δf = Doppler resolution,
 determined by adjustment
 of spectrum-analyzer filter
 bandwidth during data reduction

Figure 48-6.- Doppler Scatterometer Measurement Geometry



13.3 GHz RADAR SCATTEROMETER BLOCK DIAGRAM

Figure 48-7.- Block diagram of 13.3 GHz radar scatterometer.

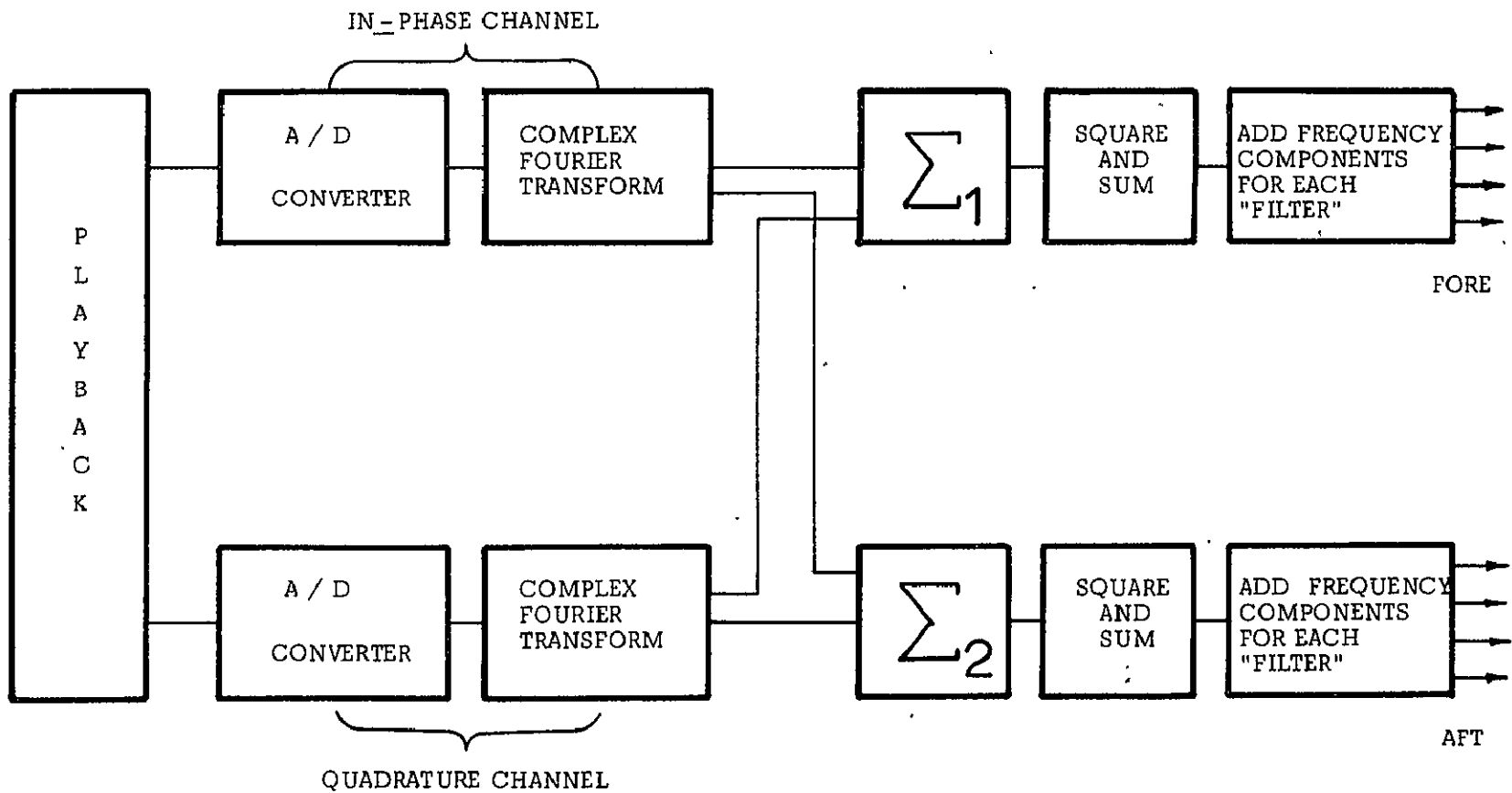


Figure 48-8.- 13.3 GHz scatterometer digital processing — present system.

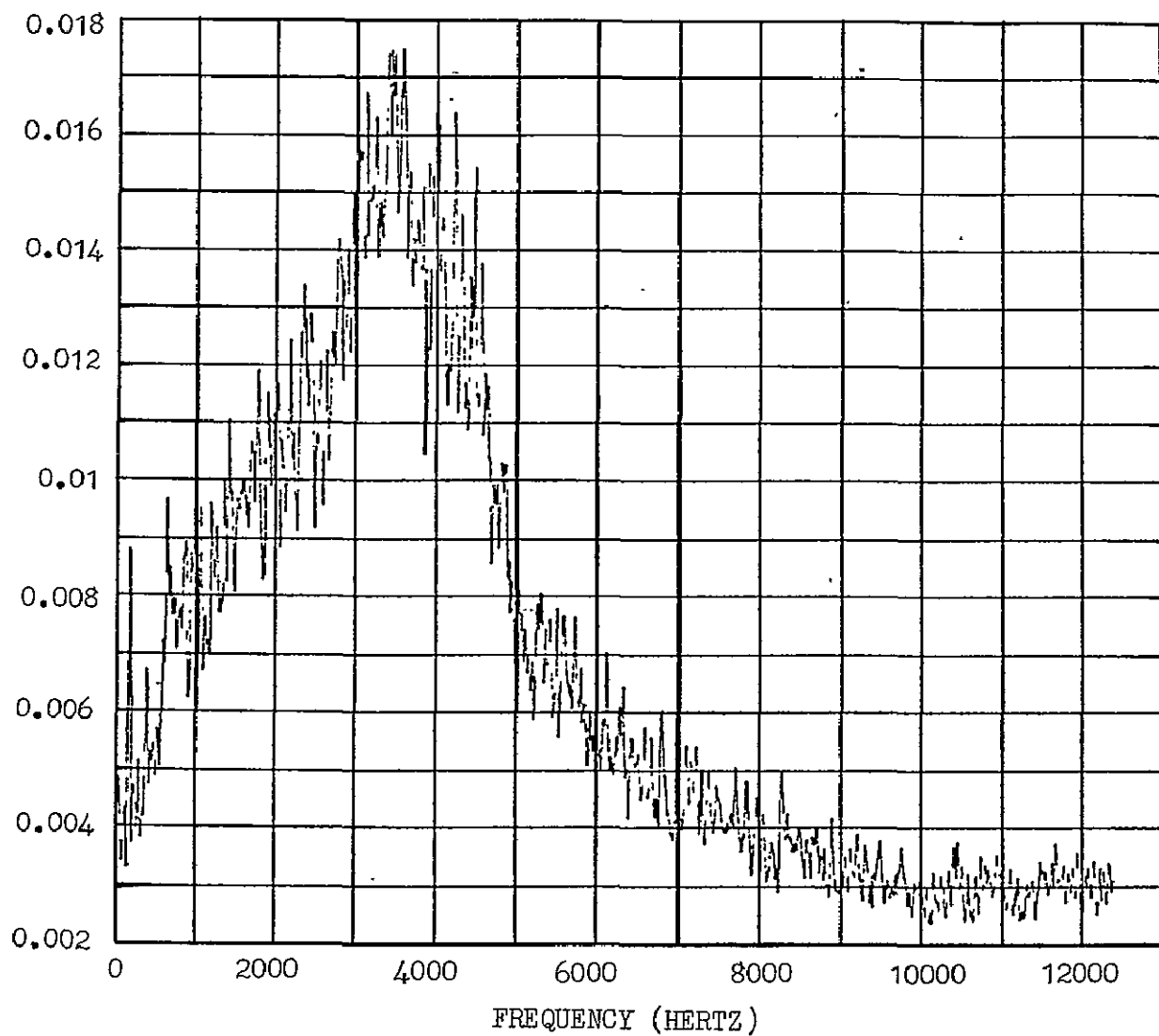


Figure 48-9.- 13.3 Scatterometer power spectral density —
for sea measurements.

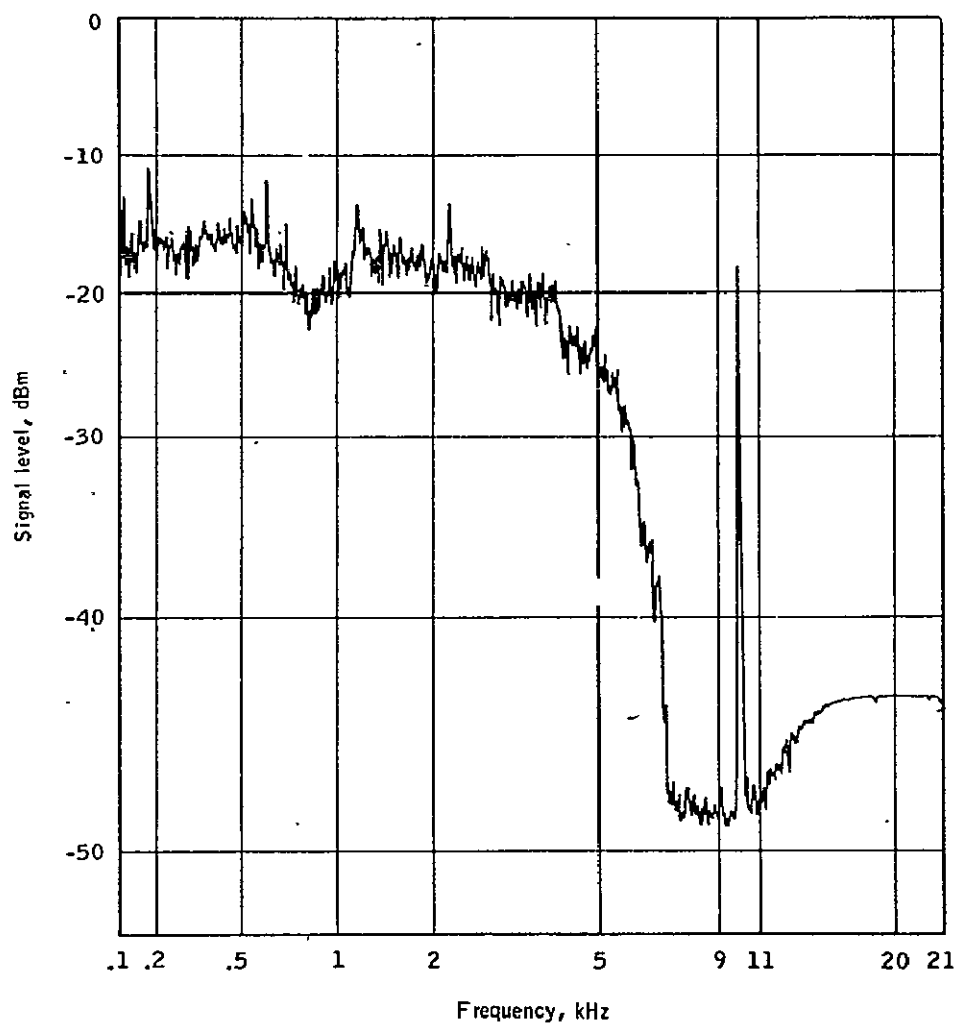


Figure 48-10.- Typical scatterometer power spectrum —
for agricultural terrain.

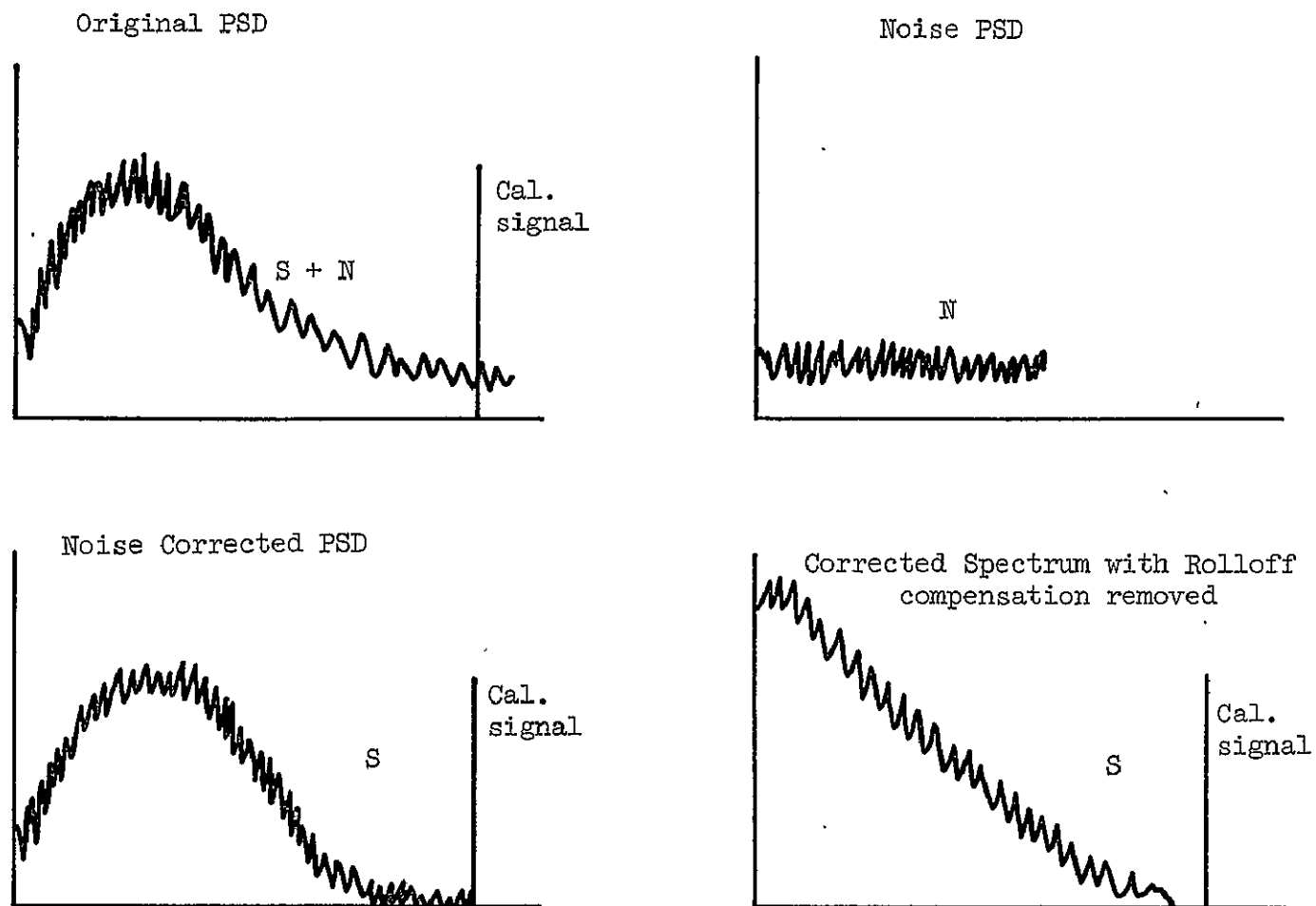


Figure 48-12.- Procedure used in digital data processing for improving data validity by removal of the scatterometer system noise from the data spectrum.

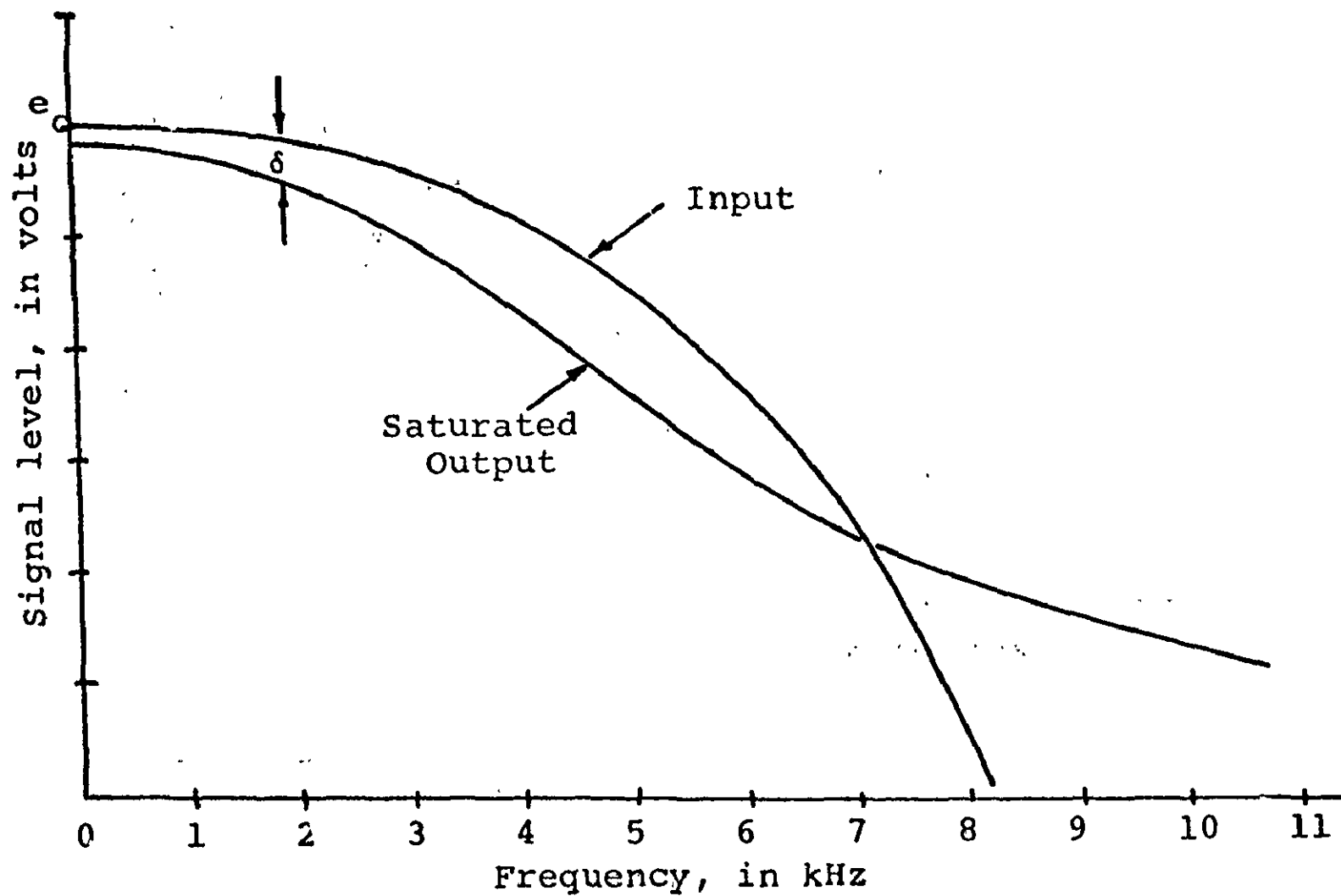


Figure 48-13.- The effect of saturation on the scatterometer data frequency spectrum.

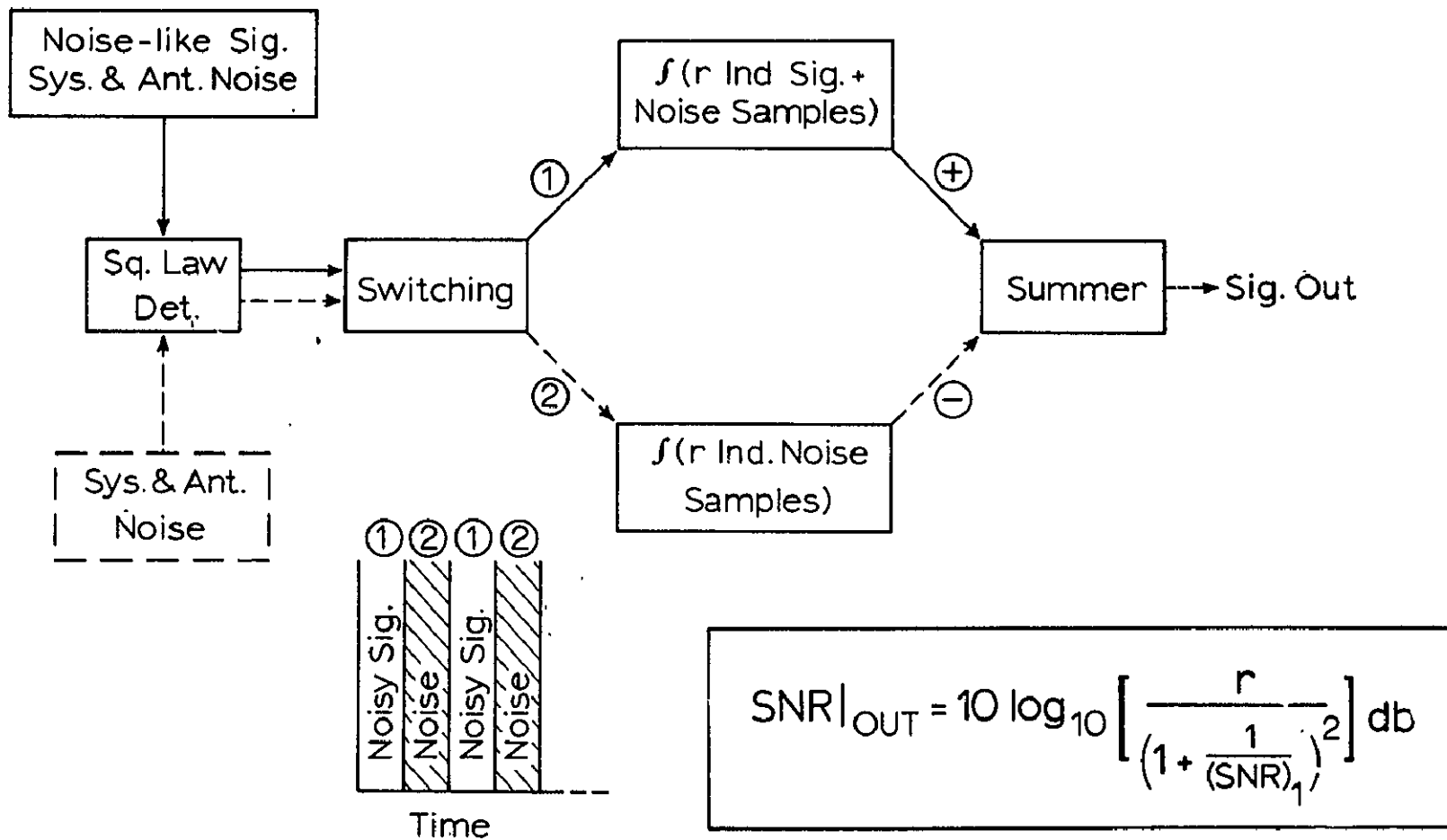


Figure 48-14.- Scheme for S/N enhancement — like noise signals.

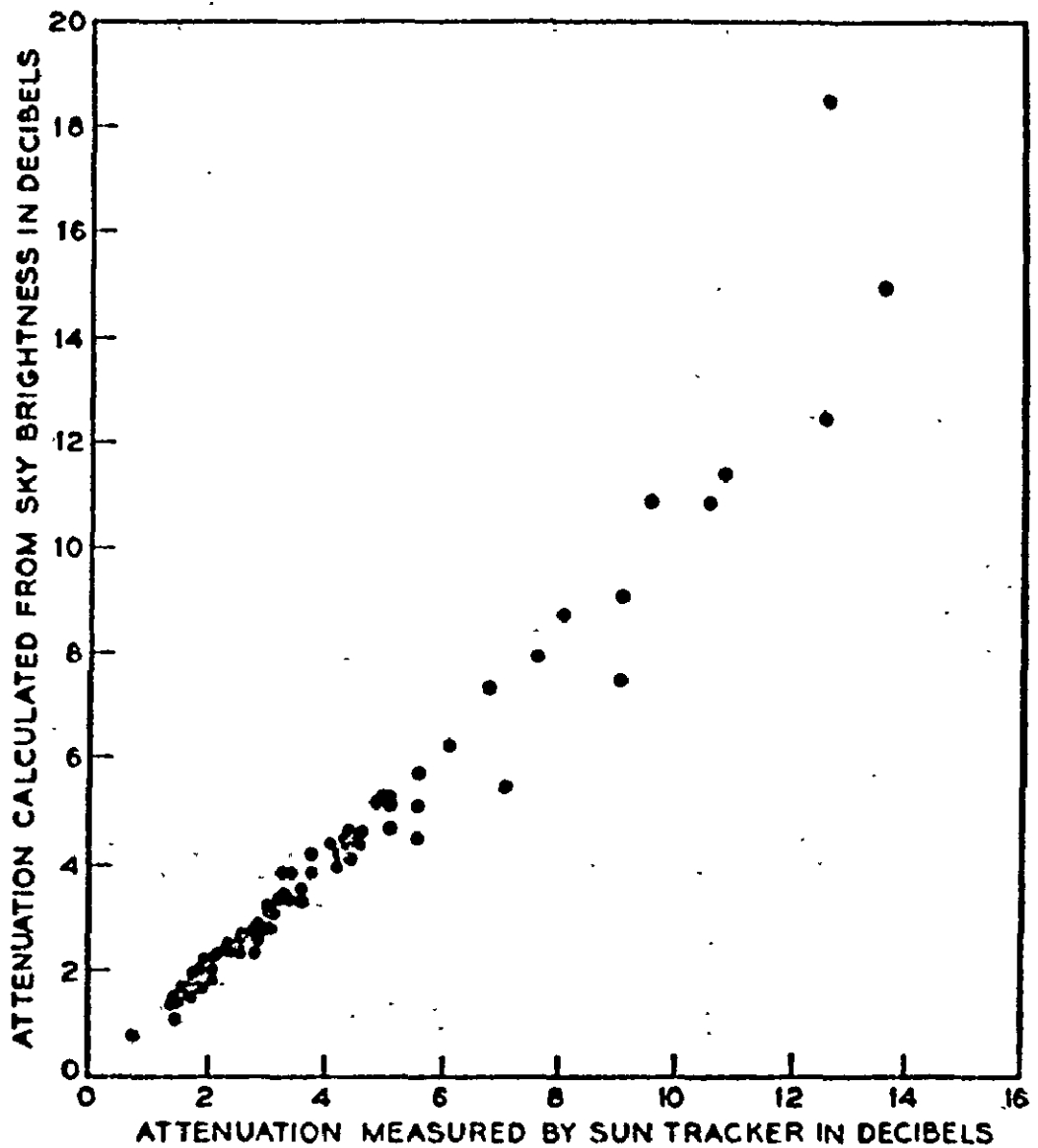


Figure 48-15.- Comparison of attenuation calculated from sky-brightness with attenuation measured by a sun-tracking radio-telescope.

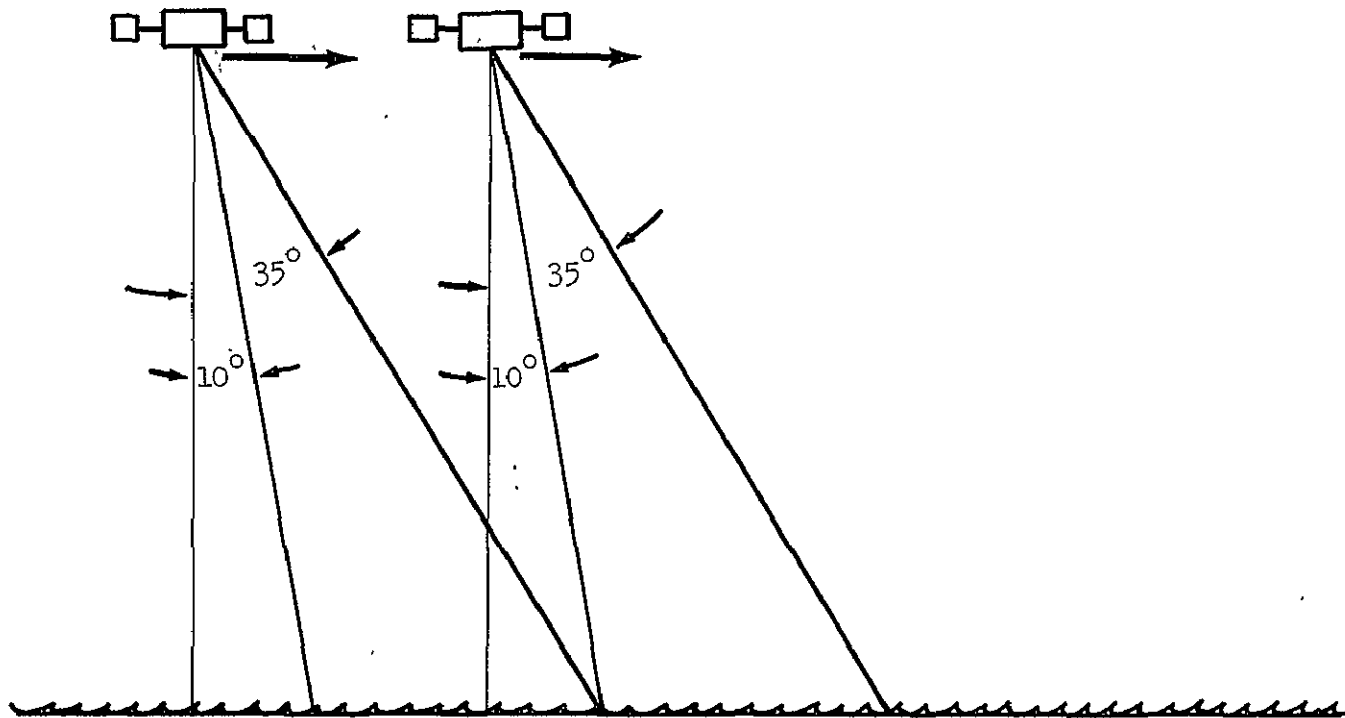


Figure 48-16.- Sattelite mounted scatterometer for sea-state measurements.

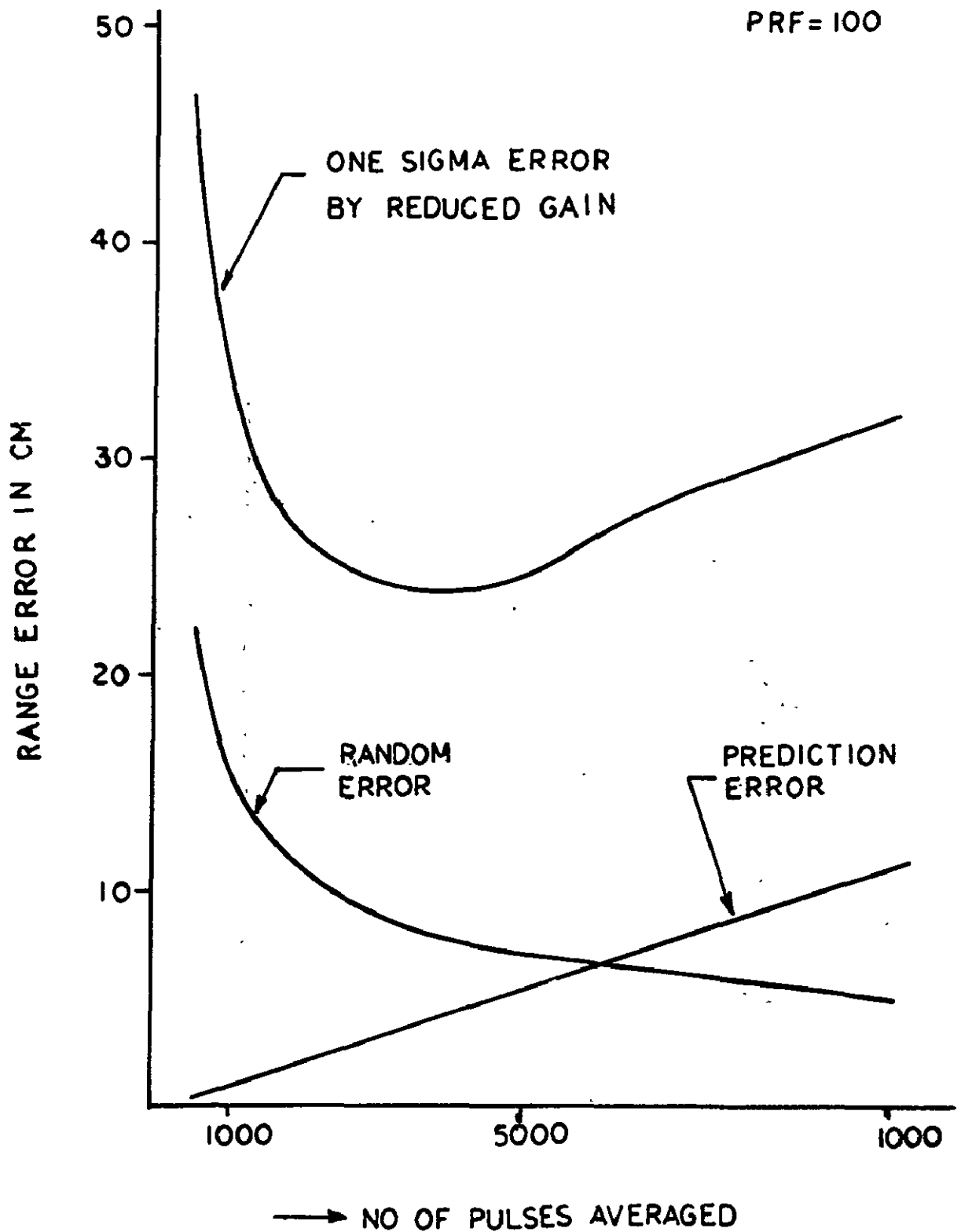


Figure 48-17.- Range of error as a function of the number of pulses averaged.

SECTION 49

Sea-Surface Temperature and Heat Flow - BOMEX

E. D. McAlister

Scripps Institution of Oceanography

University of California, San Diego.

N71-11166

ABSTRACT

A two-wavelength infrared radiometer system for airborne measurement of the total energy exchange at the sea surface was discussed at this meeting in September 1968. During the last two weeks in May 1969, this system was tested at sea off the coast of Barbados, West Indies as part of the BOMEX program. These tests involved the first use of an airborne digital data reduction system for the output of this radiometer. Data was recorded on tape for repeated 30 second flights (one mile strip of ocean) near Scripps' FLIP for ground truth. In spite of severe weather conditions, tests on several days showed values of heat flow from $0.50 \text{ cal cm}^{-2} \text{ min}^{-1}$ at 18 knots wind speed to $0.05 \text{ cal cm}^{-2} \text{ min}^{-1}$ during intermittent rain squalls. These values result from simultaneous readings of radiation at two wavelengths from the sea, sky, the two reference blackbodies and their temperatures. Thirty thousand such readings are recorded in the 30 second "fly-by" and all are used to obtain the heat flow values. This is the first time that airborne total heat flow measurements have been made. The accuracy of sea-surface temperature measurements made with this system is worthy of note as it approaches 0.01°C .

Introduction

For the last six years I have been working towards establishing the feasibility of direct airborne measurements of the total heat flow from the sea. A two-wavelength infrared radiometer system (McAlister, "Measurement of Total Heat Flow from the Sea", Applied Optics 3(5), 609-612 (1964), and U. S. Patent No. 3,373,281, 12 March 1968) has been developed for this purpose.

Success in this objective will be a major contribution to long range weather predictions which is of considerable naval and commercial relevance. This becomes apparent from the following facts: 10^{21} calories of solar energy is stored during the daylight hours of one average day in the top 30 meters of the world's oceans. The release of this energy during a 24 hour cycle depends on wind speed, cloud cover, air and water temperature and other factors. Where it is released geographically, the amount and time of release, and its transport to other parts of the globe are primary energy distribution factors which determine climate and weather.

Local studies of this heat exchange along with all controlling factors will aid in an understanding of this phenomena. Large scale measurements will demonstrate interrelationships between weather and this heat exchange.

A radiometric system for such measurements was described a year ago to this group except for the recently added digital data reduction system (airborne) which provides a great increase in accuracy of sea surface temperature and of heat flow measurements. This latter will be my thesis today and will include a review of preliminary results obtained in the BOMEX program.

The Radiometer System

The radiometer uses two wavelengths to measure the water temperature at depths of 0.025 mm and 0.075 mm. To continuously monitor detector sensitivity (which changes), two internal reference blackbodies are used. Their temperatures are continuously monitored. The radiometer compares the radiation from the sea and sky with that from the reference blackbodies about 60 times per second and the data reduction system sums these for 1/2 second and records the average in digital form on tape. A usual length of run (one mile) is 30 seconds where 100 entries are made on the tape record.

Typical BOMEX Data

Figure 1 shows a typical record (read-out by the computer and reduced to decimal form) which was selected because it includes a region of warm sky (low clouds). It is seen here that there are four radiation intensities recorded at each of the two wavelengths, then two columns of numbers from which the temperature of each blackbody is known to 0.001°C. The average of the 100 entries in each of the ten columns is shown at the bottom.

Figure 2 shows the computer print-out of these 30 second averages for May 27 from 0906 to 0946 Z beside FLIP. This is a typical set of data for a determination of the apparent temperature at the two depths for each flight. The 14 fly-bys of FLIP are made at three altitudes, 150', 300' and 450'. These are plotted on linear graph paper and a straight line extrapolation to zero altitude gives the actual temperature of the water at the two depths after correcting the values for the sky radiation reflected from the water and the emissivity of the water at the two wavelength regions.

Data Reduction

Figure 3 shows the differences between the radiation from the sea and B_1 and the sky and B_1 for each wavelength. It also shows the average temperature of B_1 and B_2 for each 30 second run.

Figure 4 shows the computer run for the May 26 exercise with final corrections for the reflection of sky radiation and the emissivity of the water for the two wavelengths. It also shows the data for obtaining the detector sensitivity for each flight past FLIP.

Figure 5 shows a part of the details of this data reduction and the altitude of observation, this altitude variation being needed for correcting for atmospheric absorption and scattering. Column 2 lists $(Sea_1 - B_1)$, column 3 $(Sky_1 - B_1)r_1$ and then column 4 is obtained by subtracting the numbers in column 3 (positive) from those in column 2 (negative). Column 4, then, is $(Sea_1 - B_1)$ corrected for sky reflection. Column 5 shows the correction for emissivity of the water for this wavelength. Column 6 is the difference $[(Sea_2 - B_1) - (Sky_2 - B_1)r_2]/\text{sensitivity ratio in the two channels, i.e., it corresponds to column 4.}$ Column 7 is column 6/ e_2 which incorporates the correction for emissivity of the water for this wavelength. Column 8 is column 7 minus column 5, which lists, for each run, the difference in radiation from the two depths 0.075 mm and 0.025 mm after correction for sky reflection and emissivity of the water as received at the indicated altitude. Column 9 lists the actual water temperature at 0.075 mm depth, calculated from column 5. Here are listed the 30 second averages for each of 14 runs.

The Effect of Sea-State

Before plotting the numbers in column 8 an examination of the influence of sea-state, wave slopes, etc. is in order. The radiometer beam is at 20° from the vertical to avoid intercepting aircraft radiation by reflection from the sea. The reflectivity of water is 2.68 and 2.10% for channel 1 and channel 2 respectively for a 20° angle of incidence. The reflectivity increases faster than linear with angle, and the question is what does this do to the amount of radiation reflected from the sky and correspondingly to the emissivity of a rough water surface? P. Saunders, of Woods Hole Oceanographic Institution, has answered this question in a paper presented before the University of Michigan 1966 Symposium on The Remote Sensing of Environment. Figure 6 shows two of his graphs from this paper on Precise Airborne Radiation Thermometry. In calculations using Cox and Munk's data on wave slopes, he comes to the conclusion that for wave conditions up to $\delta = 0.3$ (35 knot winds), the ocean is essentially flat. Thus, sea state will be ignored until greater precision in heat flow measurements is attempted.

Calculation of Total Heat Flow

Now, the figures in column 8 of Figure 5 can be plotted. They are the corrected difference in radiation coming from the two depths for each 30 second (1 mile) pass by FLIP. The errors due to changing water temperature are minimized this way as the change is small in 30 seconds time. Figure 7 results when these differences are plotted as a function of altitude. The intercept at zero altitude is the difference in radiation coming from the two depths as measured (by extrapolation down to zero altitude). The value found is 1.5 intensity units. The temperature sensitivity for this exercise was 0.0185°C per intensity unit. The temperature difference for the two depths is therefore 0.028°C . Multiplying this by

the conductivity of water and dividing by the depth difference in cm, a value of $0.48 \text{ cal cm}^{-2} \text{ min}^{-1}$ is obtained. This value is compared with other results in a later figure. Notice the remarkable constancy of water temperature in column 9 of Figure 5.

Water Temperature at Two Depths

When the water temperatures at the two depths are plotted against altitude Figure 8 results. This shows a much greater atmospheric absorption effect for the 4.5 to 5.1 micron channel as was expected. The average temperature at each altitude is circled here. It has been suggested that the absolute humidity might be obtained from the slope of the 4.5-5.1 micron line. This will be examined.

Accuracy of Temperature Values

The actual sea surface temperature can be estimated on this figure for it is the temperature at zero depth, $.013^{\circ}\text{C}$ below the temperature at .025 mm depth or 27.651°C . The error in this sea surface temperature as determined this way by 30,000 readings per point plotted is probably no more than 0.005°C relative to the internal reference blackbody and about 0.01°C absolute.

While discussing accuracy, it should be pointed out here that there are no external windows on this radiometer to fog up or get dirty. Also the rotating mirror, faced with gold on chromium, can change reflectivity with no change in accuracy, only a change in signal to noise. This is because this mirror reflects the radiation from sea, sky, and reference blackbodies onto the detector system with nothing between it and the sea, etc. If the reflectivity drops 2% this change occurs in each radiation beam from sea, sky, etc. This system could not measure heat flow with external windows.

During the BOMEX program the detectors in the system were operating at about 1/10 normal sensitivity, and no vacuum system capable of producing a hard vacuum was available to restore sensitivity. The accuracy of the above figure on heat flow (Figure 7) is estimated at $\pm 0.10 \text{ cal cm}^{-2} \text{ min}^{-1}$. Normal sensitivity, now available is expected to reduce this error to $\pm 0.03 \text{ cal cm}^{-2} \text{ min}^{-1}$.

The present practice of adjusting the two internal reference blackbodies to temperatures just above and just below that of the sea temperature adds considerably to the accuracy of the readings. These references are usually kept 1, or at most 2°C apart with the sea temperature in between. This adjustment is checked in flight by viewing the oscilloscope presentation of each channel:

A Comparison of Atmospheric Absorption in Three Atmospheric "Windows"

An auxiliary radiometer using the 8-13 micron band was used in addition to the two-wavelength system for the May 29 exercise. This provided the interesting comparison shown in Figure 9. The 8-13 micron instrument cannot read sky intensity as used, so the most noticeable feature of this comparison is that the sky correction for the 8-13 micron radiometer in this test was about 0.3°C . Also the slope of the 8-13 micron line is 2.3 times that of the 4.5-5.1 micron line and 13 times that of the 3.4-4.0 micron line. The 8-13 micron radiometer line with a sky correction has been drawn to read near the others for surface temperature.

Present Status of BOMEX Data Reduction

The present status of data reduction for the BOMEX exercises is shown on Figure 10. No data has yet been received from experimenters on FLIP although it is expected soon. Therefore, we have no "ground truth" on either water temperature, or turbulent fluxes to compare with present data. Figure 10 shows preliminary values of heat flow for three exercises which appear reasonable for the conditions under which they were taken. The values are termed preliminary because they are calculated from the average figures for each 30 second run. What remains to be done is detailed inspection of the computer runs to see if there are small increments of interference from ships radar, communications, etc. If these interferences are extensive, it is evident by cursory inspection and the record is discarded. This detailed inspection takes considerable time.

Data has not been reduced for two exercises and two more give negative results due to heavy weather while another was lost due to local interference in the aircraft.

The Statistics from Several One Mile Passes are Necessary

The average temperature in a 30 second or one mile run is a convenient size of sea surface for which the total heat flow is calculated. The temperature of 100 foot squares on the ocean are recorded every $1/2$ second, but the ocean's inherent surface "noise" as well as system noise renders this size impossible to measure with the accuracy necessary for total heat flow calculations. In other words, the statistics of several 30 second runs over the same area near FLIP are necessary here. Operation with normal detector sensitivity in place of $1/10$ normal will reduce the length of time necessary to obtain an accurate value of heat flow.

Redesign Possibilities

The present system has passed the initial tests of proving feasibility of airborne measurement of total heat flow. Before feasibility is completed

it is important to consider what a modest redesign of the system could do to speed up the ocean area surveyed in a given length of time with the desired accuracy.

Optical System. No change in size or wavelengths used is likely. Detector sensitivity as high as possible for better signal-to-noise ratio. Atmospheric absorption corrections simplified by flying at one low altitude and viewing the ocean at 20° and 60° from the vertical. With high system sensitivity these two optical path lengths to the sea surface should be sufficient. This will require two additional reading positions, controlled by magnetic switches on the mirror shaft, one for the 60° look at the sky and one for the 60° look at the sea. This will require two more entries in the data reduction system or else will require time sharing for the present one.

Redesign for Use in High Performance Aircraft. This type of redesign would be a major one. It is not at all impossible but should be done after another year of study with the present system, whether modified as suggested above or not.

Conclusions

1. The initial step in proof of feasibility has been made in the BOMEX trials. Even without the much needed ground truth from FLIP, the principle of this method of total heat measurement has been proved.
2. A new order of accuracy in sea surface temperature measurement has been shown.
3. The present system has surpassed the accuracy of oceanographic mercury thermometry. Precision measurements of the emissivity of the present internal blackbodies may show that the present system under limited conditions can make even more accurate measurements of the temperature of the sea surface and of total heat flow. This follows from the fact that the theory of operation of the method is simple and direct and the assumptions made have known limits.

RECORD 15 FILE 1 DECIMAL

SCANNER NO.1												SCANNER NO.2											
SEA(1)	DB (1)	SKY(1)	DB (2)	SEA(2)	DB (2)	SKY(2)	DB (2)	TBB(1)	TBB(2)	(SEC.)	(MIN.)	SEA(1)	DB (1)	SKY(1)	DB (2)	SEA(2)	DB (2)	SKY(2)	DB (2)	TBB(1)	TBB(2)	(SEC.)	(MIN.)
4095	1451	1902	2850	1452	1903	2851	1453	1904	2852	217	3.62	4095	1454	1905	2853	1455	1906	2854	1456	1907	2855	217	3.62
4095	1457	1914	2856	1458	1915	2857	1459	1916	2858	217	3.62	4095	1460	1917	2859	1461	1918	2860	1462	1919	2861	217	3.62
4095	1463	1922	2860	1464	1923	2861	1465	1924	2862	217	3.62	4095	1466	1925	2863	1467	1926	2864	1468	1927	2865	217	3.62
4095	1469	1934	2866	1470	1935	2867	1471	1936	2868	217	3.62	4095	1472	1937	2869	1473	1938	2870	1474	1939	2871	217	3.62
4095	1475	1944	2870	1476	1945	2871	1477	1946	2872	217	3.62	4095	1478	1947	2873	1479	1948	2874	1480	1949	2875	217	3.62
4095	1481	1954	2874	1482	1955	2875	1483	1956	2876	217	3.62	4095	1484	1957	2877	1485	1958	2878	1486	1959	2879	217	3.62
4095	1487	1964	2880	1488	1965	2881	1489	1966	2882	217	3.62	4095	1490	1967	2883	1491	1968	2884	1492	1969	2885	217	3.62
4095	1493	1974	2886	1494	1975	2887	1495	1976	2888	217	3.62	4095	1496	1977	2889	1497	1978	2890	1498	1979	2891	217	3.62
4095	1499	1984	2892	1500	1985	2893	1501	1986	2894	217	3.62	4095	1502	1987	2895	1503	1988	2896	1504	1989	2897	217	3.62
4095	1505	1994	2898	1506	1995	2899	1507	1996	2900	217	3.62	4095	1508	1997	2901	1509	1998	2902	1510	1999	2903	217	3.62
4095	1511	2004	2904	1512	2005	2905	1513	2006	2906	217	3.62	4095	1514	2007	2907	1515	2008	2908	1516	2009	2909	217	3.62
4095	1517	2014	2910	1518	2015	2911	1519	2016	2912	217	3.62	4095	1520	2017	2913	1521	2018	2914	1522	2019	2915	217	3.62
4095	1523	2024	2916	1524	2025	2917	1525	2026	2918	217	3.62	4095	1526	2027	2919	1527	2028	2920	1528	2029	2921	217	3.62
4095	1529	2034	2922	1530	2035	2923	1531	2036	2924	217	3.62	4095	1532	2037	2925	1533	2038	2926	1534	2039	2927	217	3.62
4095	1535	2044	2928	1536	2045	2929	1537	2046	2930	217	3.62	4095	1538	2047	2931	1539	2048	2932	1540	2049	2933	217	3.62
4095	1541	2054	2934	1542	2055	2935	1543	2056	2936	217	3.62	4095	1544	2057	2937	1545	2058	2938	1546	2059	2939	217	3.62
4095	1547	2064	2940	1548	2065	2941	1549	2066	2942	217	3.62	4095	1548	2067	2943	1549	2068	2944	1550	2069	2945	217	3.62
4095	1551	2074	2946	1552	2075	2947	1553	2076	2948	217	3.62	4095	1554	2077	2949	1555	2078	2950	1556	2079	2951	217	3.62
4095	1557	2084	2952	1558	2085	2953	1559	2086	2954	217	3.62	4095	1560	2087	2955	1561	2088	2956	1562	2089	2957	217	3.62
4095	1563	2094	2958	1564	2095	2959	1565	2096	2960	217	3.62	4095	1566	2097	2961	1567	2098	2962	1568	2099	2963	217	3.62
4095	1569	2104	2964	1570	2105	2965	1571	2106	2966	217	3.62	4095	1572	2107	2967	1573	2108	2968	1574	2109	2969	217	3.62
4095	1575	2114	2970	1576	2115	2971	1577	2116	2972	217	3.62	4095	1578	2117	2973	1579	2118	2974	1580	2119	2975	217	3.62
4095	1581	2124	2976	1582	2125	2977	1583	2126	2978	217	3.62	4095	1584	2127	2979	1585	2128	2980	1586	2129	2981	217	3.62
4095	1585	2134	2982	1586	2135	2983	1587	2136	2984	217	3.62	4095	1588	2137	2985	1589	2138	2986	1590	2139	2987	217	3.62
4095	1589	2144	2988	1590	2145	2989	1591	2146	2990	217	3.62	4095	1592	2147	2991	1593	2148	2992	1594	2149	2993	217	3.62
4095	1595	2154	2994	1596	2155	2995	1597	2156	2996	217	3.62	4095	1598	2157	2997	1599	2158	2998	1600	2159	2999	217	3.62
4095	1601	2164	3000	1602	2165	3001	1603	2166	3002	217	3.62	4095	1604	2167	3003	1605	2168	3004	1606	2169	3005	217	3.62
4095	1607	2174	3006	1608	2175	3007	1609	2176	3008	217	3.62	4095	1610	2177	3009	1611	2178	3010	1612	2179	3011	217	3.62
4095	1613	2184	3012	1614	2185	3013	1615	2186	3014	217	3.62	4095	1616	2187	3015	1617	2188	3016	1618	2189	3017	217	3.62
4095	1619	2194	3018	1620	2195	3019	1621	2196	3020	217	3.62	4095	1622	2197	3021	1623	2198	3022	1624	2199	3023	217	3.62
4095	1625	2204	3024	1626	2205	3025	1627	2206	3026	217	3.62	4095	1628	2207	3027	1629	2208	3028	1630	2209	3029	217	3.62
4095	1629	2214	3030	1630	2215	3031	1631	2216	3032	217	3.62	4095	1632	2217	3033	1633	2218	3034	1634	2219	3035	217	3.62
4095	1635	2224	3036	1636	2225	3037	1637	2226	3038	217	3.62	4095	1638	2227	3039	1639	2228	3040	1640	2229	3041	217	3.62
4095	1639	2234	3042	1640	2235	3043	1641	2236	3044	217	3.62	4095	1642	2237	3045	1643	2238	3046	1644	2239	3047	217	3.62
4095	1645	2244	3048	1646	2245	3049	1647	2246	3050	217	3.62	4095	1648	2247	3051	1649	2248	3052	1650	2249	3053	217	3.62
4095	1649	2254	3054	1650	2255	3055	1651	2256	3056	217	3.62	4095	1652	2257	3057	1653	2258	3058	1654	2259	3059	217	3.62
4095	1655	2264	3060	1656	2265	3061	1657	2266	3062	217	3.62	4095	1658	2267	3063	1659	2268	3064	1660	2269	3065	217	3.62
4095	1659	2274	3066	1660	2275	3067	1661	2276	3068	217	3.62	4095	1662	2277	3069	1663	2278	3070	1664	2279	3071	217	3.62
4095	1665	2284	3072	1666	2285	3073	1667	2286	3074	217	3.62	4095	1668	2287	3075	1669	2288	3076	1670	2289	3077	217	3.62
4095	1669	2294	3078	1670	2295	3079	1671	2296	3080	217	3.62	4095	1672	2297	3081	1673	2298	3082	1674	2299	3083	217	3.62
4095	1675	2304	3084	1676	2305	3085	1677	2306	3086	217	3.62	4095	1678	2307	3087	1679	2308	3088	1680	2309	3089	217	3.62
4095	1679	2314	3090	1680	2315	3091	1681	2316	3092	217	3.62	4095	1682	2317	3093	1683	2318	3094	1684	2319	3095	217	3.62
4095	1685	2324	3096	1686	2325	3097	1687	2326	3098	217	3.62	4095	1688	2327	3099	1689	2328	3100	1690	2329	3101	217	3.62
4095	1689	2334	3102	1690	2335	3103	1691	2336	3104	217	3.62	4095	1692	2337	3105	1693	2338	3106	1694	2339	3107	217	3.62
4095	1695	2344	3108	1696	2345	3109	1697	2346	3110	217	3.62	4095	1698	2347	3111	1699	2348	3112	1700	2349	3113	217	3.62
4095	1699	2354	3114	1700	2355	3115	1701	2356	3116	217	3.62	4095	1702	2357	3117	1703	2358	3118	1704	2359	3119	217	3.62
4095	1705	2364	3120	1706	2365	3121	1707	2366	3122	217	3.62	4095	1708	2367	3123	1709	2368	3124	1710	2369	3125	217	3.62
4095	1709	2374	3126	1710	2375	3127	1711	2376	3128	217	3.62	4095	1712	2377	3129	1713	2378	3130	1714	2379	3131	217	3.62
4095	1715	2384	3132	1716	2385	3133	1717	2386	3134	217	3.62	4095	1718	2387	3135	1719	2388	3136	1720	2389	3137	217	3.62
4095	1719	2394	3138	1720	2395	3139	1721	2396	3140	217	3.62	4095	1722	2397	3141	1723	2398	3142	1724	2399	3143	217	3.62
4095																							

SCANNER NO.1												SCANNER NO.2											
												REFERENCE TEMP. BB1 25.29 BB2 27.03											
REL.	SEA(1)	BB (1)	SKY(1)	BB (2)	SEA(2)	BB (1)	SKY(2)	BB (2)	TBB(1)	TBB(2)	TIME												
AVG.																							
TEMP. /																							
DEC. 8	1876.80	1915.18	2899.91	1855.41	1908.26	1965.10	2744.73	1862.83	3575.57	3167.22	6.18												
AVG.																							
TEMP. 8																							
DEC. 9	1851.31	1889.08	2974.14	1808.60	1883.92	1937.87	2722.49	1835.00	3580.18	3189.55	26.15												
AVG.																							
TEMP. 9																							
DEC. 10	1844.90	1883.04	2854.95	1802.52	1872.83	1931.55	2686.13	1828.28	3575.49	3208.62	78.68												
AVG.																							
TEMP. 10																							
DEC. 11	1851.09	1887.41	2954.52	1846.34	1889.46	1947.16	2696.60	1843.21	3565.64	3228.57	100.87												
AVG.																							
TEMP. 11																							
DEC. 12	1829.81	1866.11	2818.67	1786.37	1856.31	1917.45	2631.50	1814.12	3578.69	3256.65	142.69												
AVG.																							
TEMP. 12																							
DEC. 13	1866.68	1904.98	2846.33	1823.91	1883.30	1944.94	2649.69	1841.20	3590.26	3282.90	168.13												
AVG.																							
TEMP. 13																							
DEC. 14	1897.79	1933.88	2886.46	1852.40	1897.44	1948.98	2708.01	1845.15	3574.83	3275.77	195.53												
AVG.																							
TEMP. 14																							
DEC. 15	1872.58	1909.07	2803.12	1829.56	1910.40	1962.64	2650.03	1859.06	3566.50	3266.89	218.64												
AVG.																							
TEMP. 15																							
DEC. 16	1842.88	1880.23	2827.83	1798.87	1884.60	1941.43	2675.66	1837.95	3579.00	3265.99	15.46												
AVG.																							
TEMP. 16																							
DEC. 17	1861.30	1901.02	2852.12	1820.49	1888.01	1948.31	2686.88	1844.37	3536.49	3233.61	40.78												
AVG.																							
TEMP. 17																							
DEC. 18	1827.90	1867.14	2816.34	1787.21	1873.69	1936.35	2653.00	1833.90	3587.28	3267.24	113.51												
AVG.																							
TEMP. 18																							
DEC. 19	1852.71	1892.41	2834.43	1812.37	1887.25	1950.27	2662.89	1847.78	3585.38	3262.97	169.72												
AVG.																							
TEMP. 19																							
DEC. 20	1833.80	1878.38	2676.42	1898.54	1930.32	1988.88	2599.21	1886.92	3588.57	3264.03	196.16												
AVG.																							
TEMP. 20																							
DEC. 21	1865.77	1902.90	2856.23	1823.00	1901.95	1956.28	2713.03	1853.95	3586.78	3265.52	213.88												
AVG.																							
TEMP. 21																							

Figure 49-2.- Summary of averages for each record and blackbody temperatures.

REC.	SEA(1)-BB(1)	SKY(1)-BB(1)	SEA(2)-BB(1)	SKY(2)-BB(1)	TBB(1)-2048	TBB(2)-2048
1	0	0	0	0	-2048.00	-2048.00
2	-0	-0	-0	-0	-0	-0
3	-0	-0	-0	-0	-0	-0
4	-0	-0	-0	-0	-0	-0
5	0	0	0	0	-2048.00	-2048.00
6	-0	-0	-0	-0	-0	-0
7	0	0	0	0	-1.00	-9.00
8	-38.38	984.73	-56.84	779.63	1527.57	1119.22
9	-37.77	985.06	-53.92	784.62	1532.18	1141.55
10	-38.14	971.91	-58.72	754.58	1527.49	1160.62
11	-36.32	967.11	-57.70	749.44	1517.64	1180.57
12	-36.30	952.56	-61.14	714.05	1530.09	1208.65
13	-38.30	941.35	-61.64	704.75	1542.20	1234.90
14	-36.09	955.58	-51.54	759.03	1526.83	1227.77
15	-37.29	893.25	-52.24	687.39	1518.50	1218.89
16	-37.43	947.60	-56.83	734.43	1531.00	1217.99
17	-40.32	950.49	-60.30	738.57	1488.49	1185.61
18	-39.24	949.20	-62.75	716.65	1539.28	1219.24
19	-39.50	942.22	-63.02	711.82	1537.38	1214.97
20	-44.58	698.04	-58.56	970.33	1532.57	1216.03
21	-37.13	953.33	-54.33	756.75	1538.78	1217.52
22	-37.21	954.83	-59.00	738.55	1538.19	1206.51
23	-37.67	945.56	-58.51	737.30	1546.85	1213.02
24	-35.26	944.83	-60.28	712.46	1565.25	1217.99
25	-38.05	861.14	-60.98	670.48	1552.03	1203.00
26	-33.39	947.35	-50.74	750.86	1568.65	1215.92
27	-34.66	936.33	-51.75	752.92	1578.22	1212.28
28	-31.69	953.45	-44.87	768.25	1588.94	1200.34
29	-33.56	952.17	-47.38	787.50	1582.70	1178.17
30	0	0	0	0	-1.00	-9.00

Figure 49-3.- Tabulation of radiation differences.

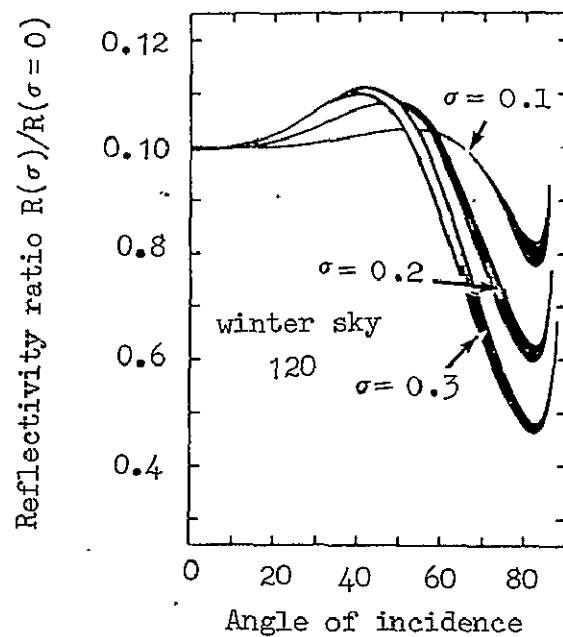
CHANNEL 1			CHANNEL 2		
REC.	SEA(1)-BB(1)	BB(1)-BB(2)	SEA(2)-BB(1)	BB(1)-BB(2)	(TR1-TR2)
8	-64.7708	79.7700	-73.2122	102.2700	-1.4260
8	-64.7708		-56.7715		-7.9998
9	-64.1596	80.4800	-70.3970	102.8700	-1.4398
9	-64.1596		-54.7531		-9.4165
10	-64.1872	80.5200	-74.5662	103.2700	-1.4584
10	-64.1872		-57.7999		-6.3873
11	-62.2385	81.0700	-73.4382	103.9500	-1.4817
11	-62.2385		-56.9394		-5.2991
12	-61.8286	79.7400	-76.1350	103.3300	-1.4939
12	-61.8286		-58.4103		-3.4183
13	-63.5282	81.0700	-76.4397	103.7400	-1.5049
13	-63.5282		-59.3866		-4.1416
14	-61.6995	81.4800	-67.4796	103.8300	-1.5114
14	-61.6995		-52.6449		-9.0547
15	-61.2291	80.3700	-66.6752	103.9800	-1.5109
15	-61.2291		-51.4325		-9.7966
16	-62.8257	81.3600	-72.2530	103.4800	-1.5005
16	-62.8257		-56.4763		-6.3494
17	-65.7931	81.1300	-75.8100	103.9400	-1.5084
17	-65.7931		-58.8275		-6.9656
18	-64.6786	79.9300	-77.7997	102.4500	-1.4950
18	-64.6786		-60.3435		-4.3390
19	-64.7515	79.8400	-77.9682	102.4900	-1.4931
19	-64.7515		-60.3826		-4.3689
20	-63.2875	79.8400	-70.5369	101.9600	-1.4977
20	-63.2875		-54.9114		-8.3761
21	-62.6792	79.9000	-70.2218	102.3300	-1.4940
21	-62.6792		-54.5093		-8.1689

*Difference in radiation from two depths received at altitude.

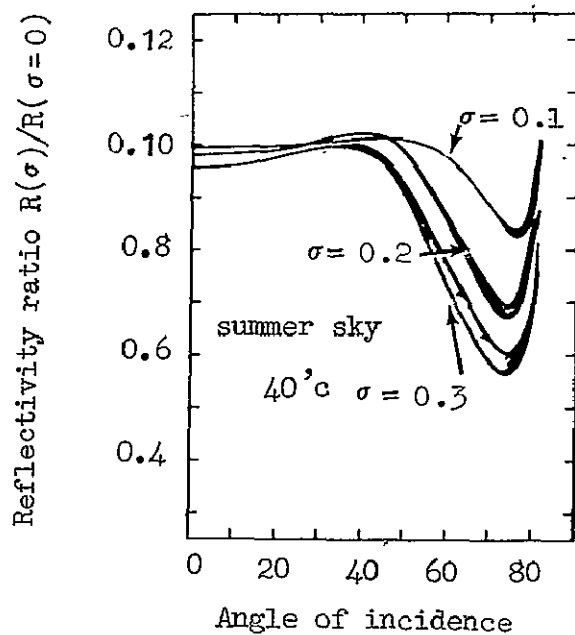
Figure 49-4.- Tabulation of final data reduction.

Record No.	1 Altitude - Feet	2 $(S_1 - B_1)$	3 $(SKY_1 - B_1)r_1$	4 Col. 2 - Col. 3	5 $4/e_1$	6 $(S_2 - B_1) -$ $(SKY_2 - B_1)r$ Sensitivity Ratio	7 $6/e_2$	8 Col. 7 - Col. 5 (Computer run)	9 Actual Water Temp. at .075 mm depth from Col. 5
8	450	-38.4	+26.4	-64.8	-66.6	-56.8	-58.0	8.0	27.665
9	450	37.8	26.4	64.2	66.0	54.6	55.7	9.4	.673
10	300	38.1	26.1	64.2	66.0	58.0	59.2	6.4	.674
11	300	36.3	25.9	62.2	63.9	57.0	58.2	5.3	.643
12	150	36.3	25.5	61.8	63.4	58.6	59.8	3.4	.670
13	150	38.3	25.2	63.5	65.2	59.6	60.8	4.1	.703
14	450	36.1	25.6	61.7	63.4	52.7	53.8	9.1	.653
15	450	37.3	23.9	61.2	62.9	51.7	52.8	9.8	.656
16	300	37.4	25.4	62.8	64.5	56.6	57.8	6.3	.676
17	300	40.3	25.5	65.8	67.6	59.3	60.6	7.0	.714
18	150	39.2	25.5	64.7	66.5	60.9	62.2	4.3	.734
19	150	39.5	25.2	64.7	66.5	60.9	62.2	4.4	.732
20	450	44.6	18.7	63.3	65.1	55.4	56.6	8.4	.703
21	450	37.1	25.5	62.6	64.3	55.1	56.3	8.2	.684

Figure 49-5.- Data reduction



The radiance of the sky is typical of clear winter weather.



The radiance of the sky is typical of clear summer weather.

Figure 49-6.- Reflectivity ration -- rough sea to smooth sea.
From P. Saunders.

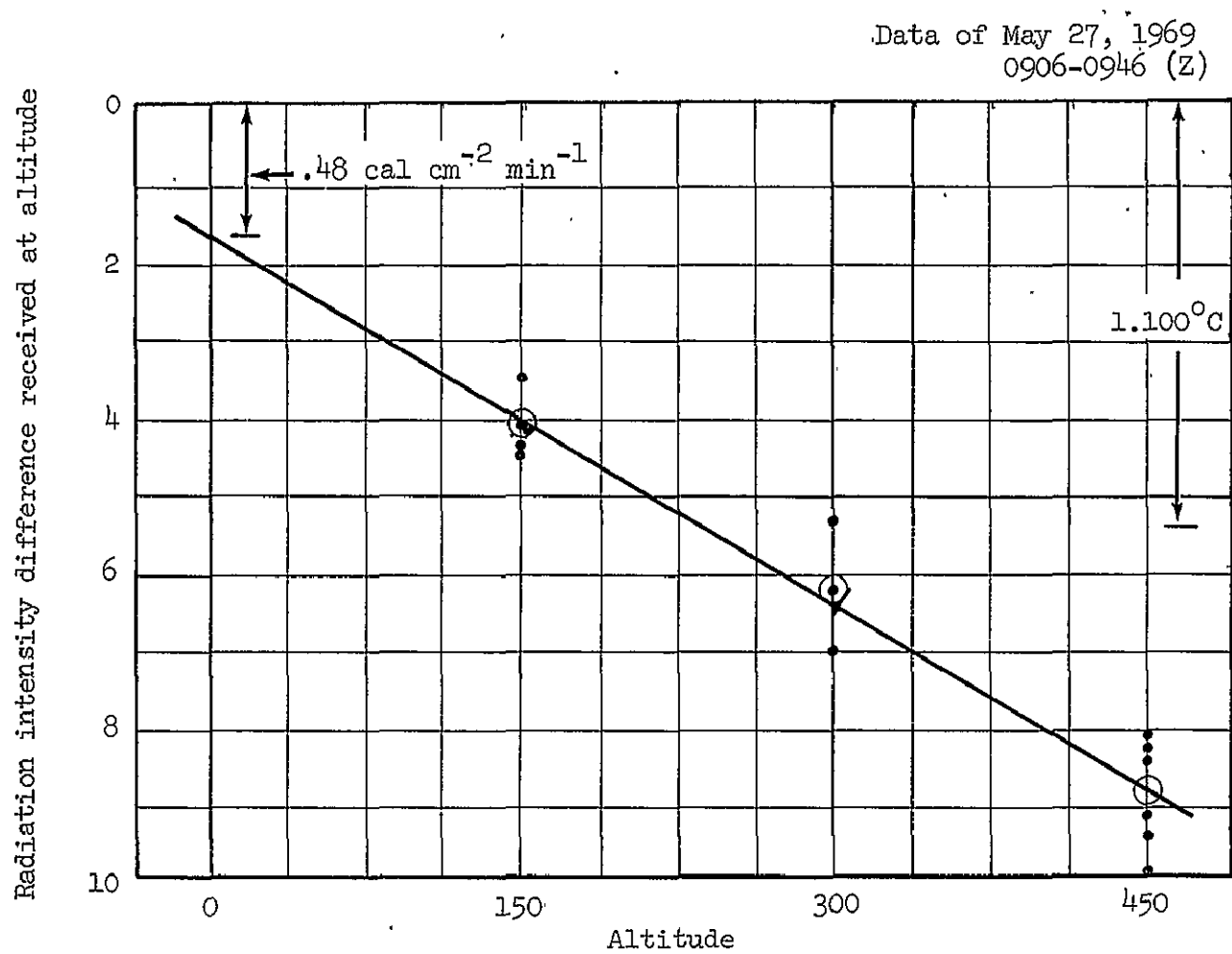


Figure 49-7.- Total heat flow calculation.

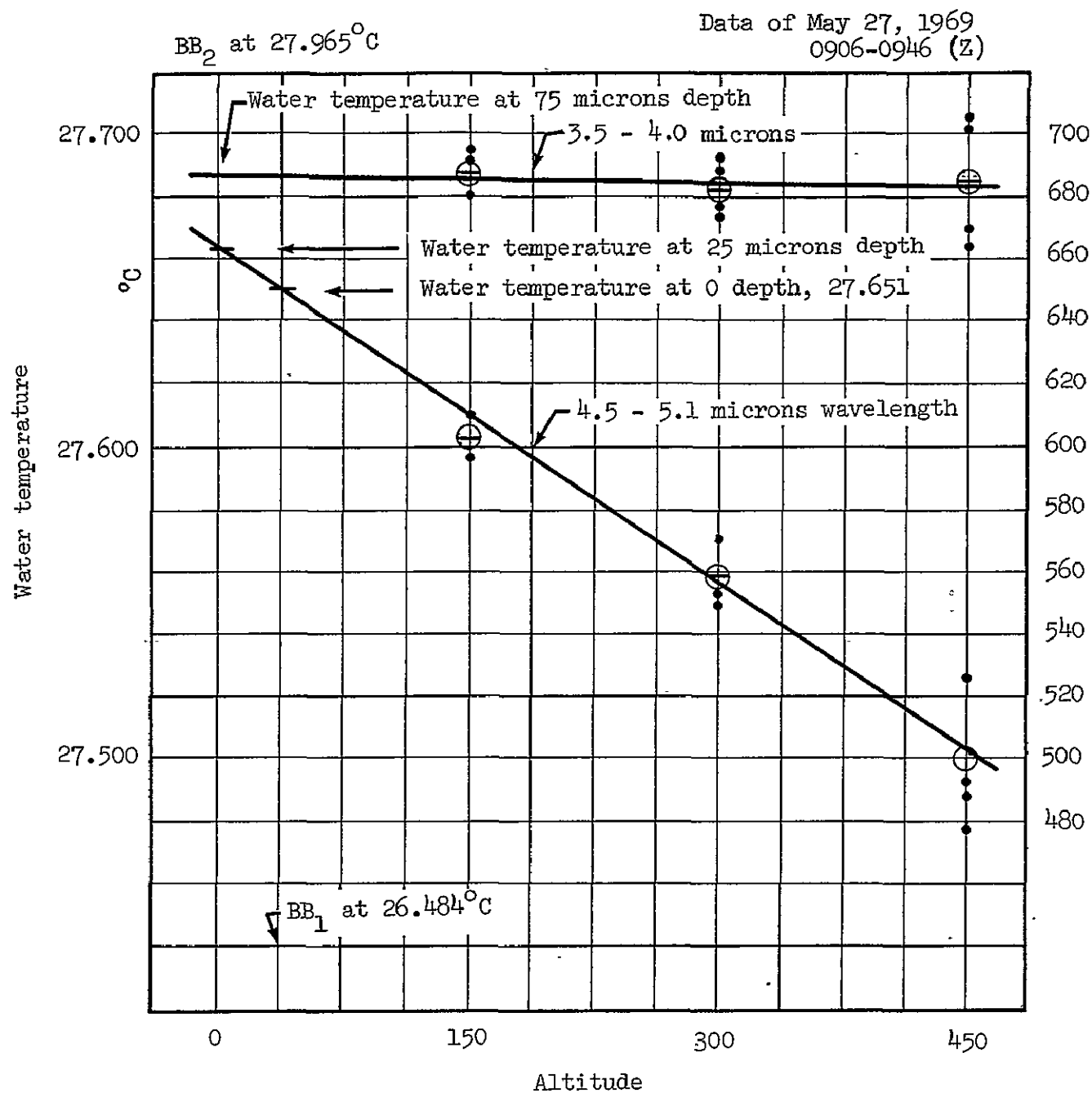


Figure 49-8.- Water temperature at depths indicated near FLIP.

Data of May 29, 1969

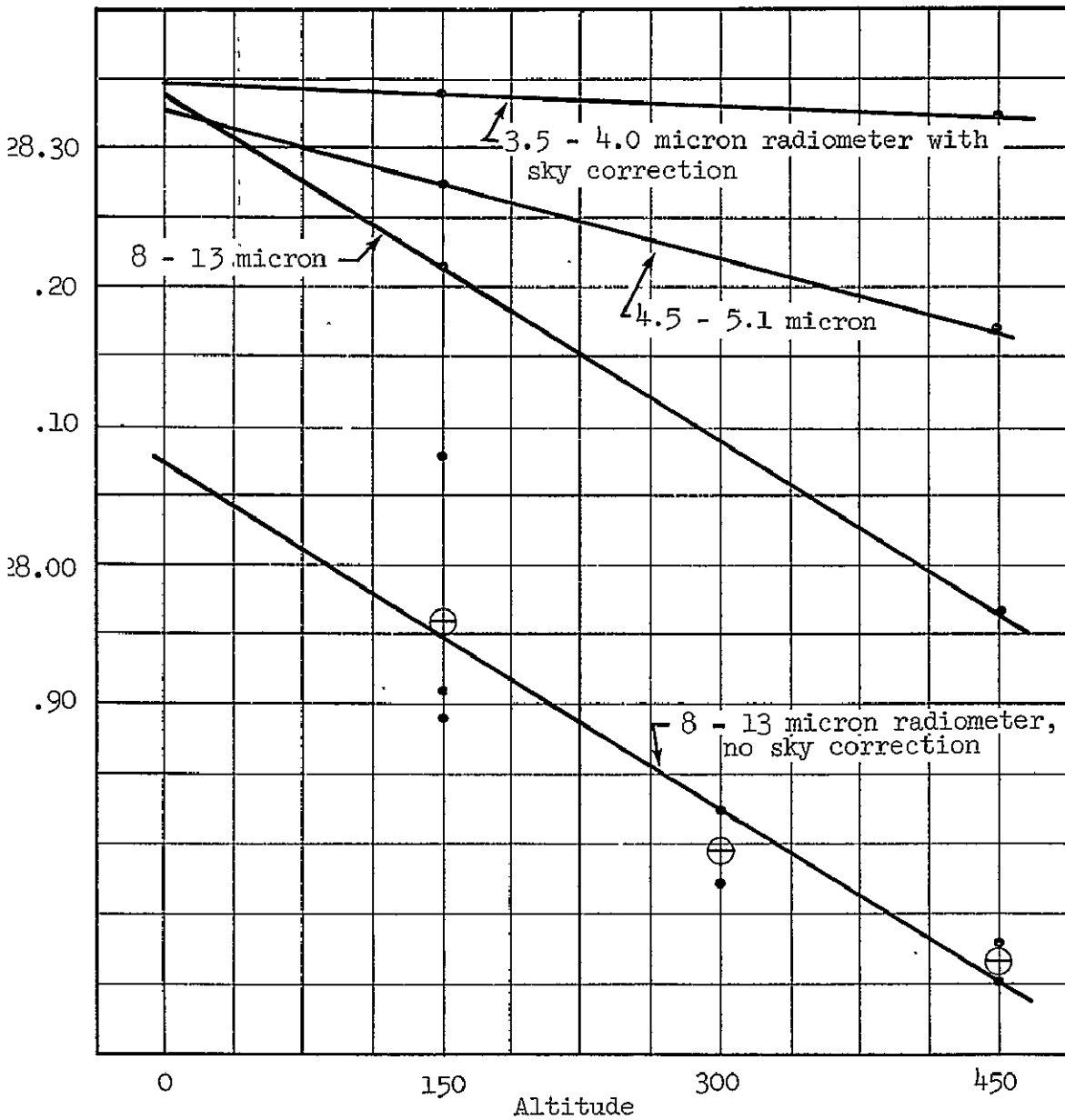


Figure 49-9.- The need for sky corrections in radiometric sea surface readings.

<u>Date</u>	<u>Time</u>	<u>Bomex No.</u>	<u>Comments</u>	<u>Results on Heat Flow</u>
24 May	2227-2258Z	6	Intermittent rain squalls	0.0 to 0.10 cal cm ⁻² min ⁻¹
26 May	2140-2238Z	8	Rain squalls nearby 13 knot wind	0.24 cal cm ⁻² min ⁻¹
27 May	0906-0946Z	9	Best weather 18 knot wind	0.50 cal cm ⁻² min ⁻¹
25 May	2146-2238Z	7	Data not reduced	
29 May	2124-2234Z	11	Data not reduced	
19 May	2204-2255Z	4	Heavy weather Altitudes uncertain	Negative
24 May	1054-1124Z	5	Internal interference from power supply	Negative
28 May	0953-1023Z	10	High gusty winds Spray below 200' altitude	Negative

Figure 49-10.- Preliminary BOMEX results.

SECTION 50

N71 - 11167

EXPERIMENTAL RESULTS OF THE REMOTE MEASUREMENT
OF OCEAN COLOR

Peter G. White

TRW Systems Group

INTRODUCTION

The data to be described in this paper were taken with one instrument from a number of locations - they include measurements of the spectral characteristics of water taken in the Pacific and Atlantic oceans and in Crater Lake in Oregon. In all cases the measurements were made remotely from an aircraft flying at altitudes between 1000 and 10000 feet.

Most of the data were obtained under contract to the Spacecraft Oceanography Project.

For the sake of consistency, the data is all plotted with spectral reflectance as a function of wavelength.

RESULTS

Clear Water

Figure 1 shows the spectral reflectance of two bodies of water noted for their clarity - the Gulf Stream and Crater Lake. The trend of the curves is similar and resembles the theoretical curve calculated by R. C. Ramsey¹. In clear water the scattering is due to the water molecules and is of the small particle or Raleigh type. The light is scattered inversely as the fourth power of the wavelength. This is why clear water appears blue. At the longer wavelengths water absorbs virtually all the radiation entering it.

The Crater Lake water has a somewhat higher reflectance at longer wavelengths. This cannot be easily explained but is not inconsistent with measurements of transmission of Crater Lake water made by Smith and Tyler² when compared with measurements of transmission of filtered ocean water made by Clarke and James³.

Water with High Plankton Content

Figure 2 is the spectral reflectance curve of water containing a high particle content, in this case chlorophyceae or green algae. The reflectance has increased in the middle wavelengths due to large particle scattering. The chlorophyll- α contained in the algae absorbs energy at 0.67μ and this absorption is evident as a reduction in reflectance at this wavelength. The theoretical clear water curve is shown as a reference.

Figure 3 is another curve of water with a higher particle content, but in this case the water contains many plankton of the genus gonyaulax. The absorption due to chlorophyll- α is still present, but a new and very strong absorption is now evident at about 0.52μ . This has been identified as due to pycobilin pigment found in gonyaulax. In other respects the curve is similar to Figure 2.

Change of Reflectance with Particle Content

Measurements of the spectral reflectance of water with various chlorophyll contents are plotted in Figure 4. It should be noted that the level of reflectance in this case is only estimated, although the relative values may be compared.

Note that as the particle concentration increases, the reflectance increases at the middle wavelengths as in Figure 2, due to large particle scattering. The reduction in reflectance at the shorter wavelengths is probably an indication that the heavy concentrations of particles are near the surface. If they were covered by a layer of relatively clear water, one would expect a higher reflectance due to Raleigh scattering by the water molecules. This would seem to indicate that it may be possible to estimate the depth of particle concentrations as well as their density.

Atmospheric Effects

Figure 5 shows the results of several spectral measurements made on a day with moderate haze from various altitudes. Unfortunately no quantitative measurements of the atmospheric haze could be made. The general increase in reflectance is due to scattering by the atmosphere. Note that the general shape of the curves remains unchanged. In this plot there is some doubt as to the absolute levels of reflectance values and it also is believed that the increase in reflectance at the long wavelengths is due to a second order spectrum in the spectrometer used to make the measurements which was not filtered out.

SUMMARY

The results shown indicate several characteristics of water spectra.

- High particle content increases reflectivity between approximately 0.5 and 0.6μ .
- High particle contents near the surface decrease reflectivity between 0.4 and 0.5μ and increase it between 0.6 and 0.7μ . This effect is minimized if there is a layer of clear water above the particles.
- Certain absorption bands can be recognized.

As an example of the use of these analysis rules, Figure 6 shows four spectral curves taken on a single flight within two minutes of one another.

From the shape and features of the curves we can deduce the following.

The solid curve represents relatively clear water as evidenced by its rapid decrease in reflectance with increasing wavelength. The other three curves show the presence of particulate matter as evidenced by the increased reflectance between 0.5 and 0.6 μ . The shallow overall slope of these three curves indicates that the material is either homogeneous or near the surface (particularly the upper dotted curve). Two of the curves indicate the presence of pycobilin pigment due to the phytoplankton *gonyaulax*, and two (possibly three) curves show the presence of chlorophyll. The second curve from the bottom also shows a small absorption at 0.515 μ which has been reported by some other investigators but is not identified.

As additional data is gathered, more will undoubtedly be learned about the analysis and interpretation of this type of spectral curve. There is little doubt that computer analysis techniques will ultimately be used to process these spectral data automatically.

REFERENCES

1. R. C. Ramsey, unpublished data, TRW Systems, 1969.
2. R. C. Smith and J. E. Tyler, "Optical Properties of Clear Natural Water", JOSA Vol. 57, May, 1967.
3. G. L. Clarke and H. R. James, "Laboratory Analysis of the Selective Absorption of Light by Sea Water", JOSA, Vol. 29, February, 1939.

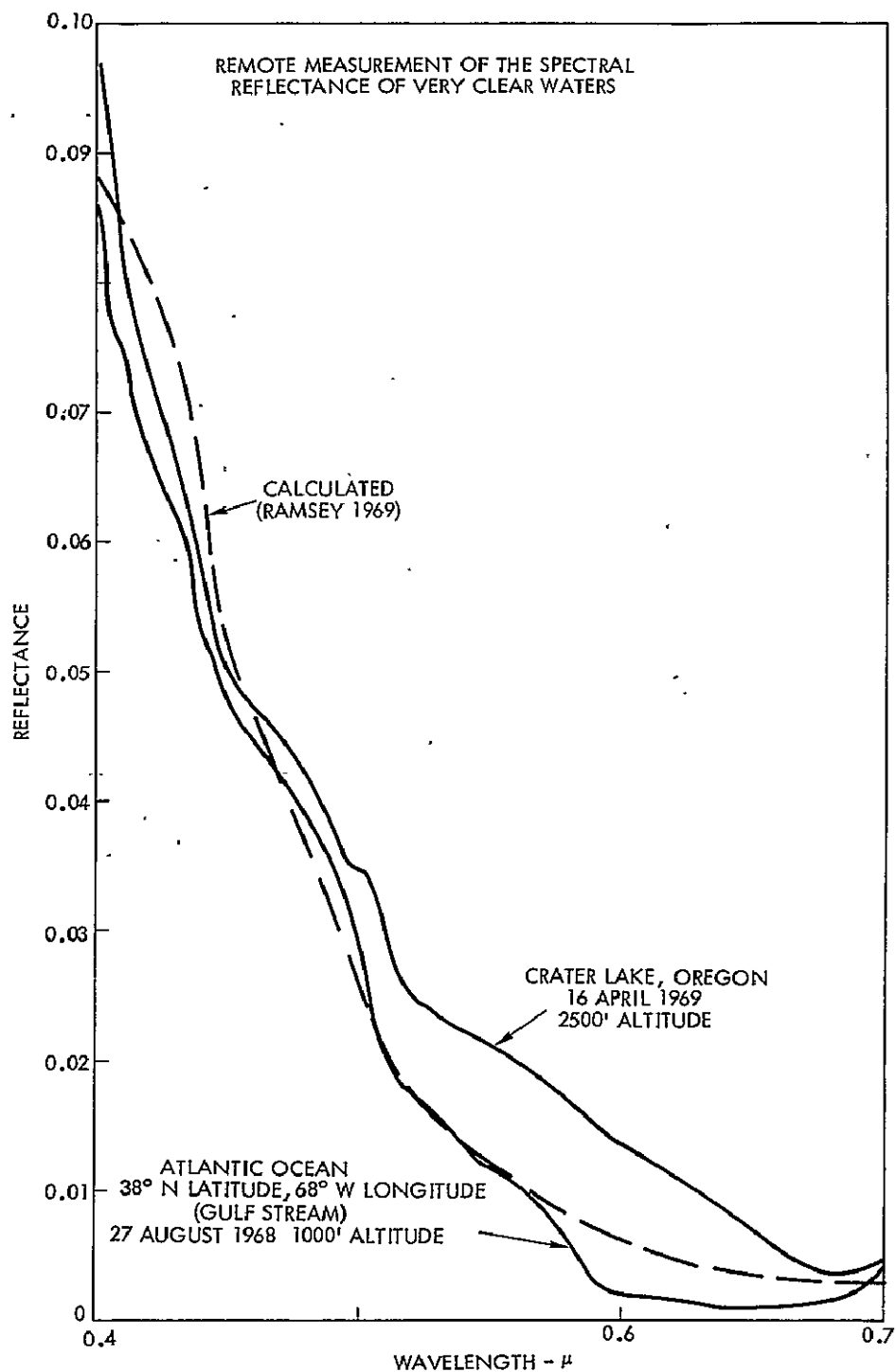


Figure 50-1.- Remote measurement of the spectral reflectance of very clear waters.

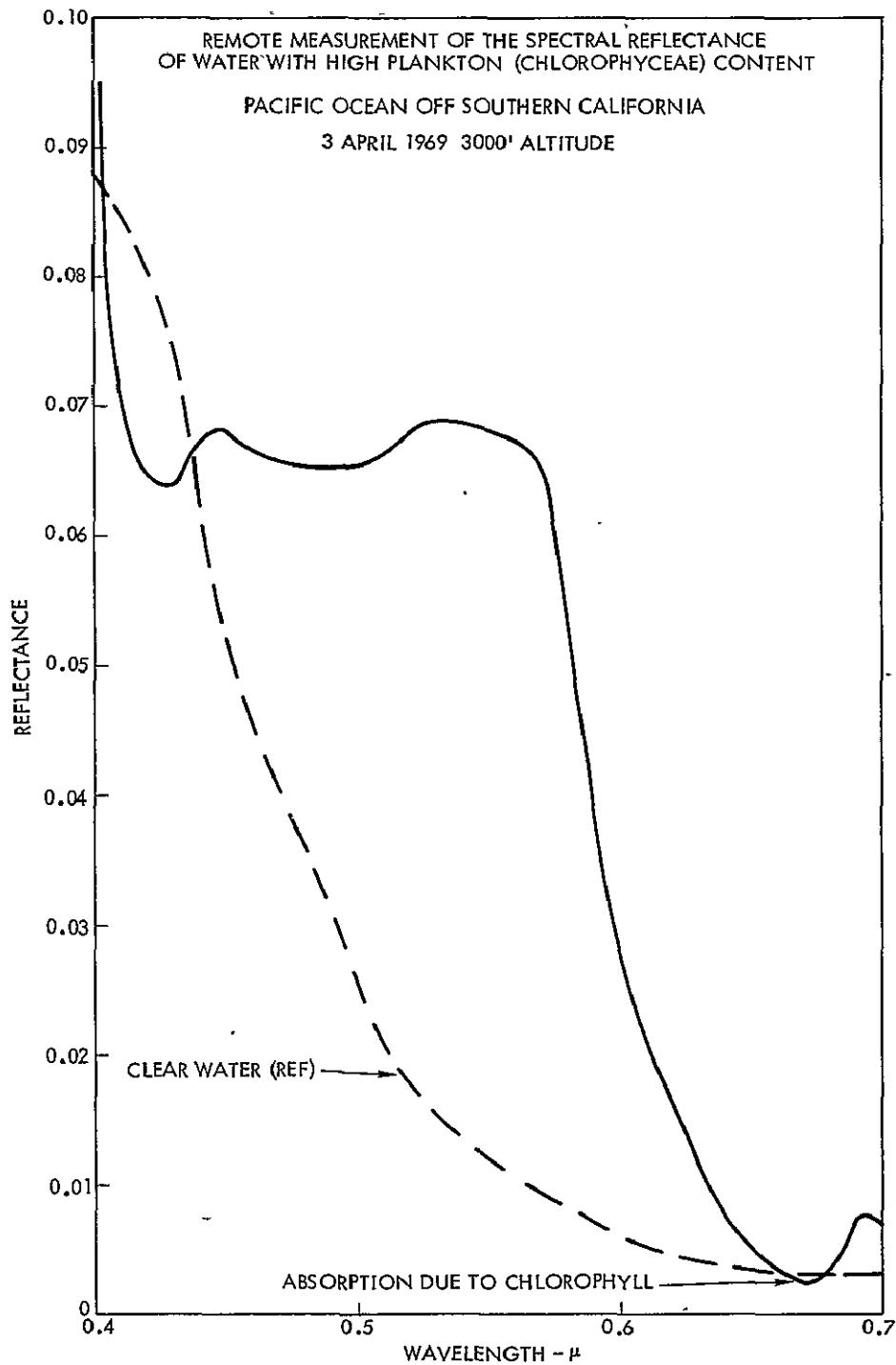


Figure 50-2.- Remote measurement of the spectral reflectance of water with high plankton (Chlorophyceae) content.

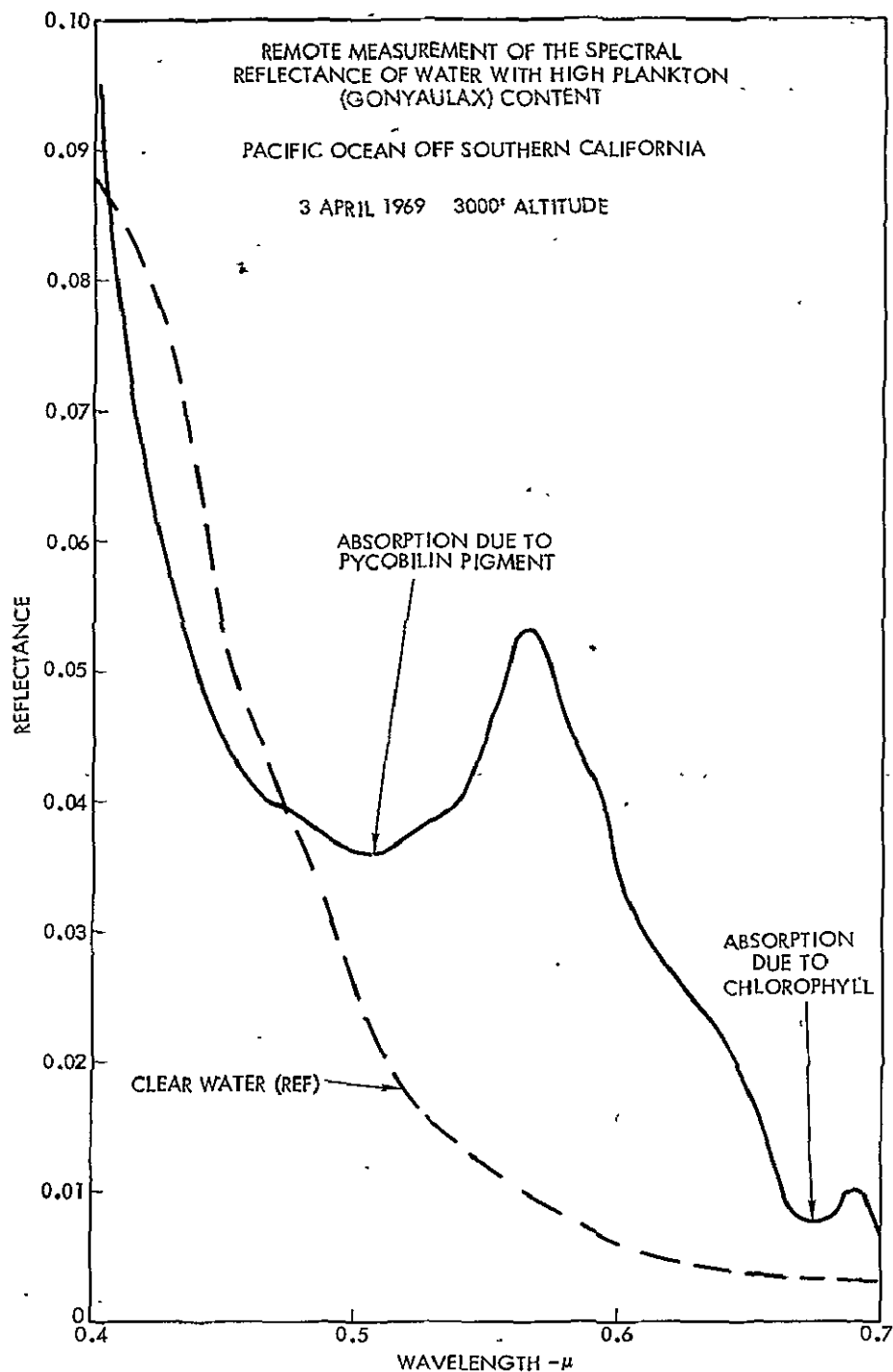


Figure 50-3.-- Remote measurement of the spectral reflectance of water with high plankton (Gonyaulax) content.

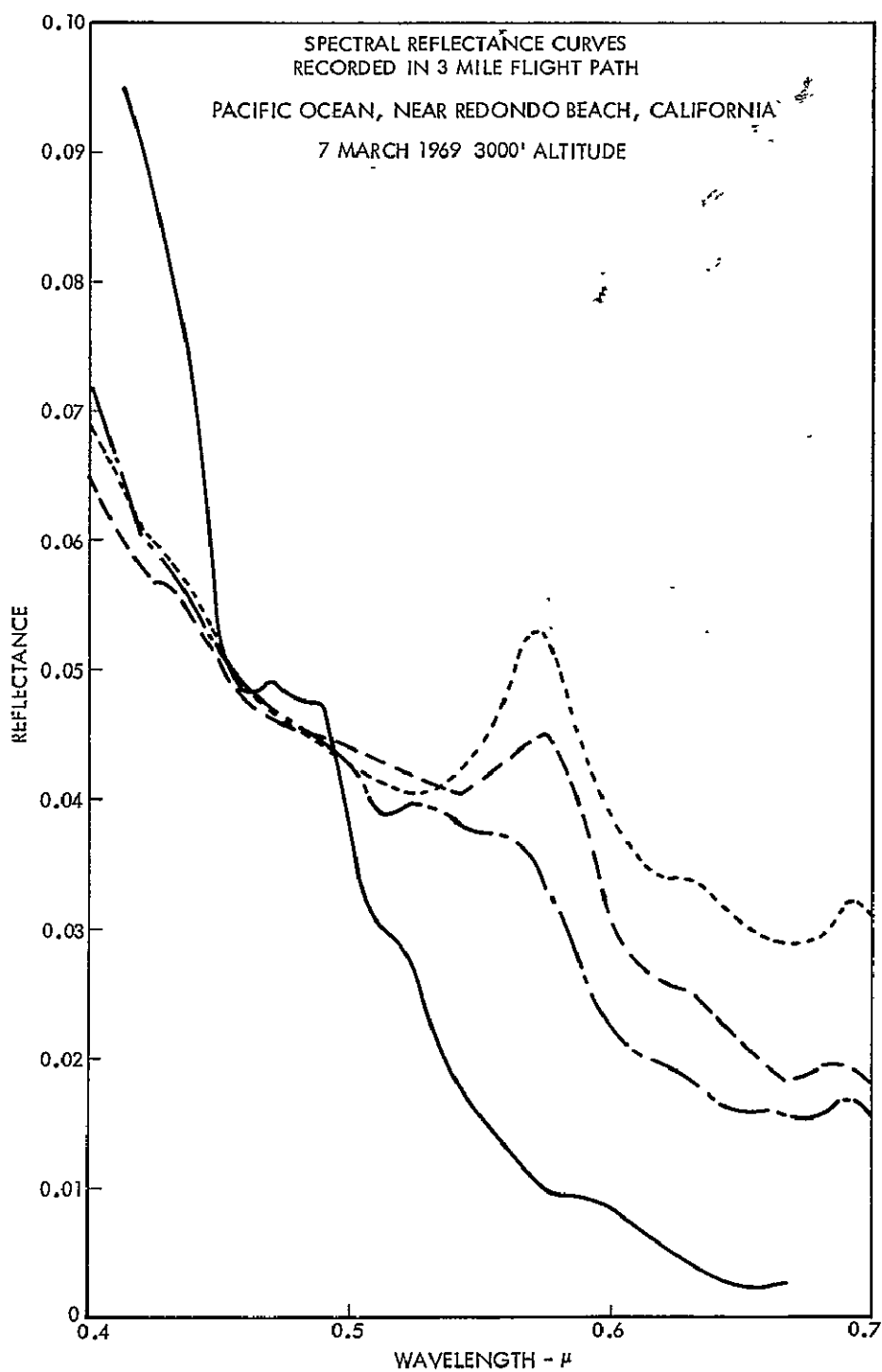


Figure 50-6.- Spectral reflectance curves recorded in a 3 mile flight path.

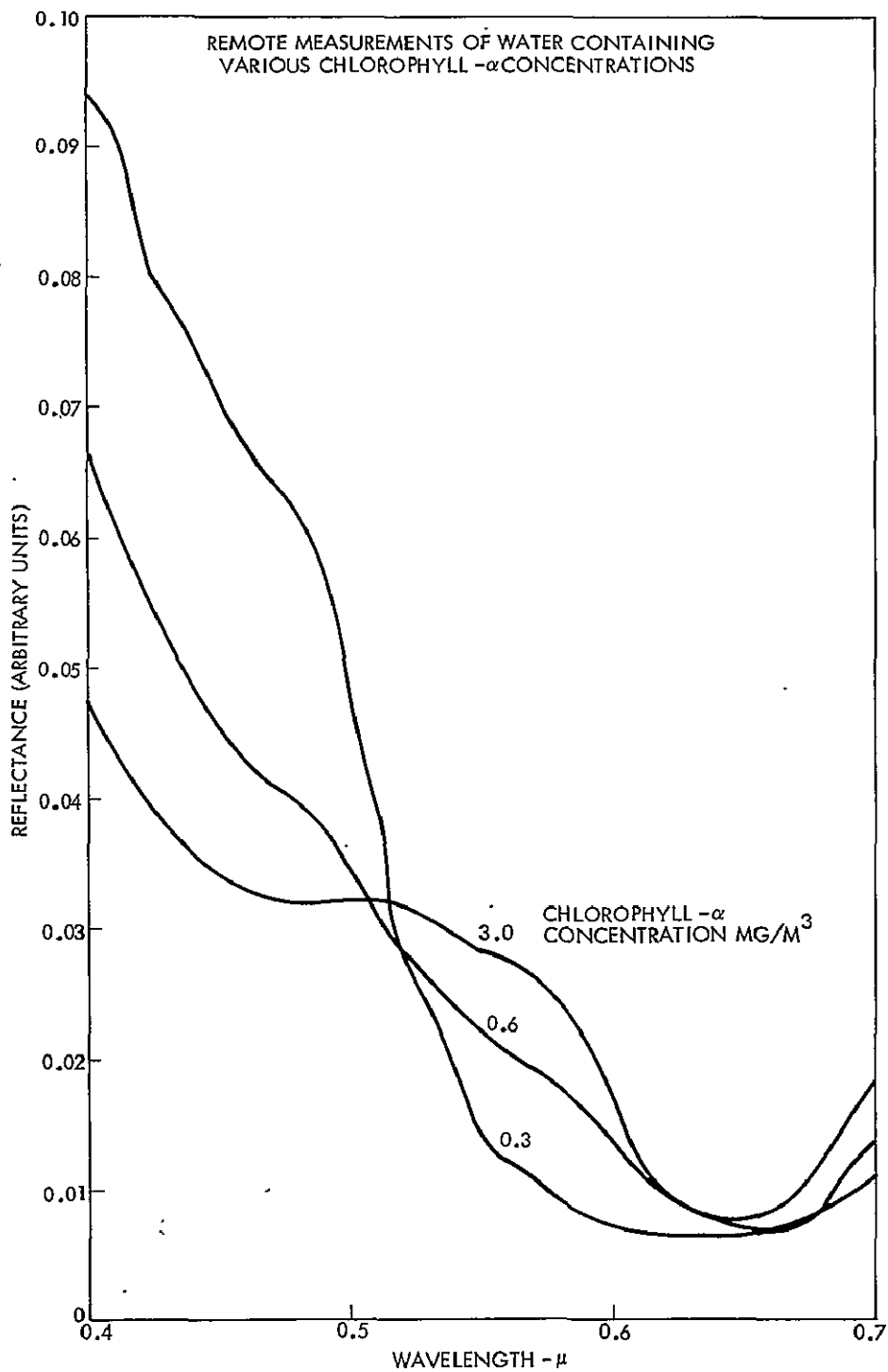


Figure 50-4.- Remote measurement of water containing various Chlorophyll concentrations.

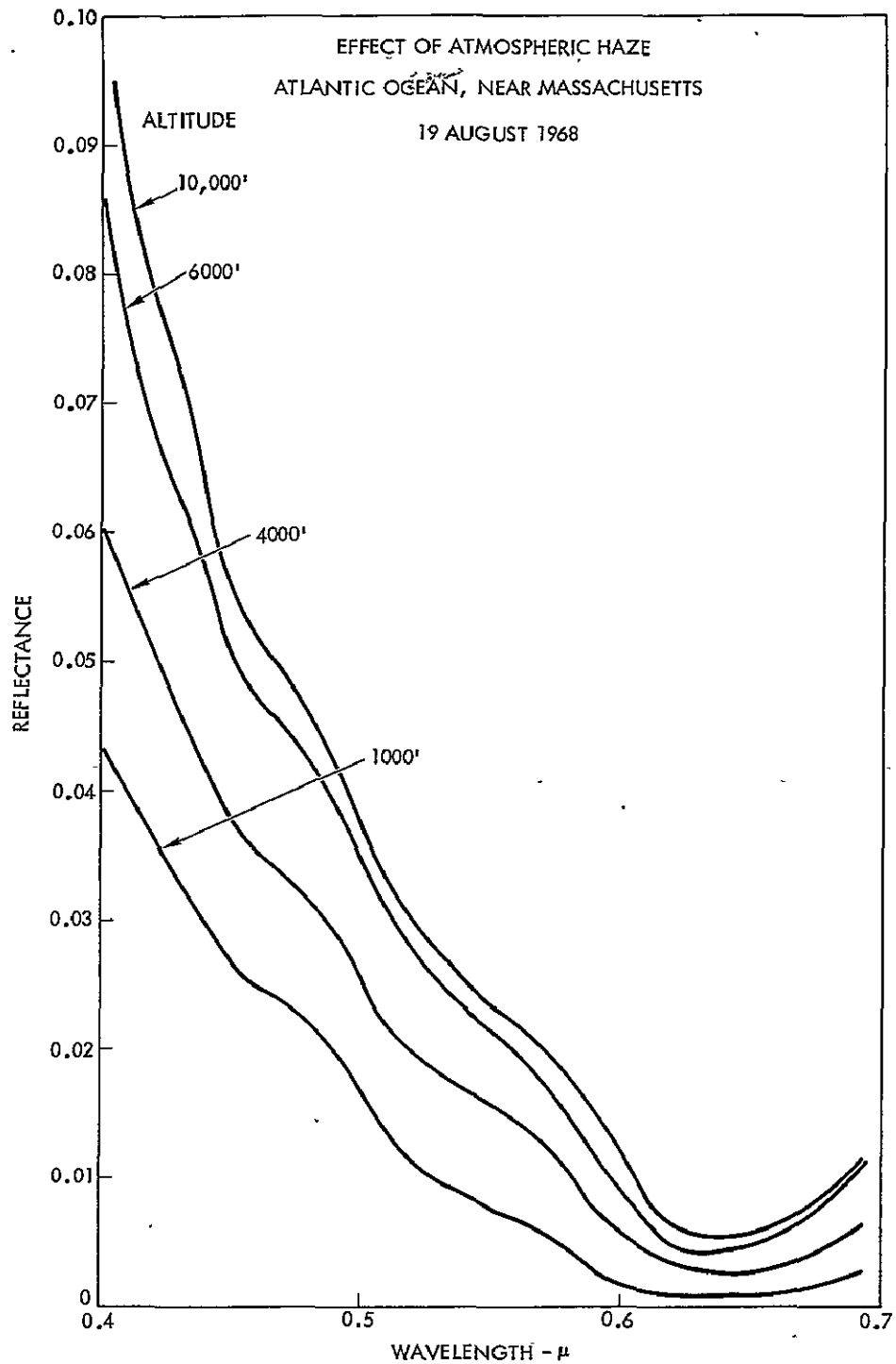


Figure 50-5.- Effect of atmospheric haze on reflectance versus wavelength measurements.

SECTION 51

EXPERIMENTS IN OCEANOGRAPHIC AEROSPACE PHOTOGRAPHY

BEN FRANKLIN SPECTRAL FILTER TESTS

Contract N62306-69-C-0072

for the

Spacecraft Oceanography Program
U.S. Naval Oceanographic Office

Prepared by

D. S. Ross and R. C. Jensen

Presented by Reece C. Jensen at the Second Annual Earth Resources
Aircraft Program Review on 16-18 September 1969.

PRECEDING PAGE BLANK NOT FILMED

51-3

EXPERIMENTS IN OCEANOGRAPHIC AEROSPACE PHOTOGRAPHY

BEN FRANKLIN Spectral Filter Tests

ABSTRACT

N71-11168

The spectral region of primary interest for oceanographic remote imaging sensors occurs within a passband approximating 400 to 580 $m\mu$. This includes the region of least light attenuation in clear water and a large percentage of coastal waters, where maximum depth penetration is possible and significant changes in upwelling luminosity occur. The practice in black-and-white aerial photography, however, is to reject image light at wavelengths shorter than 500 $m\mu$ in order to suppress effects of atmospheric haze.

Photographic color separation of many Apollo and Gemini color film images taken from space has shown that the blue record contains information significant in oceanography, despite atmospheric haze. Four-band multispectral photography with red, green, blue, and blue-green filters -- taken on flights over the BEN FRANKLIN submersible when on the surface and at 10, 15, and 25 meters in the Gulf Stream -- produced data confirming the utility of a blue filter band for oceanographic purposes. In addition, the results of the photographic evaluation were confirmed by measurements of the downward spectral irradiance made from within the submersible using a scanning spectroradiometer.

For recording ocean water color and optimizing penetration two spectral bands are recommended: 460-510 $m\mu$ and 510-560 $m\mu$. If only one passband is feasible, the 460-580 $m\mu$ region should be included.

ACKNOWLEDGEMENT

This work was performed under Contract N62306-69-C-0072 for the Spacecraft Oceanography Program, U. S. Naval Oceanographic Office, with the support of the National Aeronautics and Space Administration. The cooperation of the Grumman Aircraft Engineering Corporation, Ocean Systems Division, and time and effort contributed to the experiment by the technical and operational personnel of the BEN FRANKLIN, are gratefully acknowledged.

This paper was prepared by D. S. Ross and R. C. Jensen of the SRS Division of Philco-Ford Corporation under Contract N62306-69-C-0072 for the Spacecraft Oceanography Program, U. S. Naval Oceanographic Office. The paper was presented by Reece C. Jensen at the Second Annual Earth Resources Aircraft Program Review, 16-18 September 1969.

PURPOSE OF BEN FRANKLIN EXPERIMENT

Photographic flights were made over the BEN FRANKLIN - the largest civilian research submersible in service today - to obtain quantitative data on the possible gain that might be achieved by including more of the blue-green spectrum in oceanographic imagery from space. The data are also applicable to normal oceanographic aerial photography.

The experiment was made possible through the cooperation of the Grumman Aircraft Engineering Corporation, builder and owner of the vessel, and the active assistance of their Ocean Systems Division staff and crew at Riviera Beach, Florida.

Target Area. The BEN FRANKLIN's length of 48.7 feet and beam of 13.3 feet offered a useful target size for aerial photography. For the experiment the deck was painted with a matte white paint* (it was originally coated with a yellow anti-fouling paint) to ensure a large, diffuse, spectrally nonselective reflecting surface in the visible region. The target area was 13 x 28 feet, with the flat part of the deck 4 feet wide. A diagram of the BEN FRANKLIN is shown in Figure 1.

The sides of the hull were freshly painted with white epoxy shortly before the operation. The sail remained yellow.

Spectral Measurements. Spectral measurements were made on a large sample surface of the paint with an EG&G Scanner Spectroradiometer, which was installed inside the submersible looking up through a porthole. The instrument was used to measure the downwelling spectral irradiance in the range 350-750 m μ . Several readings of the downwelling light were taken at each depth to which the submersible was stabilized.

PHOTOGRAPHIC COVERAGE

Multispectral Camera. The Four-Lens Multispectral Camera (R4-B) used in the tests (Figure 2) was equipped with Schneider Xenotar f/2.8 lenses of 152 mm focal length (6 inches), to provide simultaneous images 3-1/2 inches square in four spectral bands. Camera characteristics are itemized below:

- a. Four simultaneous images on same film
- b. Image format, 3-1/2 x 3-1/2 inches, 40° diagonal field, 32° square field
- c. Lenses, 150 mm (6 inch) f/2.8 Schneider Xenotars

*3-M Nextel Velvet Coating Series 110-A10 (white).

- d. Spectral bands: Variable, as required
 - Nominal, Wratten 47 or 47B (Blue)
 - 58 or 61 (Green)
 - 25 or 29 (Red)
 - 89B, 88A, or 87 (Infrared)
 Blocking filters are used in conjunction with Wratten filters, to suppress transmission in secondary spectral regions, permitting the use of extended red and infrared films with Wratten filter passbands of shorter wavelength..
- e. Frame rate, 2 second cycle, nominal
- f. Shutter speed, 0.006 to 0.0013 sec
- g. A5 film magazine type

K17 Camera. A standard K17 camera, with a 6-inch focal length f/6.3 Metrogen lens and an image format of 9 x 9 inches, was also flown. As directed by the suppliers, no filter was used with the special Anscochrome film loaded in this camera.

Multispectral Camera Film and Filters. Three of the bands in the multispectral camera were equipped with standard color separation filters, Wratten Nos. 47B (blue), 58 (green), and 25 (red). The fourth band had a 2E+38 combination, which effectively bridges the zone between the blue and the green filters. Transmission curves for the filters are given in Figure 3. The 2E+38 combination has a high transmittance in a region of particular interest, 480 m μ (blue-green), where clearwater light attenuation is least. Natural color films have a sensitivity at this point which is about 50% less than in their blue and green peaks.

The 2E+38 combination transmits more light than desired above 580 m μ and in future tests will be replaced with an interference filter to reduce the surface reflectance component in this region.

The spectral sensitivity of the 2484 emulsion film used in the experiment has a peak transmission of the blue (47B) and green (58) filters at almost the same density of 1.0 above fog. The emulsion has a lower RMS granularity factor than Aerial 8403 Tri-X (37 vs. 48), despite its high sensitivity.

Special Anscochrome Film. The K17 camera was loaded with a special GAF Color film, provided through the courtesy of W. E. Vary, U.S. Naval Oceanographic Office. The film is based on Anscochrome D-500, a high-speed, natural-color film. In this version the blue-sensitive layer is omitted during manufacture. The normal yellow dye filter layer is retained to reduce sensitivity of the green layer in the region below 500 m μ .

OPERATIONS

On May 19, 1969, the BEN FRANKLIN was towed from her dock at Riviera Beach, Florida, to a position in the Gulf Stream about 8 nautical miles east of West Palm Beach, at approximately 26°51' N, 79°58' W, where water depth is in the order of 800 feet.

Four photo runs were made on the BEN FRANKLIN, while under tow, to obtain images of the deck above water. Photography of the submerged vessel began 1 hour and 20 minutes later than the surface photography.

Sun Elevation. Sun elevation for the surface photography was about 43° (1824 GMT). Changes in sun elevation during the submerged period were:

10 meters (1939 - 1939 - 1946 GMT)	41° - 40°
15 meters (1955 - 2001 GMT)	40° - 39°
25 meters (2013 - 2017 GMT)	38° - 37°

Illumination. Three layers of cloud overcast persisted during the operation, effectively blotting out direct sunlight. Under these conditions, while illumination is diminished by a factor of 3 or more from direct sunlight, less variance is found with changing sun elevation, and relative spectral irradiance on the scene is not altered significantly although the overcast sky reduces energy in the blue region somewhat. The lowest layer of cloud was between 1,100 and 1,600 feet ASL during the flights.

For practical purposes, scene illumination during the 40-minute submerged period is considered to have been constant, possible variations being within system measurement error.

Camera Exposure. The four-band camera shutter was set at 1/400 sec (0.0025 sec), with lens apertures as follows:

Band 1	Band 2	Band 3	Band 4
(47B-Blue)	(58-Green)	(25-Red)	(2E+38-Blue-Green)
f/5.6	f/5.6	f/4	f/8

The blue-green band received one full aperture stop less exposure than bands 1 and 2, while the red band had one stop more exposure. Bands 1 and 2 were oriented in the camera orthogonal to the focal plane shutter travel, to ensure that each received the same exposure, irrespective of variations in shutter acceleration. The special Anscochrome film in the K17 camera was exposed at f/6.3, 1/150 sec.

Environment. Surface winds were less than 10 knots, seas 2 to 4 feet, with moderate swell. Visual water color was blue, identifiable as the Gulf Stream. Surface current in this vicinity is shown on the charts to be about 2-1/2 to 3-1/2 knots.

Navigation. When submerged, the submersible was not visible to personnel on the PIONEER chase vessel, and her positions were called out to the surface vessel by the aircraft pilot. Navigation problems for photo flight lines were encountered as soon as visual contact with the BEN FRANKLIN was lost by the aircraft, below 25 meters.

As the surface and submerged vessels were drifting apart at different rates, changing relative headings by the minute, attempts were made from the bridge of the PIONEER to vector the aircraft by VHF onto the BEN FRANKLIN position

at depths below 25 meters by means of sonar range and bearing. The distance between the two-sonar exceeded the maximum 1000-foot limit in the operations plan; at one stage the BEN FRANKLIN was judged to be 3200 feet from the PIONEER. Analysis of flight-line data makes it unlikely that the aircraft was able to include the BEN FRANKLIN's position in any photography at depths greater than 25 meters because of cumulative vector errors of only a few degrees.

Multispectral Images Acquired. Four sets of four-band images were taken of the BEN FRANKLIN on the surface. The submersible appears in nine sets taken at 10 and 15 meter depths, and in eight sets at 25 meters. No images were acquired in the red (25) filter band below the surface. Enlargements of typical images at each depth are shown in Figures 4a through 4d.*

DENSITY READINGS

Densities were measured on the original BEN FRANKLIN images with a MacBeth Quantalog densitometer, using a 1.0 mm aperture. This instrument has an error of about ± 0.02 and repeatability of about ± 0.01 . Readings were made by two observers on different occasions. Only one set of reading, made by one observer, is used in the analysis, and no attempt has been made to favor a trend or to select "best" readings from other sets.

The density readings were corrected for gamma, filter factor, and changes in sun elevation angle, then normalized to the deck of the submersible while on the surface. Table I compiles all density data on a common base at $\gamma 1.0$ compensated for filter factors and changes in illumination, with the white deck of the BEN FRANKLIN as an equal-energy spectral irradiance reference for each filter band.

INTERPRETATION OF THE PHOTOGRAPHIC DATA

For detecting the underwater object, or in recording differences in the luminance of upwelling scattered light, photographic density of the subject must be higher than the density of the water surface. Image densities in Table I show the relative merits of bands 1, 2, and 4 in this respect, at $\gamma 1.0$. With other films and different processing, higher gammas can be achieved, and the ΔD 's would be multiplied by the higher γ factor. The linear portion of Plus-X Aerographic film, for example, reaches $\gamma 2.2$ (white light exposure), and the green-sensitive layer in the GAF Anscochrome D-500 is in the same order. As mentioned earlier, γ can also be raised to a considerable extent during reproduction.

*A complete index of the BEN FRANKLIN imagery, as well as related oceanographic photography from the Florida coast and keys, the Bahamas, and the Georgia and Carolina coasts, is contained in Appendix A to Philco-Ford SRS Division Technical Report TR-DA2108, "Experiments in Oceanographic Aerospace Photography, I - BEN FRANKLIN Spectral Filter Tests," 29 August 1969.

While the ΔD 's can be increased substantially by these means, they will remain proportional to each other in each spectral band. Since this is so, the ΔD 's provide a direct figure of merit for each spectral band. Figure 5 plots the density of the BEN FRANKLIN's image for each band at each depth, extrapolated to the densities of the water surface in the respective bands. The figure illustrates two factors:

- a. The gradient of the downward slope indicates the rate of decrease in photographic density with depth; the steeper the slope, the greater the attenuation of upwelling irradiance in the spectral band concerned. The blue band clearly shows less attenuation than the green band, while the blue-green band 4 is midway between.
- b. The value of ΔD will vary with the subject, its configuration, scale, and other variable factors. By photographic enhancement or other means, density differences in the 0.01 to 0.03 range can be separated from the image. In this case, when the densities of the BEN FRANKLIN images recorded at 25 meters are extended to meet the water surface densities in each band, it can be seen that band 2 (green) is rapidly approaching an extinction point short of 30 meters where the density of the FRANKLIN's image would be indistinguishable from the water surface. Band 1 (blue) and 4 (blue-green) would have reached their end points around 35 meters. Therefore, at any other proportionately higher gamma, the blue and blue-green bands would continue to outperform the green band in penetration.

It is important to understand that these data are relative and pertain to the conditions existing at the time of the tests, when downward illumination was less than normal by a factor of 3 to 5 times. In full sunlight, much deeper penetration would be obtained in each spectral band; nevertheless, the relative merits of each to "penetrate" would remain at or very close to the same ratio.

The photography was taken at low altitude, where atmospheric haze effects were insignificant. Most of the deleterious effects of haze in aerial photography arise at altitudes of less than 30,000 feet. The most serious absorption and scattering is caused by Mie particles, water droplets, pollen, dust, salt nuclei, and these are seldom found in serious concentrations above 15,000 feet. To obtain a better insight on the effects of haze in ocean areas on the quality of images taken with the same spectral bands, coverage was obtained from 20,000 feet and with the same multi-spectral camera along the Bahama cays and from the Florida, Georgia, and Carolina coasts to Cape Hatteras. About two-thirds of the worst atmospheric effects were below the camera.

Visual assessment of the imagery as directly recorded is not valid, since the blue record is invariably of lower contrast than the green image in this system. In Figure 6a, the blue record of a sample multispectral image set has been raised in underwater scene contrast to match that of the green (Figure 6b). It can be seen that each spectral band contains useful subsurface information. The results in "penetration" obtained in these two images taken simultaneously from 20,000 feet are very similar to the blue and green separations of a color film made from an altitude of over 100 nautical miles.

It could be argued that haze varies, and is worse on some occasions or in some regions of the earth than in others. This may be true. And the same argument can be applied to cloud cover. The Gemini and Apollo photography has amply demonstrated that despite cloud, the acquisition of earth resources imagery is feasible. It is also considered that the same photography proves the practicability of including a blue record, despite atmospheric haze, as a spectral band of great value in oceanographic remote sensing.

The failure of band 3 (red) to penetrate to a 10-meter depth is normal, as the absorption factor of water for light in this spectral region is 4 to 5 times greater than in the blue and green. Because of the high attenuation factor, the contrast of detail in shallow water appears higher in the red than in the green; however, the same information can be recorded at the same depths in either the blue or green bands, and there is no special virtue in having a red record for penetration per se. The red record is useful for aiding detection of sediments in depths down to 6 or 8 meters, and in discriminating surface effects.

ON-BOARD LIGHT MEASUREMENTS

The basic objective of the instrumentation on board the submersible was to measure the spectral distribution of a portion of the downward irradiance incident on the deck of the submersible. These measurements were to be made at a number of different depths ranging from the surface down to 45 meters. The nature of the instrument used for measurement of downward irradiance and the geometry and orientation of the instrument in the submersible were such that only the irradiance in some narrow region of the zenith direction was actually determined. The spectroradiometer used for the experiment was mechanically scanned over the visible spectrum from 350 to 750 $m\mu$ in 25 $m\mu$ steps. At each wavelength the instrument was allowed to stabilize, and at least two independent readings were taken. An x-y recorder was provided for recording the resultant data, but various instrument mounting problems prohibited the recorder from being used and all results were manually recorded.

Instrument Characteristics. The instrument used to measure downward irradiance was an EG&G Spectroradiometer Model 585. Its characteristics are:

<u>Quantity</u>	<u>Value</u>
Wavelength covered	350-750 $m\mu$
Detector photo surface	S-5
Slit size: Entrance	5.36 mm
Exit	3.0 mm
Grating bandwidth	20 $m\mu$
Beam input	*5.0°
Hooded Filter Holder Cone Angle	14.0°

*This is not the effective field of view of the instrument. A discussion of the effective field of view of the instrument is provided in Section IIIB.

<u>Quantity</u>	<u>Value</u>
Filters (Corning)	
Range (350 - 550 m μ)	CS-0-54
(550 - 800 m μ)	CS-3-69
Instrument reading for steady source	amps
Minimum power for full scale deflection	1.1x10 ⁻⁸ (watts/cm ² -m μ) at 450 m μ
Minimum instrument reading	1.0x10 ⁻¹¹ amp

The instrument measures the energy from a given source either point or finite at any desired wavelength with a discrete known bandwidth.

Determination of the Effective Aperture of Spectroradiometer (S/R). The instrument response curve derived from the instrument manufacturer (Figure 7) shows the percent of peak response as a function of the half angle of field of view. The two curves provided are for the cases where the hood is in place and removed. At approximately 12° off axis the instrument response is only 10% of the peak response with the hood in place. Since in the actual installation of the S/R in the submersible the field of view was restricted by the port (see Figure 8), the actual effective field of view was considerably less than that predicted from Figure 7. Because no actual readings were made to establish the instrument response curve, once the S/R was installed in the submersible, the actual field of view can only be estimated. It is safe to say, however, that the field of view was no smaller than 10° and certainly no larger than 20°. Since for purposes of the underwater energy measurements the energy distribution is itself falling off logarithmically from the zenith direction, an effect value for the instrument field of view of 10° was selected as best representing the 90% energy collection angle for the instrument.

Instrument Installation in Vessel. The EG&G Spectroradiometer was mounted on Bunk 3 with its optical axis pointing directly up through the port. The field of view of the S/R was essentially reduced to 10° by the port geometry. Figure 8 provided by Grumman Aircraft shows a cross section of the BEN FRANKLIN at the location of the S/R. Figure 9 shows an actual photograph of the instrument in place as it was finally installed.

Two originally planned features of the installation were not possible in the final installation. First, the distance between port and Bunk 3 did not permit the use of the standard hooded filter supplied with the instrument. In place of the hood a black shroud was installed between the port and the S/R. Second, the x-y recorder could not be used because of mounting location problems. All data had to be recorded by hand, but several independent readings were taken at each depth to minimize human errors. The shroud was equally as effective as the hood since the light level inside the submersible was quite low during the experiment.

In Figure 9 is shown a photograph of the BEN FRANKLIN on the surface with the view port for the S/R painted black. This was done to minimize the effects of stray outside light on the measurements.

DATA PROCESSING

The following is a brief description of the computer program written for processing the S/R data. The program draws a log-paper grid.

The calibration curves are tabulated in DATA statements in the program as the arrays A, B, C, D, and E. Tabulated values are in units of millimicrons and amp/(watts/cm²-mμ). The curves are interpolated by walking a quadratic,

$$\log w = a_1 + a_2 \times a_3 x^2,$$

along the monotonically stored data points. The first point to be parabolically fit is the first tabular wavelength preceding the wavelength to be interpolated for.

The intensities are stored in the array PDATA with their corresponding wavelengths from the input card. The listed output is

N	Curve number, NC (Filter 3 or 4)
WAVE	wavelength (mμ)
METER	test lamp (amp)
XI	first wavelength of tabulated curve used to fit
(Quad. Fit Coeff)	a ₁ , a ₂ , a ₃ in the equation above
W(CURVE)	interpolated spectral response
Irradiance	I = z/w
Scaled Irradiance	log I

CORRECTION FOR LARGER SLIT-SIZE CALIBRATION

The calibration curve for the instrument using the S-5 detector and standard slit sizes is shown in Figure 10. A standard WI lamp at 2900°K was used to obtain a correction factor for the effect of using the wider slits. The resultant calibration data is shown in Table II.

CORRECTION FOR WINDOW ATTENUATION AND
INSTRUMENT GEOMETRY

The light losses in passing through the window of the submersible were originally to be evaluated by (1) making irradiance measurements through the window from inside the submersible while at the dock, and (2) repeating this process outside the submersible looking straight up at a clear sky. Some difficulty was encountered with the data taken at the dock site due to the intermittent passing of smoke over the dock from the adjacent powerplant. Hence after the experiment had been completed in Florida, tests were conducted on a spare window from the BEN FRANKLIN which was borrowed from Grumman Aircraft. A jig was made to hold the window in the same geometry as it would be in the submersible, and a series of runs was made using the S/R with and without the window in place.

An approximated reduction in irradiance of 20 percent was obtained as a result of the window being in the light path. This correction factor as a function of λ was then applied to all data in a similar manner as the slit correction. The slit correction required a reduction computed energy of approximately 4 and the window correction required an increase in the computer energy of approximately 20 percent. Of course, the window correction was applied only to data taken from within the submersible.

INTERPRETATION OF SPECTRORADIOMETRIC DATA

Evaluation of the S/R Data indicates that the energy level in most cases peaks out between 450 and 550 $m\mu$; the maximum energy being received by the instrument was at or near 475 $m\mu$. Since the instrument as previously described measures energy over a 20 $m\mu$ portion of the spectrum, the significance of a specific value for the wavelength for maximum energy transmission is not meaningful. However, the band of 450-500 $m\mu$ certainly seems to contain the region of maximum energy transmission.

Figure 11 is a composite of the average energy curves taken when the vehicle was below the surface. The curves are consistent with increasing depth and they seem to indicate a higher energy transmission in the blue 430 $m\mu$ than in the green 530 $m\mu$ for all depths. All of the curves seem to have a noticeable bump near the point of peak energy transmission. This bump seems to be more pronounced for the deeper measurements.

Another characteristic of the data is the apparent increase in energy that occurs at or near 650 $m\mu$. In several cases the energy rises sharply in this region. This effect is apparently due to the very steep detector sensitivity in this region. The last section of the detector response curve 650-750 $m\mu$ is quite sensitive to the wavelength setting in this region. For this region of the spectrum and these energy levels, an S-20 detector should probably have been used. The consistency of the increase does, however, leave the question open for discussion.

Figure 12 shows the average of the measured downward spectral irradiance for the blue and green bands as a function of water depth. The interesting feature of these results is that they confirm the photographic results that indicate the additional energy in the blue over the green as the depth increases. Again a bump or increase in energy appears to have existed at or near 35 meters, which might be explained by some form of layer in the water at this depth. The fact that it occurred in both the blue and green bands rules out the effect as being measurement uncertainty.

CONCLUDING REMARKS

Current planning for multispectral remote earth resources sensing is based on images acquired in three spectral bands, essentially, green, red, and infra-red. Information useful in oceanographic interpretation can be found in varying degree in each of these spectral regions. However, unless a blue spectral record is also included, much oceanographic information of fundamental importance will not be obtained.

The blue record combined with the green permits water color and its changes to be detected and evaluated in the blue and blue-green spectral regions. This part of the spectrum is where the color of the largest percentage of the world's oceans is found, where clear water penetration is greatest, and where small changes in color are related to major ocean phenomena. It is therefore recommended that:

- a. Two spectral bands be used for oceanographic imaging, to be obtained with sharp cut-on and cut-off interference filters.
Variations in the passband with angle is not of significance with lens field angles now contemplated for orbital sensors.
- b. The two suggested passbands are 460-510 $m\mu$ and 510-560 $m\mu$.

The results from the measurements taken from within the submersible indicate that a very useful purpose can be served by this form of data. If an experiment of this type is to be meaningful, energy measurements must be taken. Such measurements should include both upward and downward irradiance as a function of depth below the surface, as well as the irradiance distribution function $f(\theta)$. The implementation of a mobile platform* should contain as a minimum a narrow-field-of-view spectroradiometer that could be scanned in both frequency and the direction of view automatically from the surface. The addition of this form of energy measurement would greatly help to increase the understanding of how remote sensors in the visible spectrum may best be applied to water color and water depth penetration applications of oceanography.

*A complete index of the BEN FRANKLIN imagery, as well as the related oceanographic photography from the Florida coast and keys, the Bahamas, and the Georgia and Carolina coasts, is contained in Appendix A to Philco-Ford SRS Division Technical Report TR-DA2108; "Experiments in Oceanographic Aerospace Photography, I - BEN FRANKLIN Spectral Filter Tests," 29 August 1969.

TABLE I
SUMMARY OF NORMALIZED DENSITIES

Roll No. 69001	BEN FRANKLIN 4-BAND MULTISPECTRAL PHOTOGRAPHY - 19 MAY 1969											
	Blue			Green			Red			Blue-Green		
	Band 1 - 47B			Band 2 - 58			Band 3 - 25			Band 4 - 2E + 38		
	Ben F.	Water Surface	ΔD	Ben F.	Water Surface	ΔD	Ben F.	Water Surface	ΔD	Ben F.	Water Surface	ΔD
Surface	2.00	1.33	0.67	2.00	1.07	0.89	2.00	0.96	1.02	2.00	1.20	0.78
10 Meters	1.73	1.33	0.41	1.55	1.07	0.48	---	0.96	---	1.74	1.20	0.44
15 Meters	1.62	1.33	0.30	1.32	1.07	0.25	---	0.96	---	1.50	1.20	0.31
25 Meters	1.47	1.33	0.14	1.16	1.07	0.10	---	0.96	---	1.34	1.20	0.14

NOTES:

1. The RMS density values in the ΔD columns were calculated from the density differences of individual negatives and not by subtracting the RMS water densities from the RMS BEN FRANKLIN densities.
2. All densities were referenced to the photography of the BEN FRANKLIN while on the surface. Primary reference was BEN FRANKLIN'S deck, and all have been made to = D.2.00. Secondary reference was established as the density of the water surface relative to the deck. Submerged BEN FRANKLIN densities have been adjusted to the secondary reference.
3. All densities are on a $\gamma 1.0$ response curve to scene luminance, and can be read in terms of lens aperture stops (0.30 unit).

TABLE II
CALIBRATION DATA FOR WIDE SLITS

Wavelength (λ) ($m\mu$)	Instrument Reading (amps)		Ratio* (A_w/A_n)
	Narrow Slits	Wide Slits	
350	6.99×10^{-10}	2.8×10^{-9}	4.00
375	1.67×10^{-9}	6.43×10^{-9}	3.85
400	3.17×10^{-9}	1.24×10^{-8}	3.91
425	5.18×10^{-9}	2.03×10^{-8}	3.92
450	7.37×10^{-9}	2.88×10^{-8}	3.91
475	9.28×10^{-9}	3.54×10^{-8}	3.81
500	1.07×10^{-8}	4.07×10^{-8}	3.80
525	1.14×10^{-8}	4.34×10^{-8}	3.81
550	1.03×10^{-8}	3.92×10^{-8}	3.81
** 550	9.69×10^{-9}	3.64×10^{-8}	3.76
575	8.14×10^{-9}	3.08×10^{-8}	3.78
600	4.21×10^{-9}	1.68×10^{-8}	3.99
625	8.48×10^{-10}	3.62×10^{-9}	3.90
650	2.38×10^{-10}	9.30×10^{-10}	3.91
675	7.65×10^{-11}	2.99×10^{-10}	3.91
700	2.70×10^{-11}	9.50×10^{-11}	3.52
725	1.26×10^{-11}	3.45×10^{-11}	2.74
750	0.82×10^{-11}	1.65×10^{-11}	2.01

*The ratio of A_w/A_n represents the increased amount of energy at the detector as a result of essentially doubling the inlet and exit slit areas. This ratio was then used to correct all data as a function of wavelength.

A_w = instrument reading using wide slits

A_n = instrument reading using narrow slits

**Filter change.

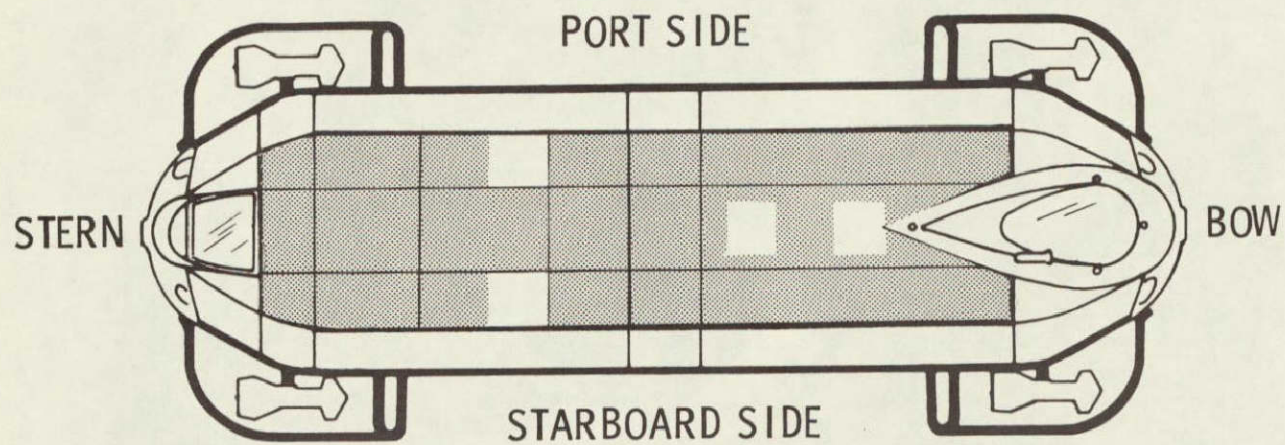


Figure 51-1.- Top deck of Grumman submersible, Ben Franklin.

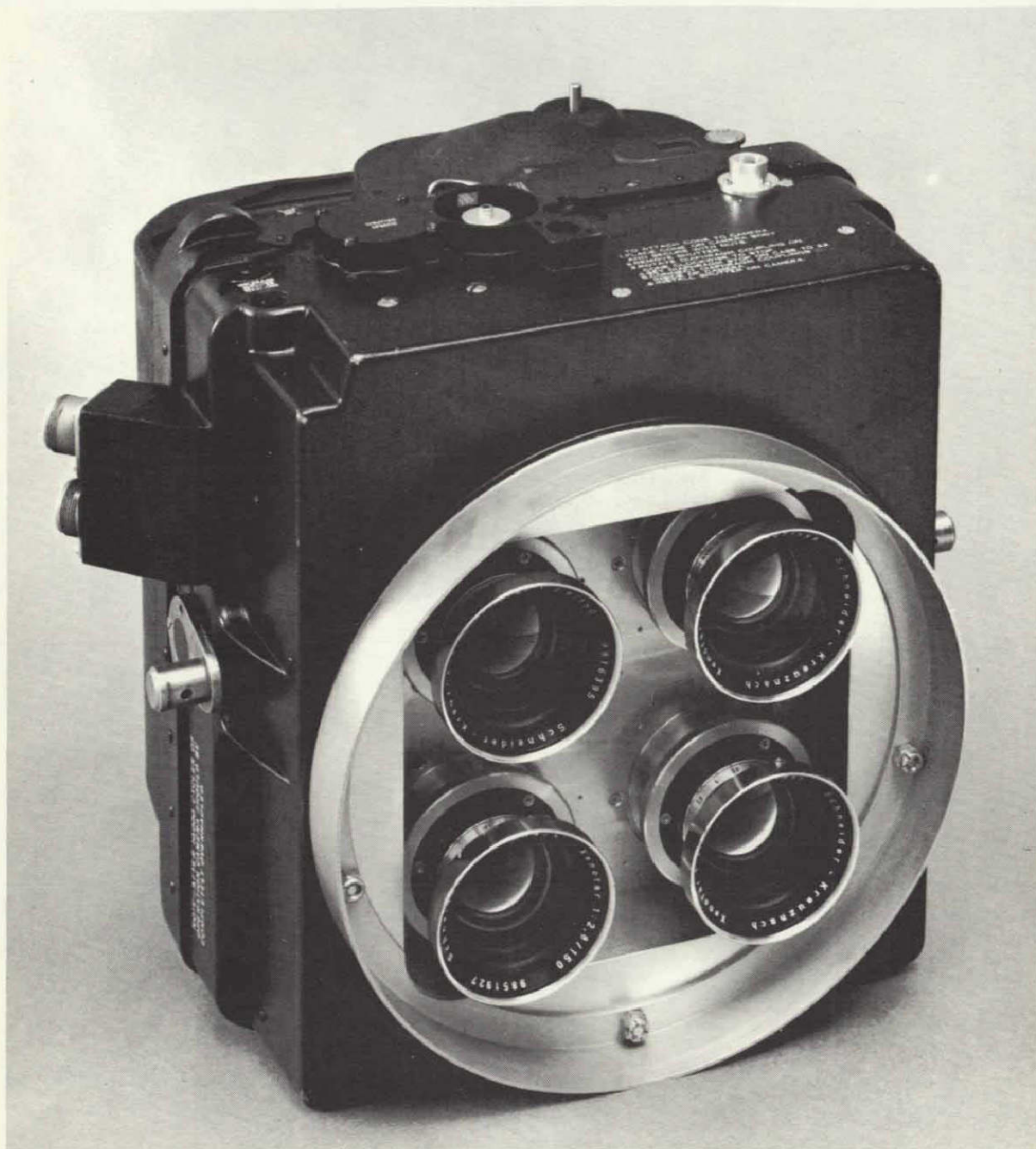


Figure 51-2.- R4-B four-lens multispectral camera.

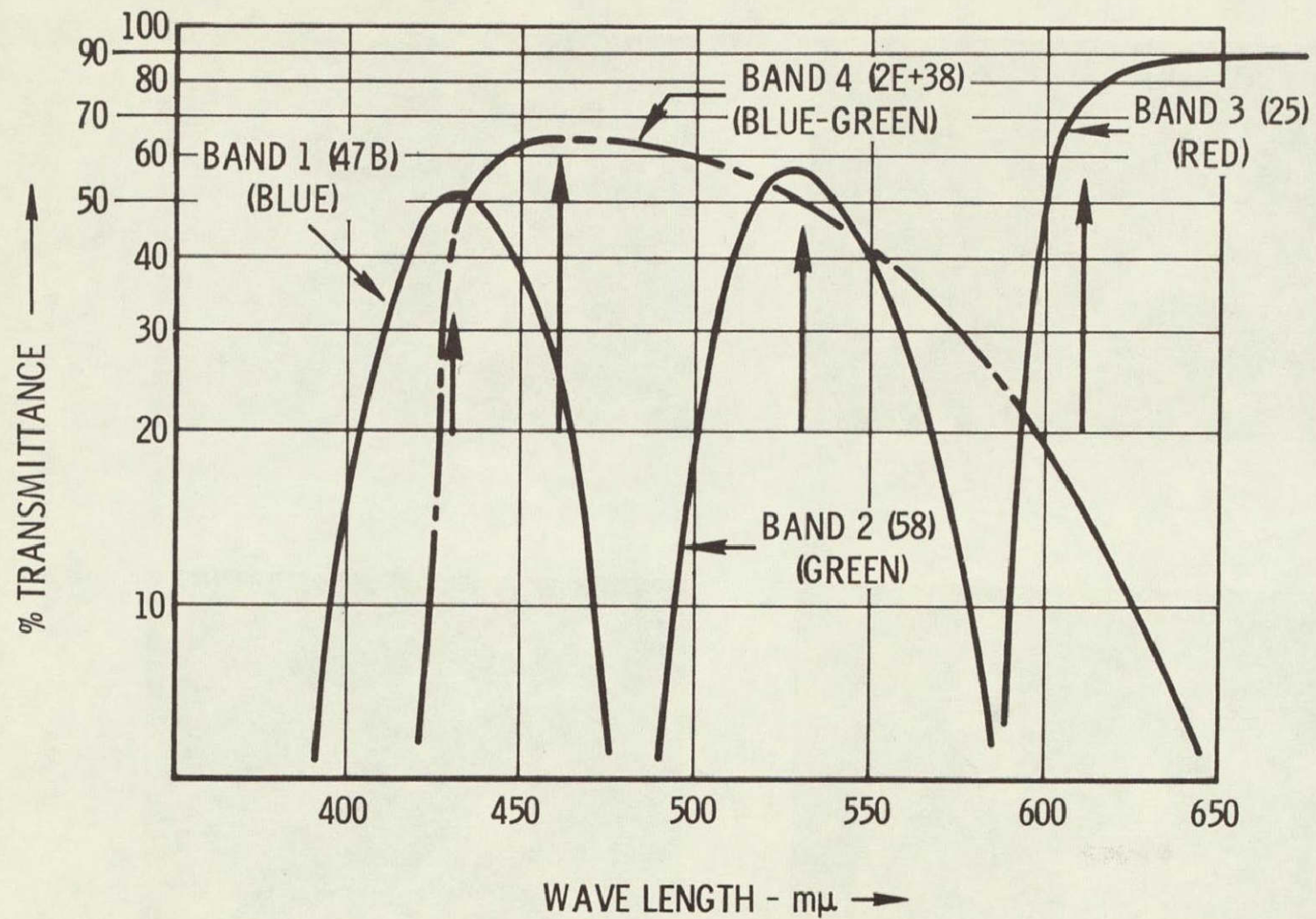


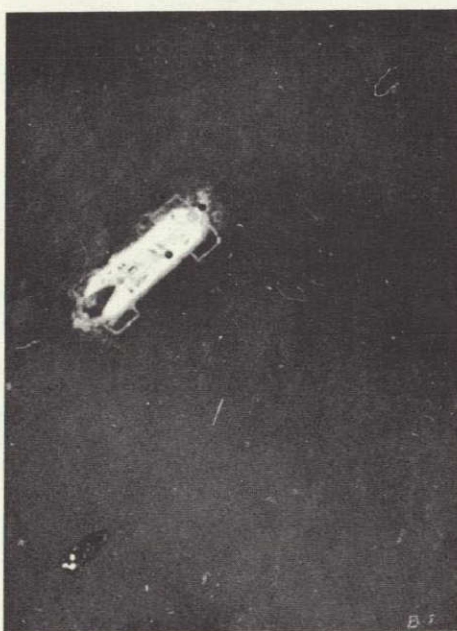
Figure 51-3.- Transmittance of filters in R4-B multispectral camera for Ben Franklin experiment.



BAND 4 - (2E + 38)
BLUE-GREEN



BAND 3 - (25)
RED



BAND 1 - (47B)
BLUE

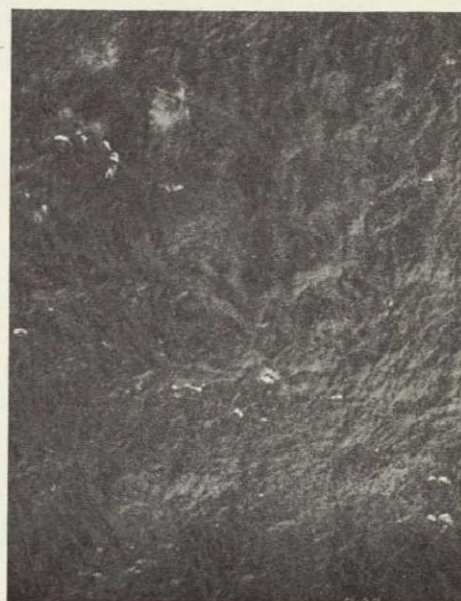


BAND 2 - (58)
GREEN

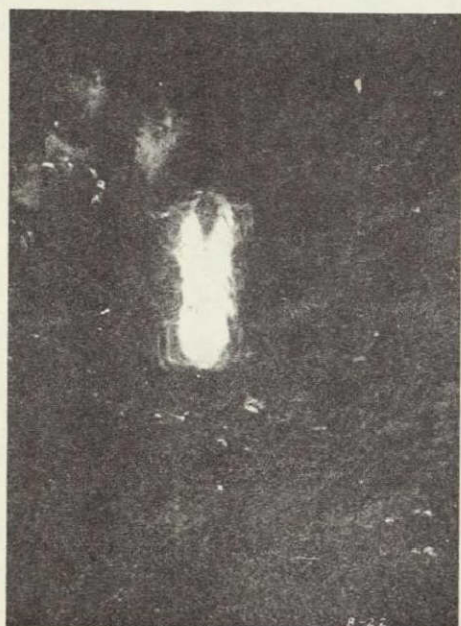
Figure 51-4a.- Ben Franklin on the surface.



BAND 4 - (2E + 38)
BLUE-GREEN



BAND 3 - (25)
RED



BAND 1 - (47B)
BLUE



BAND 2 - (58)
GREEN

Figure 51-4b.- Ben Franklin at 10 meters.

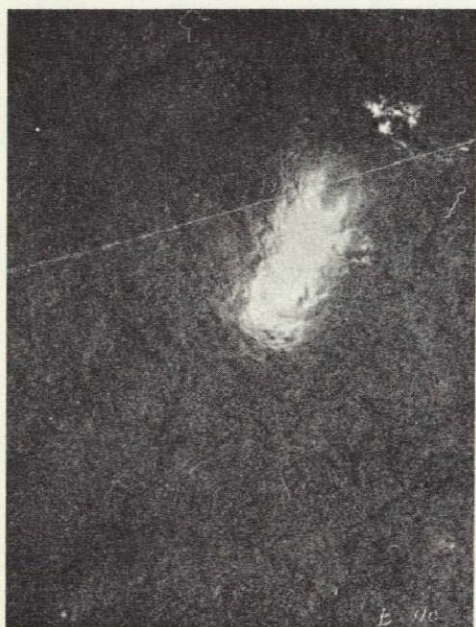
51-22



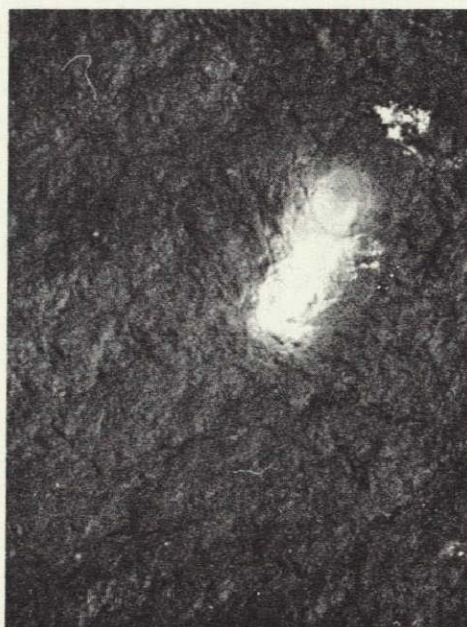
BAND 4 - (2E + 38)
BLUE-GREEN



BAND 3 - (25)
RED



BAND 1 - (47B)
BLUE



BAND 2 - (58)
GREEN

Figure 51-4c.- Ben Franklin at 15 meters.



BAND 4 - (2E + 38)
BLUE-GREEN



BAND 3 - (25)
RED



BAND 1 - (47B)
BLUE



BAND 2 - (58)
GREEN

Figure 51-4d.- Ben Franklin at 25 meters.

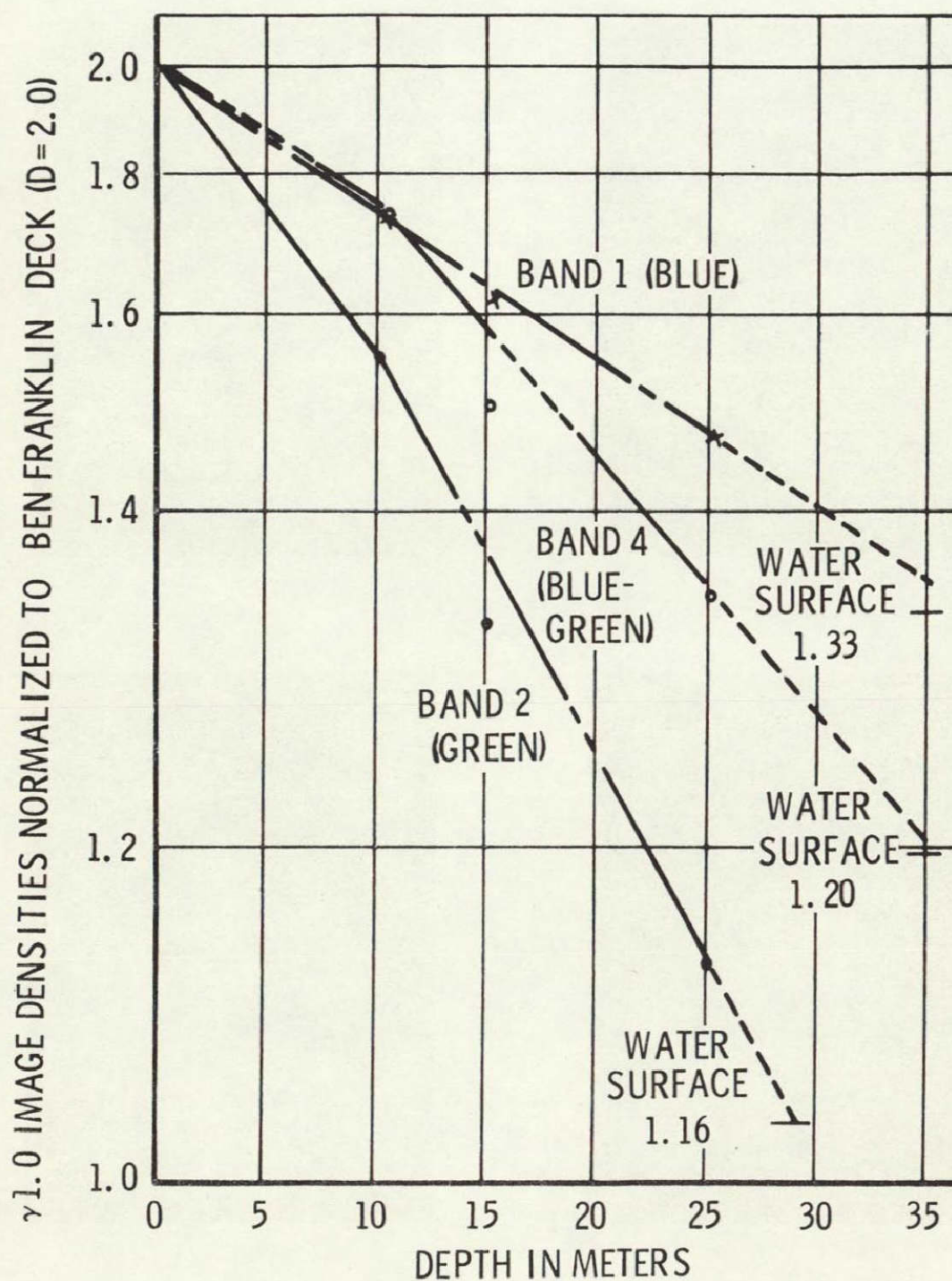


Figure 51-5.- Log decrease of Ben Franklin image density with depth by spectral band.



Figure 51-6a.- Bimini Island area - blue filter.

51-26



Figure 51-6b.- Bimini Island area - green filter.

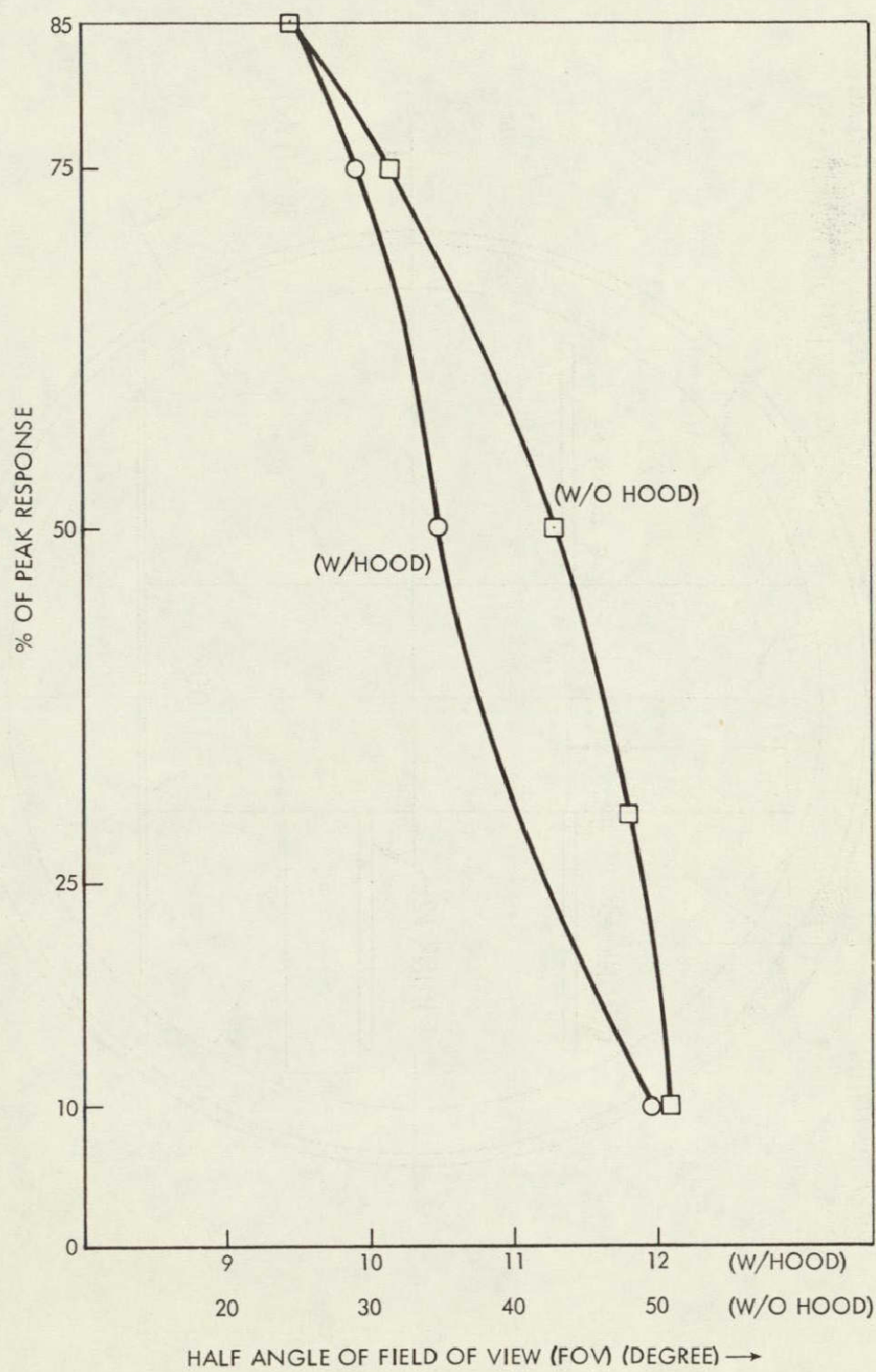


Figure 51-7.- Instrument response curve.

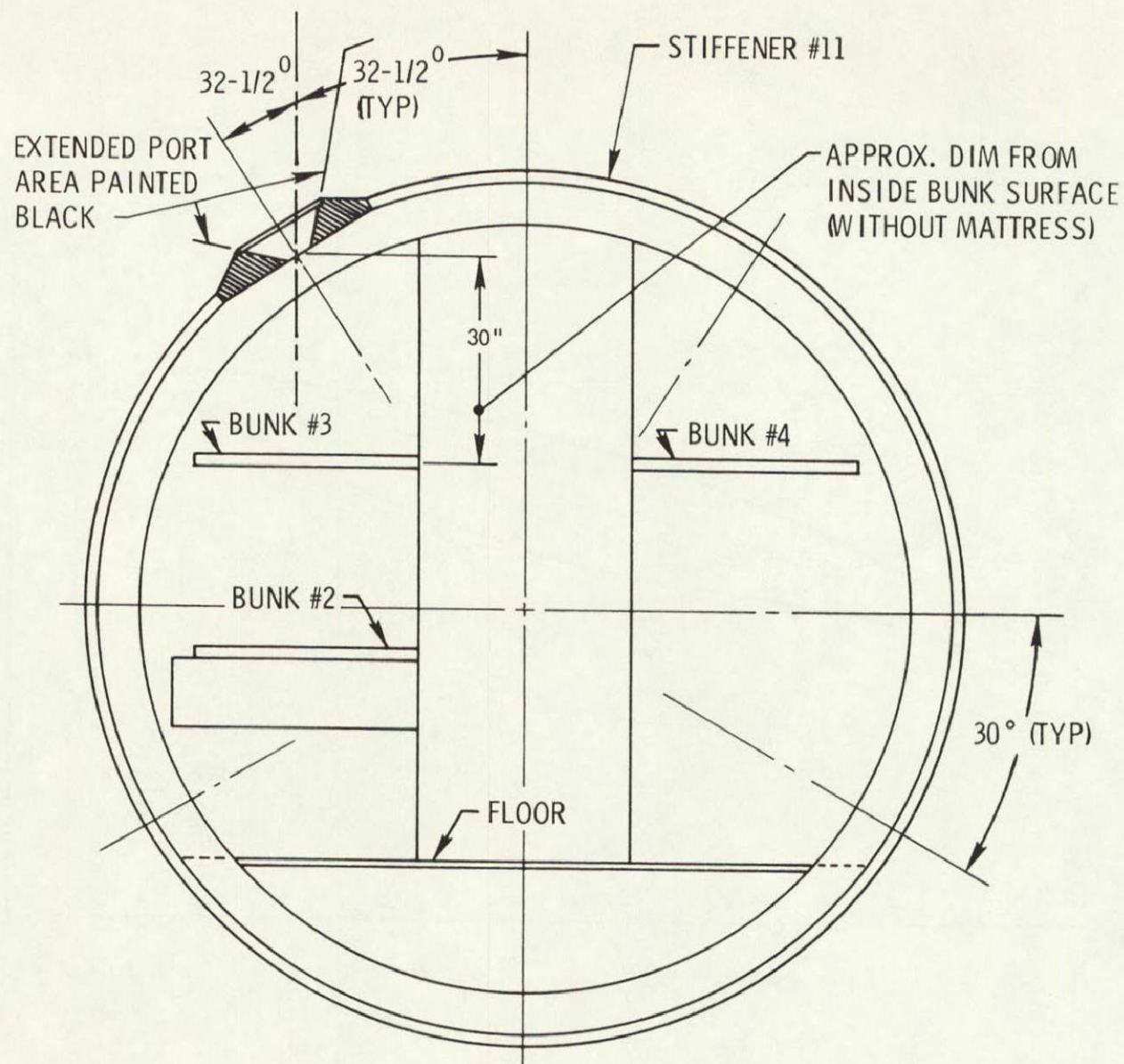
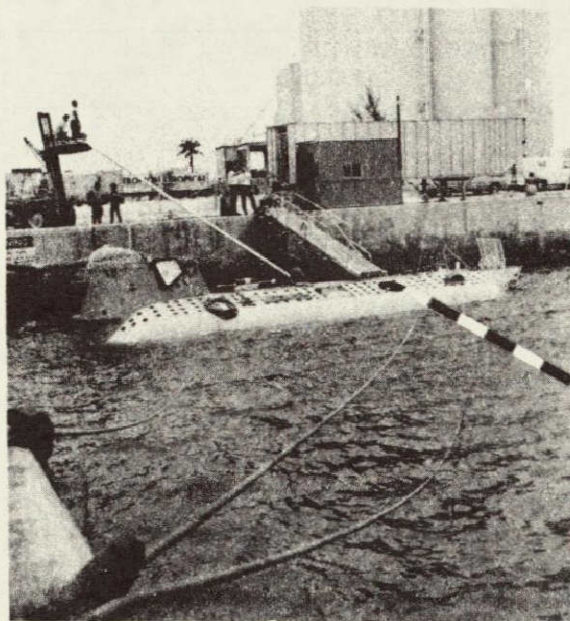


Figure 51-8.- Cross-sectional view looking forward.



Instrument Port

a.



b.

Figure 51-9.- (a) Ben Franklin on surface showing Black Port;
(b) S/R instrument mounted in Ben Franklin.

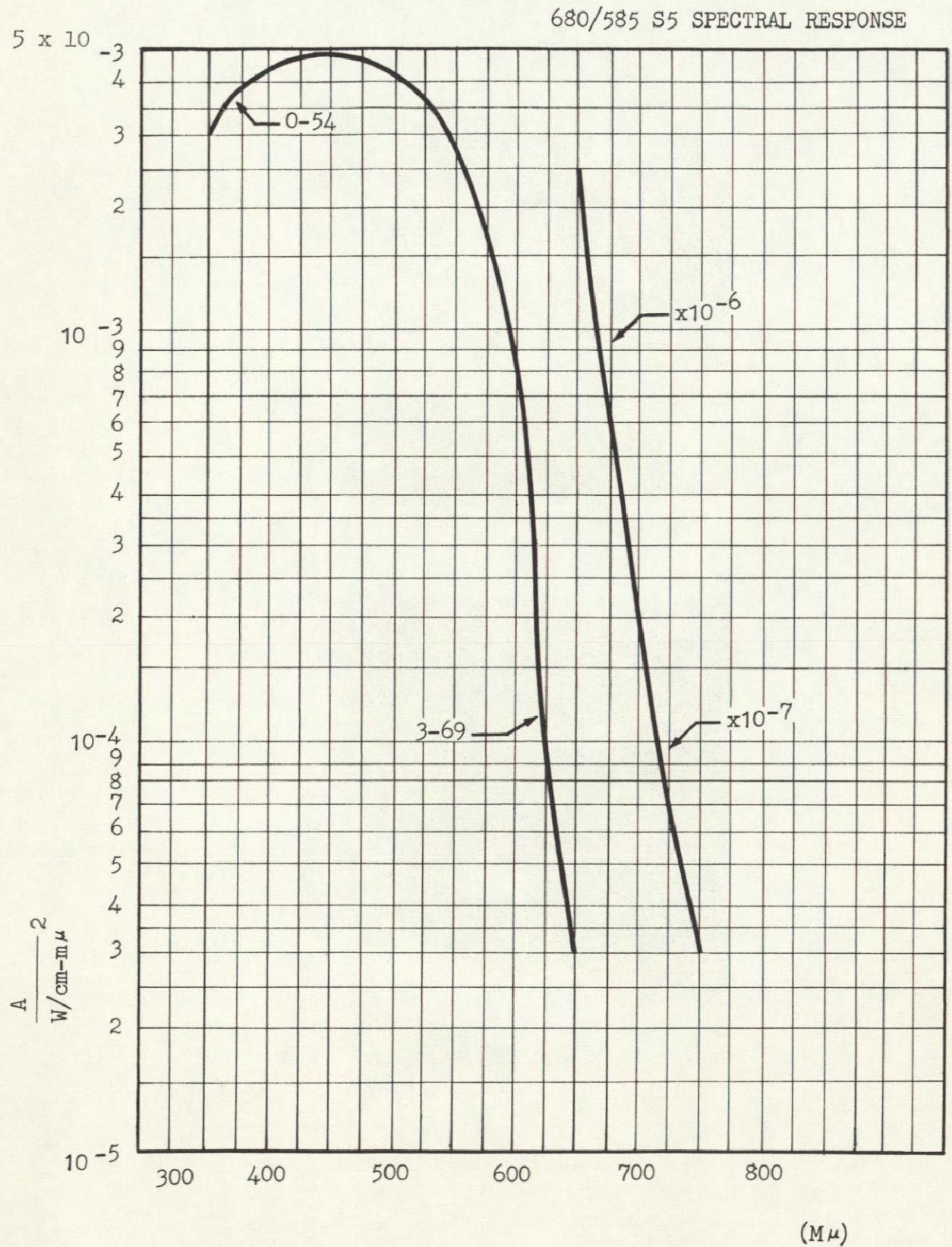


Figure 51-10.- Spectral Response

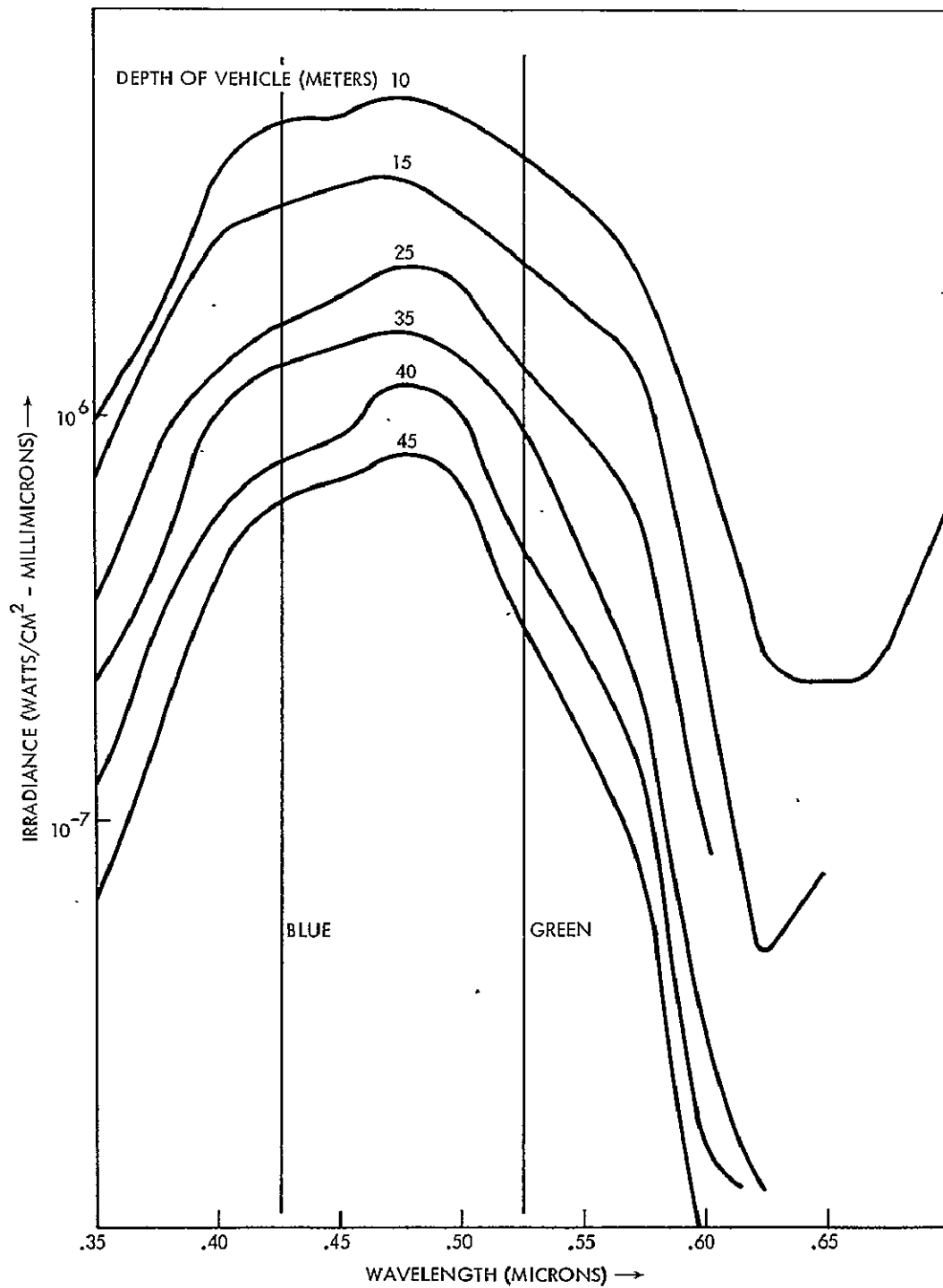


Figure 51-11.- Composite of fully correct irradiance measurements as a function of vehicle depth.

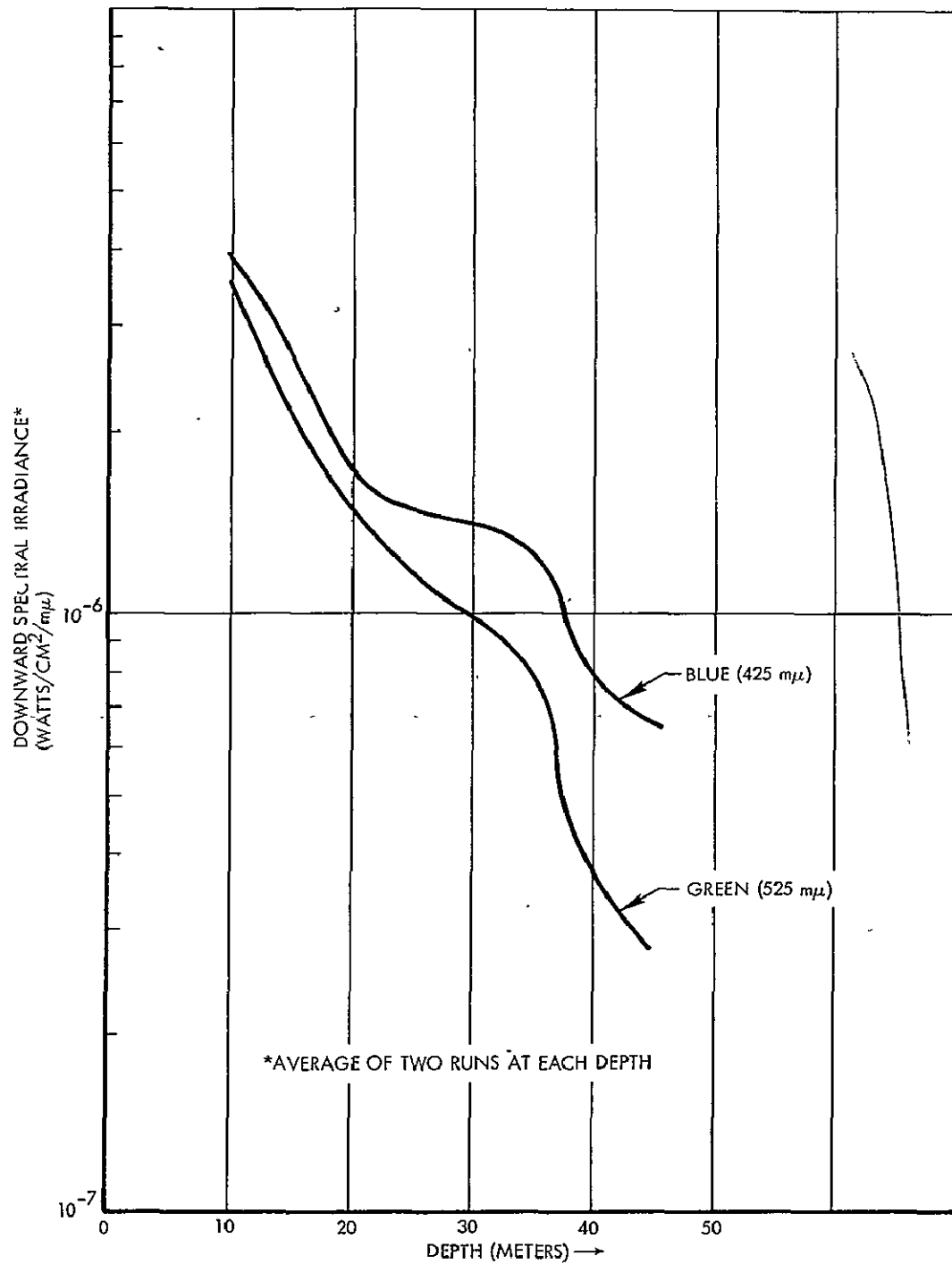


Figure 51-12.- Downward spectral irradiance in two bands as a function of water depth.

SECTION 52

DEPTH DETERMINATION BY MEASURING WAVE SURFACE EFFECTS

By F. C. Polcyn
The University of Michigan

ABSTRACT

N71-11169

Wave refraction due to shoaling is under investigation as one method which may be used to determine depth of water by remote sensing techniques. The forward velocity of individual waves decreases appreciably when the wave passes over an area in which the water depth is less than one-half the water wavelength. By photographing the wave surface and measuring the wavelength changes, an estimate of water depth is feasible. By using optical processing techniques to form the Fourier transform of the wave pattern, a method may be found to systematically search a number of aerial or space photographs to locate unknown shallow waters. So far, a number of space photographs and aerial photographs provided by NASA have been analyzed and measures of depth have been obtained whenever the wavelengths were sufficiently long to be affected by the shallow depths. Transforms have been obtained without scanning to prove first the feasibility of measuring wavelength change.

1. INTRODUCTION

The need for updating navigation charts to remove doubtful hydrographic data (ref. 1) was expressed as a major concern at the Fourth Session of the International Oceanographic Committee meeting in 1965. The use of satellites with remote sensors is being considered as a technique which may aid in the location of shallow waters or other obstructions to navigation over large areas in a relatively short time. This report covers work performed during the period September 1968 to September 1969. The work is sponsored by the Spacecraft Oceanography Project, NAVOCEANO, Washington, D. C., and is being carried out by the Willow Run Laboratories in Ann Arbor, Michigan.

Many doubtful depth soundings have been due to errors brought about in the use of the lead line in collecting the data or in the use of the echo sounder by operators of small fishing boats. The lead line usually measures too great a depth, because of the curving of the line. The echo sounder usually measures too shallow a depth, because soundings may result from intermediate scattering layers and because small-boat operators do not use their sounders continuously, with the result that the proper range scale may be in doubt. Often the error is in location and is due to inexact knowledge of the ship's position. If satellite technology is to be of any help, there must be consistent observables which the sensors can detect for location information; once a detection is made, the accuracy of the geographical position will depend on knowledge of the satellite's position, altitude, and orientation in orbit.

Observables upon which a remote sensor might operate include color and thermal change, wave refraction, and laser signal return (time difference). As in all detection problems, the final classification of a particular depth will depend on a "convergence of evidence" from several sensors, because each one by itself may not be wholly reliable, and false detections may occur from time to time. The reliability of color anomaly as an indicator of depth is influenced by the spectral quality of the sunlight, by suspended material, by bottom material type, and by the algal species present; it can be expected, though, that shallow areas will be greener and will, under certain conditions, produce water-wave refraction. If laser systems prove feasible, direct measurement of water depth can be accomplished by laser ranging. Thermal anomaly holds the least promise because it is not specifically related to water depth; it is well known that thermal differences can be observed at the surface, but it is difficult to reliably interpret the differences as being related to shallow water rather than to some other factor. (In special cases, however, thermal anomaly is related to shoal formation caused by volcanic activity.) There are several types of sensors that may be employed from spacecraft or aircraft to remotely detect the effects associated with shallow water. Consideration of cost, size, ease of processing, all-weather capability, etc., must be included in the final selection of sensors for operational use.

Some of the methods mentioned above have been used in the past for water depth determination. The emphasis in the research program underway is on applying recently developed data collection and processing techniques for making the problem of shoal detection and measurement more automatic

or more accurate (ref. 2). In the remainder of this paper, only one of the methods of depth determination is discussed, that is, the measurement of wave characteristics using photography and the subsequent use of optical data processing to obtain the Fourier transform of the wave surface.

2. WAVE ANALYSIS TECHNIQUES

Optical data processing techniques can be adapted to measure water depth by analyzing the characteristics of water waves as recorded by aerial or space photography. It is known that shoal areas and beaches influence both the wavelength and direction of waves passing over them. The forward velocity of a wave train decreases appreciably when the waves pass over an area in which the water depth is less than about half the wavelength. In addition to noting the change in typical wavelength directly on the original photograph, the change could be observed in other ways. An indirect effect is to increase the wave height and thus produce breakers when the bottom is sufficiently shallow; these breakers are another indication of shallow water. Another effect is to cause refraction of the wave, resulting in a change in azimuth of the wavefront and a corresponding change in the direction of wave advance.

The change in wavelength or wavefront orientation can be observed by subjecting the original images to certain optical data processing methods (ref. 3). If a portion of the original image is illuminated by coherent light, such as that produced by a laser, and the transmitted light is focused by the use of a spherical lens, the resulting presentation on a screen at the focal point of the lens shows in a polar coordinate frame the distribution of both wavelength and orientation contained in the illuminated portion of the original image. It should therefore be possible to analyze aerial photography of sea surfaces both to initially detect shoal areas and to measure water depth in these areas.

2.1 METHODS OF DEPTH MEASUREMENT USING WAVE ANALYSIS

Several computation procedures can be used in estimating water depth from measurements of aerial photography. The analytical basis for these various procedures is discussed in this section, and experimental studies of individual procedures are presented in a following section.

First order theory of wave swells describe, a train of waves advancing through deep water as having a velocity related to its wavelength and wave period by the following equations:

$$L_o = 5.12 T^2 \quad (1)$$

$$C_o = \frac{L_o}{T} = 5.12 T \quad (2)$$

where

L_o = wavelength, ft.

C_o = wave velocity, fps, and

T = wave period, seconds.

As waves approach shallow water of depth, d , the velocity of wave advance, C , and the wavelength, L , decrease appreciably for values of d/L_o less than about 0.5.

This change in wave velocity is related to the fact that in shallow water the motion of individual particles of water is modified. In deep water, the orbit of each particle of water is circular in shape, with the radius of the circle decreasing rapidly with depth. In shallow water, the presence of the bottom modifies the orbit to elliptical form and also has an effect on the forward velocity.

Since the wave period of a given wave train remains constant at all points along its path, the effect of a changing forward velocity is to change the wavelength. It is therefore possible to measure depth from aerial photography by measuring certain characteristics of waves both in the shoal areas and in areas where the water is known to be deep compared to the wavelength of the incoming waves. In a single aerial photograph, the wavelength in deep water and the wavelength in shallow water can be measured. The measured ratio of wavelengths, L/L_0 , is functionally related to the ratio d/L_0 , so that the depth, d , can be determined (ref. 4). The optical data processing methods discussed in the following sections provide an effective means of measuring L and L_0 .

An indirect effect of changes in velocity of wave advance is to change the wave orientation through refractive effects. The change in direction from deep to shallow water can be accurately measured by optical data processing methods. This approach is applicable, for example, in the case of straight beaches with parallel contours. For this case, the direction of the incoming wave and the direction of the wave at the point of depth measurement are observed. These two measurements determine the ratio of depth, d , to deep water wavelength, L_0 . If L_0 is also measured, the depth can be determined. However, the use of changes in wave direction for depth determination is not generally applicable without considerable complication. Where the bottom contour cannot be assumed as straight, the method must be modified by preparing a refraction diagram of the area of interest extending into the

ocean to points where the depth is equal to at least half the observed wave length. As a means of detecting shoal areas, as distinguished from measuring them, the use of wave direction changes can be effective provided the orientation of incoming waves is sufficiently regular to avoid masking the effect of the shoals.

Other approaches to depth measurement can be used if successive pictures at short intervals can be provided. Under these conditions, it becomes possible to measure not only wavelength and wave direction, but also wave velocity and wave period. If two pictures are taken at a known interval of the wave velocity in deep water, C_0 , and in the test area, C , can be determined. (To make accurate measurement of wave advance over a short time interval, a fixed reference point must be apparent in each photograph.) By noting the change in wave position, the wave velocity can be computed as the ratio of distance traveled by the wave and time interval between observations. The ratio C/C_0 derived from these pictures is equal to the ratio L/L_0 and can thus be used to determine d/L_0 . Wavelength can be measured directly from the photograph.

Another alternative would be to measure L and C in the shoal area only. Wave period, T , can be computed as the ratio of wavelength to wave velocity, L/C . The wave period remains constant as the wave travels from deep to shallow water; hence, the measurement of T provides a means of computing L_0 or C_0 by the use of Equation 1 or 2. This measurement method thus requires measurements only in the test area and eliminates the need for measurements in deep water. Its accuracy depends on the regularity of the water wave patterns present at the time of measurement and on the resolution of the photography.

2.2 APPLICATION OF FOURIER TRANSFORM PROCESSING

Optical data processing has been tried on a number of aerial photographs covering both open sea and shoal areas, such as beaches and reefs. It is found that there is a generally valid relationship between the wave characteristics as measured from the aerial photograph and the wavelength and orientation characteristics recorded by the optical processor. If a swell or local wave pattern with a clearly defined orientation and predominant wavelength content is apparent on the aerial photograph, the Fourier transform pattern produced by the optical processor will tend to show this dominant wave pattern as a curcular dot of finite size at the appropriate wavelength and angle. Distance of the dot from the center of the pattern is inversely proportional to wavelength. The finite size of the dot indicates a scatter in both wavelength and direction in the original imagery, which is to be expected in water wave patterns, even under favorable conditions. The irregularity of the fundamental pattern and the existence of local chop will tend to introduce both lower and higher frequency components into the Fourier transform. In many cases, therefore, the idealized dot pattern expected for a single sinusoidal wave component becomes elongated to include a considerable variation of wavelength components. The angular spread is less affected, so that in many examples wave direction may be determined more accurately than the wavelength itself.

The interrelation of sun elevation, view angle, and wave spectrum appears to have some effect on the transform representation of a particular area. The wave pattern is most visible at the edges of the sun glitter pattern, and may be nearly invisible at the center of the pattern or far outise the pattern. Sun glitter seems to emphasize those waves whose crests are tangent

to the sun glitter circle. If further study confirms this effect, it may be used to advantage in eliminating the confusion resulting from the existence of several wave patterns.

The conclusions reached so far are that the two-dimensional Fourier transform gives a useful indication of dominant wavelength and direction. To obtain accurate measurements, the pattern of water waves must be fairly regular and not a confused combination of several different wave trains, and the proper exposure and sun glitter pattern must be used. It is believed that further investigation will improve the definition of the best conditions of use and develop refinements in technique which would further increase the accuracy with which wavelength and wave direction can be determined.

2.3 EXAMPLES OF OPTICAL DATA PROCESSING TECHNIQUES FOR MEASURING DEPTH

As a quantitative example of the use of several wave analysis techniques for measuring water depth, an aerial photograph taken near the exit of the Grand River into Lake Michigan near Grand Haven was used. (See figures 1 and 2.) The objective of the task was to determine the depth of water in two areas, A and B. Area A is a rectangular area parallel to the shore line, with its near edge about 270 ft. offshore and with dimensions of 500 x 1300 ft. Area B is a rectangular area of the same dimensions and orientation but with its near edge about 1600 ft. offshore. To determine deep-water wavelength, L_o , wave measurements were also made over Area C. The depth of water in Area C is approximately 40-45 ft. and does not have an appreciable effect on the length or direction of the waves passing over it at the time the photograph was taken.

Two methods of calculation were used, one based on the difference in wavelength in Area A and Area C, and the other based on the change in direction of the waves in these two areas. Measurements of wavelength and wave direction were each made in more than one way to compare various techniques available.

We will consider first the determination of water depth by wavelength measurement. Measurements of wavelength were scaled directly from the aerial photograph and were also obtained from a Fourier transform made by optical processing (figure 3). The results of these measurements are shown in Table 1.

TABLE 1
WAVELENGTHS DETERMINED BY TWO METHODS

<u>Method</u>	<u>Area A</u>	<u>Area B</u>	<u>Area C</u>
Direct measurement of aerial photograph	53	82	92
Fourier Transform	56.5	70	80

Using the data taken from the Fourier transform measurements, the depth of Area A was found to be 7.9 ft. Inspection of Lake Survey Chart Number 765 of the Michigan coastline at Grand Haven indicates that the depth of Area A ranges from 6 to 10 feet. Fourier transform measurements were also used to compute the depth of Area B. The computed depth was 15 ft., compared to depths determined from the chart ranging from 14 to 18 ft.

Water depth in Area A was also computed by comparing the angle of the incoming wave in Area A with that of Area C, where the wave orientation was presumably still outside the influence of the shore. Angle measurements were made by reference to both the original photograph and the Fourier transform.

Both methods gave values of 60° for Area C and 35° for Area A, measured with respect to the shoreline. Using these values, the value of d/L_0 for Area A can be obtained by using data published such as in reference 4. The value obtained for d/L_0 was found to be 0.086, and using the wavelength of 80 ft. from Table 1, the water depth in Area A is computed as 6.9 ft., checking close with the value determined by wavelength measurements. For Area B, the angle of approach was 45° giving an estimated depth of 12.0 ft. This is appreciably less than the chart value of 14-18 ft.

2.4 EFFECT OF ALTITUDE AND CLOUD COVER

The data from Mission 72, Lake Michigan, together with data from Mission 79, Gulf of Mexico, and samples of satellite photography provided an initial data base to study the effect of increasing altitude and cloud cover on the generation of interpretable optical transforms and on the measurement of wavelength. One of the advantages in using the optical transform is that at smaller photographic scales, the dot separation from the center in the transform increases and less confusion results with the bright central portion of the transform pattern. Figure 4, taken from an area near Cayo Arenas in the Gulf of Mexico, illustrates this effect. The area is in open deep water away from the diffraction effects caused by the island or refraction effects due to submerged shoals. The photography was taken at an altitude of 22,000 ft with a 6 inch focal length lens. Note the clean separation of the dot pattern for the fundamental wave component of the sea surface. Figure 5 shows the transforms taken nearer the island at three different locations. The azimuthal changes in wave direction due to the diffraction of waves around the island are shown clearly in the transform domain when compared with figure 4.

The water wavelengths measured were in the 100 ft. range but no depth measurements were made in the area since depths of 50 ft. or less were not present. Where the wave pattern in the sun glitter was measurable. This requirement of the proper ratio of wavelength and depth less than $1/2$ the wavelength implies that a determination of depth in a given area will depend on the existence of a particular set of conditions at the time the data is taken. Since this may not always be the case a technique is needed to analyze many photographs rapidly where data is taken more routinely for a variety of purposes. It is expected that scanning the transform plane for the dot separation will be a quicker and simpler method than scanning the original photograph.

Additional tests were also made of the effects of cloud patterns in portions of the photograph. Figure 6 shows the case where two transforms are compared, these are taken from sections of a photograph with and without cloud obscuration. The fundamental wavelength component was observed in both cases. The large cloud pattern transforms generally into the lower spatial frequencies located near the center. The presence of scattered clouds does effect the overall exposure during the construction of the optical transform so that an increase in exposure time may be necessary in some cases.

2.5 SPACE PHOTOGRAPHY

Frame AS7-4-1607 taken during the Apollo 7 flight distinctly shows a widespread long wavelength swell moving in the direction of the Schouten Islands near New Guinea. The swell has an extremely regular pattern consisting of wavecrests many miles in length, essentially straight, and with little or no apparent variation in wavelength. This type of wave pattern

would have been caused by a recent storm at a considerable distance; the dispersive characteristic of water waves has separated the wavelength components in the storm area, so that only a single wavelength is present in the picture.

Optical data processing was applied to one section of this picture in which the wave pattern was most distinct (figure 7). The resulting transform shows a very definite wave component ranging from 1040 to 1220 feet and orientation angle from 40 to 50°. Corresponding to the figures derived from the transform, measurements were made from the original image indicating a typical wavelength of 1100-1200 ft. and orientation of 45°.

The swell can be seen reaching the large island shown in the picture, but the sun glitter pattern in the vicinity of the island provides only a low contrast in the wave image, making it difficult to obtain a transform pattern in this region. Measurements taken from the original image indicate that the wavelength becomes shorter in the vicinity of the island but the wave direction does not appear to change appreciably. The long wavelengths composing the swell would be sensitive to relatively great bottom depths and are thus most likely to provide useful information concerning shallow water. It would be highly desirable to obtain imagery of long swells approaching land at shorter intervals between frames so that every part of the water surface of interest is in the favorable part of the sun glitter pattern on at least one exposure.

Measurements were made from Fourier transforms taken of Apollo frame AS7-4-1607 in order to determine the precision with which wavelength and angle measurements can be determined by optical data processing techniques.

using manual data reduction by scale and protractor. This frame is distinguished by the fact that the wave system is very regular as to both wavelength and wave orientation. The results of the measurements indicate that wavelength measurements can be obtained with a precision of 2 or 3% and angle measurements with a precision of 2 or 3°. Assuming that this precision could be obtained in measuring both L and L_o , it is possible to estimate the accuracy of computing depth for a known value of d/L_o . If d/L_o is equal to 0.100, the depth could be estimated within about $\pm 10\%$. (In the Lake Michigan example previously presented, Area A had a d/L_o of about 0.100.)

3. CONCLUSIONS

Under favorable observation conditions, wave analysis techniques making use of optical data processing can measure depths with good accuracy. For values of d/L_0 equal to 0.100, depth measurement with an accuracy of 10% may eventually be achieved. Observation of long wavelength swells, in the absence of local chop, and the use of optimum conditions of resolution and contrast in the imagery used for processing would all contribute to accurate determination of water depth. The requirement to analyze a large volume of data is seen due to the need to inspect many frames of imagery for changes of wavelength in wave swells of sufficient length relative to local depth condition.

Scanning the optical transform domain appears to offer a simpler method of measuring the water wavelength automatically. In some cases, wave surface (sea state) information can be obtained from the same set of data in addition to water depth.

4. REFERENCES

1. Doubtful Hydrographic Data, Part A, North Atlantic Ocean, International Hydrographic Bureau Special Publication, No. 20, 3rd ed., Monaco, 1967.
2. F. C. Polcyn and R. A. Rollin, Remote Sensing Techniques for the Location and Measurement of Shallow-Water Features, WRL Report No. 8973-10-P January 1969.
3. P. L. Jackson, "Diffractive Processing of Geophysical Data", Applied Optics, Vol. 4, No. 4, April 1965, pp. 419-427.
4. Graphical Construction of Wave Refraction Diagrams, U.S. Naval Oceanographic Office, H. O. Pub. No. 605, 1964



Figure 52-1.- Lake Michigan shoreline at Grand Haven.

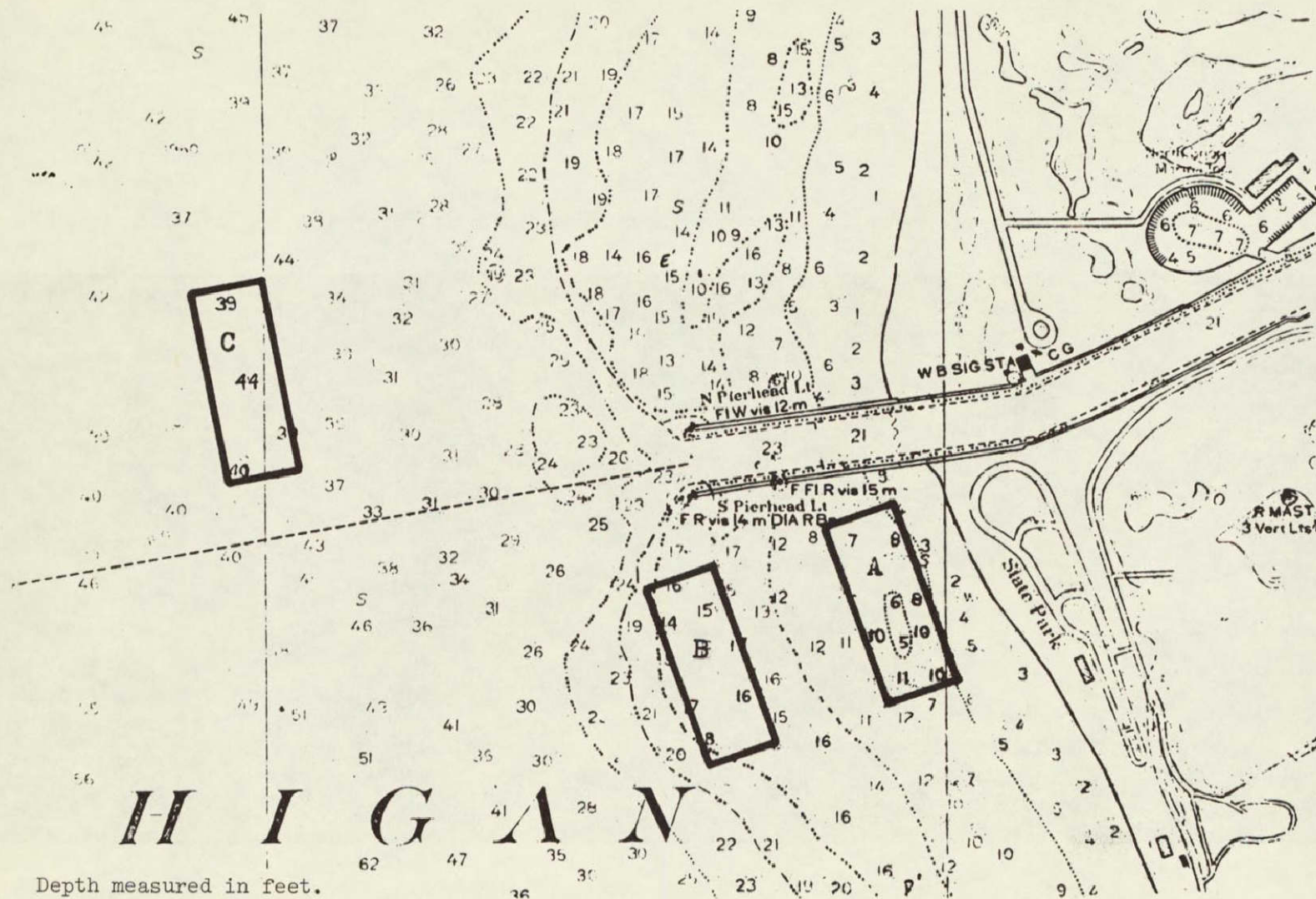


Figure 52-2.- Lake survey chart - Grand Haven, Michigan.

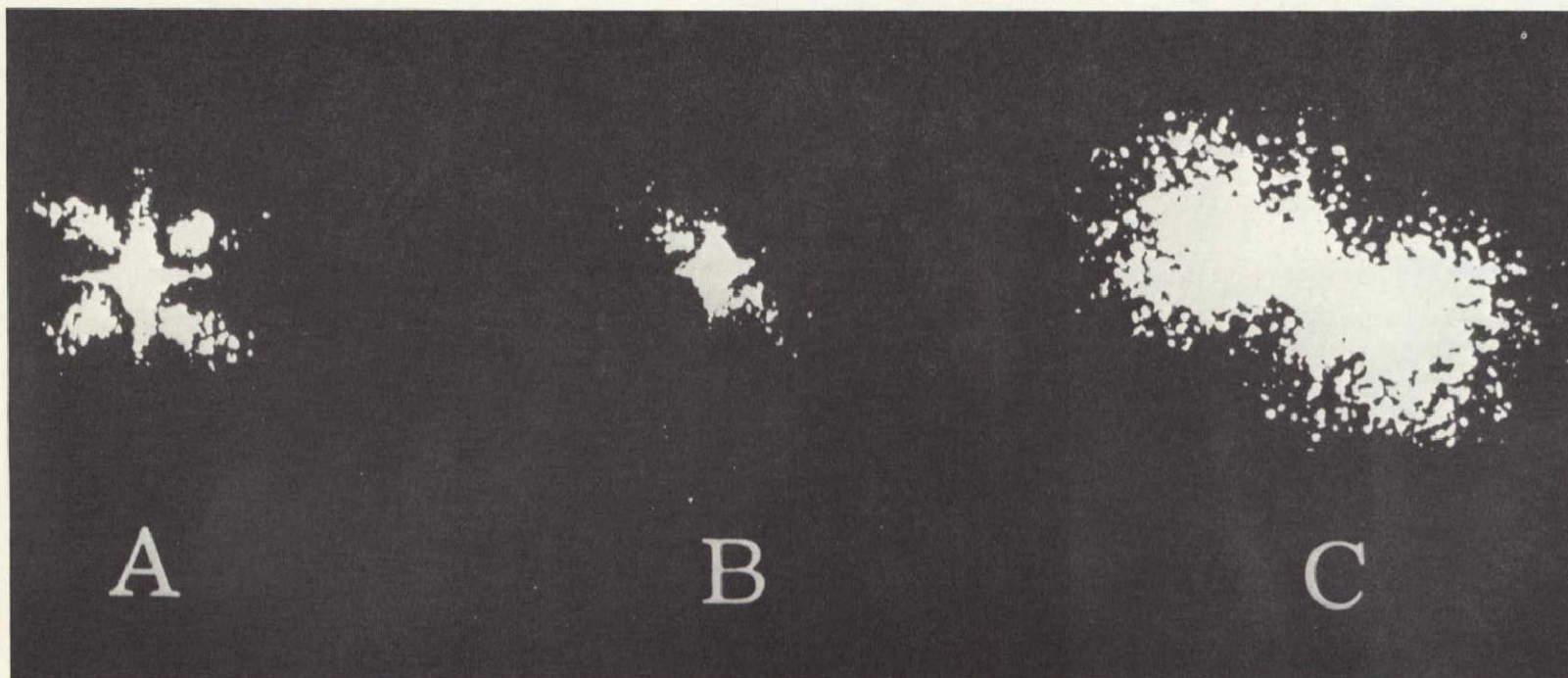
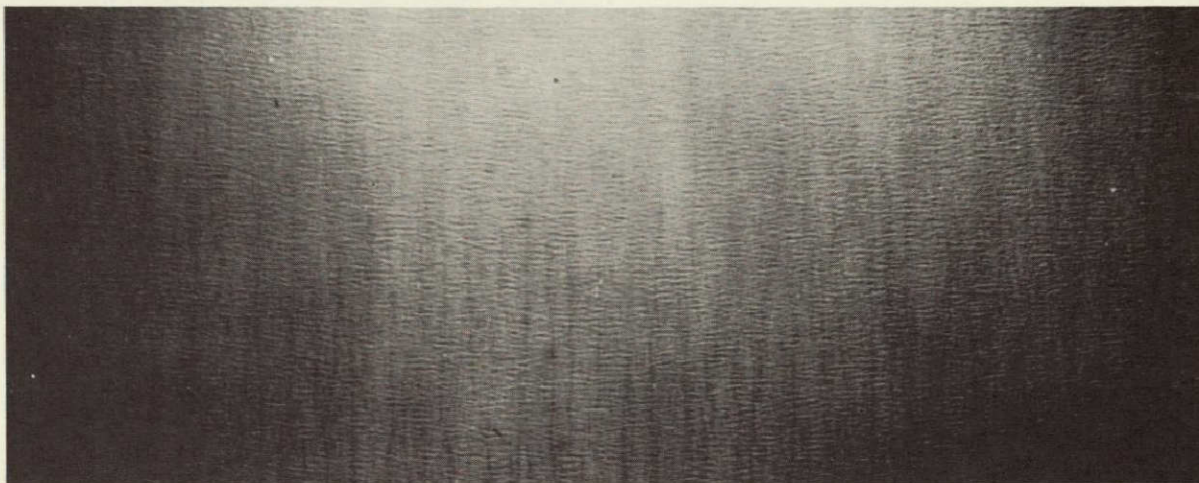


Figure 52-3.- Optical data processing of Grand Haven shoreline. Fourier transform of wave surface for areas A, B, and C.

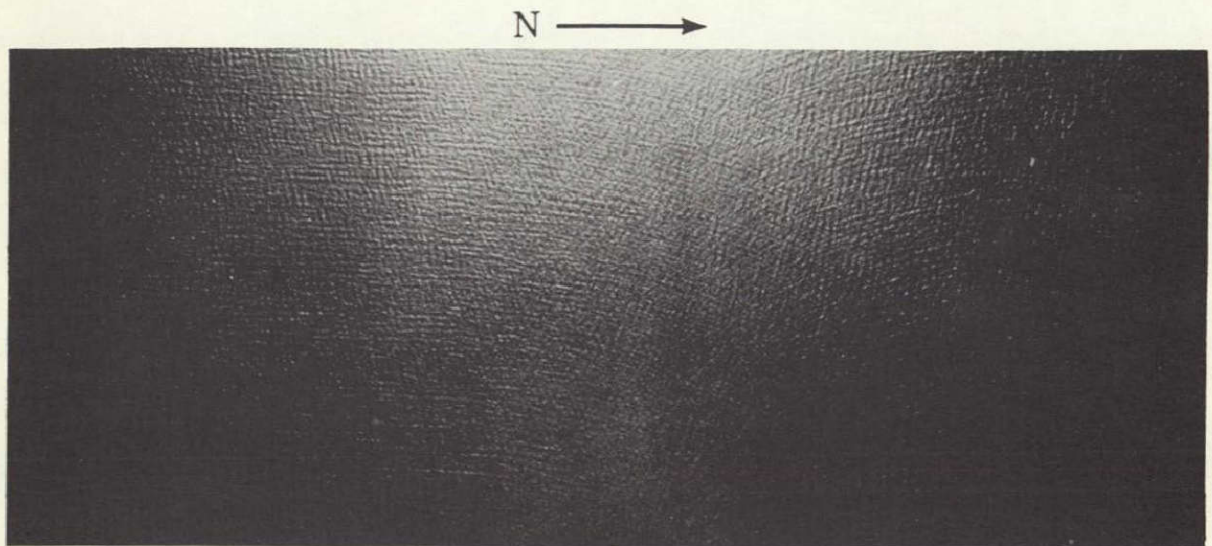


(a) Aerial photograph.

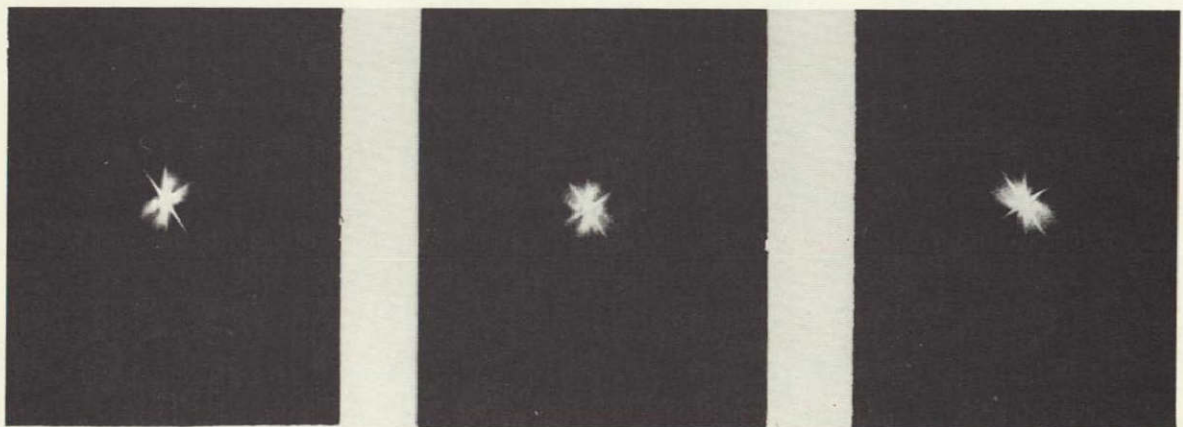


(b) Fourier transforms.

Figure 52-4.- Waves in open water.



(a) Aerial photograph (west of Cayo Arenas).

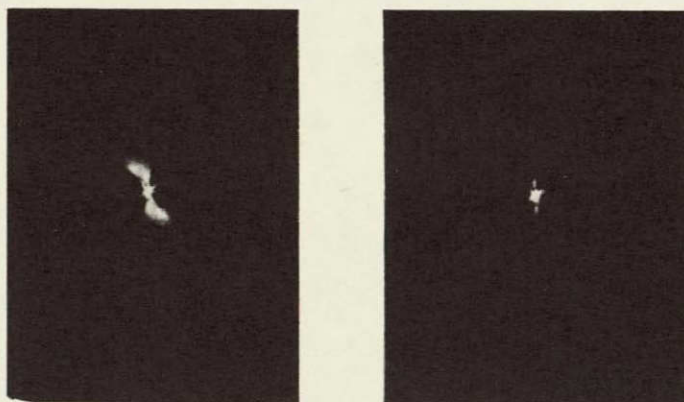


(b) Fourier transform.

Figure 52-5.- Diffraction of water waves. Transform of each corresponding area shows azimuthal change in wave direction.



(a) Aerial photograph.



(b) Fourier transform.

Figure 52-6.- Clouds and cloud shadows. Transforms of areas with partial cloud cover and without clouds show dominant wavelength of wave surface.

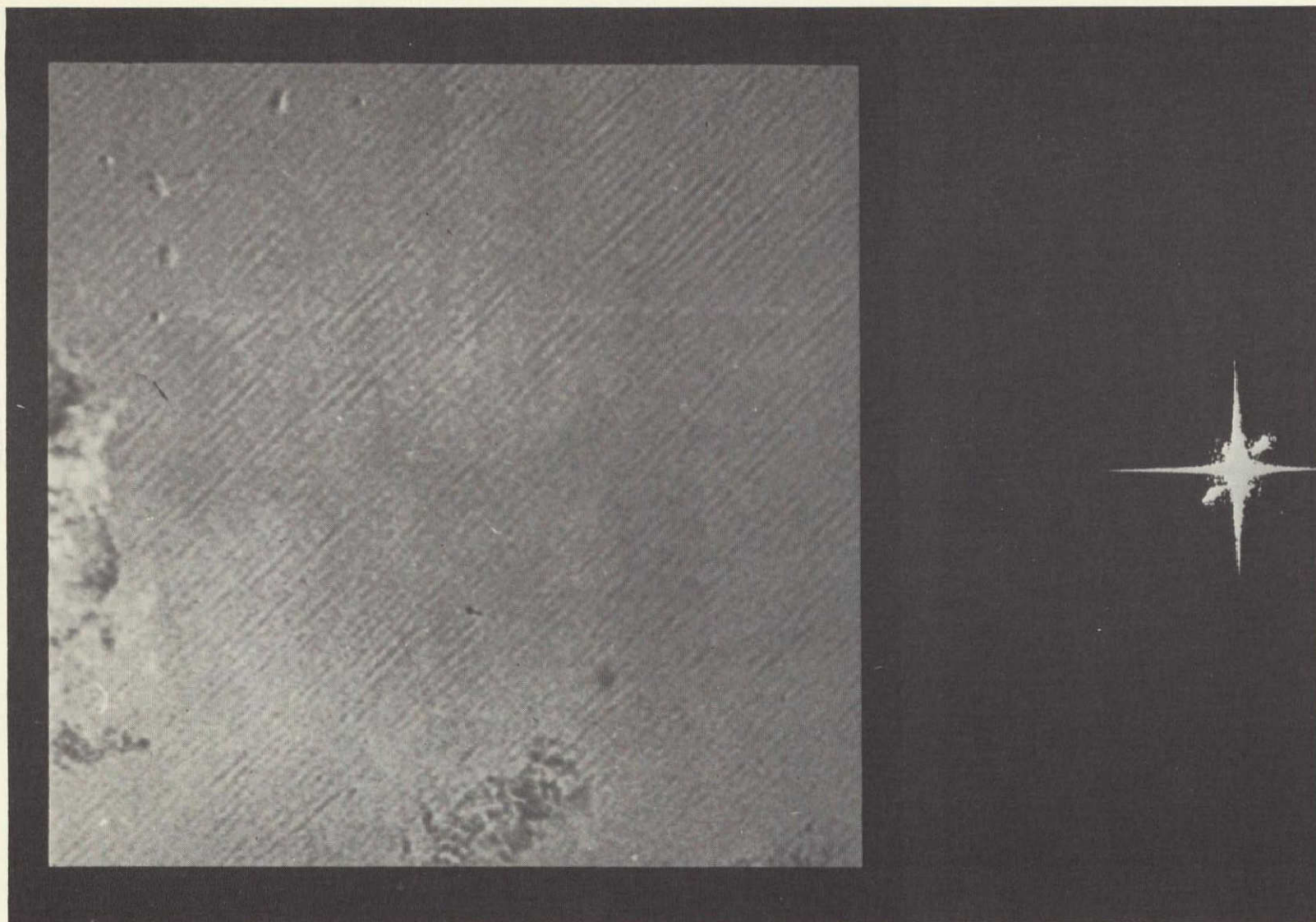


Figure 52-7.- Optical data processing of Apollo 7 frame AS 7-4-1607 (transforms at right incorrectly 90°).

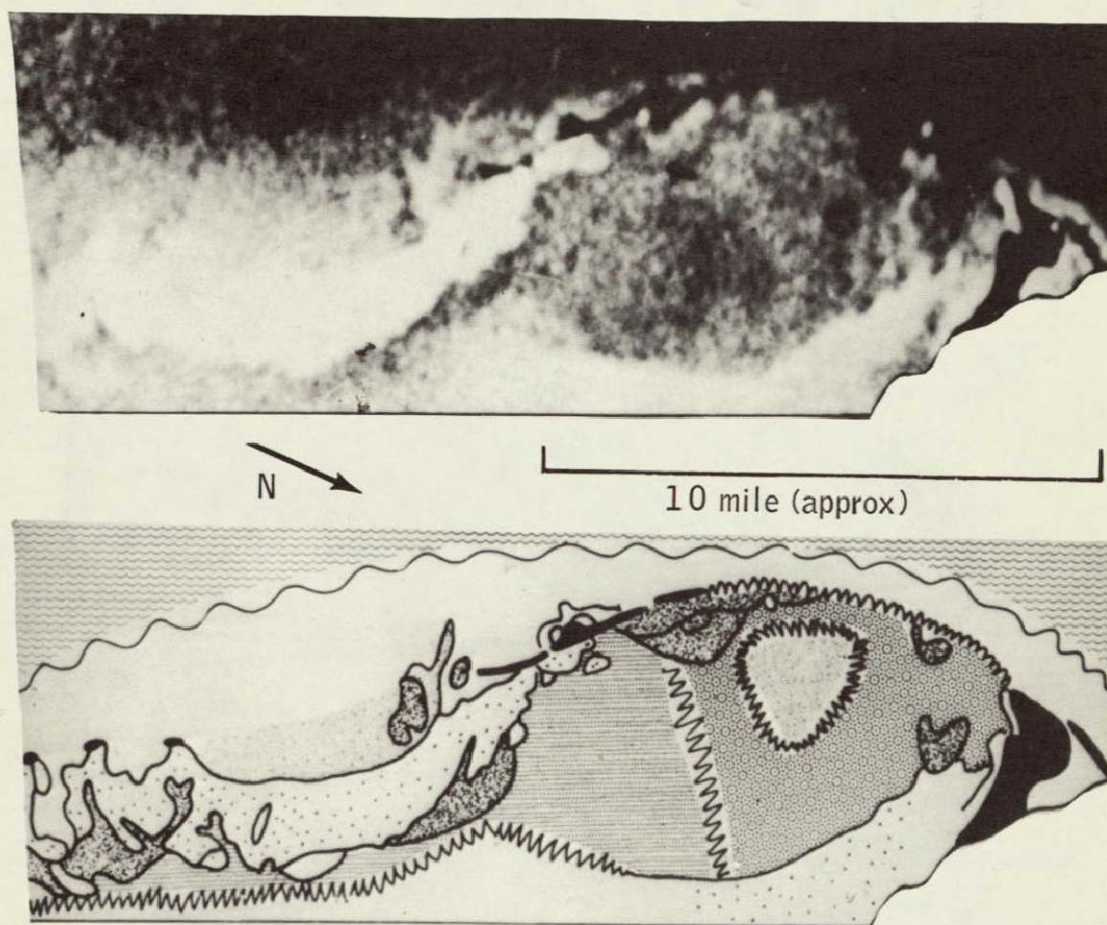


Figure 53-13.- Bottom cover map prepared from Gemini photograph of the west edge of the Bahama Banks "Figure 53-1". Different types of cover are shown as well as the islands of Bimini, Gun, N. Cat, and S. Cat Cays. Full explanation and description is given in Conrod, Kelly and Boersma (1968) and Kelly and Conrod (1969).

SECTION 53

THE STUDY OF COASTAL ECOLOGY USING REMOTE PHOTOGRAPHY

Mahlon G. Kelly,
Department of Biology,
New York University,
Bronx, N. Y., 10453.

N71-11170

INTRODUCTION

It has become well accepted, both in the popular press and by resource workers, that coastal areas are at present the regions of the oceans most important to man and that many coastal waters are threatened by pollution and misuse. Nonetheless, the ecology and distribution of coastal resources and conditions are poorly understood. The marine ecologist has in the past been handicapped by difficulties in surveying and understanding the distribution of coastal biota. Whereas the terrestrial ecologist, forester, or agriculturalist may have a good idea of the location of major biotic cover and communities, the marine worker has been limited to point sampling and line transects using remote instruments or divers. It is very difficult to gain a synoptic understanding of biotic distributions using such tedious methods, although sampling accuracy may be high. Attempts have been made to use automated equipment, continuous transect photography, etc., but these still do not provide the overall view needed.

Although terrestrial ecologists have made considerable use of remote photography and are looking forward to when satellite photography and multispectral scanning imagery will be readily available, these techniques have been little used in the marine realm. This is particularly surprising considering the surveying difficulties mentioned above. Aerial photography will resolve features as deep as 40 m. (Conrod, Kelly and Boersma, 1968), and that limit includes much of the coastal area of greatest importance to man at the present. Although the depth photographed depends on the clarity of the water and the contrast of the features being imaged, usable results may be obtained in most areas. Where dissolved and suspended materials prevent resolution of bottom cover the distribution of the materials in the water may itself be studied.

Aerial photography of submarine features was first suggested during World War I (Lee, 1922) and was used by the Navy for bathymetric reconnaissance during World War II (Lundahl, 1948). Geologists have made some use of aerial photographs for submarine work; for example Cloud (1962) has studied the Bahama Banks and the island of Saipan and Newell and co-workers have worked extensively on the Bahama Banks (1959). The only biological studies published other

than the present ones have been those of Kumpf and Randall (1961) and of Macintyre (1968). Other work has been done on the use of photography in water quality studies but has not emphasized the ecology of the biota (Strandberg, 1967).

Work has been undertaken with NAVOCEANO-SPOC support and with aircraft support from the Earth Resources Program to determine what may be learned of coastal biotic distributions and ecology using remote photography. Much of the work has involved field studies to enable descriptive interpretation and subsequent analysis of the environmental interrelationships shown by the photointerpretation. This has required development of a backlog of information and photointerpretive ability. It is impossible to describe all of the results here - rather it seems best to give examples of the types of results and information obtained, to discuss possible application of such results, and to draw some conclusions as to further work needed and possible utilization of satellite imagery. The survey work and detailed results have been more thoroughly described in Conrod, Kelly and Boersma (1968), Conrod, Boersma and Kelly (1968), Kelly and Conrod (1969 a,b), and in Kelly (1969 a,b). Reports of some of the work are now in preparation.

Thanks are due to Drs. Leonard Greenfield and Howard Teas of the University of Miami for providing facilities, and to Mr. Les Penzias for valuable assistance in the field work.

METHODS

Three test sites in the area of the Florida Straits have been examined (Fig. 1): The area south of Bimini on the Bahama Banks (NASA site 162), the southern half of Biscayne Bay (NASA site 163) and a large area around the central Florida Keys (NASA site 169). These cover a total of about 300 square miles and include many diverse environments. A study is now being started in the Long Island - New York area to examine the use of similar techniques in temperate, turbid, polluted waters.

Photography was obtained by NASA aircraft on missions 75 (site 162), 81 (site 163), 92 and 93 (sites 163 and 169), and on previous missions flown for Alfred Conrod of MIT. Various film-filter combinations have been tried, but 12,000 ft. coverage (24,000:1 scale) with RC-8 metric cameras using Aerial Ektachrome film has been used for most of the work. 25,000 and 2,000 ft. coverage was used in some cases in the Bahamas work and some 2,000 ft. coverage was used over Biscayne Bay. Aerial Infrared Ektachrome was generally unsatisfactory because of poor penetration of water by infrared radiation.

Wherever possible, photomosaics were assembled and used for photointerpretation and field studies. Paper prints were unavailable for the Keys work, so duplicate transparencies were used.

The areas were examined using standard diving transect surveys with divers towed behind boats. Quantitative samples were taken at selected points for accurate identification of the biota. Entire transects were photographed in the Biscayne Bay work using 16 mm. cameras mounted on Pegasus underwater vehicles. Specific features were investigated in detail for identification at many locations.

RESULTS AND DISCUSSION

It is impossible to detail here all the significant distributions and features seen; it seems more appropriate to cite examples of the most significant so as to show the types of information that may be gained and then to draw tentative conclusions about possible use and applications. The figures should serve to show the major types of cover found in most areas and some of the distributions seen. There are three basic uses for such photography: 1) Anomalous, unusual or previously undetected features may be found. These may be either natural or man-made. 2) Bottom biota may be mapped and it is possible to produce photointerpretive keys that may prove valuable for ecological resource surveys. 3) Most importantly, ecological interactions, again both natural and man-made, may be detected.

Examples of previously undetected features are shown in the photography. Fig. 10 shows groups of sink holes, probably solution formed, in the area of the Florida Keys. These were probably formed when the area was emergent during the Pleistocene and have not previously been reported from South Florida. In many cases they have been filled with sediments and may be detected by rooted vegetation growing in the sediments. Crescentic blow-out areas formed in grass beds during high energy storms are commonly found (Fig. 2) (Conrod, Kelly and Boersma, 1968). Typical ones are seen in nearly any soft bottom area exposed to ocean swell. In some cases they become confluent, leaving ridges of grass (Fig. 3). Patches of grass may be found in various configurations or distributions, related to various environmental factors (Fig. 8). Lineations and striations may be found where types of hard bottom cover vary because of the type of rock substrate (Fig. 10). Spillover lobes caused by currents washing sorted sediments over grass beds are to be seen in several locations (Fig. 4). Similar appearing wash-out lines are sometimes formed where directed currents sweep across grass beds (Fig. 5). Ray-like "shadows" of unattached algae may often be seen in the lee of current-washed grass patches (Fig. 8) or thin layers of sediment may be found with similar configurations (Kelly, 1969 b). Presumably differences are

due to the presence of different suspended materials. This list could be continued, but detailed descriptions have been or will be published elsewhere.

All of the features described above are fairly common and would have been readily recognized, described and understood were they found on land, but the difficulty of obtaining an overall view underwater has prevented their recognition. They are important however if we are to adequately understand conditions in coastal areas.

Man-made features may also be detected. The effects of cooling water discharge from a power-plant were seen dramatically in southern Biscayne Bay (Fig. 6) (Kelly, 1969 b). Dredged channels may be seen as well as effects of siltation caused by the dredge operation (Fig. 7). Effects of fresh-water runoff through drainage canals were also detected. The test sites are in relatively undisturbed areas and many more effects will probably be seen in heavily populated coastal areas.

It is also possible to prepare photointerpretive keys and thus maps of major types of bottom cover (Fig. 10). Again, as with unusual features, such distributions would be easily recognized on land, but cannot be underwater. Such maps have been prepared of the Bahamas and Biscayne Bay test sites (Conrod, Kelly and Boersma, 1968; Kelly, 1969 b) and are being prepared for the Florida Keys area. Such maps are not only basic to an understanding of resource distribution but also enable detection of interrelationships and aid in further research and monitoring of conditions.

Preparation of such maps has pointed out that basic types of biocenoses occur over large submarine areas, as they do on land. Similar distributions and types of benthic cover are found over hundreds of lineal miles on both sides of the Florida Straits and probably over much of the rest of the Caribbean as well. In fact, Gemini photography suggests that certain distributional types may be found world-wide. These similarities have not been previously recognized and deserve much more interest and work.

Although such general types of bottom communities occur, and although interpretive keys allow their identification, field work is necessary before definite identification may be made. There is too little known about variations in cover and appearance to allow the certainty normally applied in terrestrial work. Rigor was maintained during the present work by continued photointerpretation and field checks.

Bottom cover in the area of the test sites may first be divided into hard and soft types and these in turn may be subdivided to enable construction of interpretive keys. Soft bottom cover for example may be divided into types such

as dense grass beds of several species, grass patches, reworked grass beds, clear sandy, gravelly or muddy bottom, clear bottom with rooted calcareous green algae, mats of blue-green algae, various mixed types, etc. Hard bottom cover may be categorized as dense brown and red algae, gorgonians (soft corals or whip corals) with clumped brown algae, matted uniform filamentous green and red algae, calcareous green algae on hard bottom with thin sediment overlay, unattached mats of brown algae, dense frondose *Sargassum*, etc.

Maps of distributions of cover types and the photography itself provide valuable clues as to interactions occurring between bottom cover and environmental conditions. For example, gorgonian-algal cover is usually indicative of strong current washing (Fig. 12), wave action is seen in the location of grass bed blowouts (Fig. 2), sediment and algal shadowing behind grass patches show areas of slowed current (Fig. 8), sediment distribution is seen in different types of soft bottom cover, and so on. The most immediately important interrelationships are man-made ones. Effects of thermal outfall from a power plant, dredge spoil and siltation effects on bottom cover, and the effects of canal run-off and drainage were all seen in the photography, as mentioned above.

Of particular interest were the distribution of grass patches in the Keys and Biscayne Bay (Fig. 10). Patches apparently grow in sediments collected in solution holes formed by tree islands when the area was emergent during the Pleistocene. Mangrove peat has been found by Zieman (personal communication) in sediment cores taken in the patches. The photography showed patches to have distributions similar to modern tree islands in the Everglades and the distribution of patches seen in the photography thus apparently reflects the emergent Pleistocene drainage pattern.

Successional stages that occur during formation of bottom communities can also be seen. A progression, from cleared bottom (caused by wave action or dredging) through calcareous green algal cover, then to various species and admixtures of grasses and algae and finally to mature grass beds may be seen. Also, dynamic maintenance of sub-climax stages in strongly current-washed hard-bottom areas may be detected and described.

Environmental zonation along coasts with fresh-water runoff and on the edges of banks and shoals may also be described using the photography.

Again, all of these features and interrelationships are important to an understanding of ecological conditions in these areas. Similar features occurring on land would have already been understood by terrestrial workers, but a limited perspective has prevented their recognition underwater. They

must however be recognized if man is to recognize the effects he may have on and the benefits he may gain from coastal areas.

CONCLUSIONS AND DISCUSSION

As mentioned above, aerial photography has proven very useful for: 1) detection of unknown or unrecognized submarine biological features, 2) mapping and generalization of coastal biological resources, and 3) aiding in delineation of ecological interactions. These results have been of value in themselves and will be published in the biological literature. In addition, availability of the photography has proven to be of value to both researchers in pure marine ecology and to local agencies interested in coastal conditions.

It would appear that the ultimate value of remote visible imagery of coastal areas will depend on six different factors. First, expertise in photointerpretation of diverse coastal biota must be developed equivalent to that available for terrestrial features. A backlog of information on major features and distributions and their photoidentification must be developed if other more sophisticated techniques are to be applied and if instrumentation is to be properly designed. Second, both ecological researchers and local environmental agencies must become aware of the potential use of remote imaging methods. Third, the potential use of multispectral scanners, return-beam vidicons, imaging spectrographs, and similar instruments must be defined. Fourth, the possible application of data handling systems such as image-density photoenhancement, electronic enhancement, and computer interpretation must be explored. Fifth, the application of space-craft imagery must be understood. Finally, material must be made available to local researchers and agencies, since work in and surveillance of coastal areas is distributed among many separate organizations.

The major biological features seen in the area of the Florida Straits have become fairly well understood during the present work. However, different environments, such as highly productive tropical coastlines, polluted temperate areas, river deltas and so on must be explored. It may be possible to study dissolved and suspended materials as well. Some of these possibilities will be investigated during the coming year.

The material obtained during the present work proved of considerable use to several agencies and workers. The photography and results have been used by researchers at the Institute of Marine Science, University of Miami, in connection with studies of productivity of *Thalassia* "grass", studies of algal distribution, bottom community research, and pollution studies. Material was used by the Park Service in a survey of the Biscayne Bay National Monument, by the Dade County Pollution Control Board in investigation of thermal pollution,

and by the Florida State Department of Conservation. It appears that there are both research and applied potential for such material, and local workers must be aware of potential use and have available material for use. Satellite photography or imagery may provide such material.

Sophisticated imagery and data handling techniques will be very difficult to apply in coastal areas without more understanding of the imaged features. Spectral and tonal characters from a particular type of bottom cover are very complex. They depend on the "health" of the plants, the species present, and the scattering and absorbing characteristics and depth of the overlying water. Human photointerpretation is very difficult and depends on a number of visual cues, particularly shape, texture, edge pattern and distribution. Interpretation and identification without consideration of these cues may be impossible, and such cues are difficult to use with automated data processing. Distributions are also very complex and variable and the photoenhancement techniques applied have thus given confusing and ambiguous results (Conrod, Kelly and Boersma, 1968). Use of such techniques may await further understanding of the ecology of bottom biota and of human photointerpretation as well as development of new techniques and instrumentation. Nevertheless, these methods may have much use in examination of suspended and dissolved material in the water, since pattern, texture, shape etc. are not as important and since color, tone and contrast differences must be brought out in the imagery. These possibilities are now being investigated.

The usefulness of satellite imagery will depend on the types of instrumentation used and the resolution available. It would seem that color photography and 3-color return-beam vidicon material would be most immediately useful - the ability presently exists to understand and interpret the images. Multispectral imagery would at present seem of limited value since it would produce much ambiguous data; its application needs further study from aircraft and more field work.

The resolution needed from satellites depends on the features that should be imaged. This is difficult to generalize since the possible applications are so varied. Banks and shoals, major grass beds, tidal channels, sand bars, and so on are visible in much of the Gemini material. Biologists are taught to use a microscope very early, however, and the thinking tends to carry on. Probably some ecologists would wish to count grass blades and clumps of algae. Gemini photography nevertheless may be used to map major biological cover (Conrod, Kelly and Boersma, 1968) and certainly higher resolution is possible. Grass patches, blowouts, spillover lobes, reef features, etc. would probably be marginally seen on 30 m. resolution material. Hyperaltitude coverage of the Florida Keys area is being obtained to estimate what large-scale material will show.

SUMMARY

1) Photointerpretation of aerial photography aided by field surveys has been used at three test sites in the region of the Florida Straits in order to determine the application of such photography to coastal ecological studies.

2) It was found that the photography enabled identification and location of major unusual or unrecognized features, mapping and generalization of biotic bottom cover, and delineation of ecological relationships. Most of this would have been impossible or very difficult using usual survey methods. Examples are given.

3) Man-made features and pollution could be identified and studied.

4) It is concluded that several steps will be necessary for optimal use of remote sensing in coastal areas: a) ability in photointerpretation of diverse coastal environments must be developed; b) possible users must be made aware of the potential of such techniques; c) use of sophisticated imaging systems must be explored although they may be of limited use due to lack of photointerpretive background and complexity of environmental conditions; d) data handling systems such as enhancement and computer processing techniques must be studied, and may show greatest use in study of suspended materials such as pollutants and phytoplankton; e) application of hyper-altitude and satellite imagery must be further studied, pending availability of suitable material; f) satellite and aerial imagery must be made readily available to the diverse potential users.

5) The use of remote sensing in coastal areas should both aid in and depend upon much further development of what is now a relatively poorly known field of study.

BIBLIOGRAPHY

- Cloud, P. E. 1962. Environment of calcium carbonate deposition west of Andros Island, Bahamas. U. S. Dept. of the Interior, Geological Professional Paper 350.
- Conrod, A. C., A. Boersma and M. Kelly 1968. Investigation of visible region instrumentation for oceanographic satellites. Mass. Inst. of Technology, Experimental Astronomy Lab., Rept. no. RE-31, Vol. II.
- Conrod, A. C., M. Kelly and A. Boersma 1968. Aerial photography for shallow water studies on the west edge of the Bahama Banks. Mass. Inst. of Technology, Experimental Astronomy Lab., Rept. no. RE-42.
- Kelly, M. 1969. Aerial photography for the study of near-shore ocean biology. *in*: New Horizons in Color Aerial Photography, Seminar Proceedings, ASP - SPSE meetings, June, 1969. American Society of Photogrammetry, Falls Church, Va.
- Kelly, M. G., 1969. Applications of remote photography to the study of coastal ecology in Biscayne Bay, Florida. U. S. Naval Oceanographic Office, Report for contract N-62306-69-C-00322 52 pp.
- Kelly, M. G. and A. C. Conrod 1969. Aerial photographic studies of shallow water benthic ecology. *in*: Remote Sensing in Ecology, pp. 173-184. Univ. of Ga. Press, Athens, Ga.
- Kelly, M. G. and A. Conrod 1969. Aerial Photography. *Bio-Science* 19(4):352-353.
- Kumpf, H.E. and H. A. Randall 1961. Charting the marine environments of St. John, U. S. Virgin Islands. *Bull. Mar. Sci.* 11:543-551.
- Lee, W. T. 1922. The Face of the Earth as seen from the Air. American Geographical Society, N. Y.
- Lundahl, A. C. 1948. Underwater depth determination by aerial photography. *Phot. Eng.* 14(4):454-462.
- Macintyre, I. G. 1968. Preliminary mapping of the insular shelf off the west coast of Barbados, W. I. *Caribbean Journal of Science* (1&2):95-99.
- Newell, N. D., J. Imbrie, E. G. Purdy, and D. Thurber 1959. Organism communities and bottom facies, Great Bahama Banks. *Bull. Am. Mus. Nat. Hist.* 117:181-228.
- Strandberg, C. H. 1967. Aerial Discovery Manual. Wiley, N. Y.

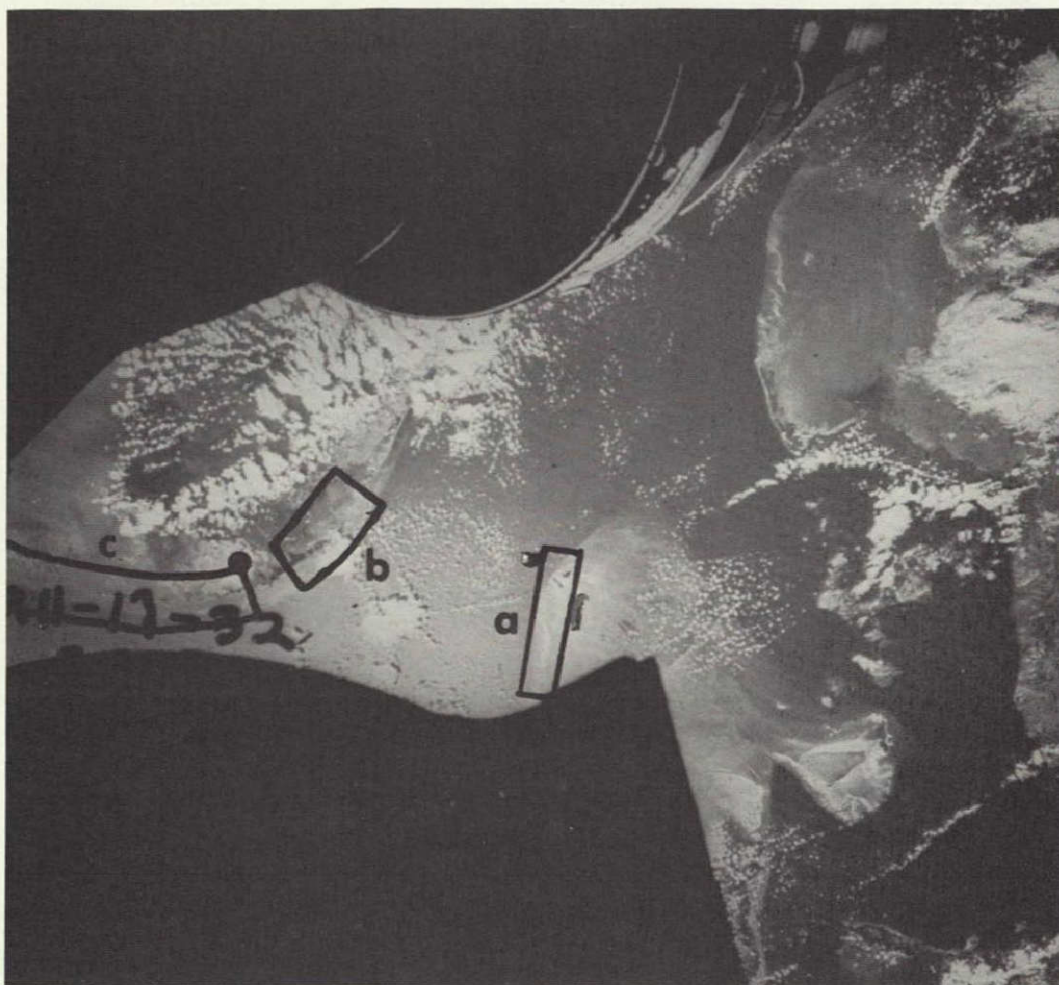


Figure 53-1.- Gemini photograph of the Florida Straits showing the test sites investigated. (a) Bahamas, site 162. (b) Biscayne Bay, site 163. (c) Florida Keys, site 169.

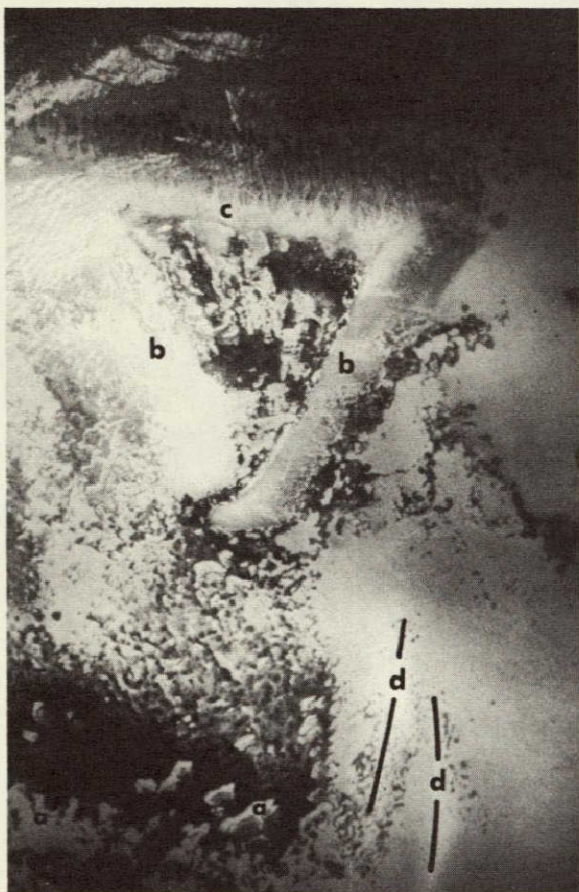


Figure 53-2.- Sambo Reef, Keys test site. (a) blowouts in grass beds. Note grass growth in storm lee of reef, also confluence of blowouts. (b) reef shoals, shaped by waves. (c) reef face. Note spur and groove formation. (d) shoal bars of sand. Note grass patches in protected lee of bars.

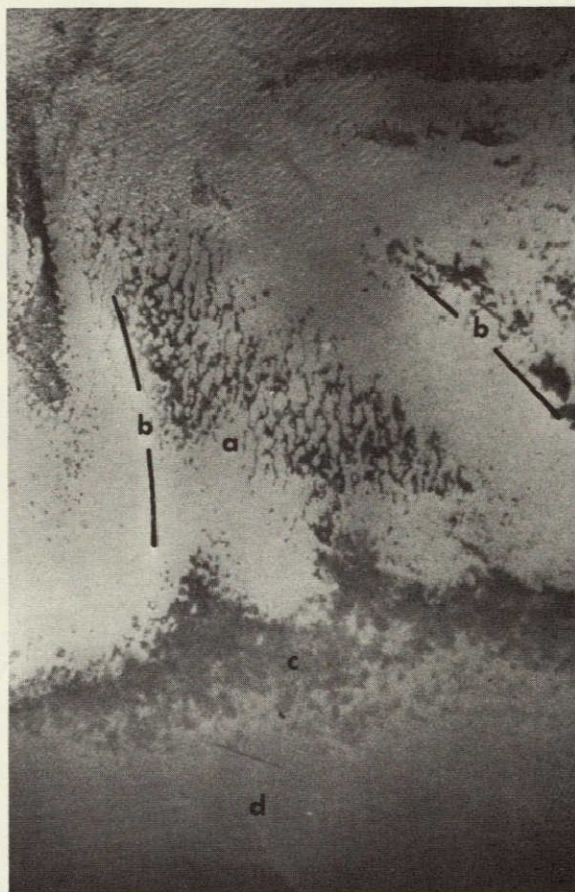


Figure 53-3.- Well-sorted sand bottom between reef-line and Hawk Channel, Florida Keys site. (a) grass patches formed as remnants of storm - surge blowouts (depth 3 to 4 m.). Note pattern caused by remnant blowout scarps. These are oriented toward waves refracted behind a shoal area not on the photograph. Note also the formation in relation to shoal bars of sand (b). (c) diffuse mixed grass in a poorly sorted muddy area on the edge of the channel. (d) Hawk Channel (depth 9 to 10 m.). Dark mottled tone caused by mats of blue-green algae.



Figure 53-4.- Ceasar's Creek south of Eliot Key, Biscayne Bay. This is a naturally-formed tidal channel. Note the spillovers at the ends of the channel and the mottled and textured bottom of mixed, patchy grass, gorgonians and algae.



Figure 53-5.- Area of hard and soft bottom, edge of Bahama Banks and south of Bimini. (a) a' - lineations in algal cover caused by character of hard-rock bottom. (b) wave cleared sandy bottom surrounded by grass beds with blowouts. (c) grass patches in depressions in bottom. (d) unexplained "ray" caused by relative lack of bottom cover seaward of an emergent rock, a fairly common feature in this area.

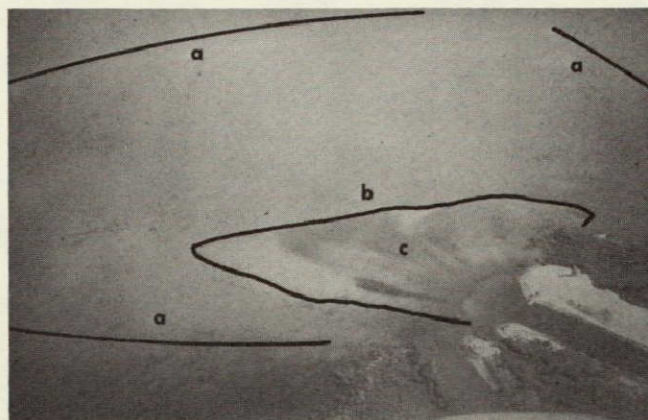


Figure 53-6.- Thermal effluent area from a powerplant, Biscayne Bay. Hand-held oblique photograph. (a) margin of zone of total bottom cover kill. (b) margin of outer zone with partial cover kill and damage. (c) suspended mangrove peat stirred up by a boat and distributed by effluent currents.



Figure 53-7.- Dredged channel, Biscayne Bay. Hand-held oblique photograph. (a) areas of lighter algal cover caused by siltation and thin silt cover. (b) grass patches in slightly thicker sediment cover.



Figure 53-8.- Area behind Marathon airport, Florida Keys. The small round dark areas are grass patches. Note that they are often arranged in lines and often surrounded by light bottom caused by a thin layer of sediment (too thin for grass growth). "Shadows" of unattached algal growth may be seen in the current lee of the patches. This is a common distributional pattern.

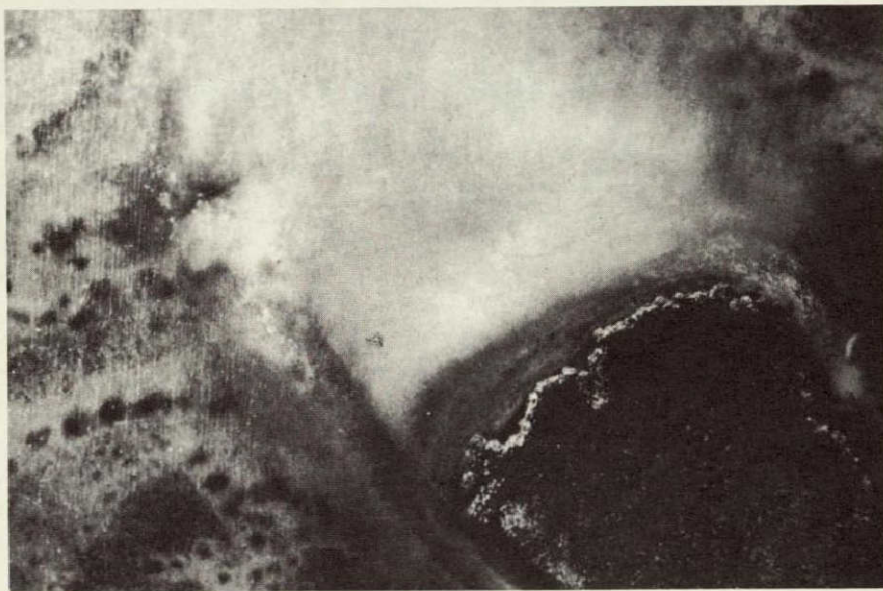
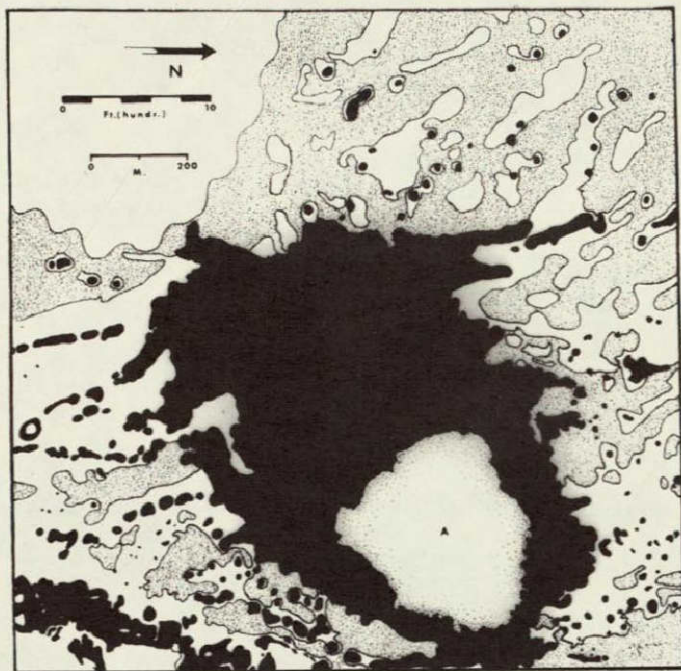


Figure 53-9 and 53-10.- Area around Arsenicker Key, Biscayne Bay. Black areas are grass beds and patches, stippled areas show hard bottom with gorgonians and algal cover. Grass patches grow in lines of solution holes in the bottom (see text). Note that they are surrounded by "halos" of thin, clear sediment.



Figure 53-11.- Grass patches and gorgonian - algal hard bottom cover. Note "halos", patch lines, and hard bottom texture.



Figure 53-12.- Current-scoured channel between Missouri and Ohio Keys, Florida Keys. Note digitation of channel, sand bars spilled from channel, and grass patches and beds. (a) channel. (b) U.S. Rt. 1. (c) sand bars. (d) mottled, mixed, variable grass, gorgonian, algal cover typical of bottom in the lee of the Florida Keys.